THE UNIVERSITY OF CHICAGO

ORGANIZED ARRAYS OF FUNCTIONAL MOLECULES SUPPORTED BY GALLIUM-PORPHYRIN MONOLAYERS ON HIGHLY ORDERED PYROLYTIC GRAPHITE

A DISSERTATION SUBMITTED TO

THE FACULTY OF THE DIVISION OF THE PHYSICAL SCIENCES

IN CANDIDACY FOR THE DEGREE OF

DOCTOR OF PHILOSOPHY

DEPARTMENT OF CHEMISTRY

BY

WING-YEUNG LAU

CHICAGO, ILLINOIS

AUGUST 2016

TABLE OF CONTENTS

Page

LIST OF FIGURES

Figure **Page**

LIST OF TABLES

LIST OF SCHEMES

Scheme **Page**

ACKNOWLEDGEMENTS

First and foremost, I would like to thank my advisor, Professor Mike Hopkins, for his support and guidance (and also for putting up with me) over the past years. Not only have I grown as a researcher under his mentorship, I have also learned much from his great sense of professionalism and scholarship. I am grateful for having the opportunity to work in his research group. I would also like to extend a special thanks to my high school chemistry teacher, Mr. Groves, who not only helped me learn the fundamentals of chemistry, but also see the fun that comes along with it. I don't think I would ever have considered becoming a chemist if it wasn't for his influence. I would also like to thank Professor Richard Jordan, and Professor Dmitri Talapin not only for serving on my thesis committee, but for letting me pass my unconditionally pass my candidacy exam.

I would also like to thank everyone in the Hopkins group that I've had the chance to work with: Cameron Iverson basically convinced me to join the materials subgroup, got me started on my project, and also helped me gain a lot of worldly knowledge by reminding me to look things up on Urban Dictionary; Ben Lovaasen and Sarah Shaner were great to have around with their wisdom of senior graduate students and for reminding me that everything was going to be okay; Dan O'Hanlon essentially fulfilled the role of the whacky older brother who provided sound advice amidst the clever schemes that should never have been attempted; Davis Moravec and his antics never failed to put a smile on my face; Nathan La Porte always astounded with his breadth of knowledge in a broad range of topics, especially on pork-related ones; Mark Westwood has always been the nicest guy around, and is always happy to help me grab things that I can't possibly reach. I have also learned much from interacting and working with several undergrads, including Dylan Lynch, Mollye Levin, Hannah Friedman, and Noah Lewis.

Judith Kamm and Hunter Vibbert deserve special acknowledgements for being the best (and worst) of friends ever since they joined the lab; Judith has been my partner in crime in the materials subgroup, and I will always remember the nights we spent working on the NSF grant proposal, the times we went on trips and conferences together, and her incomparable eye rolls; Hunter has always been willing to go on adventures together, and always available to make sure I'm not making terrible decisions on my own by making terrible choices with me. I will miss our Friday adventures, board game sessions, and movie nights, but please get rid of that cardboard cutout of me.

Much of the work that I have done would not be possible without the help of facilities staff members. I would like to thank Dr. Antoni Jukewicz, Dr. Jin Qin, Dr. Qiti Guo, and especially Dr. Justin Jureller, who was always willing to listen to my rants about various aspects of life. I would also like to thank the staff in the department office. Melinda has always been very helpful, and Vera was always willing to give advice on various matters, or just have a chat. Aside from the staff members, there are many, many other students and colleagues who have made this journey worthwhile, including but not limited to Landon Durak, Dmitriy Dolzhnikov, Matt Kurley, Chris Hansen, Tim Lau, Ken Ellis-Guardiola, Mary Andorfer, and Alex Schneider.

I want to thank my family and friends (and even my friends' families). Although I have not had the chance to be with them as often as I wanted, they have always been there for me and always happy to see me whenever I needed to get out of Chicago. My dad has never been particularly expressive, but he has always been entertained when I told him about the most inane details about my life during our Skype sessions, which somehow always made me feel a lot better; I'm sure mom would've been entertained too. Lastly, there's Greg, who has, in his own

ways, been supportive of my endeavors despite going through the PhD experience himself. I am incredibly lucky to have someone who is able to put up with me for so long.

to my family and friends with love and gratitude

ABSTRACT

Molecular self-assembly on surfaces has garnered significant interest as a nanofabrication process due to its ability to organize large assemblies of molecular building blocks with intrinsic properties. Surface-confined two-dimensional (2D) self-assembled monolayers based on small, planar organic and organometallic molecules at the solid-liquid interface have been heavily investigated due to their propensity to produce highly specific patterns that is determined by molecular design, as well as the variation in sample preparation conditions such as solution concentration, temperature, and choice in solvent. The focal point of the research presented in this work is to explore the use of metalloporphyrins, which have been shown to form well-ordered, extensive supramolecular assemblies on atomically flat substrates and can also support axial ligands through covalent interactions through the metal centers, as molecular building blocks to extend the 2D structures into functional 3D systems.

In Chapter 2, the preparation, characterization, and self-assembled monolayer formation of Ga(III) *meso*-tetra(*n*-$C_{10}H_{21}$)porphyrins [Ga($TC_{10}P$)X] with axial oligo-phenylene-ethynylene (OPE) ligands [Ga($TC_{10}P$)(OPE)] are discussed. Scanning tunneling microscopy (STM) imaging of the monolayers formed by these complexes at the solid-liquid interface shows that the packing arrangement of these structures is identical to that of the free-base derivative, which shows that the incorporation of tall, pillared structures as axial ligands does not disrupt the formation of self-assembled monolayers in which the porphyrin cores are oriented parallel to the substrate and also indicates that Ga(III)-porphyrin monolayers can be used to anchor functional molecules above the surface.

The subsequent chapters focus on Ga-porphyrin complexes prepared through alternative ligand-attachment chemistry. In Chapter 3, the synthesis and characterization of novel Ga-porphyrin-carboxylate and aryloxide complexes are presented. Taking advantage of the facile reactivity of Ga($TC_{10}P$)(OH) towards carboxylic acids and aryl alcohols, a variety of novel dyads with functional axial subunits such as chromophores and electroactive centers were prepared. The self-assembly of the newly prepared complexes at the solid-liquid interface is reported in detail in Chapter 4. In Chapter 5, the self-assembly of Ga($TC_{10}P$)(OH) at the solid-liquid interface and subsequent attempts to chemically modify the monolayers post-deposition are discussed.

CHAPTER 1

Introduction

Many of the advances made in electronic technologies depend upon the continual miniaturization of structural components. The traditional top-down approach towards device fabrication, which is well-represented by lithographic techniques, can produce intricate architectures on the nanoscale.[1, 2] While such techniques have yet to reach their fundamental physical limits, there has been a growing interest in exploring bottom-up nanofabrication. This involves the organization of pre-synthesized molecular building blocks with desired properties to create functional nanostructures. This approach is attractive for miniaturization because the size of a molecule (on the order of ~1 nm) is small compared to the scale length currently achievable by top-down nanofabrication techniques.[3, 4] A fundamental challenge for the development of bottom-up nanofabrication lies in the need to controllably organize the molecular building blocks on a large scale. Scanning probe microscopy (SPM) has allowed the precise positioning of single atoms and molecules through direct manipulation.[5-9] However, this method of organizing nanostructures is inherently not scalable due to its slowness and extreme conditions (e.g., low temperature under ultra-high vacuum (UHV)) required for the process.

An alternative strategy for bottom-up nanofabrication involves the use of molecular building blocks that can spontaneously organize into well-defined supramolecular structures through non-covalent interactions. Molecular self-assembly of functional molecules is attractive because:[10] 1) it is an inherently parallel process, which allows for the rapid generation of structures; 2) it can generate structures with sub-nanometer precision; and 3) three-dimensional architectures can be generated. Self-assembly at the interface with a surface, such as an electrode, affords the opportunity to electronically address the resulting structure. An archetypal

example are the self-assembled monolayers (SAMs) of alkanethiols on thin metal films (most commonly on Au, but SAMs on Pd, Ag, Cu, and Hg have also been studied) with metal-sulfur bonds between the substrate and the thiol head groups (Figure 1.1).[11] These systems offer the opportunity to install functional molecules above the substrate at the end of the alkanethiols orienting away from the surface. The functional entities are generally embedded into a matrix of nonfunctionalized spacer molecules either by the coadsorption of multiple components,[12-15] or by the insertion of functionalized thiols into defect sites of pre-formed SAMs.[16-20] As a result, while functional molecules can be positioned controllably in the vertical direction, their distribution within mixed adlayers is often ill-defined, thus making the preparation of systems with well-defined 2D arrangements generally difficult to achieve.

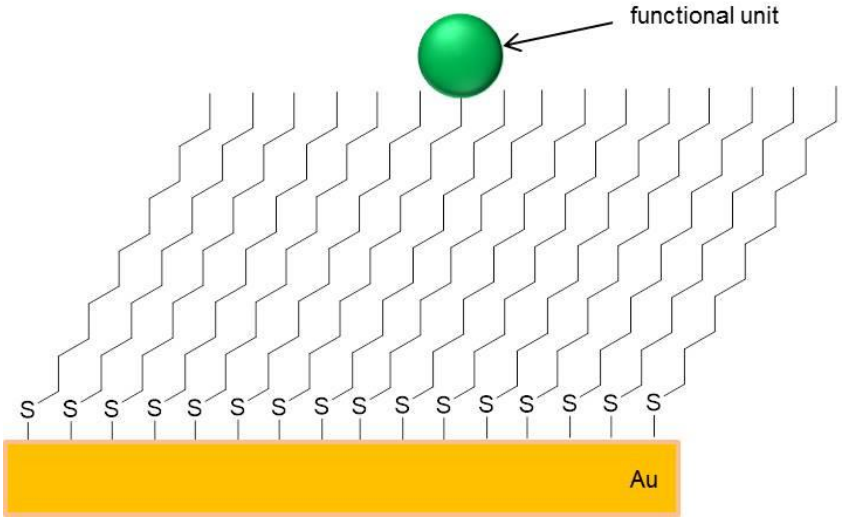

Figure 1.1. Schematic representation of an alkanethiol-based SAM on a gold surface with a randomly incorporated functional unit.

A different class of self-assembled monolayers is represented by two-dimensional supramolecular assemblies of planar organic and organometallic molecules physisorbed on atomically flat substrates, where the molecular planes are oriented parallel to the surface.[21-28] These systems have garnered significant interest since they provide opportunities to achieve two-

dimensional morphological control over molecular arrangements with sub-nanometer precision through molecular design. The packing geometry and intermolecular distances are manipulated through the incorporation of substituents that can engage in directional (e.g., hydrogen bonding, dipole-dipole, metal-ligand coordination) or non-directional (e.g., van der Waals) intermolecular interactions, as well as through other experimental variables such as supernatant concentration, temperature, and the substrate.[26] More recently, there have been efforts to control the spatial arrangements of functional molecules in all three dimensions by combining the two-dimensional proximity control afforded by supramolecular assembly of the type described above with the potential of suitably designed organic molecules to serve as supports for subunits positioned above the physisorbed molecular plane. This "platform approach" is exemplified by the use of molecules such as triazatriangulenium (TATA) derivatives[29-34] (Figure 1.2) and "Janus tectons"[35-37] (Figure 1.3) to create well-ordered, surface-confined supramolecular assemblies, which have been used to position molecular switches,[29-31] chromophores,[34] and electroactive centers[36, 37] above the self-assembled monolayers. In principle, the distance between the functional unit and the surface can be adjusted by varying the length of the spacer between the functional unit and the molecular platform. The ability to control the spatial configuration of functional units in all three dimensions makes the platform approach a promising method for the controlled organization of functional molecules.

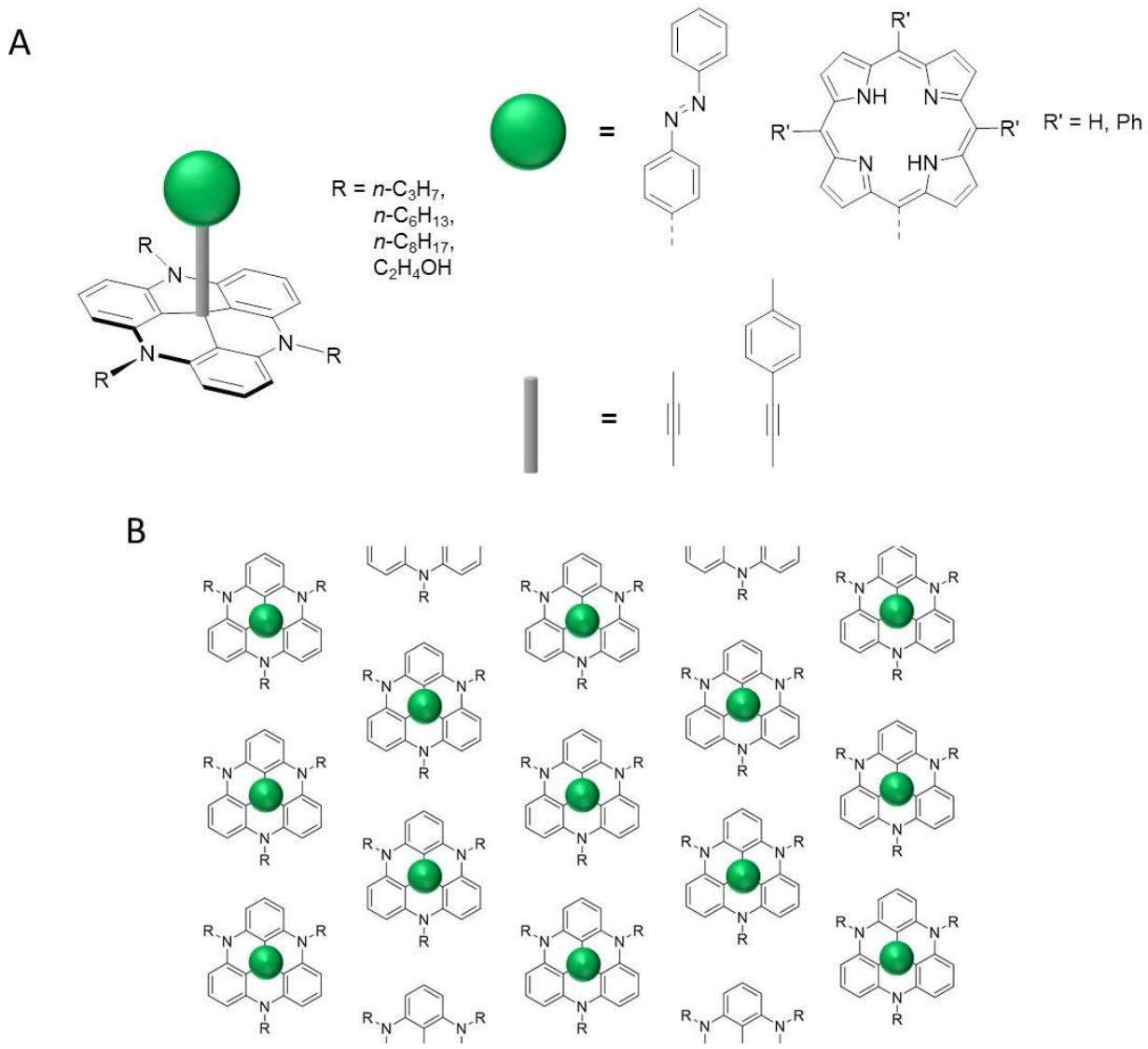

Figure 1.2. TATA molecular platforms. (A) Molecular structure of TATA derivatives. (B) Schematic representation of a TATA monolayer.

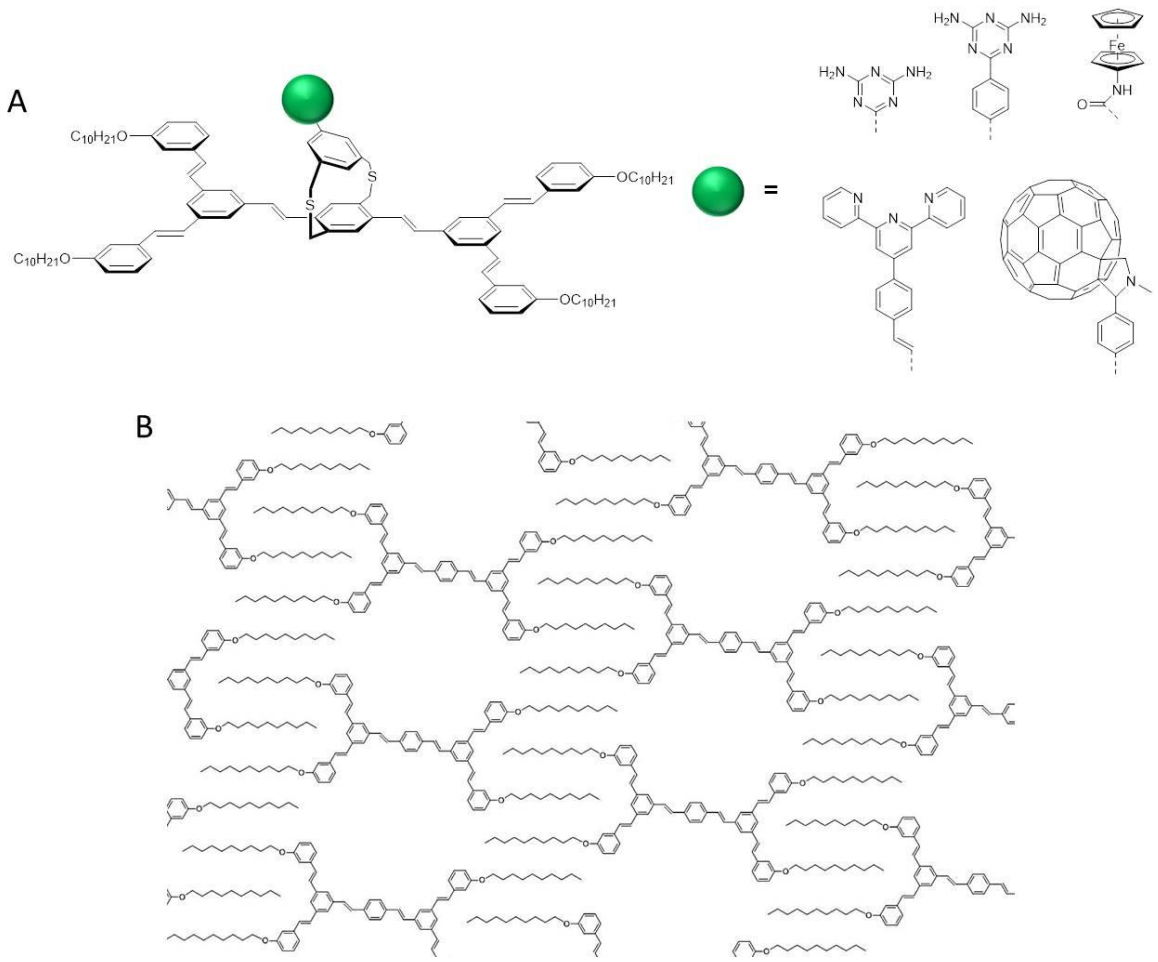

Figure 1.3. Janus tecton molecular platforms. (A) Molecular structure of a Janus tecton. (B) Schematic representation of a Janus tecton monolayer; the top layers are omitted for clarity.

Metalloporphyrins and related complexes (e.g., phthalocyanines) also hold great promise as molecular platforms due to the synthetic modularity of this class of compounds, as well as their demonstrated ability to form well-ordered structures on a variety of substrates (e.g., Au(111), Cu(111), highly oriented pyrolytic graphite (HOPG)). Self-assembled porphyrin monolayers have been shown to exhibit a wide range of structural arrangements that are controlled by structure-directing peripheral substituents,[38-41] which can be easily incorporated through synthetic organic chemistry. Some of the more commonly used peripheral substituents include *meso*-alkoxyphenyl groups, which induce the formation of lamellar structures

(characterized by alternating rows of porphyrin cores and interdigitated alkyl chains, which will be discussed in greater detail; Figure 1.4a),[42-46] *meso*-carboxyphenyl groups, which cause the formation hydrogen-bonded networks (Figure 1.4b),[47-49] and beta ethyl groups (octaethylporphyrin), which enable formation of close-packed hexagonal arrays (Figure 1.4c).[50-57] Structural perturbations to the aforementioned systems can also be introduced (such as the addition of kinks[58] and chiral centers[59] within the long-chain substituents, or the use of asymmetric porphyrins;[48, 49, 60] Figure 1.5) to diversify the packing geometries exhibited by the self-assembled monolayers. Highly ordered porphyrin supramolecular assemblies on surfaces have been investigated both under UHV conditions and also at the solid-liquid interface. While the former generally provides images of higher resolution, the latter provides the opportunity for the benchtop processing of materials and can be used to study species with low thermal stability or large size.[22] In addition, sample preparation and imaging under ambient conditions are more compatible with the goal of developing a scalable bottom-up nanofabrication method.

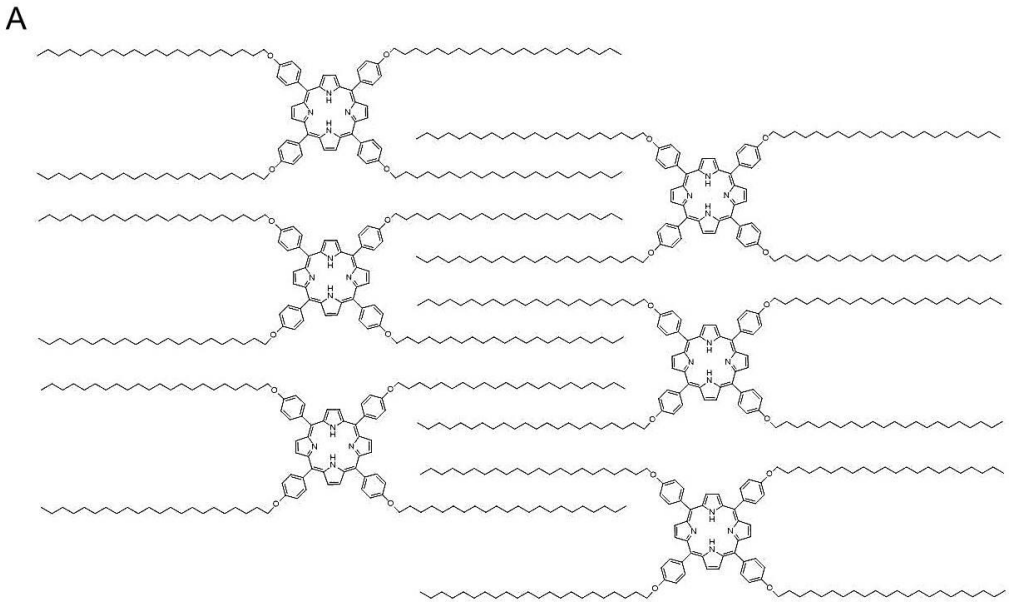

Figure 1.4a. Schematic example of porphyrin monolayer exhibiting a lamellar arrangement that is characterized by alternating rows of porphyrin cores and interdigitated peripheral alkyl side chains.

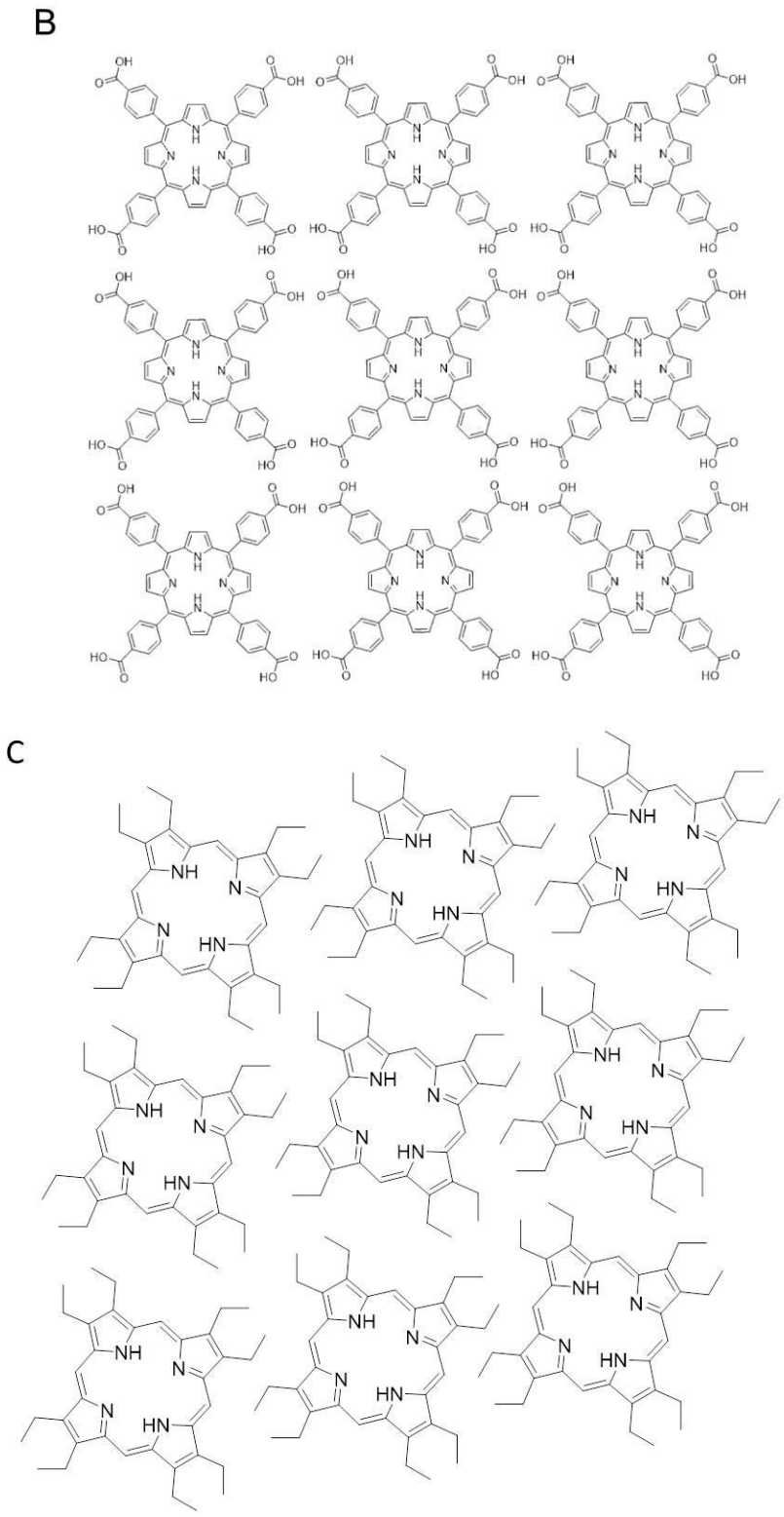

Figure 1.4b,c. Schematic example of porphyrin monolayers exhibiting (B) a square lattice based on H-bonding interactions, and (C) a hexagonally close-packed porphyrin array.

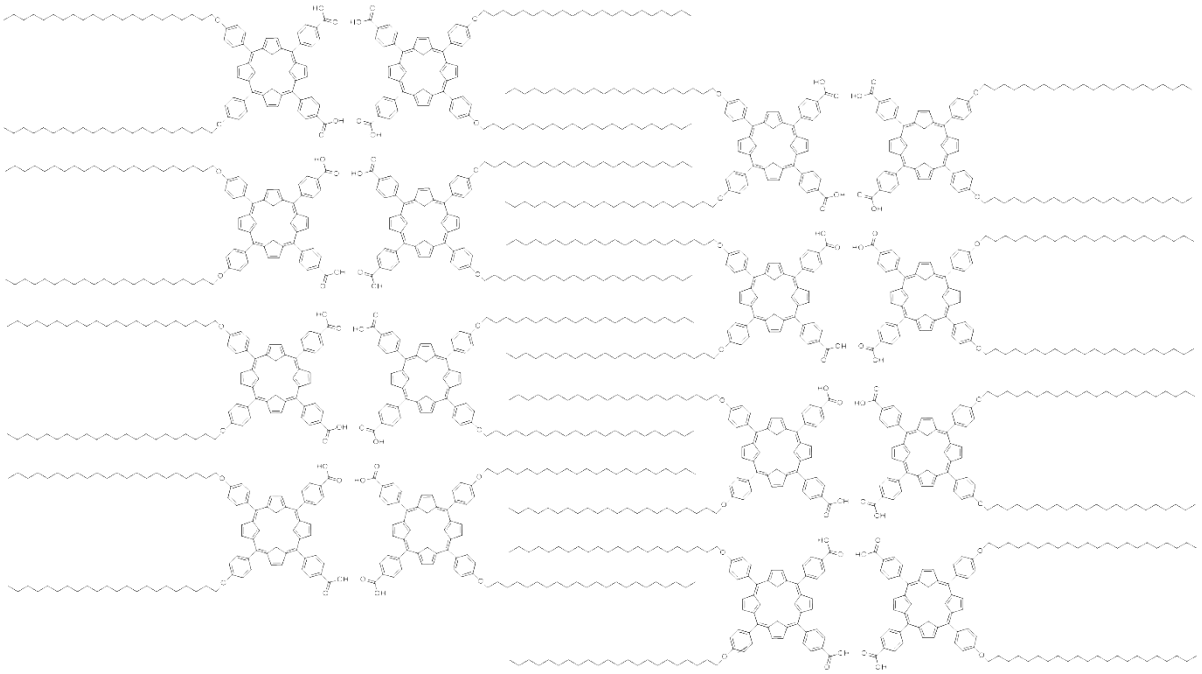

Figure 1.5. Schematic example of a porphyrin monolayer exhibiting an alternating arrangement of porphyrin dimers and interdigitated alkyl chains formed by porphyrin molecules containing both peripheral alkyl side chains and H-bonding substituents.

In addition to the two-dimensional spatial control afforded by peripheral substituents, the structural modularity of metalloporphyrins is further exemplified by the variety of metal centers that can be incorporated, which can govern the electronic and photophysical properties.[61] Moreover, by using a metal center that provides an additional coordination site, porphyrin assemblies can be extended above the surface through axial ligation. For example, zinc(II) porphyrins have been studied extensively due to their propensity to form well-ordered monolayers on substrates such as highly ordered pyrolytic graphite (HOPG) and Au(111) under various experimental conditions, as well as their affinity for nitrogenous bases which allows for the attachment of functional molecules through dative bonding (Figure 1.6).[62-66] However, this structural motif is unsuitable for constructing rigid three-dimensional structures due to the reversible nature of dative interactions. An alternative approach is to use a metal center that can covalently bind axial ligands. While most of the literature on self-assembled monolayers based

on five-coordinate metalloheterocycles involves metal-chloride[67-69] and metal-oxo compounds,[50, 53, 70] there is an example of a stable, ordered monolayer of a titanium–phthalocyanine complex on HOPG with the more complex catecholate axial ligand,[70] which hints that axial sites could be used to incorporate functional moieties through a connecting ligand.

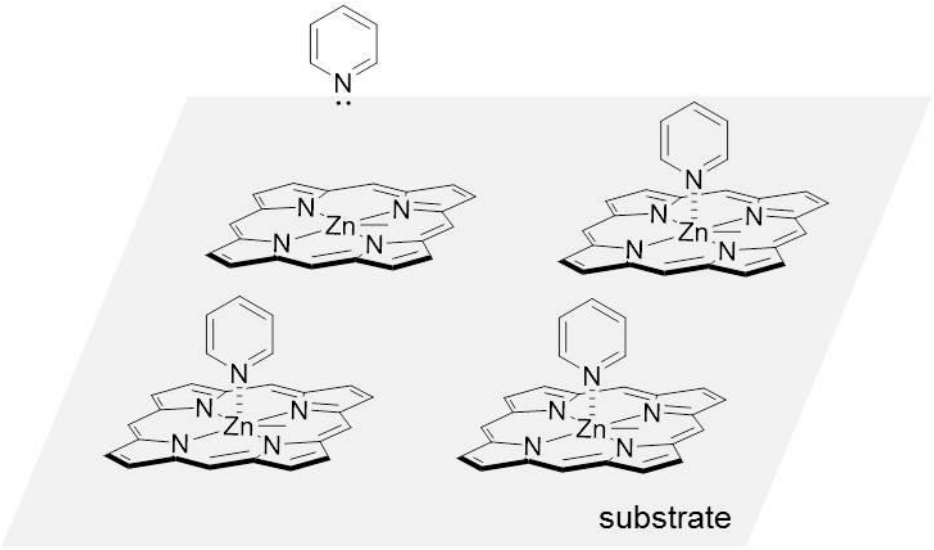

Figure 1.6. Modification of a Zn(II) porphyrin monolayer through the dative bond approach.

Research in our group directed toward this possibility has focused on the use of five-coordinate gallium(III)-porphyrins as molecular building blocks (Figure 1.7) for preparing self-assembled monolayers due to the ability of the Ga metal center to covalently bind an axial ligand. Since these complexes exhibit a square-pyramidal geometry in which the axial ligand is oriented normal to the porphyrin plane,[57, 71-80] we hypothesized that self-assembled monolayers of these five-coordinate metalloporphyrins could be used to produce defined patterns of axial functional units positioned at a controllable height above the two-dimensional assemblies, provided that self-assembled monolayer formation is not disrupted by the incorporation of the axial ligands (Figure 1.8). In the proposed system, the spatial arrangements of functional

molecules can be controlled by altering the peripheral substituents, which can define the packing geometry and intermolecular distances in the *x*,*y* plane, while the distance between the functional molecules and the substrate in the *z*-direction can be adjusted by changing the length of the spacer.

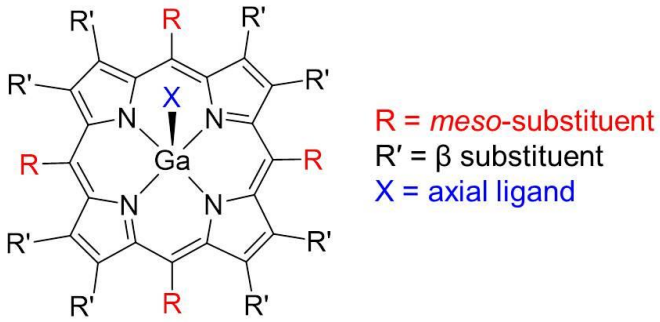

Figure 1.7. General molecular structure of a Ga(III) metalloporphyrin.

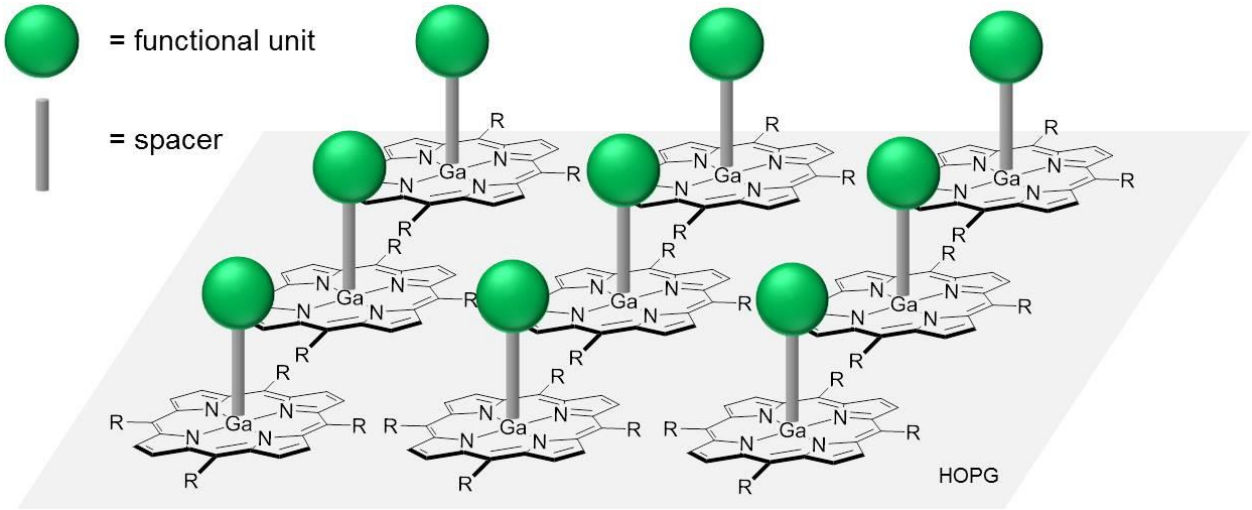

Figure 1.8. Patterning functional units using five-coordinate gallium(III)-porphyrin self-assembled monolayers on HOPG.

Our group has previously investigated the self-assembly of monolayers of Ga(III) octaethylporphyrins [Ga(OEP)X; X = Cl, Br, I, O_3SCF_3, CCPh] at the 1-phenyloctane/HOPG interface. The self-assembled monolayers were studied by scanning tunneling microscopy (STM) due to the molecular resolution provided by this technique, which allowed for the precise determination of the packing geometry and intermolecular distances exhibited by the self-

assembled structures. HOPG was chosen as the substrate due to its air stability and the ease of preparing a clean surface prior to sample deposition, which is achieved simply by manual cleavage of the top layers with adhesive tape. The decision to study the self-assembled monolayers at the solid-liquid interface, rather than at the solid-air interface or in UHV, was due to the self-repairing process that is allowed by the dynamic exchange of adsorbed and solvated molecules. This generally results in reproducible and persistent structures.[22] Our results showed that the presence of axial ligands, as well as the variations in axial ligands, had no effect on the pseudohexagonal, close-packed arrangement (Figure 1.9) that is typical of self-assembled monolayers of four-coordinate M(OEP) compounds (M = Ni,[50] Co,[51-53] Pt,[54] Cu,[55] Zn[55, 56]) under similar experimental conditions, as well as of V(OEP)(O), which is the only other five-coordinate OEP compound that has been investigated.[57] This demonstrates that the preparation of self-assembled monolayers of five-coordinate metalloporphyrins, in which the axial ligands are oriented perpendicular to the surface, can be achieved. Importantly, it was observed that the nature of the axial ligand affected the stability of the monolayer; monolayers formed by derivatives containing larger axial ligands (L = O_3SCF_3, CCPh) were found to be disrupted during STM imaging, which was potentially caused by interactions between the multiatom axial ligands and the STM tip, whereas the halide derivatives were very stable. With the interest of controllably patterning functional molecules, which may have more complex structures and greater steric bulk, alternative porphyrin building blocks for the preparation of robust self-assembled monolayers are required.

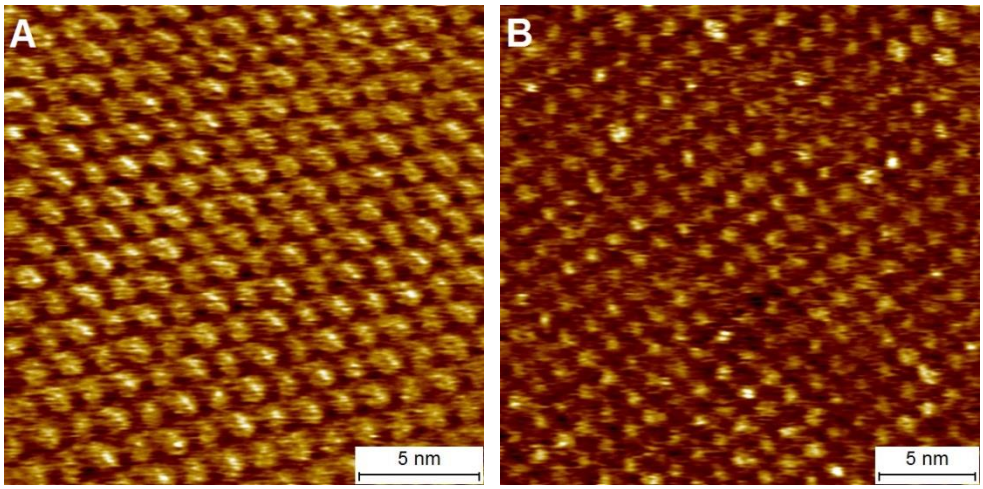

Figure 1.9. STM images of (A) a Ni(OEP) monolayer (I = 15 pA, V = −700 mV), and (B) a Ga(OEP)(CCPh) monolayer (I = 12.5 pA, V = −600 mV) on HOPG at the solid-liquid interface (1-phenyloctane, 5.0×10^{-4} M). From Ref. 64.

The use of long-chain alkyl substituents on planar molecules is a common strategy employed to stabilize their self-assembled monolayers on HOPG. The high affinity of such compounds for HOPG is driven by two main factors: the van der Waals interactions between the adsorbed molecules and the substrate that result from the near-commensurate packing of the carbon backbone of the alkyl chains on the sp^2-hybridized lattice of graphite; and the van der Waals interactions that arise from the interdigitation of neighboring alkyl groups ("crystallization").[81] The immobilization of porphyrin monolayers through the use of long-chain-alkyl substituents has been demonstrated by the self-assembly of *meso*-tetraalkylporphyrins (TC_mP),[63, 82-90] which are the porphyrins studied in this thesis, and *meso*-tetraalkoxyphenylporphyrins[42-46] (which are not used in this work) on substrates such as Au(111) and HOPG.[38] To date, STM studies on self-assembled TC_mP monolayers at the solid-liquid interface have been reported for m = 10–17[63, 82-87, 89, 90] and 19[88] under a variety of solvents such as 1-phenyloctane, *n*-tetradecane, and 1-octanoic acid at various solution concentrations (Table 1.1), and the experimental results are complimented by recent computational efforts to understand the chain-length dependence of the free energy of TC_mP monolayer formation.[89, 90]

One complication with TC_mP monolayers is that they can exhibit structural polymorphism, a phenomenon that is enabled by the conformational flexibility of the alkyl side chains and is affected by solution concentration. This phenomenon is observed in the systems to be described here. The adsorption configurations of TC_mP molecules on HOPG have been attributed to two main types of polymorphs, which are characterized by the adsorption of two alkyl chains on the substrate (higher density unit cell) or four alkyl chains on the substrate (lower density unit cell), as illustrated in Figure 1.10. In this work, the unit cells of the TC_mP self-assembled monolayers are defined by the lattice parameters a, b, and Γ, which represent the shortest intermolecular distances found within the structures and the lattice angle between the two lattice vectors, respectively. The unit cell parameters, as defined in this work and presented in Table 1.1 for previously reported systems, are represented in red in Figure 1.10.

Table 1.1. Reported Unit Cell Parameters for MTC_mP at the Liquid/HOPG Interface.

M	*m*	Solvent	Conc.(M)	*a* (nm)	*b* (nm)	*Γ* (°)	Ref.
H_2	10	1-phenyloctane	$< 1 \times 10^{-4}$	1.31(12)	1.90(10)	70(5)	83
H_2	11	1-phenyloctane	$< 1 \times 10^{-4}$	1.39(9)	2.00(13)	84(4)	83
Cu	11	1-octanoic acid	1×10^{-4}, 1×10^{-6}	1.26(5)	2.05(5)	79(4)	84, 85
				1.92(9)	2.05(5)	71(4)	
Cu	11	1-octanoic acid	1×10^{-3}, 1×10^{-4}, 1×10^{-7}	1.26(5)	1.70(15)	68(4)	85
				1.26(5)	2.05(5)	79(4)	
				1.92(9)	2.05(5)	71(4)	
				1.74(8)	2.16(14)	76(5)	
H_2	12	1-phenyloctane	$< 1 \times 10^{-4}$	1.24(6)	2.08(12)	79(4)	83
H_2	12	*n*-tetradecane	1×10^{-4}	1.4(1)	1.7(1)	72(1)	86
H_2	12	*n*-tetradecane	1×10^{-3}	1.4(1)	1.9(2)	80(6)	63
Zn	12	*n*-tetradecane	1×10^{-3}	1.4(2)	2.0(2)	88(8)	63
Zn	12	*n*-tetradecane	saturated	1.34(7)	2.08(9)	80(3)	87
H_2	13	1-phenyloctane	$< 1 \times 10^{-4}$	1.57(4)	1.71(4)	82(2)	83
H_2	13	1-phenyloctane	4×10^{-3}	1.68(4)	1.80(4)	82(2)	90
				1.94(3)	2.13(5)	77.4(1.5)	
Co	13	1-phenyloctane	4×10^{-3}	1.66(4)	1.76(5)	79(3)	90
				1.93(5)	2.12(4)	79.3(1.8)	
H_2	14	1-phenyloctane	$< 1 \times 10^{-4}$	1.49(6)	2.18(12)	75(4)	83
				2.02(11)	2.14(3)	87(7)	
H_2	15	1-phenyloctane	$< 1 \times 10^{-4}$	2.11(12)	2.14(13)	88(2)	83
H_2	15	1-phenyloctane	4×10^{-3}	2.12(3)	2.18(5)	83.0(1.6)	90
H_2	16	1-phenyloctane	$< 1 \times 10^{-4}$	1.40(8)	2.25(15)	76(5)	83
				2.07(13)	2.25(15)	85(3)	
H_2	17	1-phenyloctane	4×10^{-3}	2.13(3)	2.37(5)	86.5(1.4)	89
H_2	19	1-phenyloctane	4×10^{-3}	2.17(5)	3.38(6)	87.9(1.4)	88
Co	19	1-phenyloctane	4×10^{-3}	2.23(7)	2.54(8)	87.6(1.8)	89
CoCl	19	1-phenyloctane	4×10^{-3}	2.22(6)	2.57(9)	88.0(1.2)	89

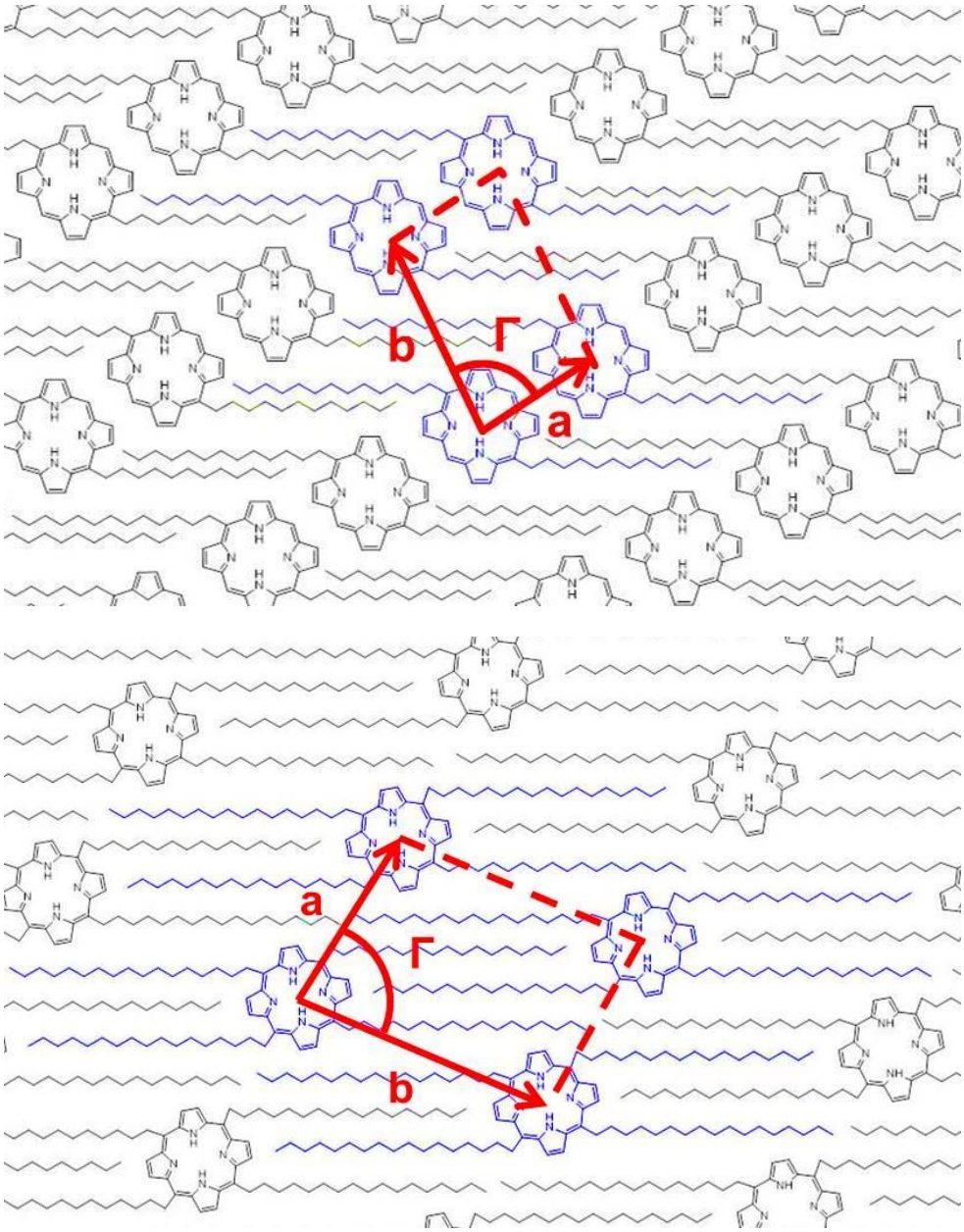

Figure 1.10. Examples of packing arrangements exhibited by *meso*-tetraalkylporphyrins monolayers at the solid-liquid interface. Top: arrangement in which two alkyl chains per porphyrin are adsorbed (nonadsorbed chains not shown); bottom: arrangement in which all four alkyl chains are adsorbed.

The research presented in this work focuses on the investigation of *meso*-tetra(*n*-$C_{10}H_{21}$)porphyrin ($TC_{10}P$) as the molecular platform. The long decyl side chains are expected to stabilize the porphyrin monolayers through enhanced adsorbate-substrate and adsorbate-adsorbate interactions. The metal center used will be Ga(III), which was shown in our prior

studies of Ga(OEP)X complexes to be suitable for supporting complex axial ligands in monolayers, and is also usually air stable. In Chapter 2, the synthesis, characterization, and self-assembly of a series of Ga(III)-porphyrin complexes containing axial oligo-phenylene-ethynylene (OPE) ligands [Ga($TC_{10}P$)(OPE); OPE = CCPh, *p*-CCC_6H_4CCPh, 4,4′-$CCC_6H_4CCC_6H_4CCPh$; Figure 1.11) are described; the ligands are chosen to show that the incorporation of tall, axial molecular wires as ligands does not disrupt the face-on adsorption configuration of the porphyrin complexes (where the porphyrin cores lie parallel to the surface) on HOPG. $H_2TC_{10}P$ and Ga($TC_{10}P$)Cl monolayers are first investigated at the 1-phenyloctane/HOPG interface as reference structures for the Ga($TC_{10}P$)(OPE) complexes. STM imaging shows that all compounds form extensive, well-ordered monolayers on HOPG, with the porphyrin parallel to the surface and the axial ligands oriented normal to the surface. Structural polymorphism was observed for the two taller Ga($TC_{10}P$)(OPE) derivatives at the onset of STM measurements, but these reverted to a single thermodynamic structure over time. This shows that the axial ligand can influence the surface chemistry of Ga($TC_{10}P$)X complexes.

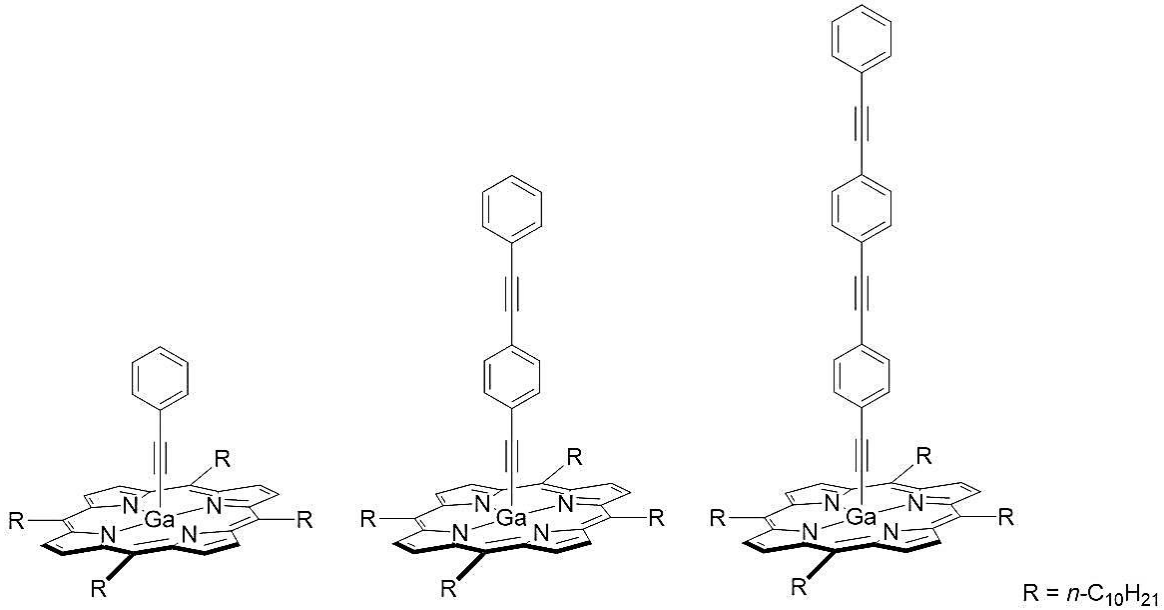

Figure 1.11. Molecular structures of Ga($TC_{10}P$)(OPE) complexes.

With the success of patterning tall, pillared ligands using Ga($TC_{10}P$) as the molecular platform, ligand attachment chemistry beyond acetylides was explored in order to expand the scope of functional molecules that can be incorporated into the self-assembled monolayers. In Chapter 3, the synthesis and characterization of a series of Ga-carboxylate [Ga($TC_{10}P$)(O_2CR)] and Ga-aryloxide [Ga($TC_{10}P$)(OR)] complexes containing functional ligands (e.g., a fluorescent dye, redox-active centers, and a charged moiety; Figure 1.12) are discussed. These linkages are of interest because carboxylic acids and aryl alcohols can be easily appended to a large variety of functional molecules, and have been shown to react with other metalloporphyrins (M = Al,[91-96] In,[97] Ge,[98, 99] Sn[100-104]) in one-step reactions to form molecular dyads or triads. Through both NMR-scale and preparatory-scale reactions, it is shown that Ga($TC_{10}P$)(O_2CR) and Ga($TC_{10}P$)(OR) compounds can be easily prepared in good yield by reacting Ga($TC_{10}P$)(OH) with the corresponding carboxylic acid or aryl alcohol in air at room temperature.

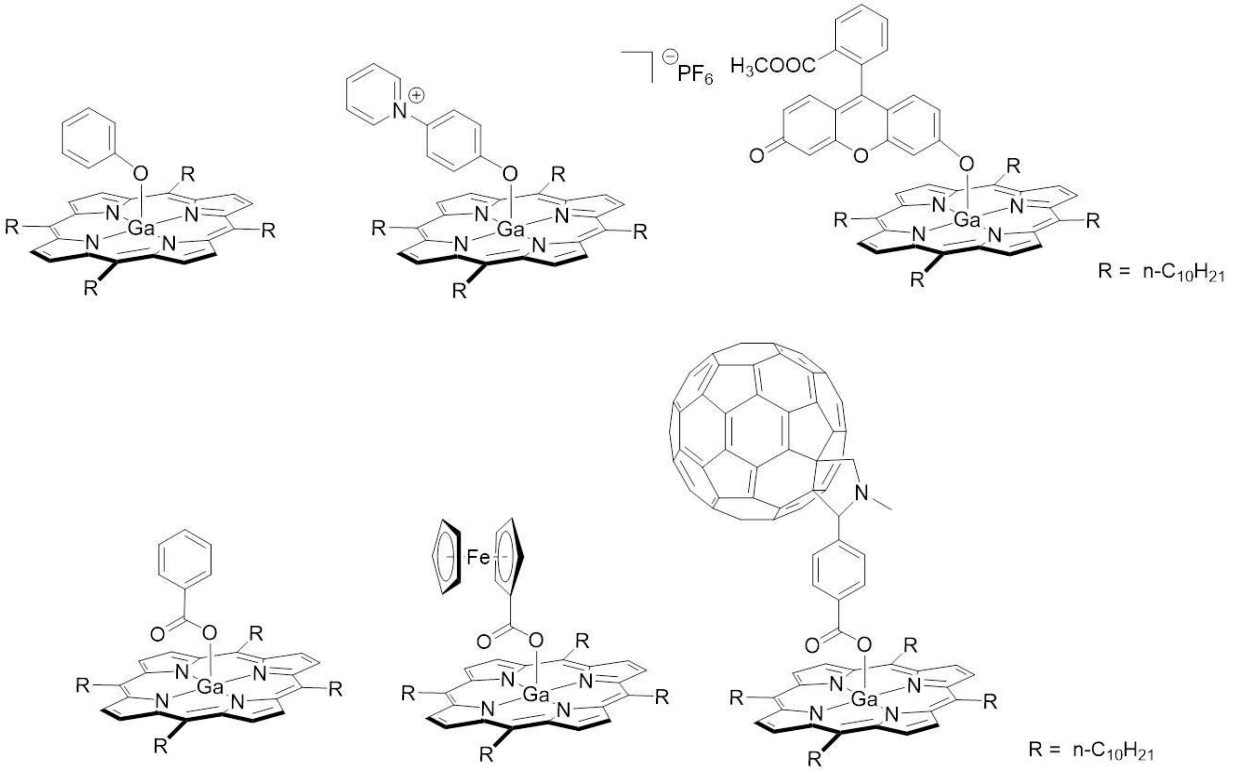

Figure 1.12. Molecular structures of Ga($TC_{10}P$)(OR) and Ga($TC_{10}P$)(O_2CR) complexes.

The feasibility of using Ga-porphyrin-carboxylate and -aryloxide complexes as building blocks for monolayers that organize functional molecules on HOPG is demonstrated by subsequent STM studies on the newly prepared dyads at the 1-phneyloctane/HOPG interface, which is presented in Chapter 4. While the Ga($TC_{10}P$)(OR) complexes are observed to usually form monolayers with the same packing structures seen in monolayers of the $TC_{10}P$-based compounds described in Chapter 2, the Ga($TC_{10}P$)(O_2CR) monolayers show unusual new structures that are enabled by the conformational flexibility of alkyl side chains.

In Chapter 5, an alternative method of preparing Ga($TC_{10}P$)(O_2CR) monolayers is investigated. Due to the facile reactivity of Ga($TC_{10}P$)(OH) towards carboxylic acids, it is hypothesized that monolayers of Ga($TC_{10}P$)(OH) can be chemically modified *in situ* to form Ga($TC_{10}P$)(O_2CR) monolayers. By sequentially depositing solutions of Ga($TC_{10}P$)(OH) and ferrocenecarboxylic acid ($FcCO_2H$) in 1-phenyloctane on HOPG, Ga($TC_{10}P$)(O_2CFc) monolayers can be prepared. The structures of these monolayers differs from those formed by depositing pre-synthesized Ga($TC_{10}P$)(O_2CFc) on HOPG, demonstrating that they are comprised of molecules formed by chemical reactions at the surface and not in solution.

1.1. References

1. Xu, Q.; Lv, Y. Z.; Dong, C. B.; Sreeprased, T. S.; Tian, A.; Zhang, H. Z.; Tang, Y.; Yu, Z. Q.; Li, N. Three-Dimensional Micro/Nanoscale Architectures: Fabrication and Applications. *Nanoscale* **2015**, *7*, 10883-10895.

2. Liddle, J. A.; Gallatin, G. M. Nanomanufacturing: A Perspective. *Acs Nano* **2016**, *10*, 2995-3014.

3. Cavallini, M.; Facchini, M.; Massi, M.; Biscarini, F. Bottom-up Nanofabrication of Materials for Organic Electronics. *Synthetic Metals* **2004**, *146*, 283-286.

4. Ariga, K.; Lee, M. V.; Mori, T.; Yu, X. Y.; Hill, J. P. Two-Dimensional Nanoarchitectonics Based on Self-Assembly. *Adv. Colloid Interface Sci.* **2010**, *154*, 20-29.

5. Eigler, D. M.; Schweizer, E. K. Positioning Single Atoms with a Scanning Tunneling Microscope. *Nature* **1990**, *344*, 524-526.

6. Stroscio, J. A.; Eigler, D. M. Atomic and Molecular Manipulation with the Scanning Tunneling Microscope. *Science* **1991**, *254*, 1319-1326.

7. Avouris, P. Manipulation of Matter at the Atomic and Molecular-Levels. *Acc. Chem. Res.* **1995**, *28*, 95-102.

8. Bartels, L.; Meyer, G.; Rieder, K. H. Controlled Vertical Manipulation of Single CO Molecules with the Scanning Tunneling Microscope: A Route to Chemical Contrast. *Appl. Phys. Lett.* **1997**, *71*, 213-215.

9. Meyer, G.; Bartels, L.; Zophel, S.; Henze, E.; Rieder, K. H. Controlled Atom by Atom Restructuring of a Metal Surface with the Scanning Tunneling Microscope. *Phys. Rev. Lett.* **1997**, *78*, 1512-1515.

10. Parviz, B. A.; Ryan, D.; Whitesides, G. M. Using Self-Assembly for the Fabrication of Nano-Scale Electronic and Photonic Devices. *IEEE Trans. Adv. Packag.* **2003**, *26*, 233-241.

11. Love, J. C.; Estroff, L. A.; Kriebel, J. K.; Nuzzo, R. G.; Whitesides, G. M. Self-Assembled Monolayers of Thiolates on Metals as a Form of Nanotechnology. *Chem. Rev.* **2005**, *105*, 1103-1169.

12. Bain, C. D.; Evall, J.; Whitesides, G. M. Formation of Monolayers by the Coadsorption of Thiols on Gold - Variation in the Head Group, Tail Group, and Solvent. *Journal of the American Chemical Society* **1989**, *111*, 7155-7164.

13. Bain, C. D.; Whitesides, G. M. Molecular-Level Control over Surface Order in Self-Assembled Monolayer Films of Thiols on Gold. *Science* **1988**, *240*, 62-63.

14. Bain, C. D.; Whitesides, G. M. Formation of 2-Component Surfaces by the Spontaneous Assembly of Monolayers on Gold from Solutions Containing Mixtures of Organic Thiols. *J. Am. Chem. Soc.* **1988**, *110*, 6560-6561.

15. Bain, C. D.; Whitesides, G. M. Formation of Monolayers by the Coadsorption of Thiols on Gold - Variation in the Length of the Alkyl Chain. *Journal of the American Chemical Society* **1989**, *111*, 7164-7175.

16. Cygan, M. T.; Dunbar, T. D.; Arnold, J. J.; Bumm, L. A.; Shedlock, N. F.; Burgin, T. P.; Jones, L.; Allara, D. L.; Tour, J. M.; Weiss, P. S. Insertion, Conductivity, and Structures of Conjugated Organic Oligomers in Self-Assembled Alkanethiol Monolayers on Au{111}. *J. Am. Chem. Soc.* **1998**, *120*, 2721-2732.

17. Wassel, R. A.; Fuierer, R. R.; Kim, N. J.; Gorman, C. B. Stochastic Variation in Conductance on the Nanometer Scale: A General Phenomenon. *Nano Letters* **2003**, *3*, 1617-1620.

18. Yokota, Y.; Fukui, K.; Enoki, T.; Hara, M. Origin of Current Enhancement Through a Ferrocenylundecanethiol Island Embedded in Alkanethiol SAMs by Using Electrochemical Potential Control. *J. Phys. Chem. C* **2007**, *111*, 7561-7564.

19. Gorman, C. B.; Carroll, R. L.; Fuierer, R. R. Negative Differential Resistance in Patterned Electroactive Self-Assembled Monolayers. *Langmuir* **2001**, *17*, 6923-6930.

20. Lewis, P. A.; Donhauser, Z. J.; Mantooth, B. A.; Smith, R. K.; Bumm, L. A.; Kelly, K. F.; Weiss, P. S. Control and Placement of Molecules via Self-Assembly. *Nanotechnology* **2001**, *12*, 231-237.

21. Kudernac, T.; Lei, S. B.; Elemans, J. A. A. W.; De Feyter, S. Two-Dimensional Supramolecular Self-Assembly: Nanoporous Networks on Surfaces. *Chem. Soc. Rev.* **2009**, *38*, 402-421.

22. De Feyter, S.; De Schryver, F. C. Self-Assembly at the Liquid/Solid Interface: STM Reveals. *J. Phys. Chem. B* **2005**, *109*, 4290-4302.

23. De Feyter, S.; De Schryver, F. C. Two-Dimensional Supramolecular Self-Assembly Probed by Scanning Tunneling Microscopy. *Chem. Soc. Rev.* **2003**, *32*, 139-150.

24. Elemans, J. A. A. W.; Lei, S. B.; De Feyter, S. Molecular and Supramolecular Networks on Surfaces: From Two-Dimensional Crystal Engineering to Reactivity. *Angew. Chem., Int. Ed.* **2009**, *48*, 7298-7332.

25. Mali, K. S.; Adisoejoso, J.; Ghijsens, E.; De Cat, I.; De Feyter, S. Exploring the Complexity of Supramolecular Interactions for Patterning at the Liquid-Solid Interface. *Acc. Chem. Res.* **2012**, *45*, 1309-1320.

26. Mali, K. S.; De Feyter, S. Principles of Molecular Assemblies Leading to Molecular Nanostructures. *Philos. Trans. R. Soc., A* **2013**, *371*, 20120304.

27. Barth, J. V. Molecular Architectonic on Metal Surfaces. *Annu. Rev. Phys. Chem.* **2007**, *58*, 375-407.

28. Ciesielski, A.; Palma, C. A.; Bonini, M.; Samorì, P. Towards Supramolecular Engineering of Functional Nanomaterials: Pre-Programming Multi-Component 2D Self-Assembly at Solid-Liquid Interfaces. *Adv. Mater.* **2010**, *22*, 3506-3520.

29. Baisch, B.; Raffa, D.; Jung, U.; Magnussen, O. M.; Nicolas, C.; Lacour, J.; Kubitschke, J.; Herges, R. Mounting Freestanding Molecular Functions onto Surfaces: The Platform Approach. *J. Am. Chem. Soc.* **2009**, *131*, 442-443.

30. Jung, U.; Kuhn, S.; Cornelissen, U.; Tuczek, F.; Strunskus, T.; Zaporojtchenko, V.; Kubitschke, J.; Herges, R.; Magnussen, O. Azobenzene-Containing Triazatriangulenium Adlayers on Au(111): Structural and Spectroscopic Characterization. *Langmuir* **2011**, *27*, 5899-5908.

31. Kuhn, S.; Baisch, B.; Jung, U.; Johannsen, T.; Kubitschke, J.; Herges, R.; Magnussen, O. Self-Assembly of Triazatriangulenium-Based Functional Adlayers on Au(111) Surfaces. *Phys. Chem. Chem. Phys.* **2010**, *12*, 4481-4487.

32. Lemke, S.; Chang, C.-H.; Jung, U.; Magnussen, O. M. Reversible Potential-Induced Switching of Alkyl Chain Aggregation in Octyl-Triazatriangulenium Adlayers on Au(111). *Langmuir* **2015**, *31*, 3115-3124.

33. Lemke, S.; Ulrich, S.; Claußen, F.; Bloedorn, A.; Jung, U.; Herges, R.; Magnussen, O. M. Triazatriangulenium Adlayers on Au(111): Superstructure as a Function of Alkyl Side Chain Length. *Surf. Sci.* **2015**, *632*, 71-76.

34. Otte, F. L.; Lemke, S.; Schütt, C.; Krekiehn, N. R.; Jung, U.; Magnussen, O. M.; Herges, R. Ordered Monolayers of Free-Standing Porphyrins on Gold. *J. Am. Chem. Soc.* **2014**, *136*, 11248-11251.

35. Bleger, D.; Mathevet, F.; Kreher, D.; Attias, A. J.; Bocheux, A.; Latil, S.; Douillard, L.; Fiorini-Debuisschert, C.; Charra, F. Janus-Like 3D Tectons: Self-Assembled 2D Arrays of Functional Units at a Defined Distance from the Substrate. *Angew. Chem., Int. Ed.* **2011**, *50*, 6562-6566.

36. Du, P.; Bléger, D.; Charra, F.; Bouchiat, V.; Kreher, D.; Mathevet, F.; Attias, A. J. A Versatile Strategy Towards Non-Covalent Functionalization of Graphene by Surface-Confined Supramolecular Self-Assembly of Janus Tectons. *Beilstein J. Nanotechnol.* **2015**, *6*, 632-639.

37. Du, P.; Kreher, D.; Mathevet, F.; Maldivi, P.; Charra, F.; Attias, A. J. Surface-Confined Supramolecular Self-Assembly of Molecular Nanocranes for Chemically Lifting and Positioning C_{60} above a Conducting Substrate. *ChemPhysChem* **2015**, *16*, 3774-3778.

38. Otsuki, J. STM Studies on Porphyrins. *Coord. Chem. Rev.* **2010**, *254*, 2311-2341.

39. Mohnani, S.; Bonifazi, D. Supramolecular Architectures of Porphyrins on Surfaces: The Structural Evolution from 1D to 2D to 3D to Devices. *Coord. Chem. Rev.* **2010**, *254*, 2342-2362.

40. Auwärter, W.; Écija, D.; Klappenberger, F.; Barth, J. V. Porphyrins at Interfaces. *Nat. Chem.* **2015**, *7*, 105-120.

41. Gottfried, J. M. Surface Chemistry of Porphyrins and Phthalocyanines. *Surf. Sci. Rep.* **2015**, *70*, 259-379.

42. Qiu, X. H.; Wang, C.; Zeng, Q. D.; Xu, B.; Yin, S. X.; Wang, H. N.; Xu, S. D.; Bai, C. L. Alkane-Assisted Adsorption and Assembly of Phthalocyanines and Porphyrins. *J. Am. Chem. Soc.* **2000**, *122*, 5550-5556.

43. Wang, H. N.; Wang, C.; Zeng, Q. D.; Xu, S. D.; Yin, S. X.; Xu, B.; Bai, C. L. Chain-Length-Adjusted Assembly of Substituted Porphyrins on Graphite. *Surf. Interface Anal.* **2001**, *32*, 266-270.

44. Ikeda, T.; Asakawa, M.; Miyake, K.; Goto, M.; Shimizu, T. Scanning Tunneling Microscopy Observation of Self-Assembled Monolayers of Strapped Porphyrins. *Langmuir* **2008**, *24*, 12877-12882.

45. Shen, Y. T.; Deng, K.; Li, M.; Zhang, X. M.; Zhou, G.; Müellen, K.; Zeng, Q. D.; Wang, C. Self-Assembling in Fabrication of Ordered Porphyrins and Phthalocyanines Hybrid Nano-Arrays on HOPG. *CrystEngComm* **2013**, *15*, 5526-5531.

46. Ikeda, T.; Asakawa, M.; Goto, M.; Miyake, K.; Ishida, T.; Shimizu, T. STM Observation of Alkyl-Chain-Assisted Self-Assembled Monolayers of Pyridine-Coordinated Porphyrin Rhodium Chlorides. *Langmuir* **2004**, *20*, 5454-5459.

47. Lei, S. B.; Wang, C.; Yin, S. X.; Wang, H. N.; Xi, F.; Liu, H. W.; Xu, B.; Wan, L. J.; Bai, C. L. Surface Stabilized Porphyrin and Phthalocyanine Two-Dimensional Network Connected by Hydrogen Bonds. *J. Phys. Chem. B* **2001**, *105*, 10838-10841.

48. Otsuki, J.; Nagamine, E.; Kondo, T.; Iwasaki, K.; Asakawa, M.; Miyake, K. Surface Patterning with Two-Dimensional Porphyrin Supramolecular Arrays. *J. Am. Chem. Soc.* **2005**, *127*, 10400-10405.

49. Yoshimoto, S.; Yokoo, N.; Fukuda, T.; Kobayashi, N.; Itaya, K. Formation of Highly Ordered Porphyrin Adlayers Induced by Electrochemical Potential Modulation. *Chem. Comm.* **2006**, 500-502.

50. Oncel, N.; Bernasek, S. L. Ni(II)- and Vanadyloctaethylporphyrin Self-Assembled Layers Formed on Bare and 5-(Octadecyloxy)isophthalic Acid Covered Graphite. *Langmuir* **2009**, *25*, 9290-9295.

51. Friesen, B. A.; Bhattarai, A.; Mazur, U.; Hipps, K. W. Single Molecule Imaging of Oxygenation of Cobalt Octaethylporphyrin at the Solution/Solid Interface: Thermodynamics from Microscopy. *J. Am. Chem. Soc.* **2012**, *134*, 14897-14904.

52. Bhattarai, A.; Mazur, U.; Hipps, K. W. Desorption Kinetics and Activation Energy for Cobalt Octaethylporphyrin from Graphite at the Phenyloctane Solution-Graphite Interface: An STM Study. *J. Phys. Chem. C* **2015**, *119*, 9386-9394.

53. Miyake, Y.; Tanaka, H.; Ogawa, T. Scanning Tunneling Microscopy Investigation of Vanadyl and Cobalt(II) Octaethylporphyrin Self-Assembled Monolayer Arrays on Graphite. *Colloids Surf., A* **2008**, *313*, 230-233.

54. Oncel, N.; Bernasek, S. L. The Effect of Molecule-Molecule and Molecule-Substrate Interaction in the Formation of Pt-Octaethyl Porphyrin Self-Assembled Monolayers. *Appl. Phys. Lett.* **2008**, *92*.

55. Zou, Z. Q.; Wei, L. Y.; Chen, F.; Liu, Z. M.; Thamyongkit, P.; Loewe, R. S.; Lindsey, J. S.; Mohideen, U.; Bocian, D. F. Solution STM Images of Porphyrins on HOPG Reveal that Subtle Differences in Molecular Structure Dramatically Alter Packing Geometry. *J. Porphyrins Phthalocyanines* **2005**, *9*, 387-392.

56. Zou, Z. Q.; Chen, F. In Situ Scanning Tunneling Microscopy Studies of Zinc(II) Octaethylporphyrin Arrays Self-Assembled on Graphite and Au(111) Surfaces in Organic Solution. *J. Appl. Phys.* **2008**, *103*.

57. Kamm, J. M.; Iverson, C. P.; Lau, W.-Y.; Hopkins, M. D. Axial Ligand Effects on the Structures of Self-Assembled Gallium-Porphyrin Monolayers on Highly Oriented Pyrolytic Graphite. *Langmuir* **2016**, *32*, 487-495.

58. Otsuki, J.; Namiki, K.; Arai, Y.; Amano, M.; Sawai, H.; Tsukamoto, A.; Hagiwara, T. Face-on and Columnar Porphyrin Assemblies at Solid/Liquid Interface on HOPG. *Chem. Lett.* **2009**, *38*, 570-571.

59. Linares, M.; Iavicoli, P.; Psychogyiopoulou, K.; Beljonne, D.; De Feyter, S.; Amabilino, D. B.; Lazzaroni, R. Chiral Expression at the Solid-Liquid Interface: A Joint Experimental and Theoretical Study of the Self-Assembly of Chiral Porphyrins on Graphite. *Langmuir* **2008**, *24*, 9566-9574.

60. Yokoyama, T.; Kamikado, T.; Yokoyama, S.; Mashiko, S. Conformation Selective Assembly of Carboxyphenyl Substituted Porphyrins on Au (111). *J. Chem. Phys.* **2004**, *121*, 11993-11997.

61. Jurow, M.; Schuckman, A. E.; Batteas, J. D.; Drain, C. M. Porphyrins as Molecular Electronic Components of Functional Devices. *Coord. Chem. Rev.* **2010**, *254*, 2297-2310.

62. Otsuki, J.; Seki, E.; Taguchi, T.; Asakawa, M.; Miyake, K. STM Observation of Labile Axial Ligands to Zinc Porphyrin at Liquid/Solid Interface. *Chem. Lett.* **2007**, *36*, 740-741.

63. Visser, J.; Katsonis, N.; Vicario, J.; Feringa, B. L. Two-Dimensional Molecular Patterning by Surface-Enhanced Zn-Porphyrin Coordination. *Langmuir* **2009**, *25*, 5980-5985.

64. Sakano, T.; Higashiguchi, K.; Matsuda, K. Comparison of Molecular Conductance Between Planar and Twisted 4-Phenylpyridines by Means of Two-Dimensional Phase Separation of Tetraphenylporphyrin Templates at a Liquid-HOPG Interface. *Chem. Commun.* **2011**, *47*, 8427-8429.

65. Ferreira, Q.; Alcácer, L.; Morgado, J. Stepwise Preparation and Characterization of Molecular Wires Made of Zinc Octaethylporphyrin Complexes Bridged by 4,4'-Bipyridine on HOPG. *Nanotechnology* **2011**, *22*, 435604.

66. Ferreira, Q.; Bragança, A. M.; Alcácer, L.; Morgado, J. Conductance of Well-Defined Porphyrin Self-Assembled Molecular Wires up to 14 nm in Length. *J. Phys. Chem. C* **2014**, *118*, 7229-7234.

67. Hulsken, B.; Van Hameren, R.; Gerritsen, J. W.; Khoury, T.; Thordarson, P.; Crossley, M. J.; Rowan, A. E.; Nolte, R. J. M.; Elemans, J. A. A. W.; Speller, S. Real-Time Single-Molecule Imaging of Oxidation Catalysis at a Liquid-Solid Interface. *Nat. Nanotechnol.* **2007**, *2*, 285-289.

68. Nicholls, D.; Ware, B.; Zhang, Z.; Oncel, N. A Scanning Tunneling Microscopy Study on Self-Assembled Fe(III) *meso*-Tetra(4-Carboxyphenyl) Porphyrin Chloride Chains. *Thin Solid Films* **2013**, *534*, 308-311.

69. Li, M.; den Boer, D.; Iavicoli, P.; Adisoejoso, J.; Uji-i, H.; Van der Auweraer, M.; Amabilino, D. B.; Elemans, J. A. A. W.; De Feyter, S. Tip-Induced Chemical Manipulation of Metal Porphyrins at a Liquid/Solid Interface. *J. Am. Chem. Soc.* **2014**, *136*, 17418-17421.

70. Takami, T.; Clark, A.; Caldwell, R.; Mazur, U.; Hipps, K. W. Building Self-Assembled Molecular Layers with Axially Substituted Titanium Phthalocyanines. *Langmuir* **2010**, *26*, 12709-12715.

71. Brancato-Buentello, K. E.; Coutsolelos, A. G.; Scheidt, W. R. Chloro(2,3,7,8,12,13,17,18-octaethylporphinato)gallium(III). *Acta Crystallogr., Sect. C: Cryst. Struct. Commun.* **1996**, *52*, 2707-2710.

72. Boukhris, A.; Lecomte, C.; Coutsolelos, A.; Guilard, R. Alkylsulfonato(Porphyrinato)Gallium(III): Crystal-Structure Determination of Methylsulfonato(Octaethyl-2,3,7,8,12,13,17,18-Porphyrinato)-Gallium(III). *J. Organomet. Chem.* **1986**, *303*, 151-165.

73. Coutsolelos, A.; Guilard, R. Synthesis and Physicochemical Characteristics of Porphyrins Containing a Metal-Carbon σ-Bond. *J. Organomet. Chem.* **1983**, *253*, 273-282.

74. Coutsolelos, A.; Guilard, R.; Bayeul, D.; Lecomte, C. Gallium(III) Porphyrins - Synthesis and Physicochemical Characteristics of Halogeno Gallium(III) Porphyrins X-Ray Crystal-Structure of Chloro-(5,10,15,20-Tetraphenylporphyrinato) Gallium(III). *Polyhedron* **1986**, *5*, 1157-1164.

75. Coutsolelos, A.; Guilard, R.; Boukhris, A.; Lecomte, C. Synthesis and Characterization of Azido-Gallium(III) and Thiocyanato-Gallium(III) Porphyrins - Crystal-Structure of Azido(2,3,7,8,12,13,17,18-Octaethyl-Porphyrinato)Gallium(III). *J. Chem. Soc., Dalton Trans.* **1986**, 1779-1783.

76. Kadish, K. M.; Boisselier-Cocolios, B.; Coutsolelos, A.; Mitaine, P.; Guilard, R. Electrochemistry and Spectroelectrochemistry of Gallium(III) Porphyrins. Redox Properties of Five-Coordinate Ionic and σ-Bonded Complexes. *Inorg. Chem.* **1985**, *24*, 4521-4528.

77. Kadish, K. M.; Cornillon, J. L.; Coutsolelos, A.; Guilard, R. Synthesis, Electrochemistry, and Ligand-Addition Reactions of Gallium(III) Porphyrins. *Inorg. Chem.* **1987**, *26*, 4167-4173.

78. Balch, A. L.; Hart, R. L.; Parkin, S. Axial Alkyl Ligand Reactivity in 5-Coordinate Gallium(III) Porphyrin Complexes. *Inorg. Chim. Acta* **1993**, *205*, 137-143.

79. Okamura, T.; Nishikawa, N.; Ueyama, N.; Nakamura, A. Synthesis and Structures of (Porphinato)(thiolato)gallium(III) Complexes. *Chem. Lett.* **1998**, 199-200.

80. Kadish, K. M.; Maiya, G. B.; Xu, Q. Y. Photoreactivity of σ-Bonded Metalloporphyrins.I. Formation of Zwitterionic Indium and Gallium Porphyrin Complexes in Tetrahydrofuran. *Inorg. Chem.* **1989**, *28*, 2518-2523.

81. Yin, S. X.; Wang, C.; Qiu, X. H.; Xu, B.; Bai, C. L. Theoretical Study of the Effects of Intermolecular Interactions in Self-Assembled Long-Chain Alkanes Adsorbed on Graphite Surface. *Surf. Interface Anal.* **2001**, *32*, 248-252.

82. Hulsken, B.; van Hameren, R.; Thordarson, P.; Gerritsen, J. W.; Nolte, R. J. M.; Rowan, A. E.; Crossley, M. J.; Elemans, J. A. A. W.; Speller, S. Scanning Tunneling Microscopy and Spectroscopy Studies of Porphyrins at Solid-Liquid Interfaces. *Jpn. J. Appl. Phys.* **2006**, *45*, 1953-1955.

83. Plamont, R.; Kikkawa, Y.; Takahashi, M.; Kanesato, M.; Giorgi, M.; Shun, A. C. K.; Roussel, C.; Balaban, T. S. Nanoscopic Imaging of *meso*-Tetraalkylporphyrins Prepared in High Yields Enabled by Montmorrilonite K10 and 3Å angstrom Molecular Sieves. *Chem. - Eur. J.* **2013**, *19*, 11293-11300.

84. Coenen, M. J. J.; Cremers, M.; den Boer, D.; van den Bruele, F. J.; Khoury, T.; Sintic, M.; Crossley, M. J.; van Enckevort, W. J. P.; Hendriksen, B. L. M.; Elemans, J. A. A. W.; Speller, S. Little Exchange at the Liquid/Solid Interface: Defect-Mediated Equilibration of Physisorbed Porphyrin Monolayers. *Chem. Commun.* **2011**, *47*, 9666-9668.

85. Coenen, M. J. J.; den Boer, D.; van den Bruele, F. J.; Habets, T.; Timmers, K. A. A. M.; van der Maas, M.; Khoury, T.; Panduwinata, D.; Crossley, M. J.; Reimers, J. R.; van Enckevort, W. J. P.; Hendriksen, B. L. M.; Elemans, J. A. A. W.; Speller, S. Polymorphism in Porphyrin Monolayers: the Relation Between Adsorption Configuration and Molecular Conformation. *Phys. Chem. Chem. Phys.* **2013**, *15*, 12451-12458.

86. Katsonis, N.; Vicario, J.; Kudernac, T.; Visser, J.; Pollard, M. M.; Feringa, B. L. Self-Organized Monolayer of meso-Tetradodecylporphyrin Coordinated to Au(111). *J. Am. Chem. Soc.* **2006**, *128*, 15537-15541.

87. Ferreira, Q.; Bragança, A. M.; Moura, N. M. M.; Faustino, M. A. F.; Alcácer, L.; Morgado, J. Dynamics of Porphyrin Adsorption on Highly Oriented Pyrolytic Graphite Monitored by Scanning Tunnelling Microscopy at the Liquid/Solid Interface. *Appl. Surf. Sci.* **2013**, *273*, 220-225.

88. Chin, Y.; Panduwinata, D.; Sintic, M.; Sum, T. J.; Hush, N. S.; Crossley, M. J.; Reimers, J. R. Atomic-Resolution Kinked Structure of an Alkylporphyrin on Highly Ordered Pyrolytic Graphite. *J. Phys. Chem. Lett.* **2011**, *2*, 62-66.

89. Reimers, J. R.; Panduwinata, D.; Visser, J.; Chin, Y.; Tang, C. G.; Goerigk, L.; Ford, M. J.; Baker, M.; Sum, T. J.; Coenen, M. J. J.; Hendriksen, B. L. M.; Elemans, J. A. A. W.; Hush, N. S.; Crossley, M. J. From Chaos to Order: Chain-Length Dependence of the Free Energy of Formation of Meso-tetraalkylporphyrin Self-Assembled Monolayer Polymorphs. *J. Phys. Chem. C* **2016**, *120*, 1739-1748.

90. Reimers, J. R.; Panduwinata, D.; Visser, J.; Chin, Y.; Tang, C. G.; Goerigk, L.; Ford, M. J.; Sintic, M.; Sum, T. J.; Coenen, M. J. J.; Hendriksen, B. L. M.; Elemans, J. A. A. W.; Hush, N. S.; Crossley, M. J. A Priori Calculations of the Free Energy of Formation from Solution of Polymorphic Self-Assembled Monolayers. *PNAS* **2015**, *112*, E6101-E6110.

91. Poddutoori, P. K.; Lim, G. N.; Sandanayaka, A. S. D.; Karr, P. A.; Ito, O.; D'Souza, F.; Pilkington, M.; van der Est, A. Axially Assembled Photosynthetic Reaction Center Mimics Composed of Tetrathiafulvalene, Aluminum(III) Porphyrin and Fullerene Entities. *Nanoscale* **2015**, *7*, 12151-12165.

92. Poddutoori, P. K.; Sandanayaka, A. S. D.; Hasobe, T.; Ito, O.; van der Est, A. Photoinduced Charge Separation in a Ferrocene-Aluminum(III) Porphyrin-Fullerene Supramolecular Triad. *J. Phys. Chem. B* **2010**, *114*, 14348-14357.

93. Kumar, P. P.; Maiya, B. G. Aluminium(III) Porphyrin Based Dimers and Trimers: Synthesis, Spectroscopy and Photochemistry. *New J. Chem.* **2003**, *27*, 619-625.

94. Davidson, G. J. E.; Tong, L. H.; Raithby, P. R.; Sanders, J. K. M. Aluminium(III) Porphyrins as Supramolecular Building Blocks. *Chem. Commun.* **2006**, 3087-3089.

95. Ghosh, A.; Maity, D. K.; Ravikanth, M. Aluminium(III) Porphyrin Based Axial-Bonding Type Dyads Containing Thiaporphyrins and Expanded Thiaporphyrins as Axial Ligands. *New J. Chem.* **2012**, *36*, 2630-2641.

96. Iengo, E.; Pantos, G. D.; Sanders, J. K. M.; Orlandi, M.; Chiorboli, C.; Fracasso, S.; Scandola, F. A Fully Self-Assembled Non-Symmetric Triad for Photoinduced Charge Separation. *Chem. Sci.* **2011**, *2*, 676-685.

97. Panda, M. K.; Lazarides, T.; Charalambidis, G.; Nikolaou, V.; Coutsolelos, A. G. Five-Coordinate Indium(III) Porphyrins with Hydroxy and Carboxy BODIPY as Axial Ligands: Synthesis, Characterization and Photophysical Studies. *Eur. J. Inorg. Chem.* **2015**, 468-477.

98. Hartmann, M.; Meyer, G.; Wohrle, D. Polykondensationsreaktionen mit Germaniumkomplexen des Phthalocyanins und *meso*-TetraphenylporphinsPolykondensationsreaktionen mit Germaniumkomplexen des Phthalocyanins und *meso*-Tetraphenylporphins. *Makromol. Chem.* **1975**, *176*, 831-847.

99. Giribabu, L.; Rao, T. A.; Maiya, B. G. "Axial-Bonding"-Type Hybrid Porphyrin Arrays: Synthesis, Spectroscopy, Electrochemistry, and Singlet State Properties. *Inorg. Chem.* **1999**, *38*, 4971-4980.

100. Patra, R.; Titi, H. M.; Goldberg, I. Crystal Engineering of Molecular Networks: Tailoring Hydrogen-Bonding Self-Assembly of Tin-Tetrapyridylporphyrins with Multidentate Carboxylic Acids As Axial Ligands. *Cryst. Gowth Des.* **2013**, *13*, 1342-1349.

101. Smith, G.; Arnold, D. P.; Kennard, C. H. L.; Mak, T. C. W. Tin(IV) Porphyrin Complexes - IV. Crystal-Structures of *meso*-Tetraphenylporphyrinatotin(IV) Complexes with Hydroxide, Water, Benzoate, Salicylate and Acetylsalicylate as Axial Ligands. *Polyhedron* **1991**, *10*, 509-516.

102. Arnold, D. P.; Blok, J. The Coordination Chemistry of Tin Porphyrin Complexes. *Coord. Chem. Rev.* **2004**, *248*, 299-319.

103. Shetti, V. S.; Pareek, Y.; Ravikanth, M. Sn(IV) Porphyrin Scaffold for Multiporphyrin Arrays. *Coord. Chem. Rev.* **2012**, *256*, 2816-2842.

104. Lazarides, T.; Kuhri, S.; Charalambidis, G.; Panda, M. K.; Guldi, D. M.; Coutsolelos, A. G. Electron vs Energy Transfer in Arrays Featuring Two Bodipy Chromophores Axially Bound to a Sn(IV) Porphyrin via a Phenolate or Benzoate Bridge. *Inorg. Chem.* **2012**, *51*, 4193-4204.

CHAPTER 2

Ordered Arrays of oligo-Phenylene-Ethynylene Pillars Supported by Gallium–Porphyrin Monolayers on HOPG

2.1. Introduction

Earlier work in our group has demonstrated that Ga(III) octaethylporphyrins [Ga(OEP)X; X = Cl, Br, I, OTf, CCPh], compounds with square-pyramidal geometries, can self-assemble into well-ordered monolayers on highly ordered pyrolytic graphite (HOPG) both at the solid-air and solid-liquid interfaces with the ligands oriented perpendicular to the surface.[1] The Ga(OEP)X monolayers all exhibit pseudo-hexagonal packing structures that are indistinguishable from each other and are also largely consistent with the reported structures of other four-coordinate M(OEP) monolayers.[2-8] Importantly, however, the Ga(OEP)X compounds with the larger axial ligands (X = CCPh, OTf) formed monolayers with lower coverage than those of the halide derivatives, and they were more readily disrupted during STM measurements. Given that a goal of this broader project is to attach more complex and functional moieties to these axial positions, it is important to investigate porphyrins other than OEP to increase the stability of the self-assembled monolayers.

A common strategy to enhance the stability of porphyrin monolayers on HOPG and to control their 2D morphology is to incorporate long peripheral side-chains. These chains provide additional van der Waals interaction between neighboring units,[9] and numerous studies have shown that long-alkyl-chain substituted heterocycles such as *meso*-tetraalkyl-[10-18] and tetraalkoxyphenylporphyrins[19-22] can reliably form highly stable self-assembled 2D structures on HOPG. In particular, one report showed that a six-coordinate Rh(III) porphyrin with *trans* axial pyridine and chloride ligands can form well-ordered monolayers on HOPG by incorporating

alkoxyphenyl substituents at the *meso* positions with an alkyl chain length of 30, even though the trans ligands prevent the porphyrin core from coming into close contact with the substrate.[23]

In this chapter, this strategy was utilized to stabilize monolayers of five-coordinate Ga(III) metalloporphyrins on HOPG with large axial ligands. Here, 5,10,15,20-tetra(*n*-$C_{10}H_{21}$)porphyrin ($TC_{10}P$) was used to prepare a family of Ga(III) complexes with oligo-phenylene-ethynylene (OPE) ligands of increasing height [Ga($TC_{10}P$)(OPE); OPE = CCPh (**1**), *p*-CCC_6H_4CCPh (**2**), 4,4′-$CCC_6H_4CCC_6H_4CCPh$ (**3**)], and their surface chemistry on HOPG at the solid-liquid and solid-air interface was probed by scanning tunneling microscopy (STM). Extending the CCPh ligand opens the possibility of supporting functional units at specific heights above a surface; taller derivatives allows us to use such molecules to probe for the possibility of incorporating larger axial ligands without disrupting the face-on absorption configuration (e.g. the molecular plane oriented parallel to the surface) of the porphyrin molecules upon adsorption onto HOPG. Furthermore, the controlled organization of OPE ligands is of great interest as these molecules and their derivatives have found use as components of dye-sensitized solar cells,[24] molecular electronics,[25] molecular switches,[26] and memory arrays.[27]

As will be described, all reported compounds form self-assembled monolayers at the 1-phenyloctane/HOPG interface with extensive surface coverage; two distinct molecular arrangements are observed. Subsequent experiments performed at the air/HOPG interface also show that the Ga($TC_{10}P$)(OPE) complexes can form ordered structures without the presence of a supernatant, showing the versatility of these porphyrin as building blocks of nanostructures under different deposition conditions.

2.2. Experimental Section

2.2.1. Materials and General Methods. All synthetic procedures were performed using standard Schlenk and glovebox techniques under a nitrogen atmosphere unless otherwise specified. Solvents used for synthesis (HPLC grade, stored under nitrogen) were purified by passing them under nitrogen pressure through an anaerobic, stainless-steel system consisting of either two 4.5 in. × 24 in. (1 gal) columns of activated A2 alumina (THF) or one column of activated A2 alumina and one column of activated BASF R3-11 catalyst (toluene).[28] Undecanal,[29] free base 5,10,15,20-tetra(*n*-$C_{10}H_{21}$)porphyrin ($H_2TC_{10}P$),[30] LiCCPh,[31] *p*-$HCCC_6H_4CCPh$,[32] and 4,4′-$Me_3SiCCC_6H_4CCC_6H_4CCPh$[32] were prepared according to published procedures. Phenylacetylene (Aldrich, 98%) was purified by bulb-to-bulb transfer under vacuum. CD_2Cl_2 was dried using 4 Å molecular sieves. THF-d_8 was stirred over NaK (1:2) alloy overnight, from which it was transferred under vacuum prior to use. All other chemicals were obtained from commercial sources and used as received.

2.2.2. Characterization of Compounds. ^{1}H-, ^{13}C{^{1}H}-, and 2D (^{1}H/^{13}C) HMQC-NMR spectra were recorded at room temperature using Bruker Avance II$^+$ 500 MHz or DRX 400 MHz NMR spectrometers. Chemical shifts were measured relative to solvent resonances.[33] ^{13}C-NMR resonances for compounds **1**–**3** were assigned on the basis of HMQC spectra. Mass spectral data were obtained using a Bruker UltrafleXtreme MALDI-TOF/TOF mass spectrometer in reflection positive mode on samples prepared on a standard stainless steel plate without a matrix; the Bruker peptide calibration standard II (750–3150 Da) was used as the calibration standard. Electronic absorption spectra were recorded using a Cary 300 UV-visible spectrophotometer of samples in quartz cuvettes under nitrogen at room temperature (1 mm and 1 cm path length). Elemental analyses were performed at Robertson Microlit Laboratories, Ledgewood NJ.

2.2.3. Preparation of *p*-LiCCC$_6$H$_4$CCPh. To a stirred, room temperature solution of *p*-HCCC$_6$H$_4$CCPh (0.042 g, 0.21 mmol) in pentane (6 mL), *n*-BuLi (0.2 mL, 1.6 M in pentane, 0.32 mmol) was added via syringe; a white precipitate formed immediately. After 2 h, the precipitate was isolated by filtration as an off-white solid, washed with pentane (15 mL), and dried under vacuum for 30 min. This product (0.040 g, 0.19 mmol, 93% yield) was suitable for use in the preparation of **2** without further purification.

2.2.4. Preparation of 4,4′-HCCC$_6$H$_4$CCC$_6$H$_4$CCPh. This compound was previously reported, but the detailed preparation procedure and spectroscopic data were not available. To a stirred, room temperature solution of 4,4′-Me$_3$SiCCC$_6$H$_4$CCC$_6$H$_4$CCPh (0.272 g, 0.73 mmol) in a mixture of CH_2Cl_2 (10 mL) and MeOH (10 mL) in air, K_2CO_3 (0.202 g, 1.46 mmol) was added. After stirring overnight, the reaction mixture was filtered, and the filtrate was washed with water (25 mL). The aqueous layer was extracted with CH_2Cl_2 (25 mL), which was added to the organic phase. The combined organic phases were dried with Na_2SO_4, filtered, and the volatile components were removed *in vacuo*. The crude product was dissolved in a minimal amount of CH_2Cl_2 and purified by column chromatography on silica gel with a mixture of hexanes/ethyl acetate (9:1) as the eluent. Removal of volatile components under vacuum from the product-containing fraction provided the product as an off-white solid (0.186 g, 0.62 mmol, 85% yield). ^{1}H NMR ($CDCl_3$, 500.13 MHz): δ 7.46–7.55 (m, 10H), 7.34–7.39 (m, 3H), 3.18 (s, 1H, C≡C<u>H</u>).

2.2.5. Preparation of 4,4′-LiCCC$_6$H$_4$CCC$_6$H$_4$CCPh. To a stirred, room temperature solution of 4,4′-HCCC$_6$H$_4$CCC$_6$H$_4$CCPh (0.073 g, 0.24 mmol) in toluene (10 mL), *n*-BuLi (0.2 mL, 1.6 M in pentane, 0.32 mmol) was added via syringe, upon which a fine, light gray suspension formed. After 2 h, the suspension was transferred onto a Celite pad atop a sintered glass filter, allowed to settle, and dried by application of a weak vacuum. The crude product was

washed with toluene (15 mL) and pentane (15 mL), dried under vacuum for 30 min, and carefully removed from the top of the Celite. The (0.043 g, 0.14 mmol, 58% isolated yield) product was suitable for use in the synthesis of **3** without further purification.

2.2.6. Characterization of $H_2TC_{10}P$. The ^{1}H-NMR data below supplements previously reported data for this compound.[30] ^{1}H NMR (C_6D_6, 500.13 MHz): δ 9.43 (s, 8H, *β*), 4.87 (t, 8H, $CH_2CH_2C\underline{H}_2Por$), 2.54 (m, 8H, $CH_2C\underline{H}_2CH_2Por$), 1.73 (m, 8H, $C\underline{H}_2CH_2CH_2Por$), 1.20–1.50 (m, 48H, $CH_3(C\underline{H}_2)_5CH_2$), 0.91 (t, 12H, CH_3), –1.89 (s, 2H, NH). ^{1}H NMR ($CDCl_3$, 500.13 MHz): δ 9.47 (s, 8H, *β*), 4.93 (t, 8H, $CH_2CH_2C\underline{H}_2Por$), 2.51 (m, 8H, $CH_2C\underline{H}_2CH_2Por$), 1.80 (m, 8H, $C\underline{H}_2CH_2CH_2Por$), 1.53 (m, 8H, $CH_3(C\underline{H}_2)_5CH_2$), 1.20–1.40 (m, 40H, $CH_3(C\underline{H}_2)_5CH_2$), 0.88 (t, 12H, CH_3), –2.64 (s, 2H, NH).

2.2.7. Preparation of Ga($TC_{10}P$)Cl. This procedure was adapted from that reported for the preparation of Ga(OEP)Cl.[34] A stirred solution of $H_2TC_{10}P$ (0.336 g, 0.386 mmol), $GaCl_3$ (0.107 g, 0.608 mmol), and NaOAc (0.308 g, 3.75 mmol) in glacial acetic acid (20 mL) was refluxed overnight, during which the color of the reaction mixture turned from dark green to dark purple. The reaction mixture was opened to air and allowed to cool to room temperature, which resulted in the precipitation of the crude product as a purple solid. The precipitate was collected via filtration, washed with cold glacial acetic acid (5 mL) and water (10 mL), extracted into toluene (20 mL), and filtered. The product was isolated as a purple solid upon removal of volatile components *in vacuo* (0.339 g, 0.348 mmol, 90% yield). ^{1}H NMR (C_6D_6, 500.13 MHz; Figure 2.1): δ 9.53 (s, 8H, *β*), 4.76 (t, 8H, $CH_2CH_2C\underline{H}_2Por$), 2.48 (m, 8H, $CH_2C\underline{H}_2CH_2Por$), 1.64 (m, 8H, $C\underline{H}_2CH_2CH_2Por$), 1.35–1.45 (m, 8H, $CH_3(CH_2)_5C\underline{H}_2$), 1.26–1.35 (m, 40H, $CH_3(C\underline{H}_2)_5CH_2$), 0.90 (t, 12H, CH_3). $^{13}C\{^1H\}$ NMR ($CDCl_3$, 125.76 MHz; Figure 2.2): δ 147.73 (*α*), 129.46 (*β*), 118.86 (*meso*), 38.68 (CH_2), 35.58 (CH_2), 32.07 (CH_2), 30.84 (CH_2), 29.87 (CH_2), 29.85 (CH_2),

29.83 (CH_2), 29.51 (CH_2), 22.85 (CH_2), 14.28 (CH_3). UV-vis (toluene; λ_{max}, nm (rel. int.); Figure 2.9): 312 (4.9), 405 (9.7), 425 (100), 523 (8.0), 563 (4.2), 602 (2.3). LDI-TOF MS (m/z): $[M]^+$ = 972.649; predicted 972.626. Anal. Calcd. for $C_{60}H_{92}N_4GaCl$: C, 73.94; H, 9.51; N, 5.75. Found: C, 74.12; H, 9.26; N, 5.68.

2.2.8. Preparation of Ga(TC$_{10}$P)(CCPh) (1). A solution of LiCCPh (0.015 g, 0.138 mmol) in THF (~1 mL) was added to a stirred solution of Ga(TC$_{10}$P)Cl (0.087 g, 0.089 mmol) in THF (20 mL) at room temperature. The color of the reaction mixture immediately changed from dark purple to dark green. After 2 h, the volatile components were removed *in vacuo*. The crude product was extracted into pentane (30 mL), filtered through Celite, and the volatile components were removed *in vacuo*. The crude product was dissolved in a mixture of THF (10 mL) and CH_3CN (20 mL), which was reduced in volume to ~20 mL under vacuum to induce precipitation of the product. The product was obtained as a purple powder via filtration, and dried under vacuum (0.087 g, 0.084 mmol, 94% yield). ^{1}H NMR (C_6D_6, 500.13 MHz; Figure 2.3): δ 9.54 (s, 8H, *β*), 6.18 (t, 1H, *J* = 7.4 Hz, *p*-Ph), 6.03 (m, 2H, *m*-Ph), 5.54 (d, 2H, *J* = 7.5 Hz, *o*-Ph), 4.79 (t, 8H, $CH_2CH_2C\underline{H}_2$Por), 2.48 (m, 8H, $CH_2C\underline{H}_2CH_2$Por), 1.61 (m, 8H, $C\underline{H}_2CH_2CH_2$Por), 1.33–1.39 (m, 8H, $CH_3(CH_2)_5C\underline{H}_2$), 1.25–1.33 (m, 40H, $CH_3(C\underline{H}_2)_5CH_2$), 0.90 (t, 12H, CH_3). ^{13}C{^{1}H} NMR (THF-d_8, 125.76 MHz; Figure 2.4): δ 148.30 (*α*), 130.79 (*o*-Ph), 129.75 (*β*), 127.03 (*m*-Ph), 125.81 (*p*-Ph), 124.87 (*ipso*-Ph), 118.62 (*meso*), 95.14 (C≡C), 38.98 (CH_2), 35.43 (CH_2), 32.66 (CH_2), 31.00 (CH_2), 30.51 (CH_2), 30.45 (CH_2), 30.10 (CH_2), 23.36 (CH_2), 14.26 (CH_3); one C≡C resonance and one CH_2 resonance were not observed. UV-vis (toluene; λ_{max}, nm (rel. int.); Figure 2.9): 317, (4.3), 410 (8.1), 431 (100), 531 (0.9), 573 (3.0), 613 (2.6). LDI-TOF MS (m/z): $[M]^+$ = 1038.702; predicted 1038.697. Anal. Calcd. for $C_{68}H_{97}N_4Ga$: C, 78.51; H, 9.40; N, 5.39. Found: C, 78.29; H, 9.60; N, 5.28.

2.2.9. Preparation of Ga($TC_{10}P$)(*p*-CCC_6H_4CCPh) (2). A solution of $LiCCC_6H_4CCPh$ (0.020 g, 0.096 mmol) in THF (~1 mL) and added to a stirred solution of Ga($TC_{10}P$)Cl (0.075 g, 0.077 mmol) in THF (20 mL) at room temperature. The color of the reaction mixture immediately changed from dark purple to dark blue-green. After 2 h, the volatile components were removed *in vacuo*. The crude product was extracted into pentane (30 mL), filtered through Celite, and the solvent was removed *in vacuo*. The crude product was dissolved in a mixture of THF (10 mL) and CH_3CN (20 mL), which was reduced in volume to ~20 mL under vacuum to induce precipitation of the product. The product was obtained as a purple powder via filtration, and dried under vacuum (0.057 g, 0.050 mmol, 65% yield). ^{1}H NMR (THF-d_8, 500.13 MHz; Figure 2.5): δ 9.69 (s, 8H, *β*), 7.19–7.25 (m, 2H, H6 or H7), 7.13–7.29 (m, 3H, H6 or H7, H8), 6.52 (d, 2H, *J* = 8.5 Hz, H3), 5.43 (d, 2H, *J* = 8.5 Hz, H2), 4.97 (t, 8H, $CH_2CH_2C\underline{H}_2Por$), 2.45 (m, 8H, $CH_2C\underline{H}_2CH_2Por$), 1.68 (m, 8H, $C\underline{H}_2CH_2CH_2Por$), 1.38–1.50 (m, 8H, $CH_3(CH_2)_5C\underline{H}_2$) 1.20–1.38 (m, 40H, $CH_3(C\underline{H}_2)_5CH_2$), 0.86 (t, 12H, CH_3). $^{13}C\{^1H\}$ NMR (THF-d_8, 125.76 MHz; Figure 2.6): δ 148.33 (*α*), 131.78 (C6 or C7), 130.81 (C2), 130.38 (C3), 129.86 (*β*), 128.80 (C6 or C7), 128.62 (C8), 124.91, 123.98, 120.84 (C1 or C4, or C5), 118.69 (*meso*), 94.83 (C≡C), 90.28 (C≡C), 89.57 (C≡C), 38.97 (CH_2), 35.44 (CH_2), 32.68 (CH_2), 31.01 (CH_2), 30.53 (CH_2), 30.47 (CH_2), 30.12 (CH_2), 23.37 (CH_2), 14.26 (CH_3); one C≡C resonance and one CH_2 resonance were not observed. UV-vis (toluene; λ_{max}, nm (rel. int.); Figure 2.9): 306 (13.3), 313 (12.7; sh), 324 (12.1), 411 (9.3), 430 (100), 531 (0.7), 572 (3.4), 613 (2.9). LDI-TOF MS (m/z): $[M]^+$ = 1138.721; predicted: 1138.728. Anal. Calcd. for $C_{76}H_{101}N_4Ga$: C, 80.05; H, 8.93; N, 4.91. Found: C, 79.89; H, 8.71; N, 4.96.

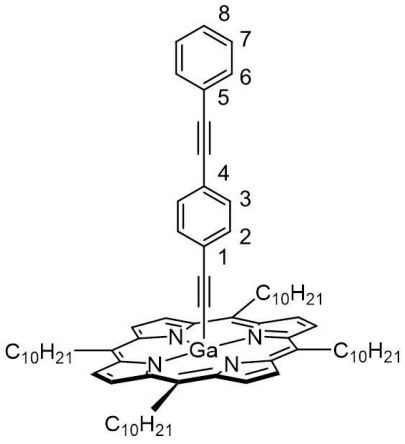

2.2.10. Preparation of Ga(TC$_{10}$P)(4,4′-CCC$_6$H$_4$CCC$_6$H$_4$CCPh) (3). A solution of 4,4′-LiCCC$_6$H$_4$CCC$_6$H$_4$CCPh (0.028 g, 0.091 mmol) in THF (~5 mL) was added to a stirred solution of Ga(TC$_{10}$P)Cl (0.082 g, 0.084 mmol) in THF (15 mL). The color of the reaction mixture immediately changed from dark purple to dark blue-green. After 2 h the volatile components were removed *in vacuo*. The crude mixture was extracted into toluene (30 mL), filtered through Celite, and the volatile components were removed *in vacuo*. The crude product was dissolved in a mixture of THF (10 mL) and CH$_3$CN (20 mL), which was reduced in volume to ~20 mL under vacuum to induce precipitation of the product. ^{1}H-NMR spectra of the crude product revealed the presence of trace 4,4′-HCCC$_6$H$_4$CCC$_6$H$_4$CCPh; this was removed by repeating the recrystallization procedure four times. The product was obtained as a purple powder via filtration, and dried under vacuum (0.060 g, 0.048 mmol, 57% yield). ^{1}H NMR (CD$_2$Cl$_2$, 500.13 MHz; Figure 2.7): δ 9.68 (s, 8H, *β*), 7.45–7.50 (m, 2H, H10 or H11), 7.37 (d, 2H, *J* = 8.5 Hz, H6 or H7), 7.30–7.35 (m, 3H, H10 or H11, H12), 7.25 (d, 2H, *J* = 8.5 Hz, H6 or H7), 6.54 (d, 2H, *J* = 8.5 Hz, H3), 5.44 (d, 2H, *J* = 8.5 Hz, H2), 5.00 (t, 8H, CH$_2$CH$_2$C<u>H$_2$</u>Por), 2.46 (m, 8H, CH$_2$C<u>H$_2$</u>CH$_2$Por), 1.69 (m, 8H, C<u>H$_2$</u>CH$_2$CH$_2$Por), 1.45–1.53 (m, 8H, CH$_3$(CH$_2$)$_5$C<u>H$_2$</u>) 1.20–1.38 (m, 40H, CH$_3$(C<u>H$_2$</u>)$_5$CH$_2$), 0.86 (t, 12H, CH$_3$). ^{13}C{^{1}H} NMR (THF-*d*$_8$, 125.76 MHz; Figure 2.8): δ 148.53 (*α*), 132.26 (C10 or C11), 132.14 (C7), 132.00 (C6), 131.04 (C2), 130.63 (C3), 130.08 (*β*), 129.27 (C12), 129.20 (C10 or C11), 125.36, 124.03 123.99, 123.88, 120.71 (C1, C4, C5, C8, C9), 118.90 (*meso*), 95.00 (C≡C), 91.83 (C≡C), 91.76 (C≡C), 90.15 (C≡C), 89.60 (C≡C), 39.16 (CH$_2$), 35.63 (CH$_2$), 32.87 (CH$_2$), 31.19 (CH$_2$), 30.72 (CH$_2$), 30.66 (CH$_2$), 30.31 (CH$_2$), 23.55 (CH$_2$), 14.44 (CH$_3$); one C≡C resonance

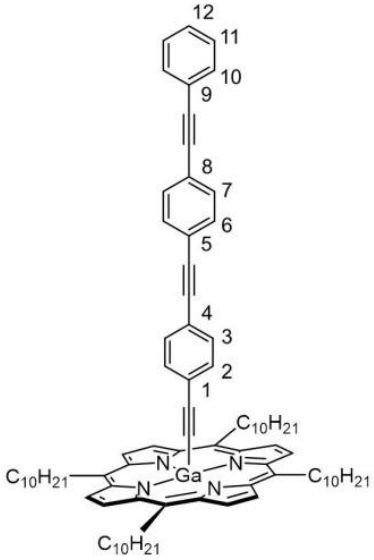

and one CH_2 resonance were not observed. UV-vis (toluene; λ_{max}, nm (rel. int.); Figure 2.9): 325 (14.5), 336 (13.9; sh), 358 (8.6; sh), 411 (7.6), 431 (100), 530 (0.6), 572 (2.8), 613 (2.3). LDI-TOF MS (m/z): $[M]^+$ = 1238.805; predicted: 1238.760. Anal. Calcd. for $C_{84}H_{105}N_4Ga$: C, 81.33; H, 8.53; N, 4.52. Found: C, 81.09; H, 8.37; N, 4.60.

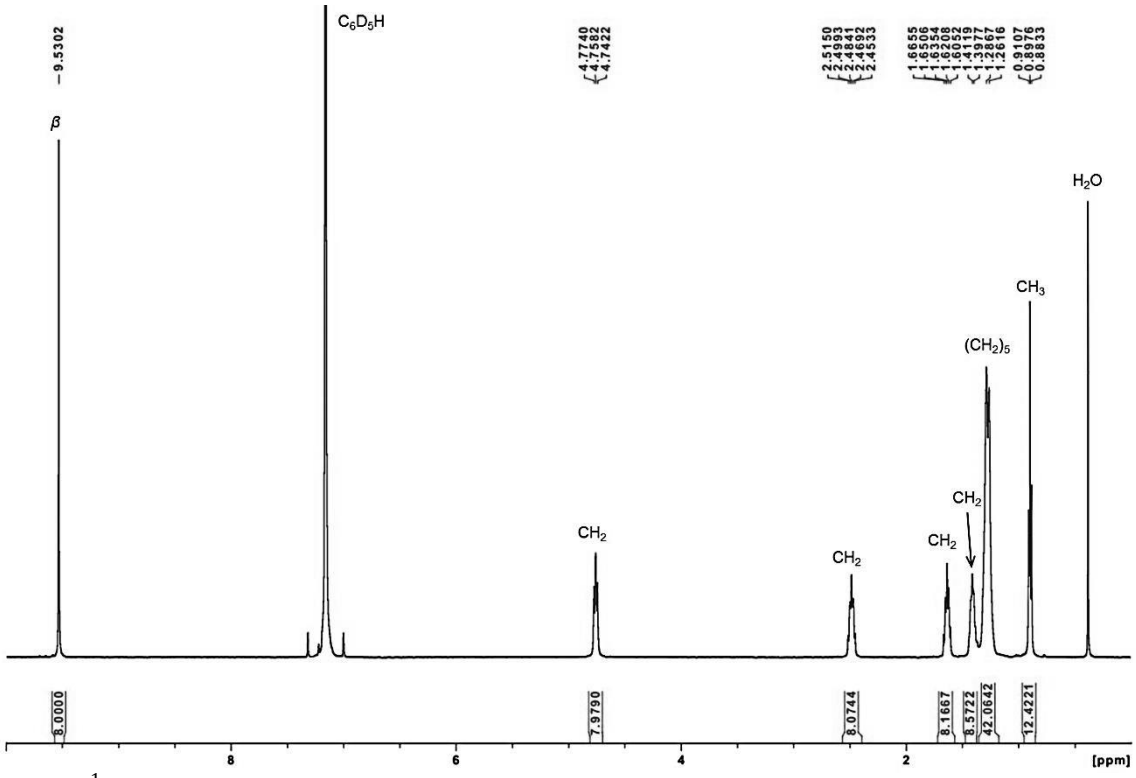

Figure 2.1. ^{1}H NMR spectrum of Ga($TC_{10}P$)Cl in C_6D_6.

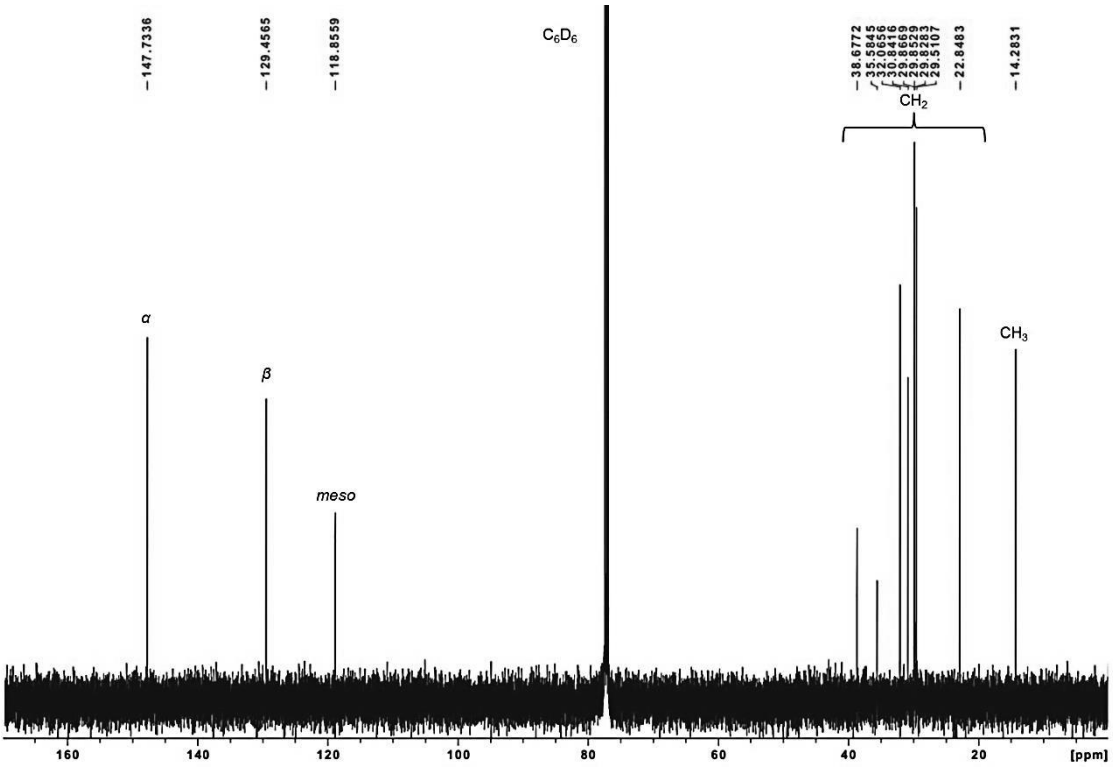

Figure 2.2. $^{13}C\{^{1}H\}$ NMR spectrum of Ga($TC_{10}P$)Cl in $CDCl_3$.

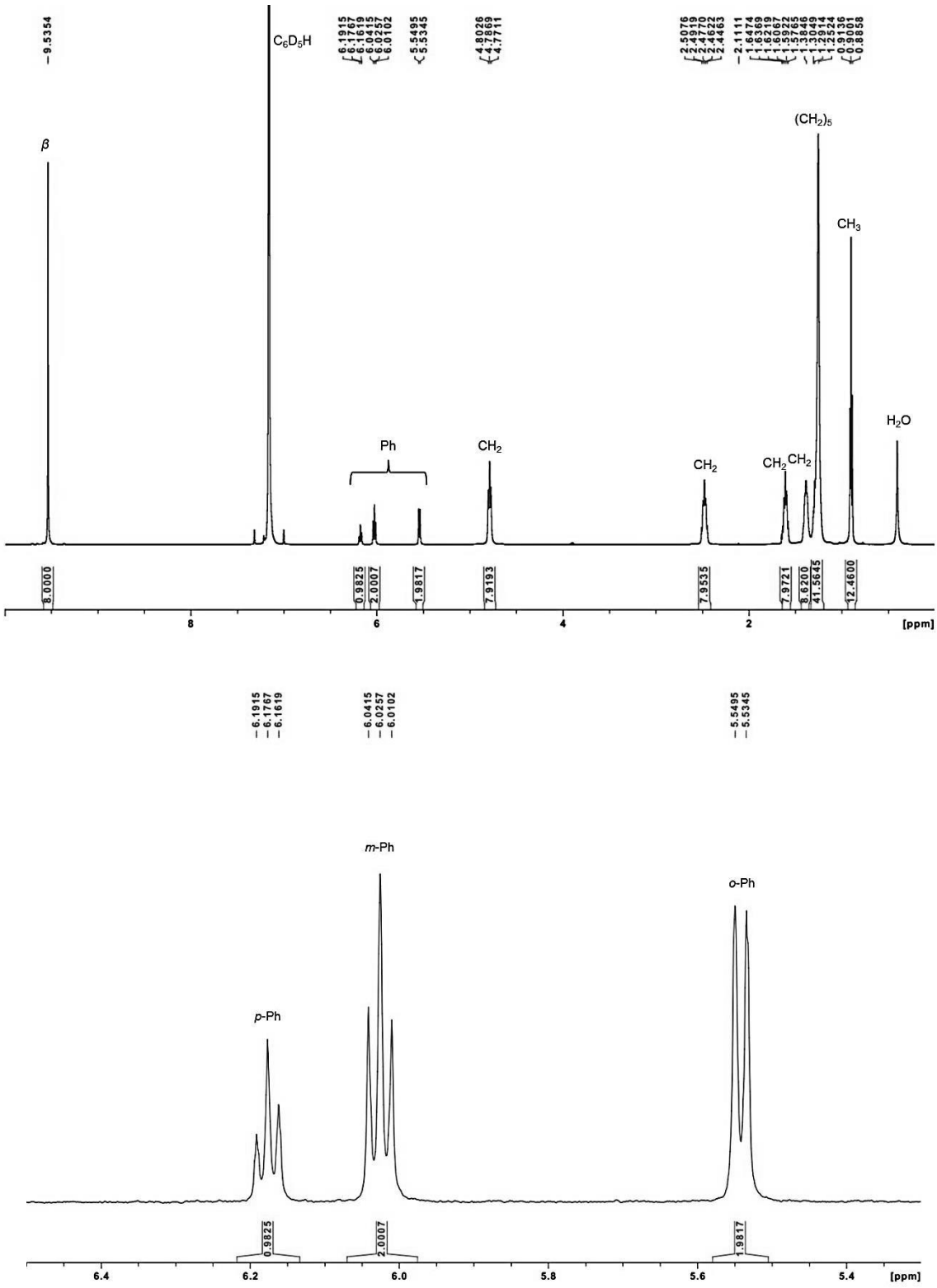

Figure 2.3. ^{1}H NMR spectrum of **1** in C_6D_6. The bottom spectrum is an expansion of the top spectrum.

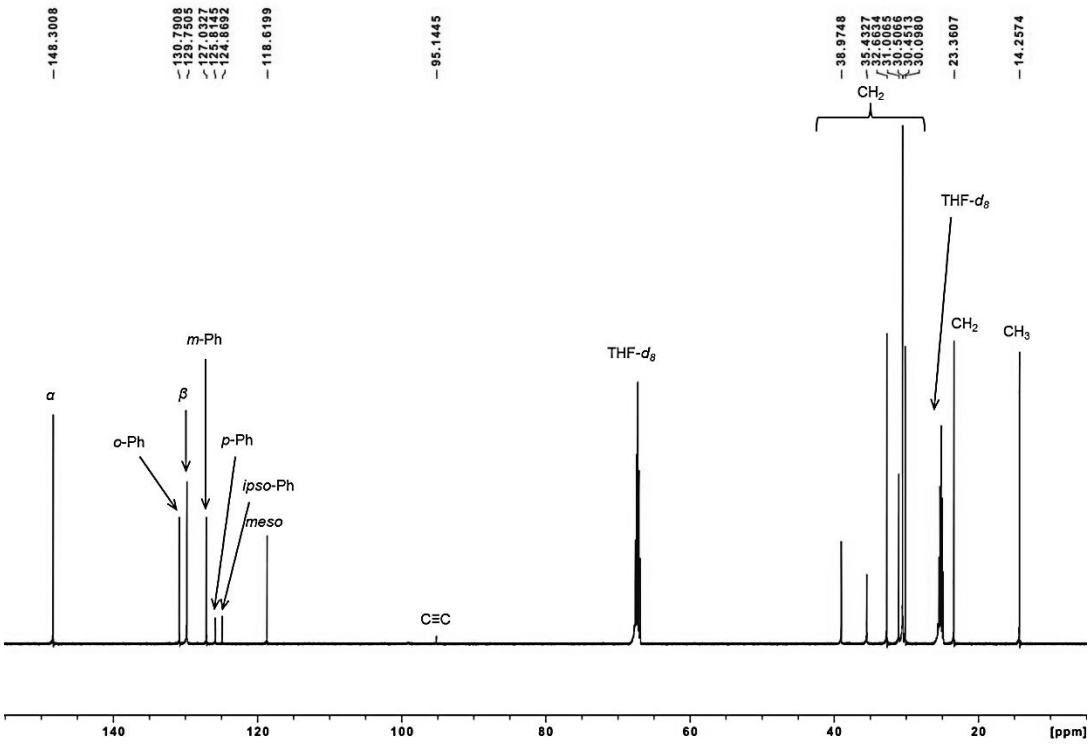

Figure 2.4. $^{13}C\{^{1}H\}$ NMR spectrum of **1** in THF-d_8.

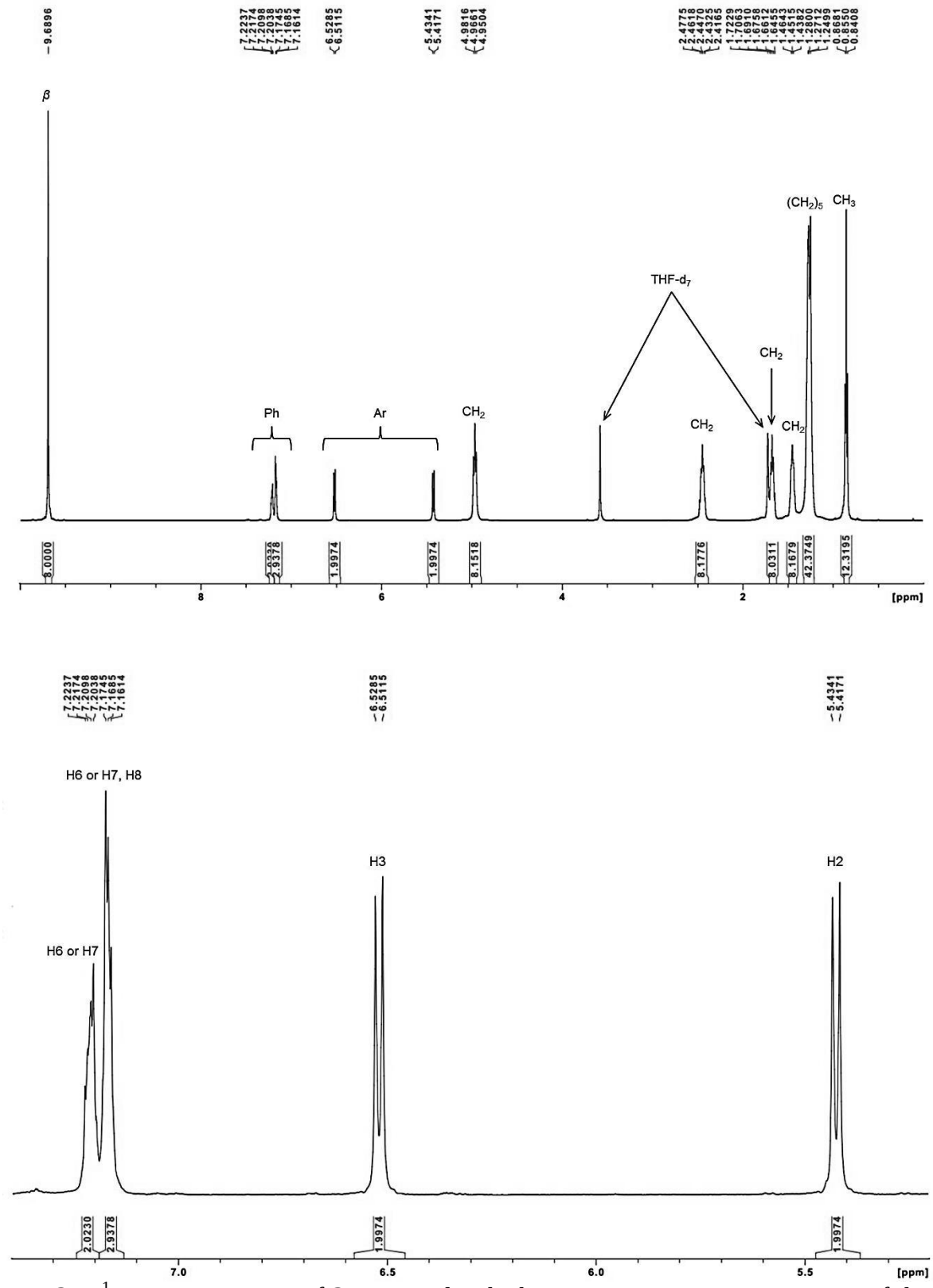

Figure 2.5. ^{1}H NMR spectrum of **2** in THF-d_8. The bottom spectrum is an expansion of the top spectrum.

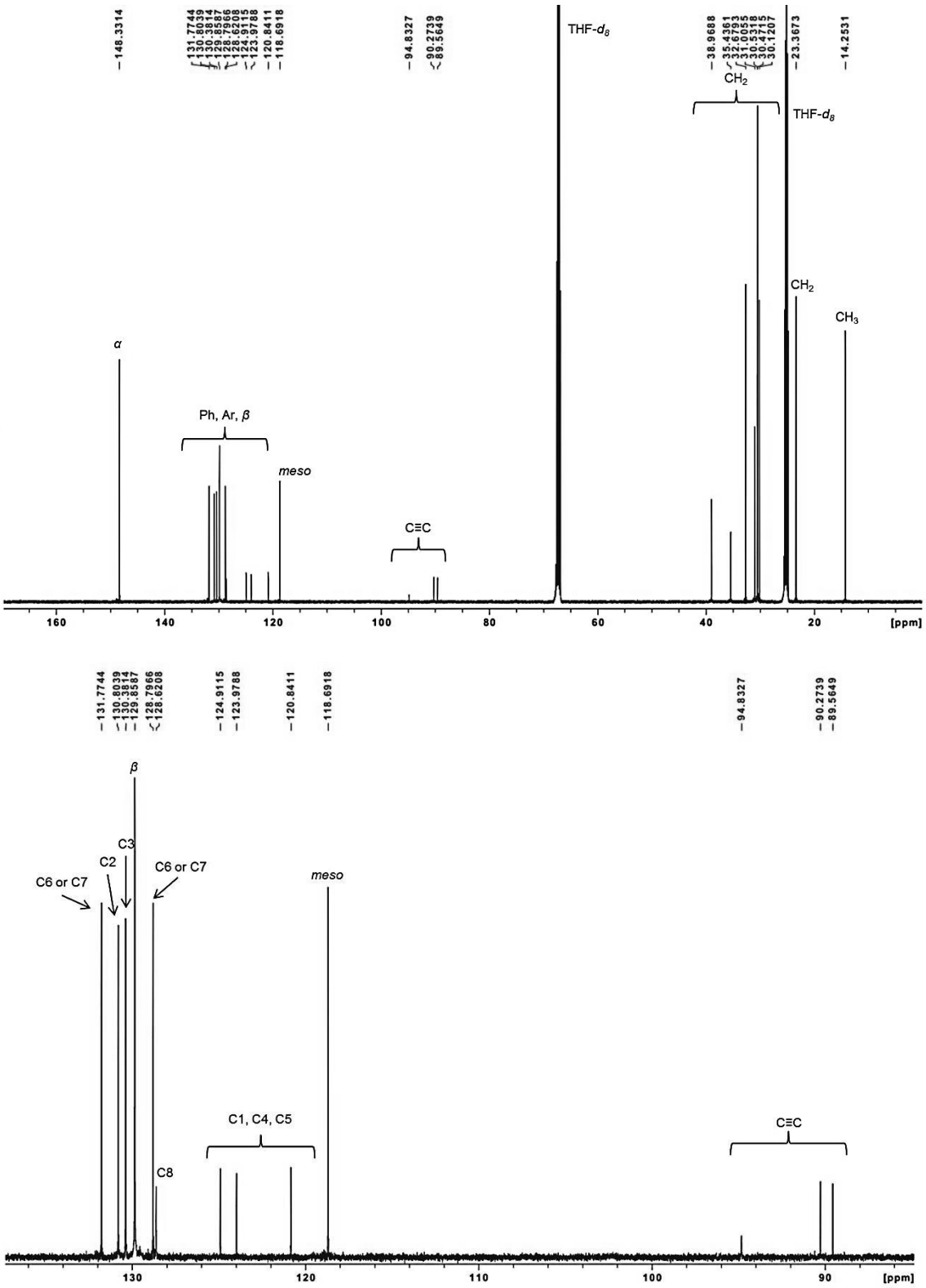

Figure 2.6. $^{13}C\{^1H\}$ NMR spectrum of **2** in THF-d_8. The bottom spectrum is an expansion of the top spectrum.

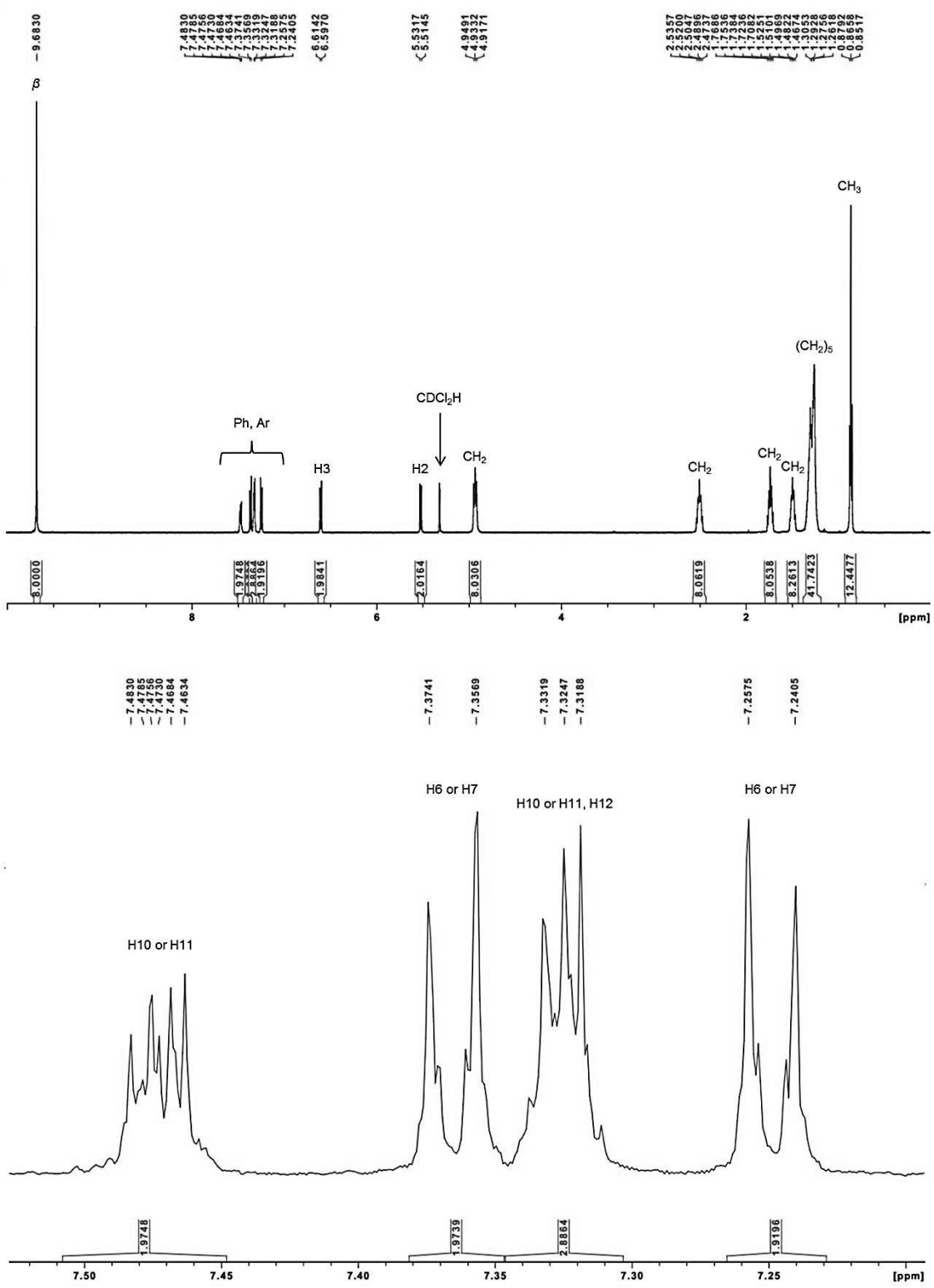

Figure 2.7. ^{1}H NMR spectrum of **3** in CD_2Cl_2. The bottom spectrum is an expansion of the top spectrum.

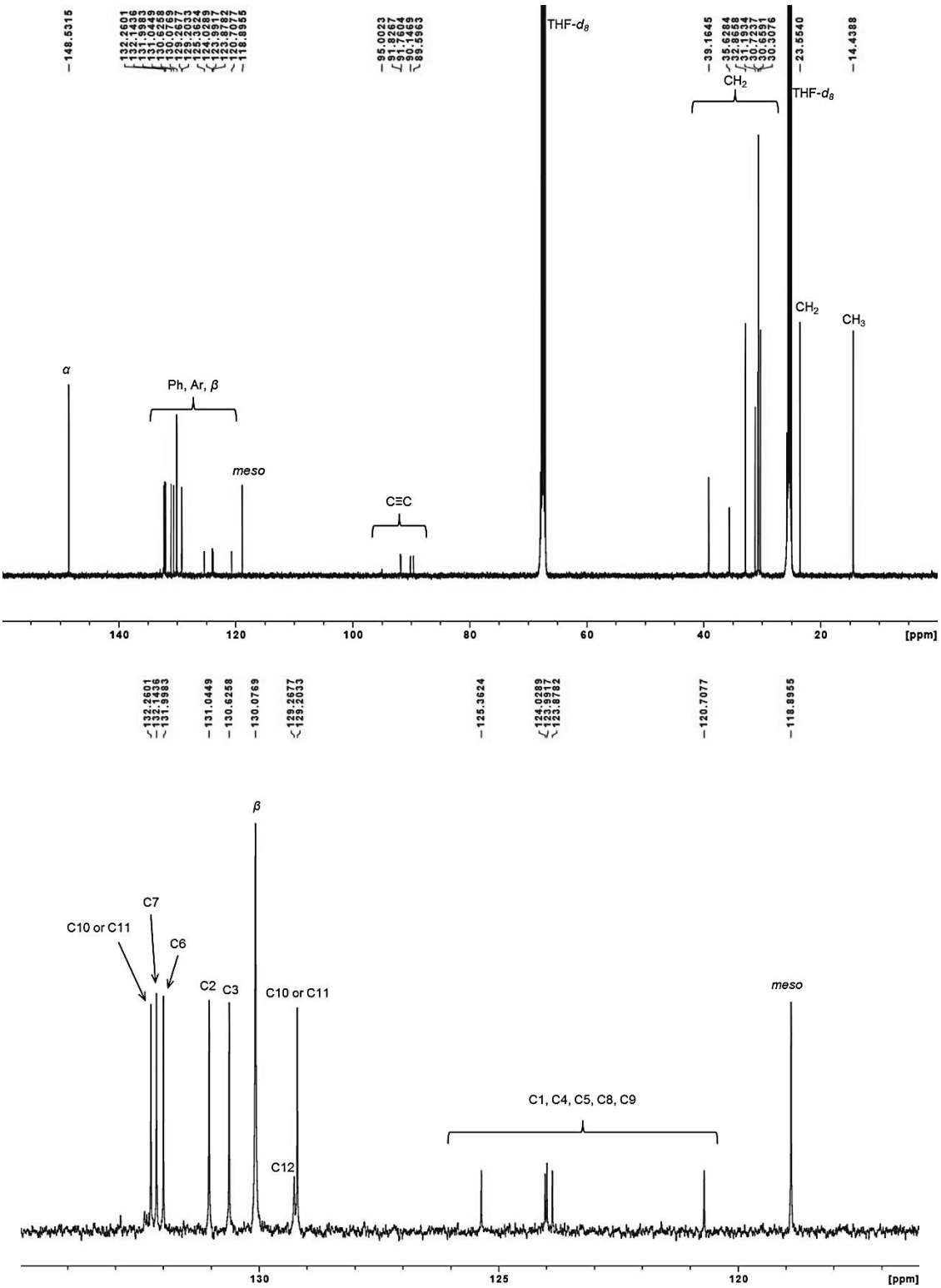

Figure 2.8a,b. $^{13}C\{^{1}H\}$ NMR spectrum of **3** in THF-d_8. The bottom spectrum is an expansion of the top spectrum.

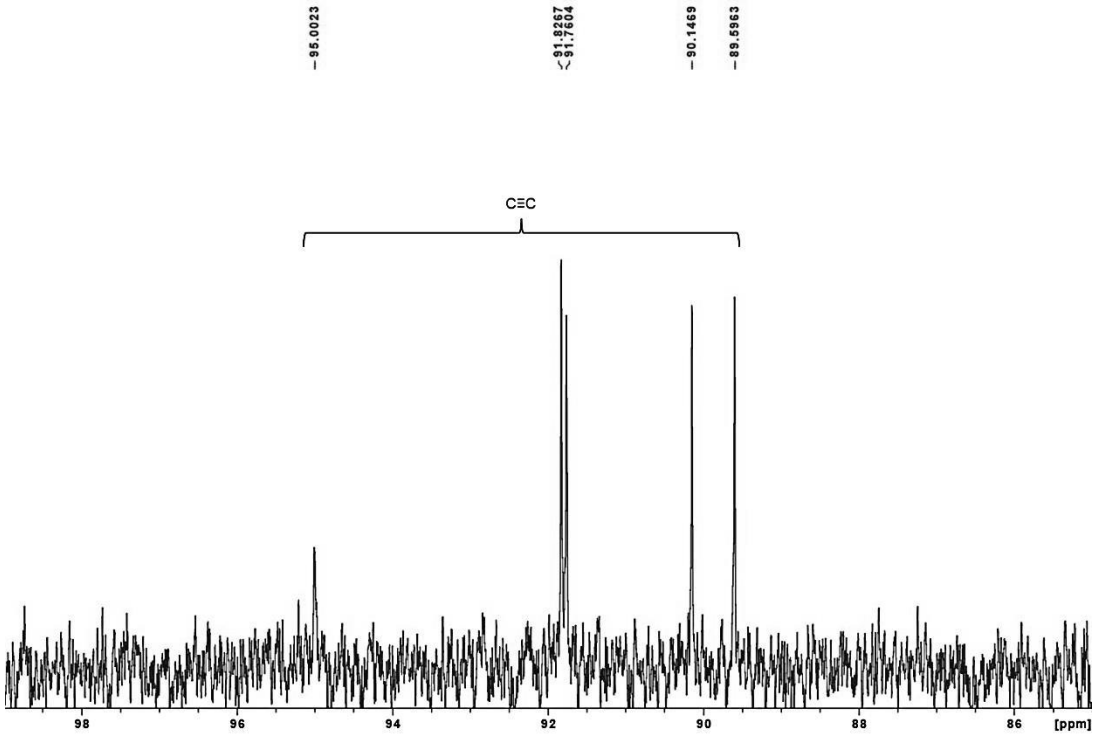

Figure 2.8c. Expansion of the C≡C region of the $^{13}C\{^{1}H\}$ NMR spectrum of **3** in THF-d_8.

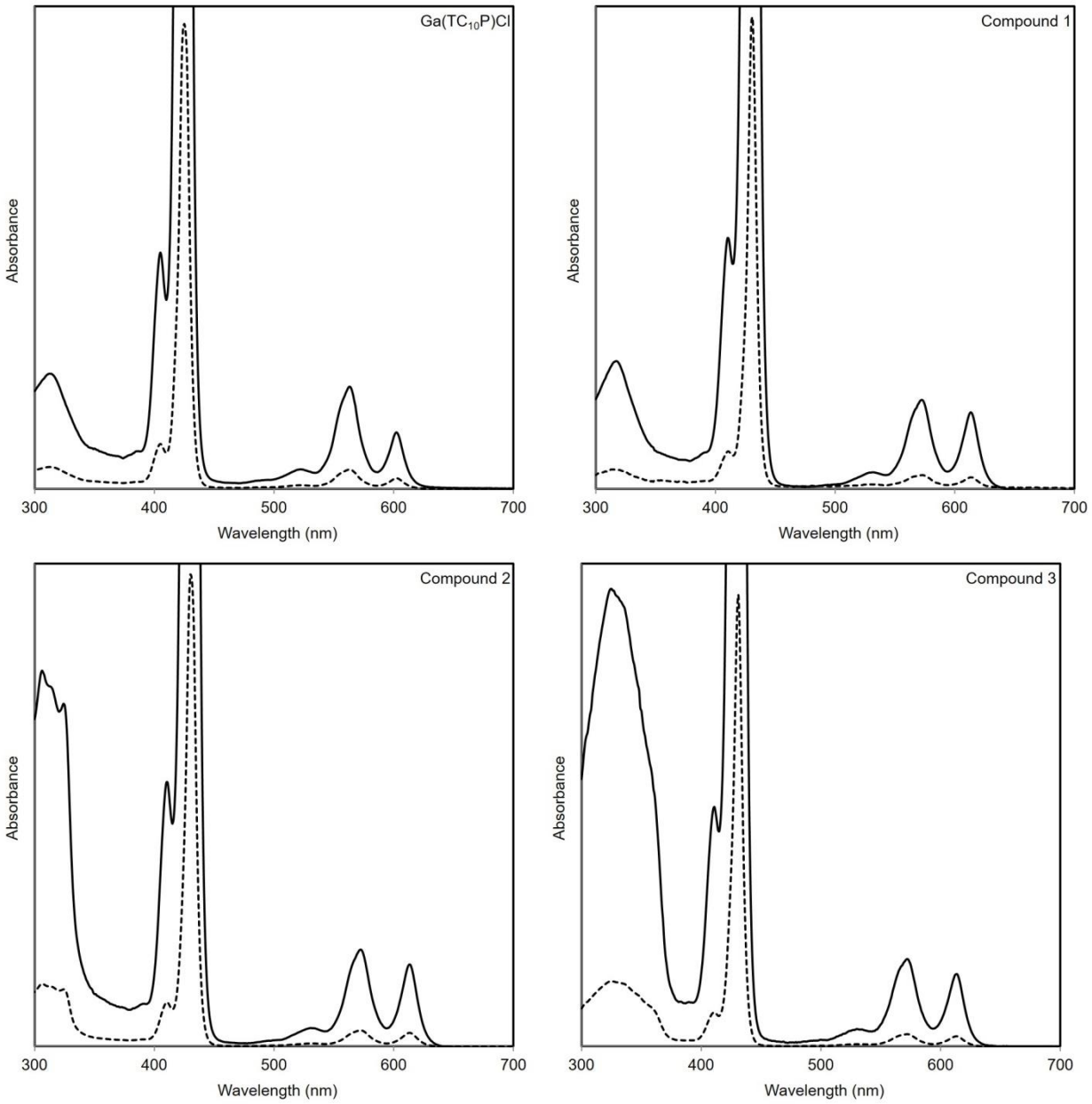

Figure 2.9. Electronic-absorption spectra of $Ga(TC_{10}P)Cl$ and compounds **1**–**3** in toluene at room temperature. The spectra represented by the solid black lines are scaled versions of those in dashed lines.

2.2.11. Sample Preparation for STM Experiments. Highly oriented pyrolytic graphite (HOPG) wafers (SPI-2 grade, SPI Supplies) measuring 7 mm × 7 mm × 1 mm were mounted to 12 mm diameter metal specimen discs with colloidal silver paste (PELCO, Ted Pella, Inc.). The surface of the HOPG substrate was cleaved with adhesive tape immediately prior to dosing. For

STM experiments performed at the solid–liquid interface, one drop of a 7.5×10^{-4} M solution of the porphyrin compound in 1-phenyloctane was deposited onto the HOPG surface with a syringe equipped with a 25-gauge needle. The STM tip was then engaged through the drop and the sample was imaged. For experiments performed at the solid–air interface, a 6 μL drop of a 2.5×10^{-4} M solution of the porphyrin compound in benzene was deposited on HOPG via a micropipette. After the benzene evaporated, one drop of neat toluene was applied to the analyte area and allowed to evaporate. The sample was then imaged by STM.

2.2.12. STM Measurements and Data Analysis. STM images were acquired at room temperature using a Digital Instruments Nanoscope IIIa standalone STM. The $Pt_{0.8}Ir_{0.2}$ tips were mechanically cut from a Pt/Ir (80/20) wire (Goodfellow). All measurements were in constant current mode. For each sample, an image of the underlying graphite surface was acquired. The data were corrected for drift post-acquisition in the SPIP software package[35] using the underlying graphite lattice parameters ($a = b = 0.246$ nm, $\Gamma = 60°$) as a reference.[36] Data analysis was performed using WSxM 5.0 software.[37] All of the images presented in the main text and SI were flattened, low-pass filtered, and sharpened by adjusting the contrast. Reported lattice parameters are averages of those determined from consecutive up-scan and down-scan images. For samples that exhibited a single packing structure (i.e., exclusively the α or β lattice), the unit-cell distances were determined from spacings within 100 sets of five consecutive porphyrin molecules, and the unit-cell angles were determined from the average of 40 measurements. For samples that exhibited mixed α/β structures, the number of adjacent unit cells of a given type was consistently less than five; for these samples the unit-cell-distances were the averages of 100 measurements of the porphyrin center-to-center distances, and the unit-cell angles were the average of 40 measurements.

2.3. Results and Discussion

2.3.1. Synthesis and Characterization of Porphyrin Compounds. $H_2TC_{10}P$ was synthesized via the "one-pot, two-step" method reported by Lindsey et al.[30] Although it was been reported by the authors that lower concentrations of the reactants afforded higher yield, reaching 25% at concentrations of 10^{-3} M for the synthesis of free base 5,10,15,20-tetra(*n*-C_5H_{11})porphyrin (H_2TC_5P), for $H_2TC_{10}P$ the starting concentrations of the reactants were kept at 2×10^{-2} M for the ease of operation. The yield for this reaction under these conditions was ~15%, which was consistent with the reported yield for the preparation H_2TC_5P with starting pyrrole and aldehyde concentrations of 10^{-2} M. In some occasions, where the porphyrin was not well-separated from the uncharacterized impurities on the silica gel column, the crude product was dissolved in toluene and filtered to remove an uncharacterized, black solid. The composition of the product was confirmed by ^{1}H NMR and LDI-TOF MS. Although the $H_2TC_{10}P$ used for this study was mostly prepared from starting material obtained from commercial sources, it was found that the undecanal used for synthesis could contain a ~3% aldehyde impurity. This caused the formation a statistical mixture of porphyrinic impurities during the preparation of $H_2TC_{10}P$, where the major impurity (~3% with respect to $H_2TC_{10}P$) can be observed in the ^{1}H NMR spectrum as a singlet at −1.84 ppm in C_6D_6 (NH resonance; $H_2TC_{10}P$: −1.89 ppm). This was circumvented by using undecanal that was prepared from 1-undecanol, which could be purchased at a higher purity (99%).

Ga($TC_{10}P$)Cl was prepared from $H_2TC_{10}P$ using the procedure for the preparation of Ga(OEP)Cl.[34] Similarly, the synthetic procedure for compounds **1–3** was based on that for Ga(OEP)(CCPh), which was previously described in detail by our group (Scheme 2.1),[1] although compounds **2** and **3** required additional purification due to the presence of residual free ligand.

Since only one set of porphyrinic ^{1}H-NMR resonances could be identified, the residual free acetylene present in the sample was attributed to unreacted material from the lithiation procedure and not from product degradation, which would have resulted in signals from more than one porphyrinic species within the sample. Due to the disparity between the solubilities of the Ga(TC$_{10}$P)(OPE) complexes and the free acetylenes in acetonitrile, compounds **2** and **3** could be purified and isolated as purple powders through repeated precipitation from THF/acetonitrile.

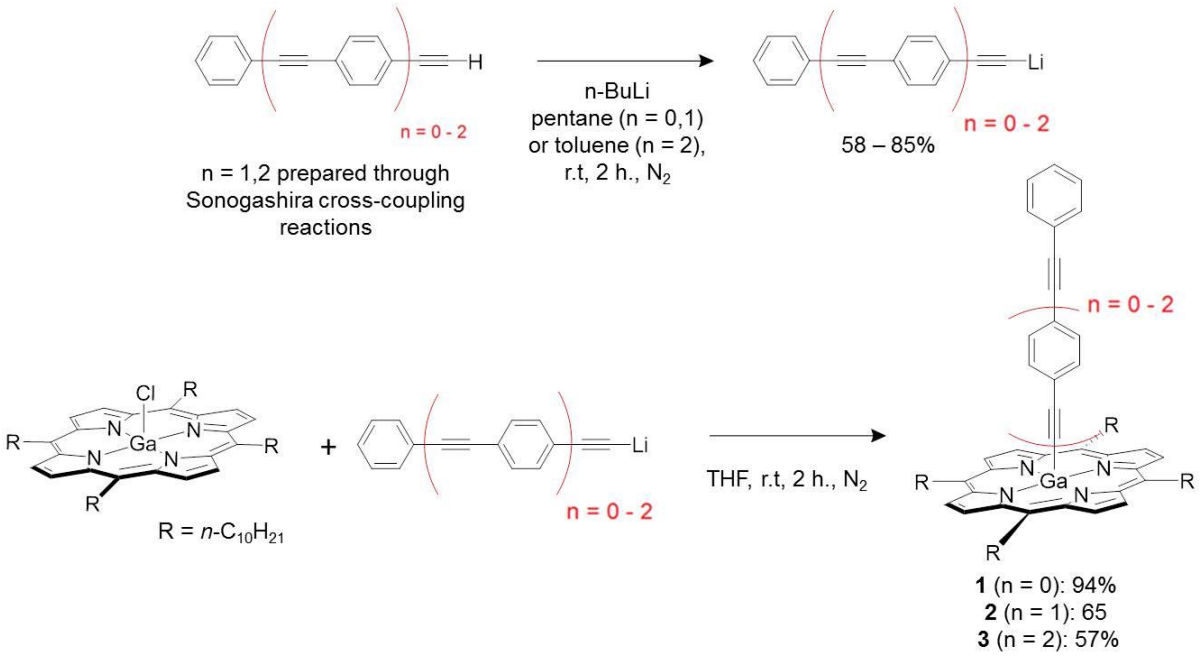

Scheme 2.1. Synthesis of Ga(TC$_{10}$P)(OPE) complexes (n = 1–3).

All newly prepared compounds were fully characterized from ^{1}H NMR, ^{13}C{^{1}H} NMR, UV-vis, LDI-TOF MS, and elemental analysis (C, H, N). For compounds **1**–**3**, the attachment of the acetylide ligands could be inferred from the upfield shifting of the aryl and/or phenyl proton resonances, compared to the analogous resonances of the free acetylenes. The shifts in proton resonances were most profound for the aryl protons (phenyl for **1**) closest to the porphyrin ring and noticeably smaller for protons that are further removed from the porphyrin plane. These shifts arise from ring current effects.[38] For compounds **2** and **3**, the ^{1}H NMR spectra of were

obtained in THF-d_8 and/or CD_2Cl_2 in order to avoid the overlapping of shifted phenyl/aryl resonances with the solvent protio impurity resonances of C_6D_6.

For all Ga($TC_{10}P$)(OPE) complexes one of the expected C≡C resonances was not observed in the $^{13}C\{^1H\}$ NMR spectra, most likely due to the combination of a long relaxation time and coupling to the $^{69}Ga/^{71}Ga$ (spin = 3/2) metal center.[39] For the $^{13}C\{^1H\}$ NMR spectra recorded in THF-d_8, one of the CH_2 resonances was unaccounted for, but was likely to be overlapping with other CH_2 resonances in the same chemical shift range. Despite these observations, the identities of the compounds were supported by the clear observations of the parent ion peaks in the LDI-TOF mass spectra, as well as results from elemental analysis (C, H, N).

All compounds were stable for at least 3 days in C_6D_6 and toluene when exposed to air, and solid samples showed no signs of degradation after several months of storage in air under ambient conditions. Thus, they are stable under the conditions of the STM experiments.

2.3.2. STM Imaging of $H_2TC_{10}P$ and Ga($TC_{10}P$)Cl at the 1-Phenyloctane/HOPG Interface. The self-assembly of $H_2TC_{10}P$ and Ga($TC_{10}P$)Cl at the 1-phenyloctane/HOPG interface are investigated to gain insight into the types of packing geometries that can be exhibited by $TC_{10}P$-based compounds. The self-assembly of $H_2TC_{10}P$ at the 1-phenyloctane/HOPG interface was previously studied by Plamont et al.,[10] at concentration of < 1.0×10^{-4} M, which is lower than that employed in our studies (below). They found that the adsorbed molecules form a periodic structure that was described as alternating rows of bright squares and dark regions that corresponded to the porphyrin cores and interdigitated alkyl chains, respectively. Although the alkyl chains were not imaged, two of the four alkyl chains were assumed to be dangling in solution.

We reinvestigated the surface chemistry of $H_2TC_{10}P$ at the higher solution concentration (7.5×10^{-4} M) relevant to our subsequent studies of the Ga($TC_{10}P$)(OPE) compounds. $H_2TC_{10}P$ self-assemble into highly ordered monolayers on HOPG upon deposition from a solution in 1-phenyloctane, as revealed by STM imaging. Representative images are shown in Figure 2.10, which shows long-range surface coverage by the self-assembled monolayer. The resulting monolayers adopt a lamellar structure, in which alternating rows of bright, disk-like features, which correspond to the porphyrin cores lying flat on the surface, and dark areas, which are attributed to interdigitated decyl chains, can be distinguished. A cross-sectional profile across the alternating bright and dark rows of a smaller scale STM image of a $H_2TC_{10}P$ monolayer shows that the spacings between the bright features are consistent across the lattice, which confirms the periodicity of the self-assembled structure. A model of a $H_2TC_{10}P$ monolayer based on observed unit cell parameters is shown in Figure 2.11. The lamellar arrangement (hereby denoted as the α structure) is characterized by the lattice parameters a = 1.37 ± 0.04 nm, b = 1.75 ± 0.05 nm, Γ = 86 ± 2˚ (Table 2.1). No domains containing other packing structures were observed. These values are not within experimental error of those previously reported for this compound at lower concentration,[10] but are reproducible across various samples and at various time points post-deposition. That monolayer structure can be affected by solvent and/or solution concentration is well known.[40, 41]

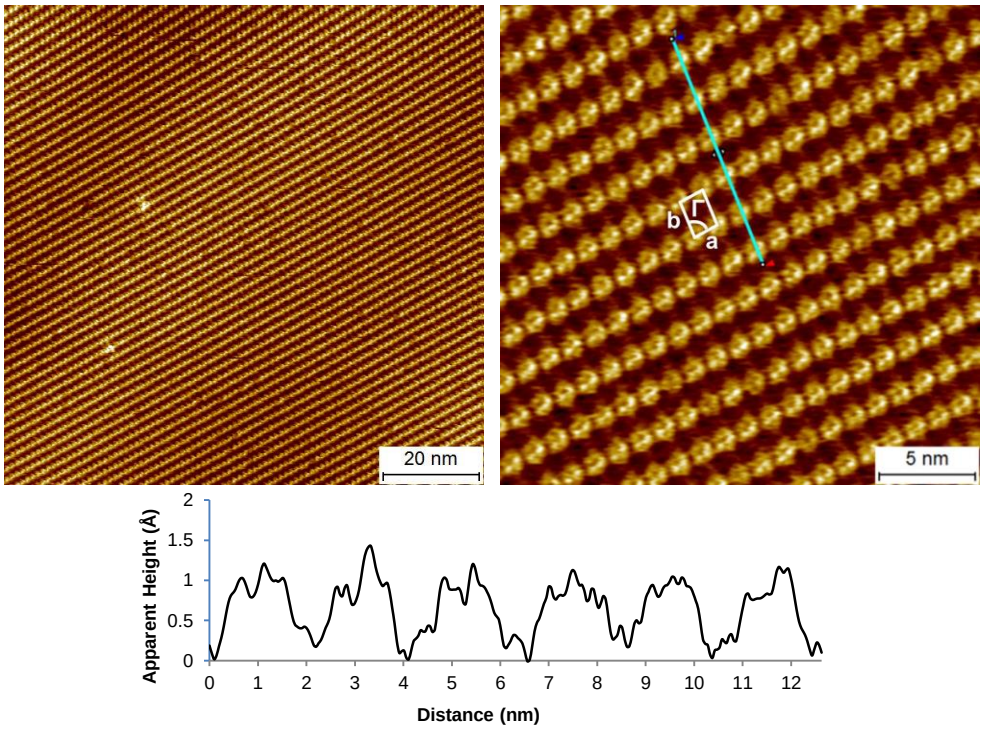

Figure 2.10. STM images and cross-sectional profile of a $H_2TC_{10}P$ monolayer on HOPG at the solid–liquid interface (1-phenyloctane, 7.5×10^{-4} M; I = 9 pA, V = –650 mV). The cross-sectional profile corresponds to the teal line in the image, drawn along the *b* lattice vector.

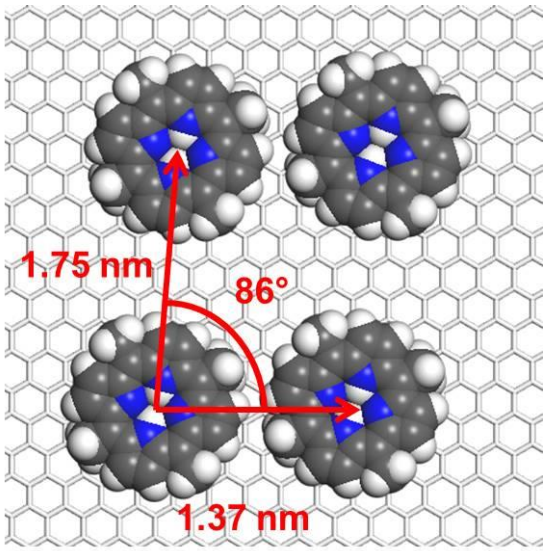

Figure 2.11. Molecular model of a $H_2TC_{10}P$ unit cell constructed using the lattice parameters obtained from the STM images. The alkyl chains are omitted since their orientations are not observed; the rotational orientation of the porphyrin relative to the lattice vectors is not known.

Table 2.1. Lattice Parameters of Monolayers of $TC_{10}P$-Containing Compounds at the 1-Phenyloctane (7.5×10^{-4} M)/HOPG Interface.[a]

parameter	$H_2TC_{10}P$ (α)[b]	$Ga(TC_{10}P)Cl$ (β)	**1** (α)	**2** (α)	**2** (β)	**3** (α)	**3** (β)
a (nm)	1.37(4)	1.71(3)	1.34(3)	1.33(8)	1.61(7)	1.39(3)	1.68(13)
b (nm)	1.75(5)	2.09(4)	1.72(5)	1.72(7)	2.12(7)	1.70(5)	2.16(4)
Γ (°)	86(2)	70(2)	85(2)	86(2)	71(2)	85(2)	71(3)
A (nm^2)	2.39(14)	3.36(17)	2.30(13)	2.28(24)	3.23(29)	2.35(13)	3.43(39)
density ($molecules/nm^2$)	0.42	0.30	0.44	0.44	0.31	0.43	0.30

[a] Values in parentheses are standard deviations of the last digit(s). [b] Previously reported lattice parameters for a sample prepared with a concentration of $< 1.0 \times 10^{-4}$ M in 1-phenyloctane: a = 1.31(2) nm, b = 1.90(10) nm, Γ = 70(5)° (Plamont, R.; Kikkawa, Y.; Takahashi, M.; Kanesato, M.; Giorgi, M.; Shun, A. C. K.; Roussel, C.; Balaban, T. S., *Chem–Eur. J.* **2013**, *19*, 11293–11300).

$Ga(TC_{10}P)Cl$ also forms ordered monolayers on HOPG at the solid-liquid (1-phenyloctane) interface measuring hundreds of nanometers in width, as revealed by STM (Figure 2.12). The adsorbed molecules appear as sharp, bright dots, in contrast to the disk-like features seen in STM images of $H_2TC_{10}P$ monolayers. This is consistent with the STM observations previously reported by our group for Ga(OEP)Cl monolayers on HOPG;[1] as in that study, we ascribe these bright features to the Cl ligands that extend above the porphyrin plane. Compared to monolayers of $H_2TC_{10}P$ at the 1-phenyloctane/HOPG interface, monolayers of $Ga(TC_{10}P)Cl$ adopt a structure with a unit cell (hereby denoted as β) that is defined by the lattice parameters a = 1.71 ± 0.03 nm, b = 2.09 ± 0.04 nm, Γ = 70 ± 2°. A model of a $Ga(TC_{10}P)Cl$ monolayer based on the observed unit cell parameters is shown in Figure 2.13. This structure is reproducible across samples and experimental time points post-deposition, indicating that the observed arrangement is thermodynamically stable. The growth of the self-assembled monolayers can occasionally be observed (Figure 2.14).

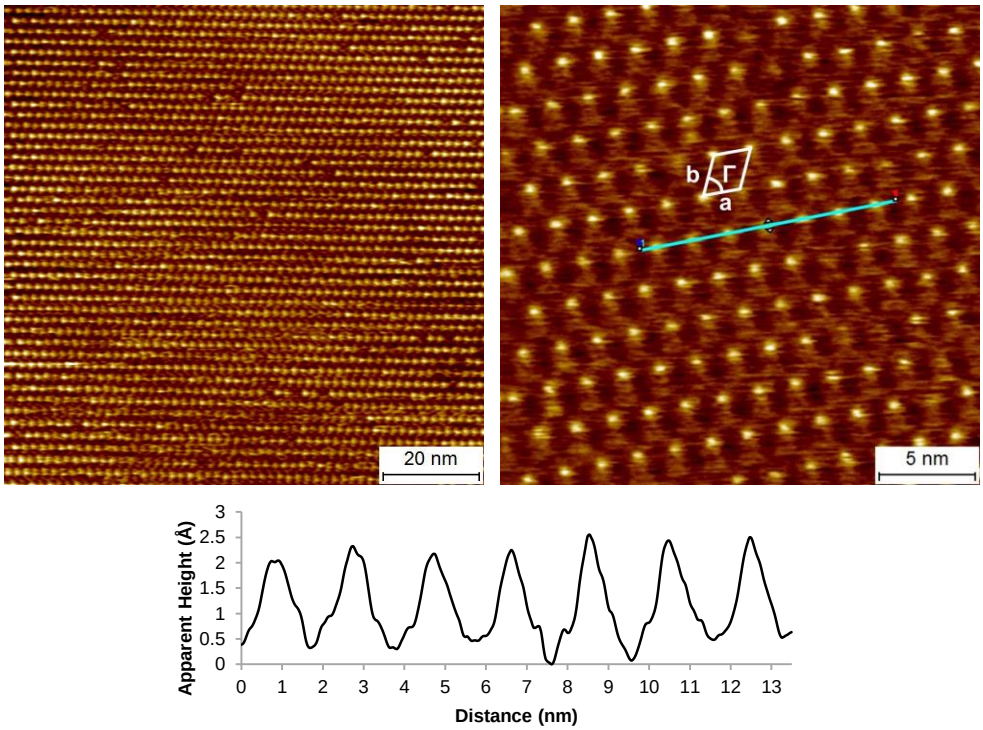

Figure 2.12. STM images and cross-sectional profile of Ga(TC_{10}P)Cl monolayers on HOPG at the solid–liquid interface (1-phenyloctane, 7.5×10^{-4} M; left: I = 6 pA, V = –800 mV; right: I = 8 pA, V = –275 mV). The cross-sectional profile corresponds to the teal line in the image, drawn along the *a* lattice vector.

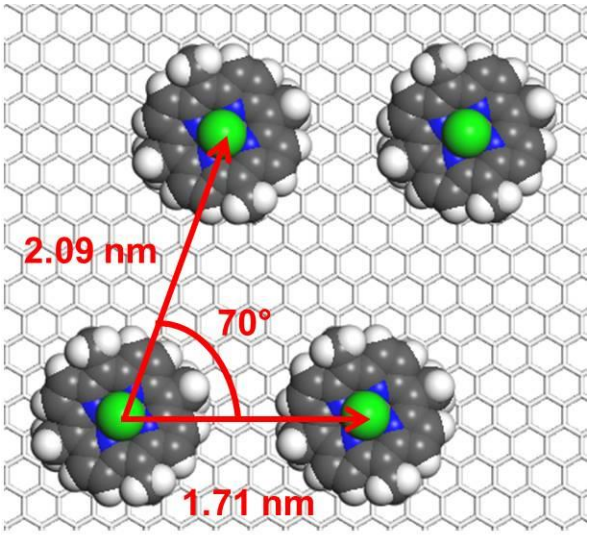

Figure 2.13. Molecular model of a Ga(TC_{10}P)Cl unit cell constructed using the lattice parameters obtained from the STM images. The alkyl chains are omitted since their orientations are not observed; the rotational orientation of the porphyrin relative to the lattice vectors is not known.

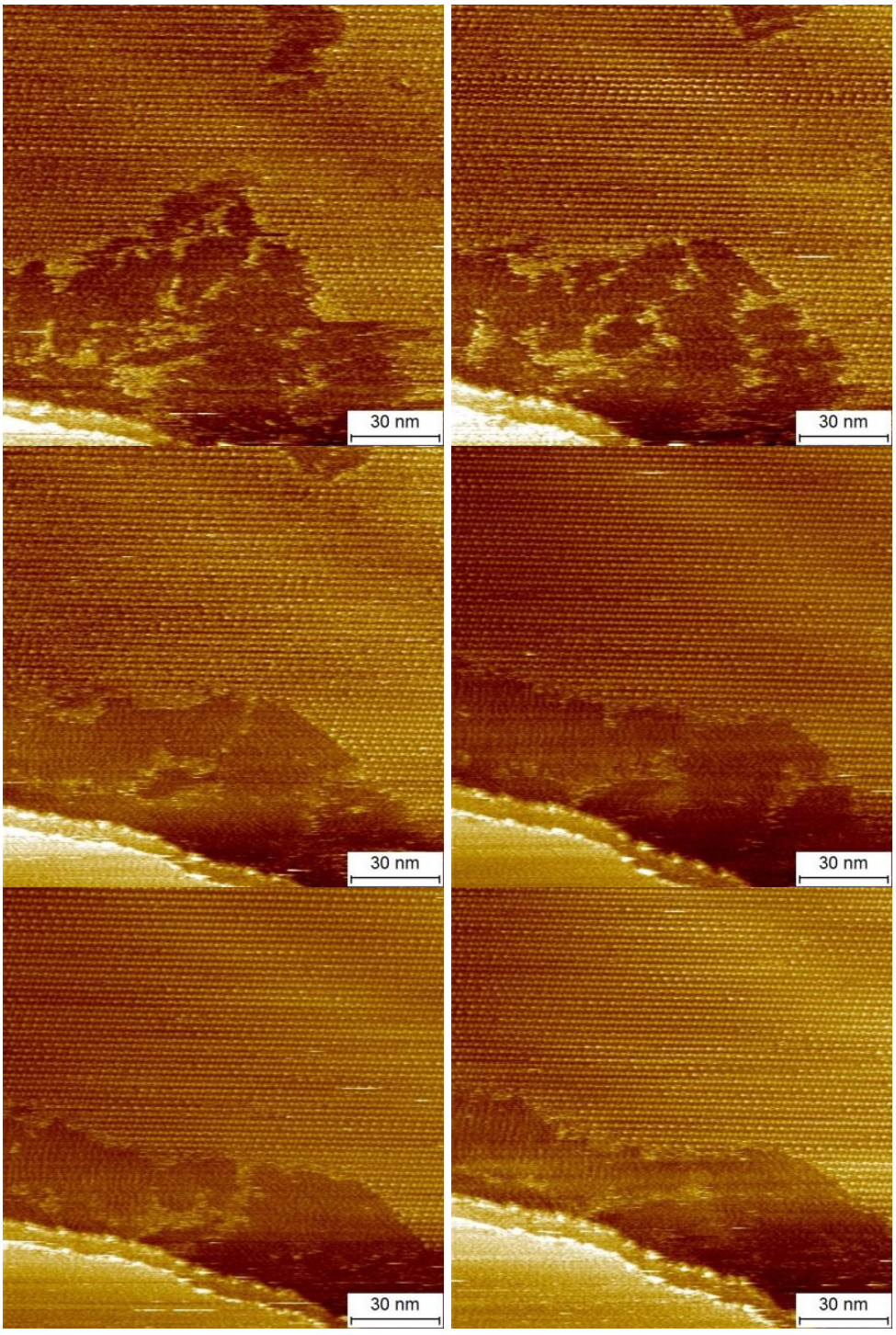

Figure 2.14. Consecutive STM images showing the growth of a monolayer of $Ga(TC_{10}P)Cl$ on HOPG at the solid–liquid interface (1-phenyloctane, 7.5×10^{-4} M; I = 6 pA, V = –800 mV). The feature at the lower left is a HOPG step edge.

There are few studies that compare the monolayers formed by five-coordinate metalloporphyrins with long alkyl-chained substituents to those of four-coordinate compounds.[2, 42, 43] Mazur et al. previously conducted STM experiments to demonstrate the structure-directing effects of the vanadyl ion (VO^{2+}) on the self-assembly of the 2,9,16,23-tetraphenoxy-29*H*,31*H*-phthalocyanine complex (VOPcPhO) at the *n*-alkyl benzene/HOPG interface.[42] It was discovered that VOPcPhO was able to form at least three stable molecular patterns, while the free base analog only formed one; the stark difference in organization behavior was attributed to the presence of a central dipole in VOPcPhO. Nicholls *et al*., in a study on self-assembled structures formed by the coadsorption of 5,10,15,20-tetra(carboxyphenyl)porphyrins (TCP) and 5-(octadecyloxy)isophthalic acid, observed that CuTCP forms hexagonally close-packed domains directly on HOPG at the 1-phenyloctane/HOPG interface, while the same phenomenon was not observed for Fe(TCP)Cl; this result was attributed to the enhancement of the molecule-substrate interaction by the Fe-Cl complex.[43, 44] While these examples highlighted the possible importance of the dipole moment induced by the central metal complex, further work will be required to understand whether it is relevant to the observation of different structures for $H_2TC_{10}P$ and $Ga(TC_{10}P)Cl$.

2.3.3. Analysis of Unit Cell Areas for $H_2TC_{10}P$ and $Ga(TC_{10}P)Cl$ Monolayers. In the STM images of the monolayers of $H_2TC_{10}P$ and $Ga(TC_{10}P)Cl$ on HOPG, the *n*-$C_{10}H_{21}$ side chains are not resolved. Prior STM studies of alkyl-porphyrin compounds at the solid–liquid interface have reported, in some cases, monolayers with unit-cell areas that are smaller than the maximum surface-contact area of the molecule; this has been interpreted as being consistent with some portion of the alkyl side chains being in the solvent phase rather than adsorbed to the surface,[10, 13, 14] or with overlap of alkyl side chains on the surface.[12]

From the lattice parameters of the $H_2TC_{10}P$ and Ga($TC_{10}P$)Cl monolayers, the unit cell areas are calculated to be 2.39 ± 0.14 nm^2 and 3.36 ± 0.17 nm^2, respectively. The estimated surface-contact area of a porphyrin ring is ~1.0 nm^2 .[45] The maximum area occupied by a fully adsorbed decyl chain is estimated to be approximately 0.6 nm^2. This estimate is based on the findings by Watel et al., who studied the adsorption of hexatriacontane (*n*-$C_{36}H_{74}$) at the decane/HOPG interface[46] and found they formed close-packed parallel strips with a strip width of 4.7 nm, which corresponds to the length of a *n*-$C_{36}H_{74}$ molecule. The intermolecular distance between molecules within the same strip was measured to be 0.44 ± 0.02 nm, which was consistent with the carbon skeletons lying parallel to the surface. From these two values, the area occupied by each *n*-$C_{36}H_{74}$ molecule was approximated to be ~2.1 nm^2. Simple proportionality between chain lengths suggests that an adsorbed decyl chain in the same orientation would occupy ~0.6 nm^2 if fully adsorbed on the surface. The maximum contact area of a $TC_{10}P$-containing molecule with four fully extended decyl chains adsorbed on the substrate is therefore estimated to be ~3.4 nm^2, while a molecular configuration in which only two of the decyl chains are adsorbed should occupy an area of ~2.2 nm^2. These values correspond approximately to the unit cell areas found for $H_2TC_{10}P$ and Ga($TC_{10}P$)Cl monolayers; hence, the α unit cell can accommodate two decyl chains (net) adsorbed on the surface, while the β packing arrangement can accommodate the adsorption of all four decyl side chains.

2.3.4. STM Imaging of 1 at the 1-Phenyloctane/HOPG Interface. Upon deposition, **1** forms ordered monolayers on HOPG that span hundreds of nanometers in width, as shown in Figure 2.15. Adsorbed **1** is not removed as a result of repeated scanning. These results contrast with those obtained for Ga(OEP)(CCPh), which did not consistently form monolayers with extensive surface coverage and were disrupted during STM experiments.[1] Small scale images of

a monolayer of **1** show that the adsorbed molecules adopt a highly periodic structure where the bright and dark features seem to alternate in a similar fashion to $H_2TC_{10}P$ monolayers but with less uniform features in terms of observed molecular shape and apparent height. Structural analysis reveals that the lattice parameters (a = 1.34 ± 0.03 nm, b = 1.72 ± 0.05 nm, Γ = 85 ± 2°; Table 2.1) are within experimental error of those of $H_2TC_{10}P$, which indicates that **1** exhibits α-type packing. This is consistently observed for all samples examined under the same experimental conditions, and also for the same samples studied ~2 h after initial sample preparation. The fact that the molecular arrangements of $Ga(TC_{10}P)Cl$ and **1** monolayers are different finds precedent in a study of titanyl phthalocyanine and a catechol-ligated derivative by Hipps and coworkers,[47] where the two molecules with structurally distinct axial ligands were shown to respectively form pseudo-hexagonal monolayers and pseudo-square monolayers at the 1-phenyloctane/HOPG interface.

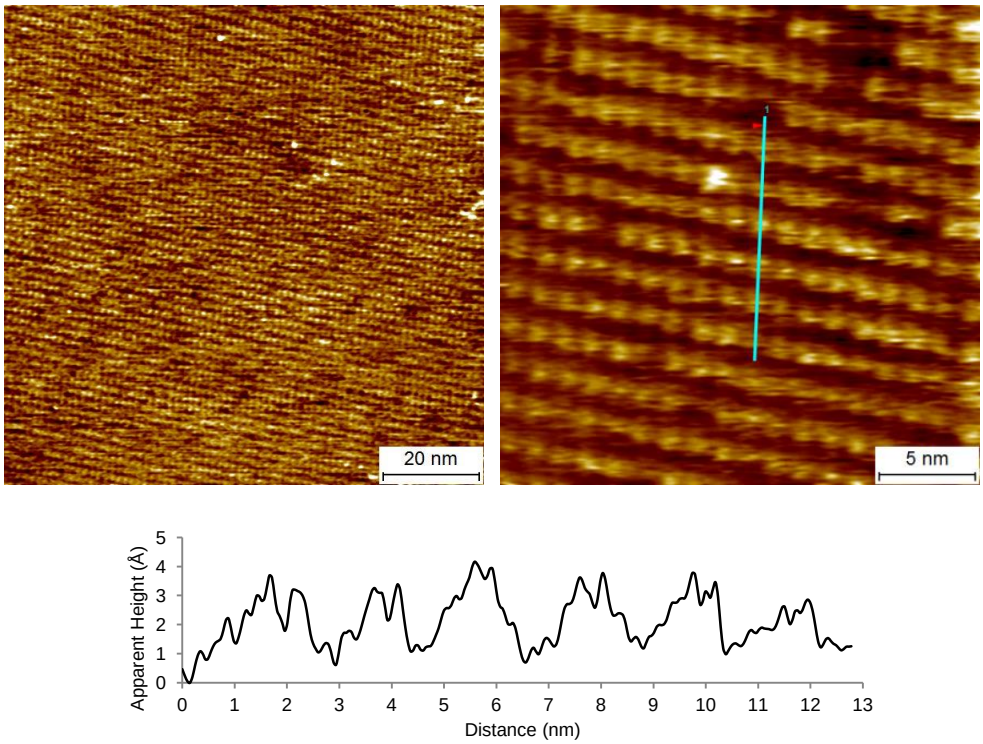

Figure 2.15. STM images and cross-sectional profile of a monolayer of **1** on HOPG at the solid–liquid interface (1-phenyloctane, 7.5×10^{-4} M; I = 10 pA, V = –1400 mV). The cross-sectional profile corresponds to the teal line in the image, draw along *b* lattice vector.

Unlike the well-defined, dot-like features seen in Ga(TC_{10}P)Cl monolayers, molecules of **1** appear more diffuse, which is consistent with our previous observations with self-assembled monolayers of Ga(OEP)(CCPh).[1] The observed height of **1** ranges from ~2 Å to 4 Å depending on the bias voltage, which is shorter than the DFT calculated distance of ~8.5 Å between the gallium metal center and the *para*-H (see Appendix B). This discrepancy is attributed to the low electronic coupling between the ligand and the porphyrin macrocycle, because the apparent height is a measure of the local tunneling probability and therefore largely influenced by electronic effects.[48, 49] In a study on the difference in apparent height between planar and twisted 4-phenylpyridine derivatives bound to rhodium porphyrins, both ligands were observed to have broad distributions of apparent heights that are shorter than the physical heights of the molecules,

which suggests that both the height discrepancy and variation are common in systems with multi-atom axial ligands.[50]

2.3.5. STM Imaging of 2 and 3 at the 1-Phenyloctane/HOPG Interface. Compounds **2** and **3** both consistently form self-assembled monolayers on HOPG with extensive surface coverage upon deposition, which can be readily observed by STM (Figures 2.16 and 2.17). The individual molecules of **2** and **3** appear as diffuse spots with small apparent heights, similar to **1** adsorbed on HOPG. The discrepancies between the observed apparent height of **2** and **3** are much greater than that for **1**, mostly due to negligible changes in apparent height as a function of the length of the axial ligand.

Unlike monolayers of **1**, self-assembled monolayers of **2** and **3** both exhibit structural polymorphism, where the coexistence of two distinct packing geometries can be observed. In the 25 nm × 25 nm image of a self-assembled monolayer of **2** (Figure 2.16), rows of tightly spaced structures, formed by porphyrin dimers, can be seen on the right side of the image, while the left side of the image contains a uniform lattice with a lower packing density. A careful analysis of the array on the left reveals that the region adopts a packing geometry that is described by the following unit cell parameters: $a = 1.61 \pm 0.07$ nm, $b = 2.12 \pm 0.07$ nm, $\Gamma = 71 \pm 2°$. This is statistically indistinguishable from that of $Ga(TC_{10}P)Cl$ (β) under identical experimental conditions (Table 2.1), and it can be assumed that all four alkyl chains are adsorbed on HOPG based on the same approximations. For the tightly packed rows of porphyrins seen on the right side of the image, the intra-row and inter-row porphyrin-to-porphyrin distances are determined to be 1.33 ± 0.08 nm and 1.72 ± 0.07 nm respectively, where the lattice angle is $86 \pm 2°$ (Table 2.1); these values are essentially identical to the α unit cell parameters of both $H_2TC_{10}P$ and

monolayers of **1**. The alternating arrangement is observed to be randomly scattered within domains that are largely dominated by the β packing structure.

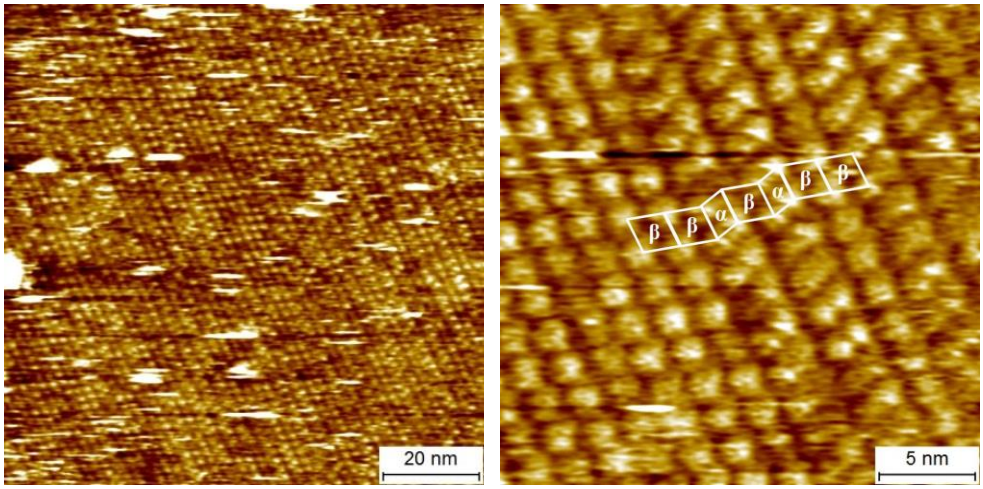

Figure 2.16. STM images of a monolayer of **2** on HOPG at the solid–liquid interface (1-phenyloctane, 7.5 × 10^{-4} M), acquired shortly following deposition, showing structural polymorphism: (A) I = 15 pA, V = –700 mV; (B) I = 8 pA, V = –1200 mV).

For monolayers of **3**, the same phenomenon is also observed. Figure 2.17 shows two distinct packing patterns within the same domain, and structural analysis reveals that the porphyrin-to-porphyrin distances (α: a = 1.39 ± 0.03 nm, b = 1.70 ± 0.05 nm, Γ = 85 ± 2°; β: a = 1.68 ± 0.13 nm, b = 2.16 ± 0.04 nm, Γ = 71 ± 3°; Table 2.1) are within experimental error of those obtained for monolayers of **2** exhibiting structural polymorphism. In all cases where mixed-structure monolayers are observed, the transition between packing geometries is continuous, with no disruptions in surface coverage in between, as highlighted by the unit cells superimposed on the 25 nm × 25 nm STM images in Figures 2.16 and 2.17. Coenen et al. reported similar observations in their study on $CuTC_{11}P$ self-assembled monolayers at the 1-octanoic acid/HOPG interface, where the porphyrin monolayers exhibited structural polymorphism.[11, 51] The authors identified four distinct types of unit cells, three of which were observed to coexist within a single array and were connected seamlessly due to the sharing of unit cell vectors, which was enabled by the conformational flexibility of the peripheral alkyl

chains (this will be discussed in greater detail in Chapter 4). For **2** and **3**, the *b* lattice vector of the α unit cell (**2**: 1.72 ± 0.07 nm; **3**: 1.70 ± 0.05 nm) is within experimental error of the *a* lattice vector of the β unit cell (**2**: 1.61 ± 0.07 nm; **3**: 1.68 ± 0.13 nm; Table 2.1), which leads to the hypothesis that the seamless connection between regions in the mixed monolayers is also a result of the sharing of unit cell vectors.

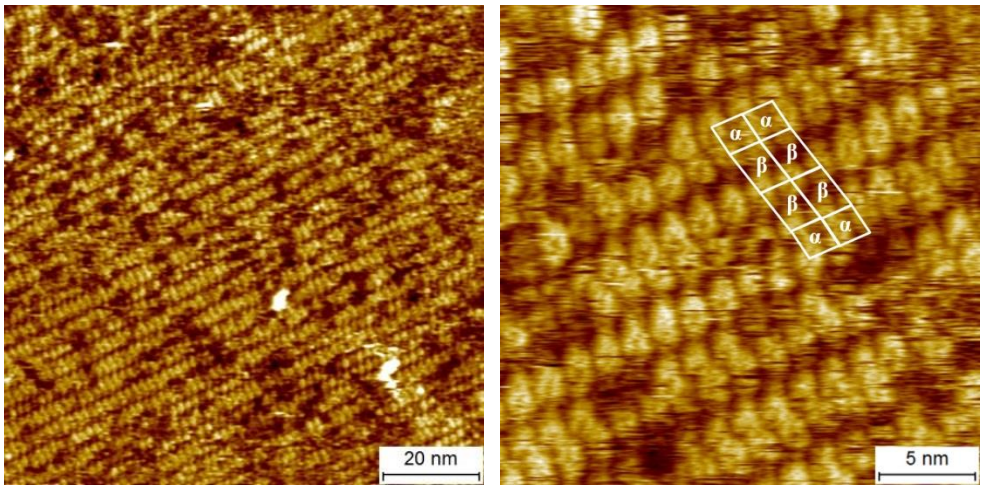

Figure 2.17. STM images of a monolayer of **3** on HOPG at the solid–liquid interface (1-phenyloctane, 7.5 × 10^{-4} M), acquired shortly following deposition, showing structural polymorphism (*I* = 12.5 pA, *V* = –1200 mV).

In addition to the mixed-structure monolayers, **2** and **3** also form extensive, structurally uniform monolayers with the α packing geometry (Figures 2.18 and 2.19). These monolayers are observed exclusively during STM experiments performed on samples long after deposition (~2 h). While we were unable to observe transformation of the mixed structure into α domains in monolayers of **2** and **3**, it is believed that the α packing geometry represents the thermodynamically favored polymorph due to the absence of mixed-structure monolayers or pure β domains (only observed for **3** in one trial) on samples that previously exhibited structural polymorphism.

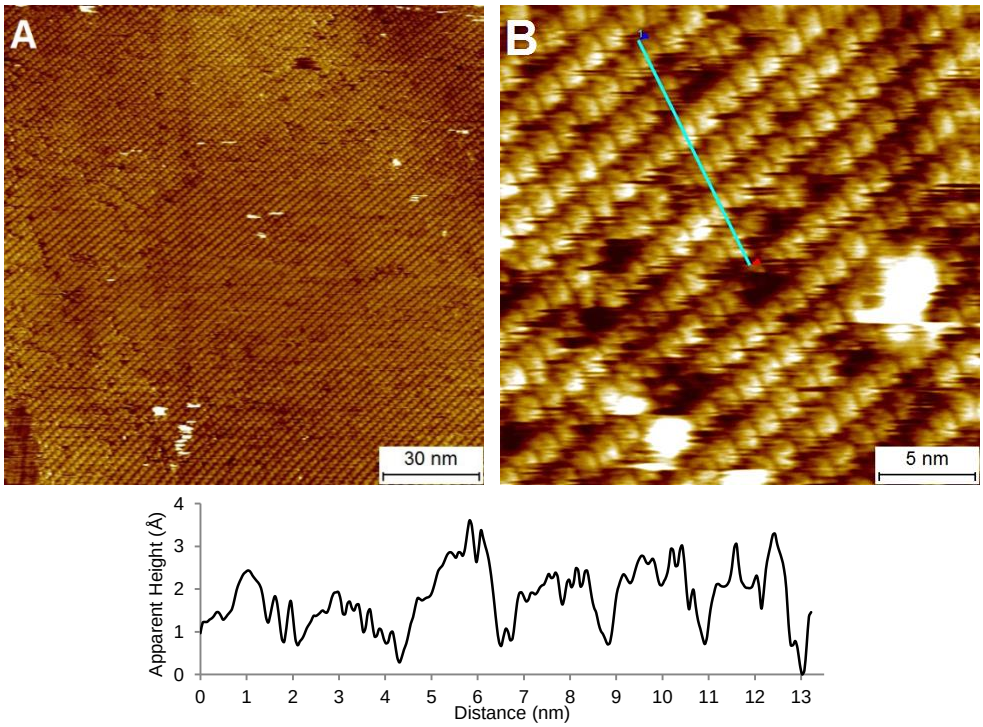

Figure 2.18. STM images and a cross-sectional profile of monolayers of **2** on HOPG at the solid–liquid interface (1-phenyloctane, 7.5×10^{-4} M) acquired ~2 h after initial deposition, exhibiting the α lattice: (A) I = 25 pA, V = –900 mV (exposed graphite can be seen on the lower left corner of the image); (B) same array as (A), I = 9 pA, V = –900 mV; unidentified defects are seen as the bright features at the bottom and the right edge of the image. The cross-sectional profile was taken along the teal line shown on (B), drawn along the *b* lattice vector.

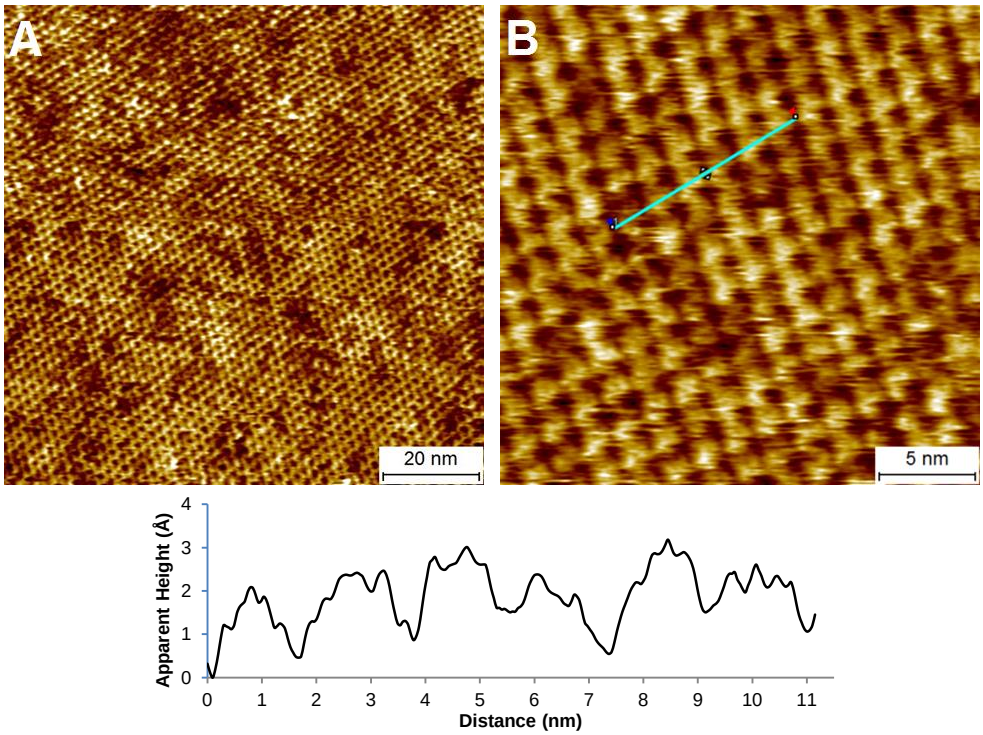

Figure 2.19. STM images and a cross-sectional profile of monolayers of **3** on HOPG at the solid–liquid interface (1-phenyloctane, 7.5×10^{-4} M) acquired ~2 h after initial deposition, exhibiting the α lattice: (A, B) same array, I = 8 pA. V = –1200 mV. The cross-sectional profile was taken along the teal line shown on (B), drawn along the *b* lattice vector.

Based on these results, we conclude that the incorporation of OPE molecular wires as axial ligands does not disrupt the formation of well-ordered, self-assembled Ga($TC_{10}P$)X monolayers at the solid–liquid interface. This is evidenced by the propensity of the Ga($TC_{10}P$)(OPE) monolayers to conform to the α packing structure exhibited by $H_2TC_{10}P$ monolayers, where the porphyrin cores are oriented parallel to the graphite surface. Interestingly, the fact that compound **3** can form self-assembled monolayers with the α packing structure shows that Ga($TC_{10}P$)X monolayers can be used to pattern axial ligands with heights that far exceed the 2D lattice vectors, since the physical height of **3** (~2.2 nm, as approximated by the distance between the Ga atom and the *para*-H atom in the gas-phase optimized; see Appendix B) is much greater than the lengths of the unit cell vectors (a = 1.39 ± 0.03 nm, b = 1.70 ± 0.05 nm) of the α structure (Figure 2.20).

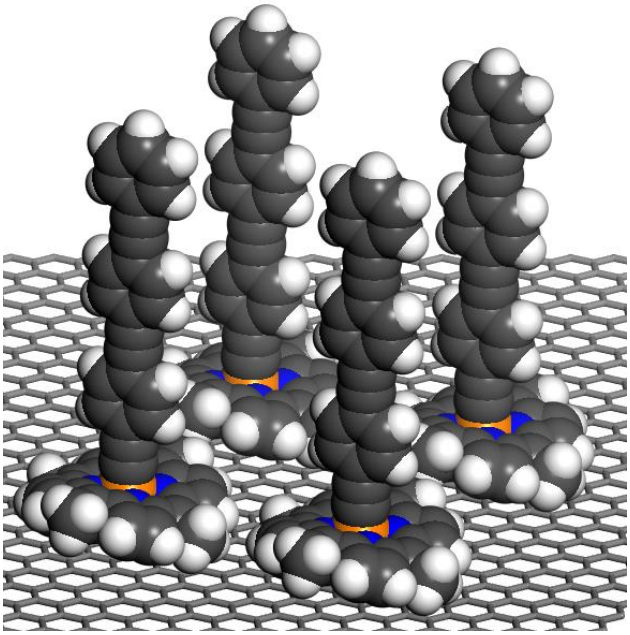

Figure 2.20. Molecular model of a monolayer of **3** exhibiting the α packing structure. The alkyl chains are omitted since their orientations are not determined.

2.3.6. STM Imaging of Ga($TC_{10}P$)(OPE) complexes at the Air/HOPG Interface. In order to determine whether supernatant is necessary for the formation of Ga($TC_{10}P$)(OPE) monolayers on HOPG, the self-assembly of compounds **1**–**3** at the air/HOPG interface has also been investigated. STM samples are prepared by drop-casting a 2.5×10^{-4} M porphyrin solution in benzene onto a piece of freshly cleaved HOPG, followed by a drop of neat toluene on the evaporated film to anneal the material. It has been previously shown that using higher boiling solvents for deposition, such as toluene and xylene, as opposed to lower boiling solvents, such as CH_2Cl_2 or $CHCl_3$, can greatly increase the homogeneity of Pt(OEP) monolayers on HOPG, and can also reduce the size and number of microcrystalline clusters on the substrate.[52] We assume that the same holds true for the solvent-annealing process since weakly bound molecules and crystallites should be redissolved upon addition of a solvent droplet. This was evidenced by the disappearance of the "coffee ring" that initially formed from the evaporation of the benzene dosing solution.

For compound **1**, STM measurements reveal the formation of a periodic structure in which the porphyrin molecules self-assemble into a near-rectangular pattern (Figure 2.21a). The unit cell of the self-assembled structure is described by the following parameters: a = 1.35 ± 0.06 nm, b = 1.64 ± 0.08 nm, Γ = 88 ± 1° (Table 2.2). These values are within experimental error of those obtained for the 1-phenyloctane/HOPG interface experiments as described earlier, where the porphyrin molecules adsorb with the heterocyclic cores lying parallel to the surface (α cell). The roughly circular bright features represent the porphyrin macrocycle, while the darker regions are attributed to the regions occupied by peripheral alkyl chains. Features corresponding to edge-on porphyrin molecules, which should appear as thin, disc-like features,[53-55] were never observed; hence, we conclude that **1** self-assembles into monolayers with the heterocyclic cores parallel to the surface and the ligands oriented perpendicular to the substrate.

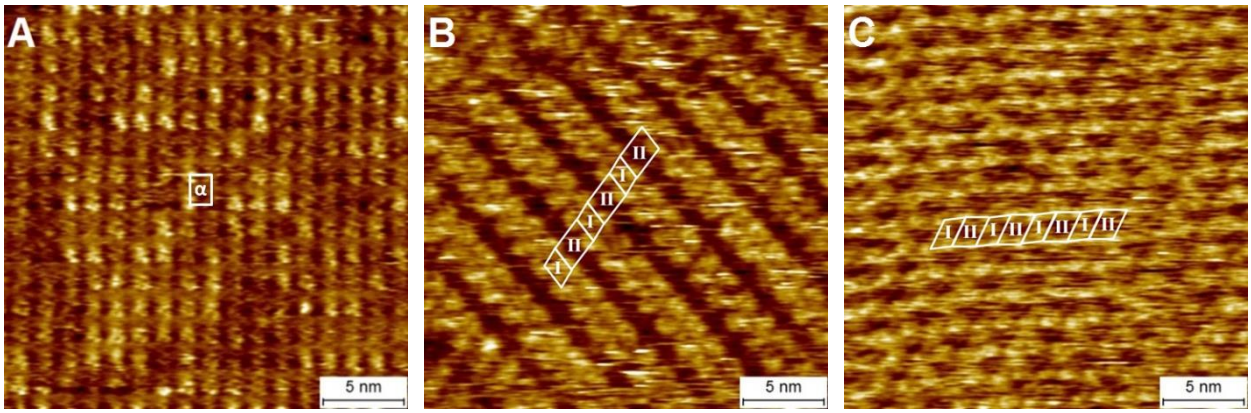

Figure 2.21. STM images of Ga($TC_{10}P$)(OPE) monolayers on HOPG at the solid–air interface. (A) **1**, I = 7.5 pA, V = –650 mV; (B) **2**, I = 9 pA, V = –900 mV; (C) **3**, I = 8 pA, V = –750 mV.

Table 2.2. Lattice Parameters of Compounds **1**–**3** at the Air/HOPG Interface.[a]

parameter	**1** (α)	**2** (I)	**2** (II)	**3** (I)	**3** (II)
a (nm)	1.35 (6)	1.31 (9)	1.65 (9)	1.21 (9)	1.45 (8)
b (nm)	1.64 (8)	1.65 (9)	2.18 (11)	1.70 (9)	1.70 (9)
Γ (°)	88 (1)	74 (4)	64 (3)	67 (3)	71 (3)
A (nm^2)	2.21 (21)	2.08 (30)	3.23 (41)	1.89 (28)	2.33 (29)
Density (molecules/nm^2)	0.45	0.48	0.31	0.53	0.43

[a] Values in parentheses are standard deviations of the last digit(s).

For **2**, monolayers formed as above are found by STM to consist of alternating arrangements of bright, circular features and dark regions (Figure 2.21b). Neither edge-on porphyrin molecules nor OPE-like features,[56-58] which should appear as bright, narrow rods with well-defined dimensions, are observed, suggesting that the face-on orientation of adsorbed porphyrins is retained. However, in contrast to the self-assembled monolayers of **1**, monolayers of **2** adopt a structure in which the adsorbed molecules are arranged in a packing geometry that is characterized by alternating unit cells. Since the sample preparation procedure for **2** is identical to that for **1**, we can eliminate solvent effects and evaporation time as factors that affect the resulting structure. Structural analysis reveals that the observed structure is a periodic combination of two distinct unit cells. The smaller unit cell has lattice parameters $a = 1.31 \pm 0.09$ nm, $b = 1.65 \pm 0.09$ nm, $\Gamma = 74 \pm 4°$, and the larger unit cell is described by lattice parameters $a = 1.65 \pm 0.09$ nm, $b = 2.18 \pm 0.11$ nm, $\Gamma = 64 \pm 3°$ (Table 2.2). Neither of these cells corresponds to the α and β cells found for these compounds at the solid-liquid interface. The observation of polymorphism is unsurprising because evaporation of the solvent results in trapping of the polymorphic monolayer formed at short times at the solid-liquid interface. In fact, because solvent evaporation is rapid compared to the time at which initial STM measurements of monolayers of **2** at the solid-liquid interface, the non-α/non-β structure may represent an earlier kinetic phase.

STM images of the drop-cast samples of **3** reveal a structure that is noticeably more compact than those of **1** and **2** (Figure 2.21c). The packing arrangement of the monolayer, which is reproducible across several trials, is a periodic structure also characterized by an alternating unit cell arrangement, with unit cell parameters $a = 1.21 \pm 0.09$ nm, $b = 1.70 \pm 0.09$ nm, $\Gamma = 67 \pm 3°$, and $a = 1.45 \pm 0.08$ nm, $b = 1.70 \pm 0.09$ nm, $\Gamma = 71 \pm 3°$ (Table 2.2). These cell lengths are

shorter than those of monolayers formed by **2**, but are comparable to the lattice vectors previously reported for both $H_2TC_{10}P$ monolayers and monolayers of TC_mP compounds with slightly longer chain lengths (m = 11, 12: see Table 1.1). Features attributable to edge-on porphyrin molecules and edge/face-on OPE-type features are not observed. This precludes the presence of molecules that are not adsorbed in the face-on configuration. A comparison between the lengths of the observed unit cell vectors and the calculated height of **3** (~2.2 nm) further supports this analysis, since a molecule of **3** that is "toppled over" would require a larger unit cell to be adsorbed on the surface than that allowed by the observed arrangements.

Based on the unit cell areas derived from the lattice parameters, one can conclude that the cells are too small to accommodate adsorption of all four decyl chains on the surface. In their study on the self-assembly of $CuTC_{11}P$ at the solid-liquid interface, Coenen et al. proposed molecular arrangements that involved alkyl chains that were folded and overlapped with those that were adsorbed on the surface; this was supported by the observation of regions with slightly greater apparent heights where the alkyl chains were thought to overlap.[51] Although the resolution of our STM images does not allow us to determine the orientation of the alkyl substituents or to detect apparent height variations in the alkyl regions, we tentatively attribute the observed morphology to the folding and overlapping of alkyl chains. When comparing the morphologies of the self-assembled monolayers form by the three molecules studied, it is clear that the lengthening of the axial ligand has a noticeable effect on the formation of the monolayer. However, as the systems presented are not subjected to conditions compatible with achieving thermodynamic structures (e.g., thermal annealing, addition of a supernatant), it is likely that the structures observed are kinetically trapped systems. Nonetheless, the STM experiments conducted at the solid-air interface demonstrates the possibility of forming well-ordered, self-

assembled monolayers presenting orthogonal OPE pillars on HOPG without the presence of a supernatant.

2.4. Conclusions

We have demonstrated that five-coordinate Ga($TC_{10}P$)(OPE) complexes can reliably form self-assembled monolayers at the 1-phenyloctane/HOPG interface, and are also capable of forming ordered arrays at the air/HOPG interface. Incorporating long alkyl chain substituents into the porphyrin periphery allows for the formation of stable supramolecular structures even for derivatives with larger axial ligands such as CCPh, which was previously shown to be challenging with systems based on Ga(III) octaethylporphyrins. The axial ligands appear to have influence over the two-dimensional packing of the porphyrin molecules, as shown by the observation of structural polymorphism. For the 1-phenyloctane/HOPG interface experiments, two distinct unit cells, either in homogeneous arrays or mixed arrays depending on the axial ligand, were observed; for samples prepared and studied in air, all three Ga($TC_{10}P$)(OPE) complexes adopted distinct packing geometries. This phenomenon is made possible by the conformational freedom provided by the alkyl substituents. While controlling the periodicity of the self-assembled arrays based on $TC_{10}P$ complexes will likely require thermodynamic control during sample preparation, the propensity of these molecules to form self-assembled structures under various deposition conditions make them suitable for patterning more complex, functional modules on surfaces.

2.5. References

1. Kamm, J. M.; Iverson, C. P.; Lau, W.-Y.; Hopkins, M. D. Axial Ligand Effects on the Structures of Self-Assembled Gallium-Porphyrin Monolayers on Highly Oriented Pyrolytic Graphite. *Langmuir* **2016**, *32*, 487-495.

2. Oncel, N.; Bernasek, S. L. Ni(II)- and Vanadyloctaethylporphyrin Self-Assembled Layers Formed on Bare and 5-(Octadecyloxy)isophthalic Acid Covered Graphite. *Langmuir* **2009**, *25*, 9290-9295.

3. Friesen, B. A.; Bhattarai, A.; Mazur, U.; Hipps, K. W. Single Molecule Imaging of Oxygenation of Cobalt Octaethylporphyrin at the Solution/Solid Interface: Thermodynamics from Microscopy. *J. Am. Chem. Soc.* **2012**, *134*, 14897-14904.

4. Bhattarai, A.; Mazur, U.; Hipps, K. W. Desorption Kinetics and Activation Energy for Cobalt Octaethylporphyrin from Graphite at the Phenyloctane Solution-Graphite Interface: An STM Study. *J. Phys. Chem. C* **2015**, *119*, 9386-9394.

5. Miyake, Y.; Tanaka, H.; Ogawa, T. Scanning Tunneling Microscopy Investigation of Vanadyl and Cobalt(II) Octaethylporphyrin Self-Assembled Monolayer Arrays on Graphite. *Colloids Surf., A* **2008**, *313*, 230-233.

6. Oncel, N.; Bernasek, S. L. The Effect of Molecule-Molecule and Molecule-Substrate Interaction in the Formation of Pt-Octaethyl Porphyrin Self-Assembled Monolayers. *Appl. Phys. Lett.* **2008**, *92*.

7. Zou, Z. Q.; Chen, F. In Situ Scanning Tunneling Microscopy Studies of Zinc(II) Octaethylporphyrin Arrays Self-Assembled on Graphite and Au(111) Surfaces in Organic Solution. *J. Appl. Phys.* **2008**, *103*.

8. Zou, Z. Q.; Wei, L. Y.; Chen, F.; Liu, Z. M.; Thamyongkit, P.; Loewe, R. S.; Lindsey, J. S.; Mohideen, U.; Bocian, D. F. Solution STM Images of Porphyrins on HOPG Reveal that Subtle Differences in Molecular Structure Dramatically Alter Packing Geometry. *J. Porphyrins Phthalocyanines* **2005**, *9*, 387-392.

9. Otsuki, J. STM Studies on Porphyrins. *Coord. Chem. Rev.* **2010**, *254*, 2311-2341.

10. Plamont, R.; Kikkawa, Y.; Takahashi, M.; Kanesato, M.; Giorgi, M.; Shun, A. C. K.; Roussel, C.; Balaban, T. S. Nanoscopic Imaging of *meso*-Tetraalkylporphyrins Prepared in High Yields Enabled by Montmorrilonite K10 and 3Å angstrom Molecular Sieves. *Chem. - Eur. J.* **2013**, *19*, 11293-11300.

11. Coenen, M. J. J.; Cremers, M.; den Boer, D.; van den Bruele, F. J.; Khoury, T.; Sintic, M.; Crossley, M. J.; van Enckevort, W. J. P.; Hendriksen, B. L. M.; Elemans, J. A. A. W.; Speller, S. Little Exchange at the Liquid/Solid Interface: Defect-Mediated Equilibration of Physisorbed Porphyrin Monolayers. *Chem. Commun.* **2011**, *47*, 9666-9668.

12. Coenen, M. J. J.; den Boer, D.; van den Bruele, F. J.; Habets, T.; Timmers, K. A. A. M.; van der Maas, M.; Khoury, T.; Panduwinata, D.; Crossley, M. J.; Reimers, J. R.; van Enckevort, W. J. P.; Hendriksen, B. L. M.; Elemans, J. A. A. W.; Speller, S. Polymorphism in Porphyrin Monolayers: the Relation Between Adsorption Configuration and Molecular Conformation. *Phys. Chem. Chem. Phys.* **2013**, *15*, 12451-12458.

13. Katsonis, N.; Vicario, J.; Kudernac, T.; Visser, J.; Pollard, M. M.; Feringa, B. L. Self-Organized Monolayer of meso-Tetradodecylporphyrin Coordinated to Au(111). *J. Am. Chem. Soc.* **2006**, *128*, 15537-15541.

14. Visser, J.; Katsonis, N.; Vicario, J.; Feringa, B. L. Two-Dimensional Molecular Patterning by Surface-Enhanced Zn-Porphyrin Coordination. *Langmuir* **2009**, *25*, 5980-5985.

15. Ferreira, Q.; Bragança, A. M.; Moura, N. M. M.; Faustino, M. A. F.; Alcácer, L.; Morgado, J. Dynamics of Porphyrin Adsorption on Highly Oriented Pyrolytic Graphite Monitored by Scanning Tunnelling Microscopy at the Liquid/Solid Interface. *Appl. Surf. Sci.* **2013**, *273*, 220-225.

16. Chin, Y.; Panduwinata, D.; Sintic, M.; Sum, T. J.; Hush, N. S.; Crossley, M. J.; Reimers, J. R. Atomic-Resolution Kinked Structure of an Alkylporphyrin on Highly Ordered Pyrolytic Graphite. *J. Phys. Chem. Lett.* **2011**, *2*, 62-66.

17. Reimers, J. R.; Panduwinata, D.; Visser, J.; Chin, Y.; Tang, C. G.; Goerigk, L.; Ford, M. J.; Baker, M.; Sum, T. J.; Coenen, M. J. J.; Hendriksen, B. L. M.; Elemans, J. A. A. W.; Hush, N. S.; Crossley, M. J. From Chaos to Order: Chain-Length Dependence of the Free Energy of Formation of Meso-tetraalkylporphyrin Self-Assembled Monolayer Polymorphs. *J. Phys. Chem. C* **2016**, *120*, 1739-1748.

18. Reimers, J. R.; Panduwinata, D.; Visser, J.; Chin, Y.; Tang, C. G.; Goerigk, L.; Ford, M. J.; Sintic, M.; Sum, T. J.; Coenen, M. J. J.; Hendriksen, B. L. M.; Elemans, J. A. A. W.; Hush, N. S.; Crossley, M. J. A Priori Calculations of the Free Energy of Formation from Solution of Polymorphic Self-Assembled Monolayers. *PNAS* **2015**, *112*, E6101-E6110.

19. Qiu, X. H.; Wang, C.; Zeng, Q. D.; Xu, B.; Yin, S. X.; Wang, H. N.; Xu, S. D.; Bai, C. L. Alkane-Assisted Adsorption and Assembly of Phthalocyanines and Porphyrins. *J. Am. Chem. Soc.* **2000**, *122*, 5550-5556.

20. Wang, H. N.; Wang, C.; Zeng, Q. D.; Xu, S. D.; Yin, S. X.; Xu, B.; Bai, C. L. Chain-Length-Adjusted Assembly of Substituted Porphyrins on Graphite. *Surf. Interface Anal.* **2001**, *32*, 266-270.

21. Ikeda, T.; Asakawa, M.; Miyake, K.; Goto, M.; Shimizu, T. Scanning Tunneling Microscopy Observation of Self-Assembled Monolayers of Strapped Porphyrins. *Langmuir* **2008**, *24*, 12877-12882.

22. Shen, Y. T.; Deng, K.; Li, M.; Zhang, X. M.; Zhou, G.; Müellen, K.; Zeng, Q. D.; Wang, C. Self-Assembling in Fabrication of Ordered Porphyrins and Phthalocyanines Hybrid Nano-Arrays on HOPG. *CrystEngComm* **2013**, *15*, 5526-5531.

23. Ikeda, T.; Asakawa, M.; Goto, M.; Miyake, K.; Ishida, T.; Shimizu, T. STM Observation of Alkyl-Chain-Assisted Self-Assembled Monolayers of Pyridine-Coordinated Porphyrin Rhodium Chlorides. *Langmuir* **2004**, *20*, 5454-5459.

24. Cheng, Y. J.; Yang, S. H.; Hsu, C. S. Synthesis of Conjugated Polymers for Organic Solar Cell Applications. *Chem. Rev.* **2009**, *109*, 5868-5923.

25. Bunz, U. H. F. Poly(aryleneethynylene)s: Syntheses, Properties, Structures, and Applications. *Chem. Rev.* **2000**, *100*, 1605-1644.

26. Lewis, P. A.; Inman, C. E.; Maya, F.; Tour, J. M.; Hutchison, J. E.; Weiss, P. S. Molecular Engineering of the Polarity and Interactions of Molecular Electronic Switches. *J. Am. Chem. Soc.* **2005**, *127*, 17421-17426.

27. Li, C.; Zhang, D. H.; Liu, X. L.; Han, S.; Tang, T.; Zhou, C. W.; Fan, W.; Koehne, J.; Han, J.; Meyyappan, M.; Rawlett, A. M.; Price, D. W.; Tour, J. M. Fabrication Approach for Molecular Memory Arrays. *Appl. Phys. Lett.* **2003**, *82*, 645-647.

28. Pangborn, A. B.; Giardello, M. A.; Grubbs, R. H.; Rosen, R. K.; Timmers, F. J. Safe and Convenient Procedure for Solvent Purification. *Organometallics* **1996**, *15*, 1518-1520.

29. Khan, A. A.; Chee, S. H.; Stocker, B. L.; Timmer, M. S. M. The Synthesis of Long-Chain α-Alkyl-β-Hydroxy Esters Using Allylic Halides in a Frater-Seebach Alkylation. *Eur. J. Org. Chem.* **2012**, 995-1002.

30. Lindsey, J. S.; Schreiman, I. C.; Hsu, H. C.; Kearney, P. C.; Marguerettaz, A. M. Rothemund and Adler-Longo Reactions Revisited - Synthesis of Tetraphenylporphyrins under Equilibrium Conditions. *J. Org. Chem.* **1987**, *52*, 827-836.

31. Brandsma, L., *Preparative Acetylenic Chemistry*. Elsevier: Amsterdam, 1988; pp 24-25.

32. Hwang, J. J.; Tour, J. M. Combinatorial Synthesis of Oligo(Phenylene Ethynylene)s. *Tetrahedron* **2002**, *58*, 10387-10405.

33. Fulmer, G. R.; Miller, A. J. M.; Sherden, N. H.; Gottlieb, H. E.; Nudelman, A.; Stoltz, B. M.; Bercaw, J. E.; Goldberg, K. I. NMR Chemical Shifts of Trace Impurities: Common Laboratory Solvents, Organics, and Gases in Deuterated Solvents Relevant to the Organometallic Chemist. *Organometallics* **2010**, *29*, 2176-2179.

34. Coutsolelos, A.; Guilard, R.; Bayeul, D.; Lecomte, C. Gallium(III) Porphyrins - Synthesis and Physicochemical Characteristics of Halogeno Gallium(III) Porphyrins X-Ray Crystal-Structure of Chloro-(5,10,15,20-Tetraphenylporphyrinato) Gallium(III). *Polyhedron* **1986**, *5*, 1157-1164.

35. *SPIP Software*, version 6.0.9; Image Metrology A.S: Hørsholm, Denmark

36. Chung, D. D. L. Review Graphite. *J. Mater. Sci.* **2002**, *37*, 1475-1489.

37. Horcas, I.; Fernandez, R.; Gomez-Rodriguez, J. M.; Colchero, J.; Gomez-Herrero, J.; Baro, A. M. WSXM: A Software for Scanning Probe Microscopy and a Tool for Nanotechnology. *Rev. Sci. Instrum.* **2007**, *78*, 013705.

38. Buchler, J. W.; Puppe, L.; Rohbock, K.; Schneehage, H. H. Metal-Complexes of Tetrapyrrole Ligands, VIII. Methoxo-Metal and Phenoxo-Metal Complexes of Octaethylporphin Containing Central Ions of Type M^{3+}, M^{4+}, and $MO3^{+}$: New Tungsten and Rhenium Porphins. *Chem. Ber.* **1973**, *106*, 2710-2732.

39. Wrackmeyer, B.; Klimkina, E. V. $^{69/71}$Ga and ^{115}In NMR Spectroscopy of Lithium Tetra(tert-butyl)gallate and -indate: Spin-Spin Coupling Constants $^{1}J(^{69/71}Ga,^{13}C)$ and $^{1}J(^{115}In,^{13}C)$. *Z. Naturforsch.* **2009**, *64*, 41-46.

40. Yang, Y. L.; Wang, C. Solvent Effects on Two-Dimensional Molecular Self-Assemblies Investigated by Using Scanning Tunneling Microscopy. *curr. Opin. Colloid Interface Sci.* **2009**, *14*, 135-147.

41. Mali, K. S.; De Feyter, S. Principles of molecular assemblies leading to molecular nanostructures. *Philosophical Transactions of the Royal Society a-Mathematical Physical and Engineering Sciences* **2013**, *371*.

42. Mazur, U.; Hipps, K. W.; Riechers, S. L. Organization of Vanadyl and Metal-Free Tetraphenoxyphthalocyanine Complexes on Highly Oriented Pyrolytic Graphite in the Presence of Paraffinic Solvents: A STM Study. *J. Phys. Chem. C* **2008**, *112*, 20347-20356.

43. Nicholls, D.; Ware, B.; Zhang, Z.; Oncel, N. A Scanning Tunneling Microscopy Study on Self-Assembled Fe(III) *meso*-Tetra(4-Carboxyphenyl) Porphyrin Chloride Chains. *Thin Solid Films* **2013**, *534*, 308-311.

44. Nicholls, D.; McKinzie, W. P.; Oncel, N. 5-(Octadecyloxy) Isophthalic Acid-Assisted Copper(II) meso-Tetra(4-Carboxyphenyl)Porphyrin Adsorption on Highly Ordered Pyrolytic Graphite. *j. Phys. Chem. C* **2010**, *114*, 14983-14985.

45. Beggan, J. P.; Krasnikov, S. A.; Sergeeva, N. N.; Senge, M. O.; Cafolla, A. A. Self-Assembly of Ni(II) Porphine Molecules on the Ag/Si(111)-Ag/Si(111)-($\sqrt{3} \times \sqrt{3}$)R30° Surface Studied by STM/STS and LEED. *J. Phys.: Condens. Matter* **2008**, *20*, 015003.

46. Watel, G.; Thibaudau, F.; Cousty, J. Direct Observation of Long-Chain Alkane Bilayer Films on Graphite by Scanning Tunneling Microscopy. *Surf. Sci.* **1993**, *281*, L297-L302.

47. Takami, T.; Clark, A.; Caldwell, R.; Mazur, U.; Hipps, K. W. Building Self-Assembled Molecular Layers with Axially Substituted Titanium Phthalocyanines. *Langmuir* **2010**, *26*, 12709-12715.

48. Scudiero, L.; Hipps, K. W. Controlled Manipulation of Self-Organized Ni(II)-Octaethylporphyrin Molecules Deposited from Solution on HOPG with a Scanning Tunneling Microscope. *J. Phys. Chem. C* **2007**, *111*, 17516-17520.

49. Lu, X.; Hipps, K. W.; Wang, X. D.; Mazur, U. Scanning tunneling microscopy of metal phthalocyanines: d(7) and d(9) cases. *Journal of the American Chemical Society* **1996**, *118*, 7197-7202.

50. Sakano, T.; Higashiguchi, K.; Matsuda, K. Comparison of Molecular Conductance Between Planar and Twisted 4-Phenylpyridines by Means of Two-Dimensional Phase Separation of Tetraphenylporphyrin Templates at a Liquid-HOPG Interface. *Chem. Commun.* **2011**, *47*, 8427-8429.

51. Coenen, M. J. J.; den Boer, D.; van den Bruele, F. J.; Habets, T.; Timmers, K. A. A. M.; van der Maas, M.; Khoury, T.; Panduwinata, D.; Crossley, M. J.; Reimers, J. R.; van Enckevort, W. J. P.; Hendriksen, B. L. M.; Elemans, J. A. A. W.; Speller, S. Polymorphism in porphyrin monolayers: the relation between adsorption configuration and molecular conformation. *Physical Chemistry Chemical Physics* **2013**, *15*, 12451-12458.

52. Bussetti, G.; Trabattoni, S.; Uttiya, S.; Sassella, A.; Riva, M.; Picone, A.; Brambilla, A.; Duò, L.; Ciccacci, F.; Finazzi, M. Controlling Drop-Casting Deposition of 2D Pt-Octaethyl Porphyrin Layers on Graphite. *Synth. Met.* **2014**, *195*, 201-207.

53. Zhou, Y. S.; Wang, B.; Zhu, M. Z.; Hou, J. G. Observation of Co-existence of 'Face-On' and 'Edge-On' Stacking Styles in a Porphyrin Monolayer. *Chem. Phys. Lett.* **2005**, *403*, 140-145.

54. Otsuki, J.; Namiki, K.; Arai, Y.; Amano, M.; Sawai, H.; Tsukamoto, A.; Hagiwara, T. Face-on and Columnar Porphyrin Assemblies at Solid/Liquid Interface on HOPG. *Chem. Lett.* **2009**, *38*, 570-571.

55. Sakano, T.; Hasegawa, J.; Higashiguchi, K.; Matsuda, K. Chronological Change from Face-On to Edge-On Ordering of Zinc-Tetraphenylporphyrin at the Phenyloctane-Highly Oriented Pyrolytic Graphite Interface. *Chem. Asian J.* **2012**, *7*, 394-399.

56. Gong, J. R.; Yan, H. J.; Yuan, Q. H.; Xu, L. P.; Bo, Z. S.; Wan, L. J. Controllable Distribution of Single Molecules and Peptides Within Oligomer Template Investigated by STM. *J. Am. Chem. Soc.* **2006**, *128*, 12384-12385.

57. Gong, J. R.; Zhao, J. L.; Lei, S. B.; Wan, L. J.; Bo, Z. S.; Fan, X. L.; Bai, C. L. Molecular Organization of Alkoxy-Substituted Oligo(Phenylene-Ethynylene)s Studied by Scanning Tunneling Microscopy. *Langmuir* **2003**, *19*, 10128-10131.

58. Mu, Z. C.; Yang, X. Y.; Wang, Z. Q.; Zhang, X. Influence of Substituents on Two-Dimensional Ordering of Oligo(phenylene-ethynylene)s - A Scanning Tunneling Microscopy Study. *Langmuir* **2004**, *20*, 8892-8896.

CHAPTER 3

Synthesis and Characterization of Five-Coordinate Gallium–Porphyrin Carboxylate and Aryloxide Complexes Containing Functional Axial Subunits

3.1. Introduction

In Chapter 2, the preparation and characterization of gallium(III) 5,10,15,20-tetra(*n*-$C_{10}H_{21}$)porphyrins with axial oligo-phenylene-ethynylene (OPE) ligands [Ga($TC_{10}P$)(OPE)] was reported. Scanning tunneling microscopy (STM) studies revealed that this class of molecules reproducibly self-assemble on highly ordered pyrolytic graphite (HOPG) to form large, ordered monolayers with the porphyrin parallel to the surface and the OPE ligand perpendicular to it, despite the fact that the OPE–HOPG interaction strength increases with OPE length. While the formation of some of these arrays was accompanied by structural polymorphism, as has been observed for monolayers of other porphyrins with long, flexible alkyl side chains,[1-4] all derivatives ultimately formed an identical lamellar lattice structure, suggesting a high degree of structural consistency can be expected for self-assembled arrays of the Ga($TC_{10}P$)X class of compounds.

While our initial investigations focused on monolayers of porphyrins with gallium–acetylide units (Ga(porphyrin)(CCR)) due to the rigidity and hence predictable height of such ligands, it was of interest to explore alternative ligands to expand the scope of molecules one can use to assemble novel surface structures in conjunction with the porphyrin platform. In addition, there is also a necessity to develop alternative synthetic methods for attaching functional molecules that may not be compatible with the use of organolithium reagents, which are used for preparing the lithium–acetylide precursors for the synthesis of Ga(porphyrin)(CCR) complexes. Ideally, the alternative ligand binding motif should: 1) be commonly found in or easily appended

to a large variety of functional molecules; 2) allow for the facile attachment to the gallium(III) center without the need for multi-step syntheses; and 3) provide air stable complexes.

The chemistry of Ga(porphyrin)X complexes has not been extensively explored, and as a consequence the range of axial ligands found in these complexes is not especially diverse. Previously reported derivatives are limited to X = halide,[5, 6] N_3,[7] O_3SR,[6, 8] OR,[9] OOR,[9] SR,[10] SCN,[7] alkyl,[9, 11, 12] alkenyl,[11, 12] aryl,[11, 13] CCR,[6, 11, 12] OAc,[5, 14] OPh.[15] Among those axial ligating groups that are not intrinsically terminal and, therefore, potentially suitable for supporting functional subunits, alkyl, alkenyl, and aryl ligands do not fulfill our criteria because their complexes are not air-stable. In contrast, air stable gallium-porphyrins with carboxylate and aryloxide ligands of the form Ga(Por)(OAc)[5, 14] and Ga(OEP)(OPh)[15] are known. However, in both cases, the routes by which they were synthesized are not readily adaptable to preparation of related derivatives: Ga(Por)(OAc) was a side-product from a porphyrin metalation reaction using $GaCl_3$ with glacial acetic acid as the solvent, while Ga(OEP)(OPh) was the product of porphyrin metalation using $Ga(acac)_3$ and molten phenol as the solvent. Therefore, to identify potential general synthetic routes to Ga(porphyrin)X aryloxide and carboxylate complexes, we examined preparative routes to porphyrin complexes of these ligands at other metal centers.

Al(porphyrin)X complexes are close structural analogues to, and more common than, Ga(III) porphyrins. Numerous Al(porphyrin)X complexes with axial carboxylate and aryloxide ligands have been reported, and these complexes have been used to produce supramolecular structures such as molecular dyads,[16-21] linear[18] and cyclic[22] porphyrin triads, and a porphyrin pentad.[19] Five- and six-coordinate metalloporphyrin complexes of Sn, Ge, In, Si, and Sn containing M-OR and M-O_2CR linkages are also known,[23-31] where the synthetic conditions vary in temperature and reaction time. These are summarized in Table 3.1 and Table 3.2. Most

commonly, these complexes are prepared via reaction between a M(porphyrin)$(OH)_n$ (n = 1, 2) complex and an alcohol or carboxylic acid. Drawing on these synthetic approaches as inspiration, we decided to prepare the previously unknown complex Ga(TC_{10}P)(OH) and to investigate its reactivity towards carboxylic acids and aryl alcohols, including those bearing functional moieties (Scheme 3.1). The functional subunits targeted for incorporation into Ga(TC_{10}P)X complexes include a fluorescent dye, redox-active centers, and a charged moiety (Scheme 3.2).

Table 3.1. Selected Examples of Reported M(porphyrin)$(OR)_n$ Complexes.

M	n	X	R	Reaction Conditions	Ref.
Al	1	OH	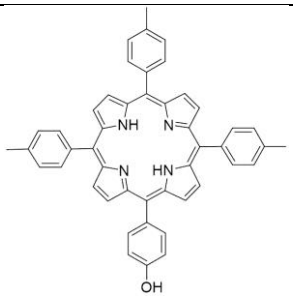	Refluxed in dry C_6H_6 for 12 h under nitrogen.	18
Al	1	OH	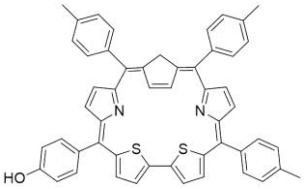	Refluxed in dry C_6H_6 for 12 h under nitrogen.	20
In	1	Cl	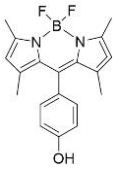	Refluxed in dry toluene overnight under nitrogen in the presence of NaH.	23
Ge	2	OH	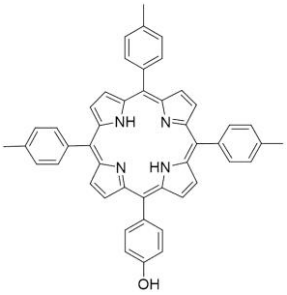	Refluxed in dry C_6D_6 for 12 h under nitrogen.	26
Sn	2	OH	*p*-cresol	Refluxed in C_6D_6 for 1h.	29
Sn	2	OH	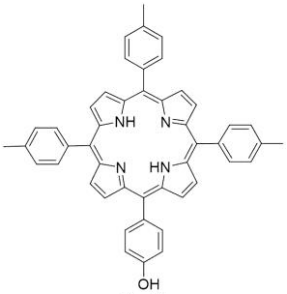	Refluxed in dry C_6D_6 for 12 h under nitrogen	30
Sn	2	OH	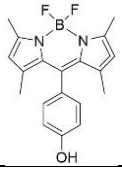	Refluxed in dry $CHCl_3$ for 12 h under nitrogen.	31

Table 3.2. Selected Examples of Reported M(porphyrin)$(O_2CR)_n$ Complexes.

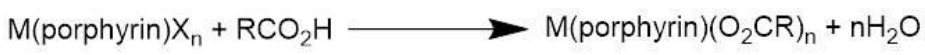

M	n	X	RCO_2H	Reaction Conditions	Ref.
Al	1	OH	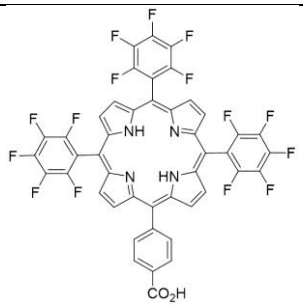	Stirred in dry CH_2Cl_2 for 12 h at room temperature under nitrogen in the presence of anhydrous Na_2SO_4.	16
Al	1	OH	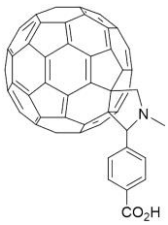	Stirred in dry toluene for 12 h at 65°C under argon.	17
Al	1	OH	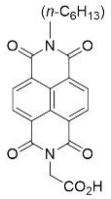	Stirred in $CHCl_3$ for 30 min at room temperature.	21
In	1	Cl	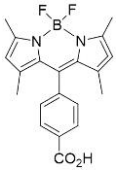	Refluxed in dry toluene overnight under nitrogen in the presence of NaH.	23
Si	2	Cl	terephthalic acid	Refluxed in DMF for 2 h. 98 equiv. terephathlic acid	24
Sn	2	OH	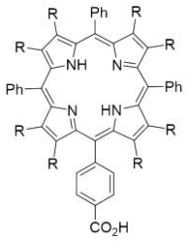 R = 3,5-difluorophenyl	Refluxed in toluene for 12 h.	30
Sn	2	OH	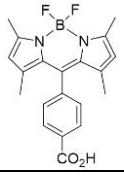	Stirred in dry toluene at room temperature for 2 h under nitrogen.	31

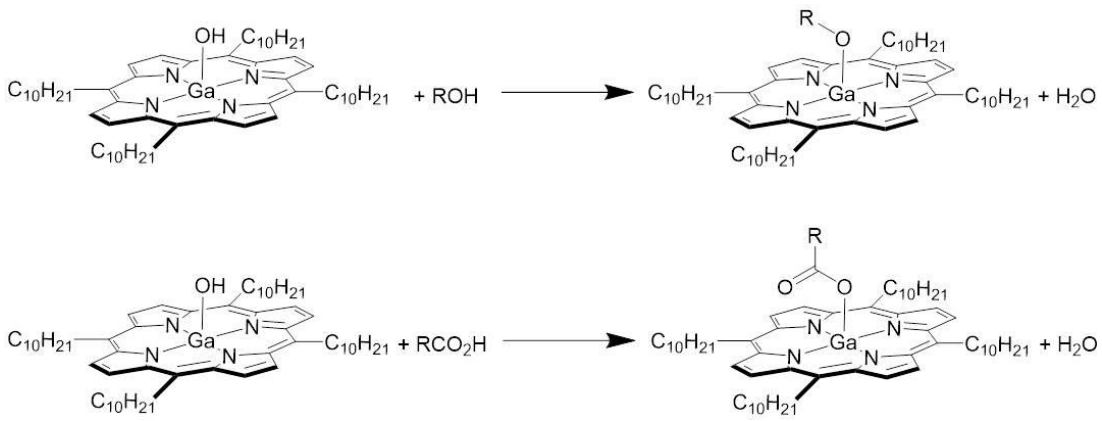

Scheme 3.1. Synthesis of Ga($TC_{10}P$)(OR) and Ga($TC_{10}P$)(O_2CR) complexes.

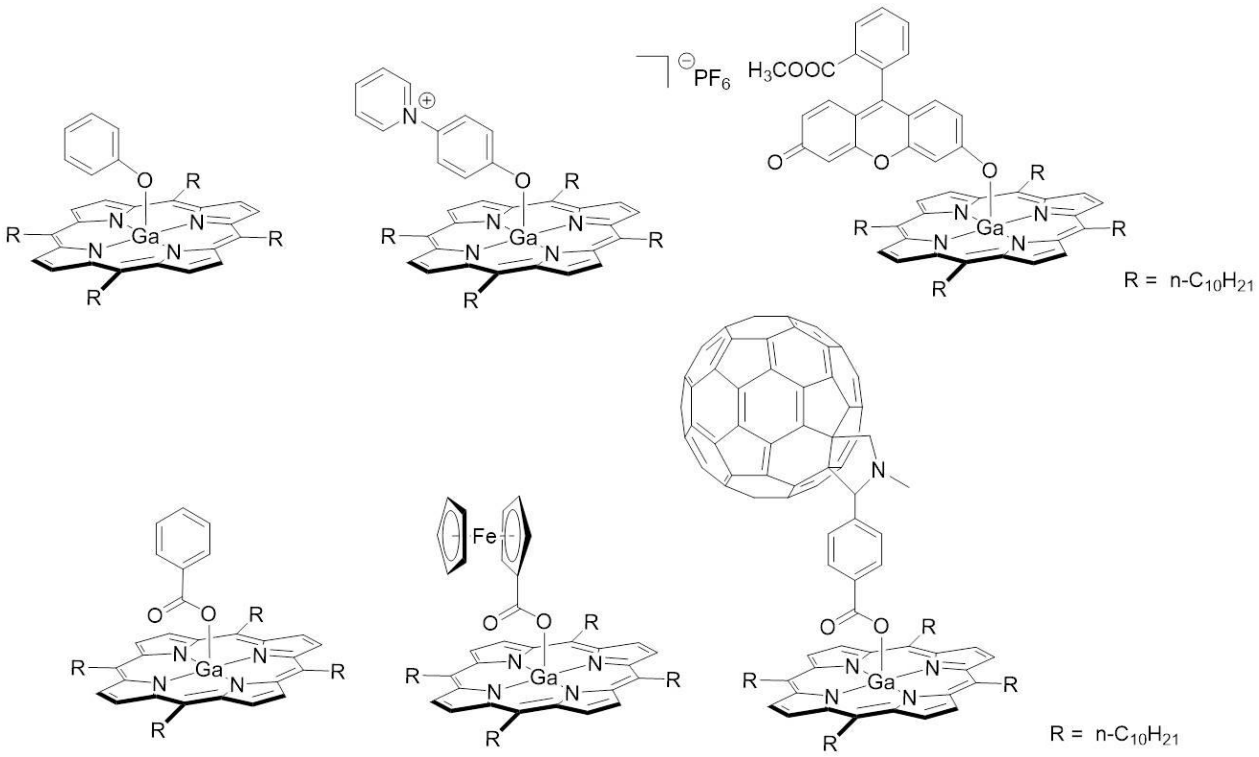

Scheme 3.2. Molecular structures (left to right, top to bottom) of Ga($TC_{10}P$)(OPh), [Ga($TC_{10}P$)(OC_6H_4py)][PF_6], Ga($TC_{10}P$)(FME), Ga($TC_{10}P$)(O_2CPh), Ga($TC_{10}P$)(O_2CFc), and Ga($TC_{10}P$)($O_2CC_6H_4pyrC_{60}$).

The selection of ligands used in this study is motivated not only by the interest in showing the versatility of this synthetic method, but also by the implications of the controlled organization of functional molecules for the development of nanoscale devices. The complex Ga($TC_{10}P$)(FME) (FME-H = fluorescein methyl ester) incorporates a derivative of the well-

known luminescent dye fluorescein, where has been extensively used in biochemical research as a fluorescent label.[32] The parent compound of FME-H, fluorescein free acid (FA) (Scheme 3.3), contains both an OH group on the aromatic xanthene core and a benzoic acid moiety, both of which may be able to serve as points of ligand attachment. In order to prevent the formation of constitutional isomers from the subsequent reaction with Ga($TC_{10}P$)(OH), the carboxylic acid moiety of FA was esterified to provide FME-H, which should react to form a Ga–O bond only at the aryl oxygen. The formation of self-assembled monolayers on atomically flat surfaces by dye-bearing porphyrin complexes of this general design should allow for the patterning of chromophores normal to the surface. Introduction of this new functionality into self-assembled porphyrin arrays allows for the development of spectroscopic techniques for the characterization for such assemblies, as well as the investigation of possible energy-transfer phenomena in the surface-bound structures.

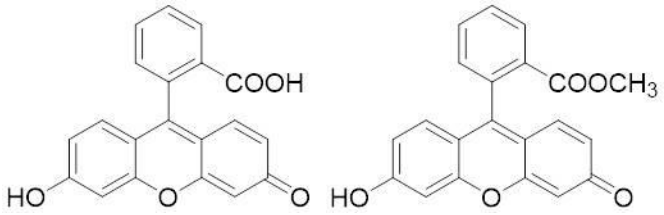

Scheme 3.3. Molecular structures of FA and FME-H.

The complexes Ga($TC_{10}P$)(O_2CFc) (Fc = ferrocenyl) and Ga($TC_{10}P$)($O_2CC_6H_4pyrC_{60}$) were prepared to allow incorporation of redox-active functional units into organized monolayers. Molecular polyads containing covalently linked porphyrins, ferrocenes, and fullerenes have been investigated for their potential application as artificial photosynthetic mimics,[33] as well as potential components of molecular electronic devices.[34] However, most reported systems employ the porphyrin meso positions for the attachment of ferrocene moieties,[34] which could interfere with porphyrin adsorption to the surface. Axial ligation to the metal center of a metalloporphyrin

offers an attractive alternative for surface organization. Poddutoori et al. reported molecular dyads and triads based on aluminum(III) tetraphenylporphyrin (TPP) axially ligated with fullerene derivatives (see example in Table 3.2), which were combined with additional ferrocene[17] (tethered through the *meso*-phenyl substituent of the porphyrin) and tetrathiafulvalene[16] moieties (datively bound through the metal center, trans to the modified C_{60} ligand). These systems were used to demonstrate light-induced electron transfer processes between the various components, which illustrated the utility of these molecular constructs as building blocks for donor-acceptor systems. Both $Ga(TC_{10}P)(O_2CFc)$ and $Ga(TC_{10}P)(O_2C_6H_4pyrC_{60})$ can potentially self-assemble on HOPG; the organization of donor-acceptor systems on surfaces has implications for the development of photovoltaic devices since well-defined, flat donor-acceptor interfaces can reduce carrier losses due to charge recombination.[35, 36]

In addition to the neutral dyads, the charged compound $[Ga(TC_{10}P)(OC_6H_4py)][PF_6]$ was prepared. The pyridinium-containing axial ligand is commonly used as a component of rotaxanes, which have garnered interest in the context of molecular machines because these mechanically interlocked systems undergo configurational changes due to external stimuli.[37] The attachment of such moieties onto Ga-porphyrins can potentially allow for the controlled assembly of rotaxanes on surfaces, and the successful patterning of such systems is important for the development of molecular functional devices.[38, 39]

In this chapter, the syntheses and characterization of the complexes shown in Scheme 3.2 are described. All complexes were prepared by reaction between the acid forms (carboxylic acid or alcohol) of the free ligands and $Ga(TC_{10}P)(OH)$, where the reactions were performed at room

temperature in air. The composition and purity of all complexes were established by an array of standard analytical methods.

3.2. Experimental Section

3.2.1. Materials and General Methods. All synthetic and purification procedures were performed in air at room temperature unless noted otherwise. CD_2Cl_2 was dried using 4 Å molecular sieves and stored under nitrogen. Toluene used for the purification of $[Ga(TC_{10}P)(OC_6H_4py)][PF_6]$ was purified by passing it under nitrogen pressure through an anaerobic, stainless-steel system consisting of one column of activated A2 alumina and one column of activated BASF R3-11 catalyst.[40] Chlorobenzene was dried using 4 Å molecular sieves and stored under nitrogen. The synthesis of $Ga(TC_{10}P)Cl$ is reported in Chapter 2. N-(2,4-Dinitrophenyl)pyridinium chloride was prepared according to literature procedures.[41] All other solvents, compounds, and reagents were obtained from commercial sources and used as received.

3.2.2. Characterization of Compounds. ^1H-, $^{13}C\{^1H\}$-, $^{31}P\{^1H\}$-, and 2D ($^1H/^{13}C$) HMQC-NMR spectra were recorded at room temperature using a Bruker Avance II$^+$ 500 MHz NMR spectrometer. Chemical shifts for all ^1H NMR and $^{13}C\{^1H\}$ NMR spectra are reported relative to $SiMe_4$ and were measured relative to solvent resonances.[42] $^{31}P\{^1H\}$ NMR spectra were measured using 85% phosphoric acid as the external reference. The ^1H NMR spectrum of N-(4-hydroxyphenyl)pyridinium hexafluorophosphate ($[pyC_6H_4OH][PF_6]$) was assigned by analogy to the previously reported perchlorate salt.[43] $^{13}C\{^1H\}$ NMR resonances for $[pyC_6H_4OH][PF_6]$, $Ga(TC_{10}P)(OPh)$, $Ga(TC_{10}P)(FME)$, $[Ga(TC_{10}P)(OC_6H_4py)][PF_6]$, $Ga(TC_{10}P)(O_2CPh)$, $Ga(TC_{10}P)(O_2CFc)$ and $Ga(TC_{10}P)(O_2CC_6H_4pyrC_{60})$ were assigned on the basis of HMQC spectra. The mass spectrum for fluorescein methyl ester (FME-H) was obtained using an Agilent 6130 ESI LC-MS system. All other mass spectra were obtained using a Bruker

UltrafleXtreme MALDI-TOF/TOF mass spectrometer in reflection positive mode or reflection negative mode on samples prepared on a standard stainless steel plate without a matrix; the Bruker peptide calibration standard II (750–3150 Da) was used as the calibration standard. Electronic absorption spectra were recorded using a Cary 300 UV-visible spectrophotometer of samples in quartz cuvettes at room temperature (1 mm and 1 cm path length). Elemental analyses were performed at Robertson Microlit Laboratories, Ledgewood NJ.

3.2.3. NMR Scale Reactions between Ga($TC_{10}P$)(OH) and ROH/RCO_2H. Test reactions of Ga($TC_{10}P$)(OH) with phenol, FME-H, benzoic acid, $FcCO_2H$, and $C_{60}pyrC_6H_4CO_2H$ were performed using NMR samples prepared in C_6D_6. For each trial, the ^1H NMR spectrum of Ga($TC_{10}P$)(OH) was first obtained, then the alcohol or carboxylic acid was added to the NMR sample as a solid. The relative concentrations of the reagents were determined by integrating resonances assigned to the starting materials and products: phenol, 7 equiv.; benzoic acid, 2.25 equiv.; $FcCO_2H$, 1.5 equiv.; FME-H and $C_{60}pyrC_6H_4CO_2H$, not determined. For test reactions performed with phenol and FME-H, the reaction progress was monitored at various time points (phenol: 5 min, 30 min, 60 min; FME: 5 min, 30 min, 75 min) after the initial addition of the ligands. Because FME-H is insoluble in C_6D_6, the sample was manually agitated every 15 minutes. For benzoic acid, $FcCO_2H$, and $C_{60}pyrC_6H_4CO_2H$, the reactions were complete by the time the first ^1H NMR spectrum could be obtained after the addition of the free ligands (~ 5 min).

3.2.4. Preparation of Fluorescein Methyl Ester (FME-H).[44] The preparation of this compound followed literature procedure, albeit at a reduced scale and without the use of a drying tube containing 3 Å molecular sieves. To a suspension of fluorescein free acid (0.621 g, 1.87 mmol) in methanol (3 mL), concentrated sulfuric acid (0.5 mL) was added dropwise, and the mixture was refluxed for 12 h. The reaction mixture was cooled to room temperature, after which

ice (1 g) and sodium bicarbonate (2 g) were added, and the resulting suspension was collected by filtration. The crude product was suspended in a 2% sodium bicarbonate solution (20 mL) to remove residual H_2SO_4, filtered, and washed with water (20 mL); this three step purification process was repeated four times. The resulting dull, red solid was washed with 1% acetic acid (20 mL) and water (20 mL). The ^{1}H NMR spectrum of the product revealed the presence of unreacted fluorescein free acid (~2%). Thus, in addition to these literature purification procedures, the compound was purified via silica gel chromatography using $CHCl_3$/methanol (9:1) as the eluent; this resulted in removal of the fluorescein free acid. Removal of the volatile components under vacuum provided the product as a bright red solid (0.478 g, 1.37 mmol, 73% yield). ^{1}H NMR (DMSO-d_6, 500.13 MHz; Figure 3.1): δ 8.20 (d, 1H, J = 7.5 Hz, H), 7.86 (m, 1H), 7.77 (m, 1H), 7.49 (d, 1H, J = 7.5 Hz), 6.78 (d, 2H, J = 9.2 Hz, xanthene), 6.10–7.10 (v br, 4H, xanthene), 3.58 (s, 3H, OCH_3). The chemical shifts in the ^{1}H NMR spectrum were consistent with values reported by Kazarian et al.,[45] but did not agree with values reported by Adamczyk et al., where all xanthene proton resonances were reported as peaks with well-defined splitting patterns.[44] Literature values for ^{1}H NMR (300 MHz, DMSO-d_6): δ 8.25 (d, 1H, J = 7.5 Hz), 7.90 (td, 1H, J = 7.2 Hz, 1.4 Hz), 7.82 (td, 1H, J = 7.2 Hz, 1.4 Hz), 7.51 (d, 1H, J = 7.6 Hz), 7.09 (d, 2H, J = 9.2 Hz), 7.00 (d, 2H, J = 1.5 Hz), 6.76 (dd, 2H, J = 9.2 Hz, 2.0 Hz), 3.56 (s, 3H);[44] δ 8.18 (d, 1H, J = 7.2 Hz), 7.84 (m, 1H), 7.75 (m, 1H), 7.46 (d, 1H, J = 7.2 Hz), 6.77 (d, 2H, J = 9.0 Hz), 6.55 (m, 4H), 3.56 (s, 3H).[45] UV-vis (CH_2Cl_2; λ_{max}, nm (rel. int.)): 308 (35.0), 353 (33.1), 404 (49.7), 435 (87.2), 455 (100), 486 (63.2). ESI-MS (m/z): $[M + H]^+$ = 347.1; predicted 347.1.

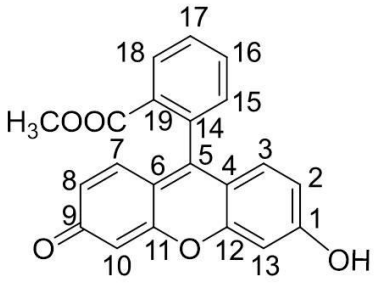

3.2.5. Preparation of $[pyC_6H_4OH][PF_6]$.[46] This procedure was adapted from the synthesis of $[pyC_6H_4OH][ClO_4]$.[43] A bright red solution of 4-aminophenol (0.400 g, 3.60 mmol) and 1-(2,4-dinitrophenyl)pyridinium chloride (0.680 g, 2.40 mmol) in absolute ethanol (7 mL) was refluxed for 48 h, during which the color of the reaction mixture turned red-brown. The solution was cooled to room temperature and filtered. The filtrate was reduced to dryness *in vacuo*, and the resulting brown residue was suspended in water (20 mL) and boiled for 10 min. The resulting yellow solution extracted from the brown residue was allowed to cool to room temperature and filtered to remove any residual 2,4-dinitroaniline, which formed as a byproduct during the reaction. Addition of KPF_6 (0.883 g, 4.80 mmol) to the filtrate induced precipitation of the product as a brown-yellow solid, which was collected via filtration and dried under vacuum (0.268 g, 0.845 mmol, 35% yield). ^{1}H NMR (DMSO-d_6, 500.13 Hz; Figure 3.2): δ 10.42 (s, 1H, OH), 9.25 (d, 2H, J = 5.7 Hz, H5), 8.71 (t, 1H, J = 7.8 Hz, H7), 8.25 (m, 2H, H6), 7.69 (d, J = 7.0 Hz, H3), 7.05 (d, J = 7.0 Hz, H2). ^{13}C{^{1}H} NMR (DMSO-d_6, 125.76 Hz; Figure 3.3): δ 159.86 (C1), 145.74 (C7), 144.65 (C5), 134.60 (C4), 128.06 (C6), 126.00 (C3), 116.37 (C2). ^{31}P{^{1}H} NMR (DMSO-d_6, 202.45 Hz): δ –145.23 (sept, PF_6).

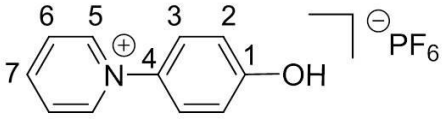

3.2.6. Preparation of $C_{60}pyrC_6H_4CO_2H$. The synthesis of this compound has been previously described by two different reports.[17, 47] The following synthetic procedure is modified from the procedure reported by Hau, et al.[47] C_{60} (0.200 g, 0.28 mmol), 4-carboxybenzaldehyde (0.041 g, 0.28 mmol), and sarcosine (0.250 g, 2.8 mmol) were added to chlorobenzene (60 mL) and refluxed overnight under an atmosphere of nitrogen. The volatile components were removed *in vacuo*, and the crude mixture was purified by column chromatography on silica gel; elution with toluene removed unreacted C_{60} as a purple band, then elution with toluene/THF (2:1)

allowed isolation of the crude product as a brown band. The volatile components were removed *in vacuo*, and the brown solid was suspended in CH_2Cl_2 (5 mL), collected via filtration, and dried under vacuum (0.057 g, 0.06 mmol, 23% yield). The chemical shifts in the ^{1}H NMR spectrum obtained in $CDCl_3$ with added CD_3OD were consistent with reported values[17] and are not re-reported here, but the ^{1}H NMR data obtained in DMSO-d_6 did not agree with literature values[47] and are listed below. ^{1}H NMR (500.13 MHz, DMSO-d_6): δ 13.03 (s, 1H, CO_2H), 8.03 (d, 2H, J = 8.0 Hz, H2), 7.94 (br s, 2H, H3), 5.22 (s, 1H, H5), 5.10 (d, 1H, J = 9.5 Hz, H6), 4.34 (d, 1H, J = 9.5 Hz, H6), 2.75 (s, 3H, NCH_3). Literature values for ^{1}H NMR (DMSO-d_6, 300 MHz):[47] 10.12 (s, 1H), 8.15 (d, 2H, J = 8.4 Hz), 8.03 (d, 2H, J = 8.4 Hz), 6.89 (s, 1H), 6.65 (s, 1H), 2.20 (s, 3H). LDI-TOF MS (m/z): $[M]^+$ = 897.160; predicted 897.079.

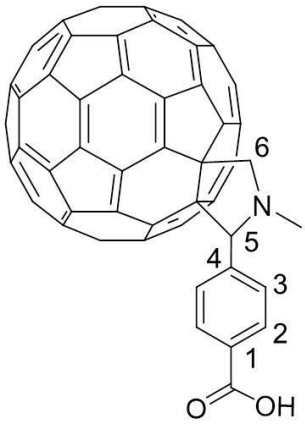

3.2.7. Preparation of Ga(TC$_{10}$P)(OH). To a stirred solution of Ga(TC$_{10}$P)Cl (0.196 g, 0.207 mmol) in CH_2Cl_2 (20 mL), a 2 N NaOH solution (20 mL) was added. The resulting solvent layers were stirred vigorously to form an emulsion for 1 h. The organic layer was separated, washed with water, and dried with $NaSO_4$. The volatile components were removed *in vacuo*, and the product was obtained as a purple solid (0.185 g, 0.193 mmol, 93% yield). ^{1}H NMR (CD_2Cl_2, 500.13 MHz; Figure 3.4): δ 9.63 (s, 8H, *β*), 4.86 (t, 8H, $CH_2CH_2C\underline{H}_2$Por), 2.56 (m, 8H, $CH_2C\underline{H}_2CH_2$Por), 1.86 (m, 8H, $C\underline{H}_2CH_2CH_2$Por), 1.58 (m, 8H, $CH_3(CH_2)_5C\underline{H}_2$) 1.22–1.46 (m, 40H, $CH_3(C\underline{H}_2)_5CH_2$), 0.88 (t, 12H, CH_3), –6.91 (s, 1H, OH). ^{13}C{^{1}H} NMR (CD_2Cl_2, 125.76 MHz; Figure 3.5): δ 148.26 (*α*), 129.49 (*β*), 119.09 (*meso*), 39.21 (CH_2), 35.82 (CH_2), 32.34 (CH_2), 31.14 (CH_2), 30.16 (CH_2), 30.12 (CH_2), 30.11 (CH_2), 29.79 (CH_2), 23.12 (CH_2), 14.31 (CH_3). UV-vis (CH_2Cl_2; λ_{max}, nm (rel. int.); Figure 3.20): 311 (4.9), 400 (17.1), 421 (100), 520

(0.7), 558 (3.3), 597 (1.6). LDI-TOF MS (m/z): $[M]^-$ = 954.687; predicted 954.660. Anal. Calcd. for $C_{60}H_{93}N_4OGa$: C, 75.37; H, 9.80; N, 5.86. Found: C, 75.14; H, 9.56; N, 5.71.

3.2.8. Preparation of Ga(TC$_{10}$P)(OPh). To a solution of Ga(TC$_{10}$P)(OH) (0.054 g, 0.056 mmol) in toluene (25 mL), phenol (0.010 g, 0.11 mmol) was added, and the reaction mixture was stirred for 1.5 h. The volatile components were then removed *in vacuo*, after which the purple residue was dissolved in a mixture of THF (20 mL) and acetonitrile (20 mL). The solvent volume was reduced *in vacuo* to ~20 mL, which induced precipitation of the product as a purple solid and a color change of the solution from purple to faint green. The product was isolated via filtration, and washed with acetonitrile (3 × 5 mL), and dried under vacuum (0.056 g, 0.054 mmol, 96% yield). ^{1}H NMR (CD_2Cl_2, 500.13 MHz; Figure 3.6): δ 9.46 (s, 8H, *β*), 5.51–5.61 (m, 3H, *m*-Ph, *p*-Ph), 4.68 (t, 8H, $CH_2CH_2C\underline{H}_2$Por), 2.46 (m, 8H, $CH_2C\underline{H}_2CH_2$Por), 2.07 (d, 2H, *J* = 7.4 Hz, *o*-Ph), 1.84 (m, 8H, $C\underline{H}_2CH_2CH_2$Por), 1.56 (m, 8H, $CH_3(CH_2)_5C\underline{H}_2$), 1.25–1.40 (m, 40H, $CH_3(C\underline{H}_2)_5CH_2$), 0.91 (t, 12H, CH_3). $^{13}C\{^1H\}$ NMR (CD_2Cl_2, 125.76 MHz; Figure 3.7): δ 157.33 (*ipso*-Ph), 148.16 (*α*), 129.21 (*β*), 126.57 (*m*-Ph), 119.12 (*meso*), 117.33 (*o*-Ph), 115.73 (*p*-Ph), 39.12 (CH_2), 35.66 (CH_2), 32.38 (CH_2), 31.15 (CH_2), 30.18 (CH_2), 30.14 (CH_2), 29.83 (CH_2), 23.14 (CH_2), 14.33 (CH_3); one CH_2 resonance was not resolved due to signal overlap. UV-vis (CH_2Cl_2; λ_{max}, nm (rel. int.); Figure 3.20): 307 (3.8), 400 (17.9), 421 (100), 519 (0.6), 559 (3.3), 599 (1.8). Anal. Calcd. for $C_{66}H_{97}N_4OGa$: C, 76.80; H, 9.47; N, 5.43. Found: C, 76.51; H, 9.49; N, 5.29.

3.2.9. Preparation of Ga(TC$_{10}$P)(FME). To a solution of Ga(TC$_{10}$P)(OH) (0.090 g, 0.094 mmol) in toluene (15 mL), FME-H (0.041 g, 0.118 mmol) was added to form a suspension. The reaction mixture was stirred for 1.5 h, during which the solution color changed from purple to red. The mixture was then filtered to remove unreacted FME-H. The product was isolated as a

red-purple solid after the removal of volatile components *in vacuo* (0.111 g, 0.086 mmol, 91% yield). ^{1}H NMR (CD_2Cl_2, 500.13 MHz; Figure 3.8): δ 9.53 (s, 8H, *β*), 7.99 (d, 1H, *J* = 7.6 Hz, H15 or H18), 7.46–7.55 (m, 2H, H16, H17), 6.87 (d, 1H, J = 7.2 Hz, H15 or H18), 5.60–6.60 (v br, "xanthene"), 4.71 (t, 8H, $CH_2CH_2C\underline{H}_2$Por), 3.35 (s, 3H, OCH_3), 2.44 (m, 8H, $CH_2C\underline{H}_2CH_2$Por), 1.78 (m, 8H, $C\underline{H}_2CH_2CH_2$Por), 1.50 (m, 8H, $CH_3(CH_2)_5C\underline{H}_2$), 1.20–1.45 (m, 40H, $CH_3(C\underline{H}_2)_5CH_2$), 0.90 (t, 12H, CH_3); complete assignment of the xanthene core resonances (H2, H3, H7, H8, H10, H13) was not possible due to very broad feature(s) (centered at 6.15 ppm) and/or missing peaks; see Section 3.3.4. ^{13}C{^{1}H} NMR (CD_2Cl_2, 125.76 MHz; Figure 3.9): δ 165.62, 150.94, 148.05 (*α*), 135.13, 132.37 (C15 or C18), 132.37 (C15 or C18), 130.91 (C16 or C17), 129.59 (*β*), 129.35 (C16 or C17), 119.39 (*meso*), 103.95, 52.20 (OCH_3), 39.00 (CH_2), 35.57 (CH_2), 32.35 (CH_2), 31.07 (CH_2), 30.18 (CH_2), 30.09 (CH_2), 30.04 (CH_2), 29.80 (CH_2), 23.12 (CH_2), 14.32 (CH_3); chemical shifts at 165.62 ppm, 150.94 ppm, 135.13 ppm and 103.95 ppm are not assigned since FME ligand resonances (C1–C14, C19) were not all observed. UV-vis (CH_2Cl_2; λ_{max}, nm (rel. int.); Figure 3.20): 307 (5.1), 402 (11.8), 420 (100), 472 (6.8), 504 (5.8), 558 (3.6), 597 (1.9).

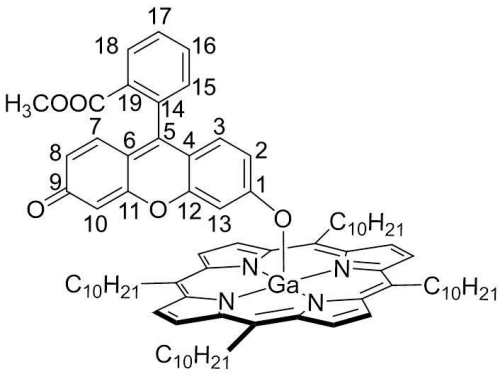

3.2.10. Preparation of [Ga(TC$_{10}$P)(OC$_6$H$_4$py)][PF$_6$].[46] To a solution of Ga(TC$_{10}$P)(OH) (0.200 g, 0.208 mmol) in a mixture of toluene (10 mL) and acetonitrile (10 mL) was added [pyC_6H_4OH][PF_6] (0.066 g, 0.21 mmol), and the mixture was stirred for 2 h. The volatile components were then removed *in vacuo*, and the residue was extracted into toluene (20 mL) and filtered to remove the unreacted free ligand. The crude product was precipitated from solution upon the reduction of solvent volume to ~10 mL and addition of hexanes (30 mL). The solid was

filtered, washed with hexanes (3 × 5 mL), and dissolved in anhydrous toluene (10 mL) under an atmosphere of nitrogen. The product was precipitated by layering the toluene solution with hexamethyldisiloxane (30 mL) and cooling to –30 °C overnight under nitrogen. The pure product was isolated via filtration as a brown solid and dried under vacuum (0.050 g, 0.040 mmol, 25% yield). ^{1}H NMR (CD_2Cl_2, 500.13 MHz; Figure 3.10): δ 9.58 (s, 8H, *β*), 8.38 (t, 1H, *J* = 7.8 Hz, H7), 8.11 (d, 2H, *J* = 5.9 Hz, H5), 7.93 (m, 2H, H6), 5.84 (d, 2H, *J* = 8.9 Hz, H3), 4.77 (t, 8H, $CH_2CH_2C\underline{H}_2$Por), 2.47 (m, 8H, $CH_2C\underline{H}_2CH_2$Por), 2.31 (d, 2H, *J* = 5.9 Hz, H2), 1.83 (m, 8H, $C\underline{H}_2CH_2CH_2$Por), 1.54 (m, 8H, $CH_3(CH_2)_5C\underline{H}_2$), 1.25–1.45 (m, 40H, $CH_3(C\underline{H}_2)_5CH_2$), 0.90 (t, 12H, CH_3). ^{13}C{^{1}H} NMR (CD_2Cl_2, 125.76 MHz; Figure 3.11): δ 162.00 (C1), 148.19 (*α*), 145.19 (C7), 143.00 (C5), 130.93 (C4), 129.67 (*β*), 128.87 (C6), 121.93 (C3), 119.41 (*meso*), 119.29 (C2), 39.17 (CH_2), 35.60 (CH_2), 32.35 (CH_2), 31.06 (CH_2), 30.18 (CH_2), 30.14 (CH_2), 30.11 (CH_2), 29.80 (CH_2), 23.12 (CH_2), 14.32 (CH_3). ^{31}P{^{1}H} NMR (C_6D_6, 202.45 MHz): δ –142.14 (sept, PF_6). UV-vis (toluene, λ_{max}, nm (rel. int.); Figure 3.20): 312 (3.5), 367 (3.1), 383 (3.1), 403 (9.8), 423 (100), 485 (0.3), 519 (0.7), 559 (3.5), 598 (1.8). LDI-TOF MS (m/z): [M – PF_6]$^{+}$ = 1108.667; predicted 1108.726.

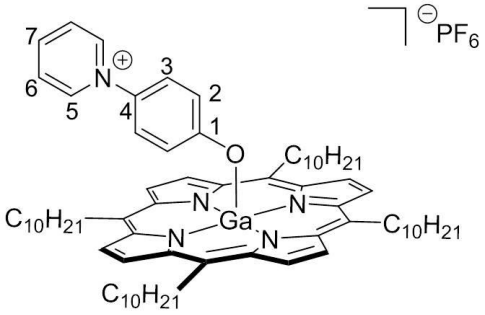

3.2.11. Preparation of Ga(TC$_{10}$P)(O$_2$CPh). To a solution of Ga(TC$_{10}$P)(OH) (0.056 g, 0.059 mmol) in toluene (15 mL), benzoic acid (0.009 g, 0.074 mmol) was added. The reaction mixture was stirred for 15 min, and the volatile components were removed *in vacuo*. The crude product was dissolved in diethyl ether (5 mL), after which acetonitrile (15 mL) was added. The solution was reduced in volume to ~15 mL under vacuum to induce precipitation of the product, which was isolated by filtration, washed with acetonitrile (5 mL), and dried under vacuum (0.047

g, 0.044 mmol, 75% yield). ^{1}H NMR (CD_2Cl_2, 500.13 MHz; Figure 3.12): δ 9.62 (s, 8H, *β*), 6.62 (t, 1H, *J* = 7.3 Hz, *p*-Ph), 6.30 (m, 2H, *m*-Ph), 5.23 (d, 1H, *J* = 5.2 Hz, *o*-Ph), 4.83 (t, 8H, $CH_2CH_2C\underline{H}_2$Por), 2.46 (m, 8H, $CH_2C\underline{H}_2CH_2$Por), 1.74 (m, 8H, $C\underline{H}_2CH_2CH_2$Por), 1.49 (m, 8H, $CH_3(CH_2)_5C\underline{H}_2$), 1.20–1.42 (m, 40H, $CH_3(C\underline{H}_2)_5CH_2$), 0.89 (t, 12H, CH_3). ^{13}C{^{1}H} NMR (CD_2Cl_2, 125.76 MHz; Figure 3.13): δ 163.42 (CO_2Ga), 148.18 (*α*), 133.13 (*ipso*-Ph), 129.78 (*p*-Ph), 129.52 (*β)*, 127.72 (*o*-Ph), 126.55 (*m*-Ph), 119.21 (*meso*), 38.77 (CH_2), 35.58 (CH_2), 32.34 (CH_2), 30.97 (CH_2), 29.77 (CH_2), 23.11 (CH_2), 14.30 (CH_3); two CH_2 resonances were not resolved due to signal overlap. UV-vis (toluene; λ_{max}, nm (rel. int.); Figure 3.21): 314 (2.9), 385 (1.1), 403 (6.9), 423 (100), 485 (0.2), 520 (0.5), 560 (3.0), 599 (1.4). LDI-TOF MS (m/z): $[M]^-$ = 1058.673; predicted 1058.687. Anal. Calcd. for $C_{67}H_{97}N_4O_2Ga$: C, 75.90; H, 9.22; N, 5.28. Found: C, 75.87; H, 8.93; N, 5.38.

3.2.12. Preparation of Ga(TC$_{10}$P)(O$_2$CFc). To a solution of Ga($TC_{10}P$)(OH) (0.062 g, 0.065 mmol) in toluene (15 mL), $FcCO_2H$ (0.016 g, 0.070 mmol) was added. The reaction mixture was stirred for 15 min, and the volatile components were removed *in vacuo*. The crude mixture was then dissolved in diethyl ether (5 mL), to which acetonitrile (15 mL) was added. The solvent was reduced in volume to ~15 mL under vacuum to induce precipitation of the product, which was isolated by filtration, washed with acetonitrile (5 mL), and dried under vacuum (0.049 g, 0.042 mmol, 65% yield). ^{1}H NMR (CD_2Cl_2, 500.13 MHz; Figure 3.14): δ 9.66 (s, 8H, *β*), 4.87 (t, 8H, $CH_2CH_2C\underline{H}_2$Por), 3.18 (m, 2H, 3,4-C_5H_4), 2.64 (s, 5H C_5H_5), 2.57 (m, 8H, $CH_2C\underline{H}_2CH_2$Por), 2.32 (m, 2H 2,5-C_5H_4), 1.83 (m, 8H, $C\underline{H}_2CH_2CH_2$Por), 1.55 (m, 8H, $CH_3(CH_2)_5C\underline{H}_2$), 1.23–1.44 (m, 40H, $CH_3(C\underline{H}_2)_5CH_2$), 0.89 (t, 12H, CH_3). ^{13}C{^{1}H} NMR (CD_2Cl_2, 125.76 MHz; Figure 3.15): δ 166.93 (CO_2Ga), 148.36 (*α*), 129.51 (*β*), 119.30 (*meso*), 74.85 (1-C_5H_4), 68.75 (3,4-C_5H_4), 68.72 (C_5H_5), 68.67 (2,5-C_5H_4), 39.09 (CH_2), 35.76 (CH_2),

32.35 (CH_2), 31.08 (CH_2), 30.15 (CH_2), 30.12 (CH_2), 29.79 (CH_2), 23.12 (CH_2), 14.31 (CH_3); one CH_2 resonance was not resolved due to signal overlap. UV-vis (toluene; λ_{max}, nm (rel. int.); Figure 3.21): 314 (3.0), 385 (1.1), 404 (7.2), 423 (100), 487 (0.2), 520 (0.5), 561 (3.1), 600 (1.5). LDI-TOF MS (m/z): $[M]^-$ = 1166.625; predicted 1166.653. Anal. Calcd. for $C_{71}H_{101}N_4O_2GaFe$: C, 73.00; H, 8.71; N, 4.80. Found: C, 72.89; H, 8.48; N, 4.98.

3.2.13. Preparation of Ga(TC$_{10}$P)(O$_2$CC$_6$H$_4$pyrC$_{60}$). To a solution of Ga(TC$_{10}$P)(OH) (0.027 g, 0.028 mmol) in toluene (10 mL), $C_{60}pyrC_6H_4CO_2H$ (0.025 g, 0.028 mmol) was added. The reaction mixture was stirred for 15 min, filtered, then reduced in volume under vacuum to ~5 mL. Hexanes (30 mL) was added, and the mixture was cooled overnight at −20 °C to induce precipitation of the product. The product was collected via filtration, washed with hexanes (5 mL), and dried under vacuum (0.040 g, 0.022 mmol, 77% yield). ^{1}H NMR (CD_2Cl_2, 500.13 MHz; Figure 3.16): δ 9.54 (s, 8H, *β*), 6.72 (br s, 2H, H3), 5.37 (d, 2H, *J* = 8.5 Hz, H2), 4.82 (t, 8H, $CH_2CH_2C\underline{H}_2$Por), 4.53 (d, 1H, *J* = 9.5 Hz, H6), 4.25 (s, 1H, H5), 3.76 (d, 1H, *J* = 9.5 Hz, H6), 2.40 (m, 8H, $CH_2C\underline{H}_2CH_2$Por), 2.25 (s, 3H, NCH_3), 1.75 (m, 8H, $C\underline{H}_2CH_2CH_2$Por), 1.48 (m, 8H, $CH_3(CH_2)_5C\underline{H}_2$), 1.22–1.40 (m, 40H, $CH_3(C\underline{H}_2)_5CH_2$), 0.89 (t, 12H, CH_3). $^{13}C\{^1H\}$ NMR (CD_2Cl_2, 125.76 MHz; Figure 3.17): δ 163.26 (CO_2Ga), 156.38, 154.05, 153.25, 152.98, 148.35 (*α* or C_{60}), 148.34 (*α* or C_{60}), 147.17, 147.14, 146.44, 146.42, 146.18, 146.07, 146.00, 145.99, 145.98, 145.93, 145.91, 145.77, 145.73, 145.64, 145.56, 145.46, 145.41, 145.34, 145.28, 145.17, 145.16, 145.11, 145.00, 144.85, 144.55, 144.24, 144.14, 142.87, 142.80, 142.50, 142.38, 142.32, 142.16, 142.11, 142.00, 141.95, 141.88, 141.87, 141.58, 141.54, 141.52, 141.43, 141.17, 139.95, 139.53, 139.04,

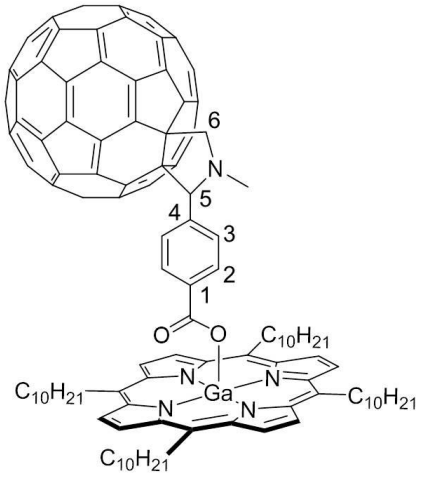

138.88, 136.51, 136.34, 135.67, 135.60, 133.27, 129.45 (*β*), 128.14 (C2), 119.41 (*meso*), 82.98 (C5), 76.90, 69.92 (C6), 69.04, 66.06, 39.53 (NCH_3), 38.88 (CH_2), 35.74 (CH_2), 32.39 (CH_2), 31.08 (CH_2), 30.18 (CH_2), 30.17 (CH_2), 30.16 (CH_2), 29.84 (CH_2), 23.16 (CH_2), 14.36 (CH_3); 65 of the 68 $C_{60}pyrC_6H_4CO_2$ resonances were observed. UV-vis (toluene; λ_{max}, nm (rel. int.); Figure 3.21): 311 (10.9), 329 (10.0), 380 (3.2), 403 (7.9), 423 (100), 486 (0.5), 520 (0.7), 560 (3.2), 599 (1.5). Anal. Calcd. for $C_{130}H_{102}N_5O_2Ga$: C, 85.05; H, 5.60; N, 3.81. Found: C, 84.78; H, 5.31; N, 3.80.

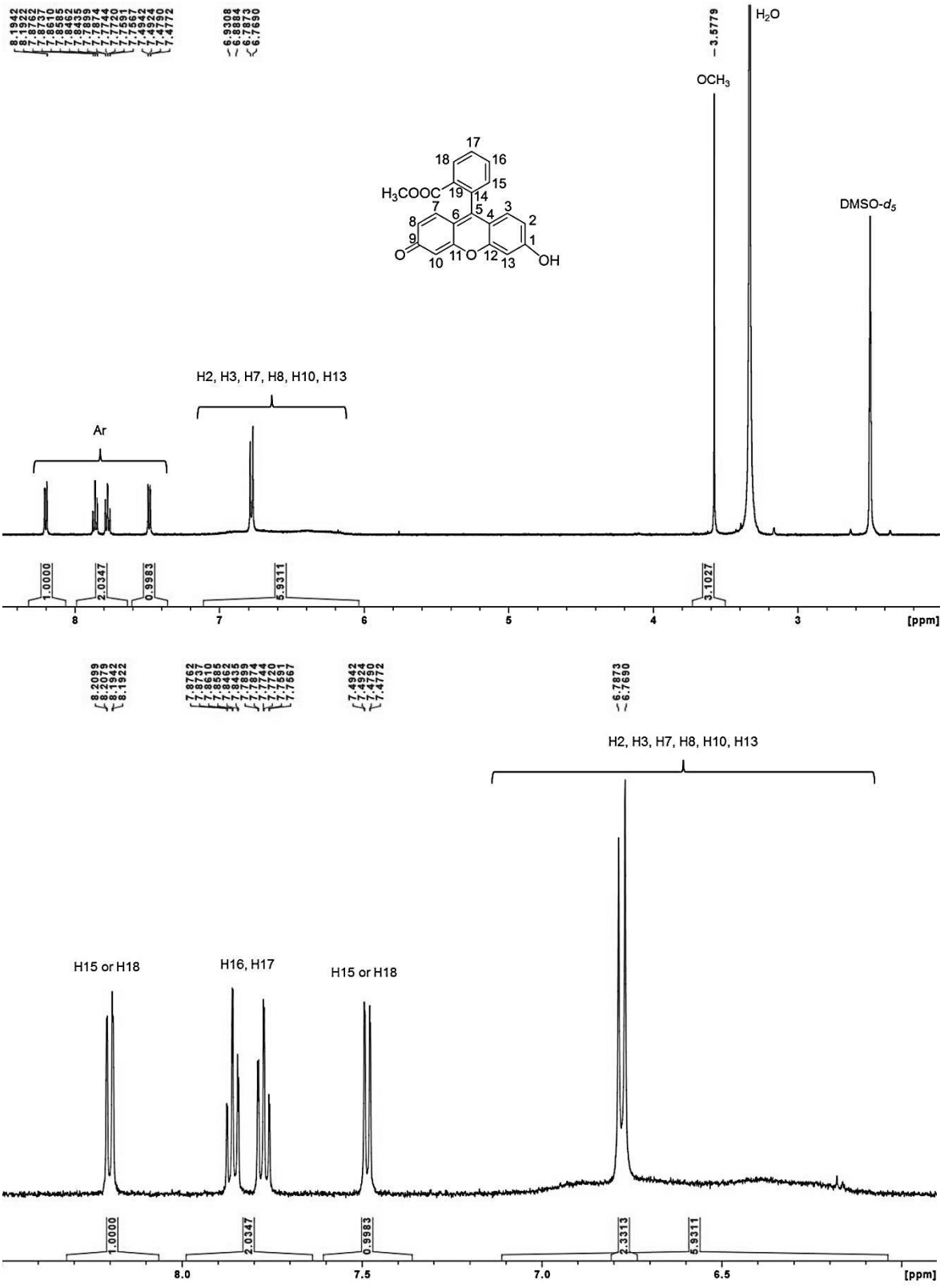

Figure 3.1. [1]H NMR spectrum of FME-H in DMSO-d_6. The bottom spectrum is an expansion of the top spectrum.

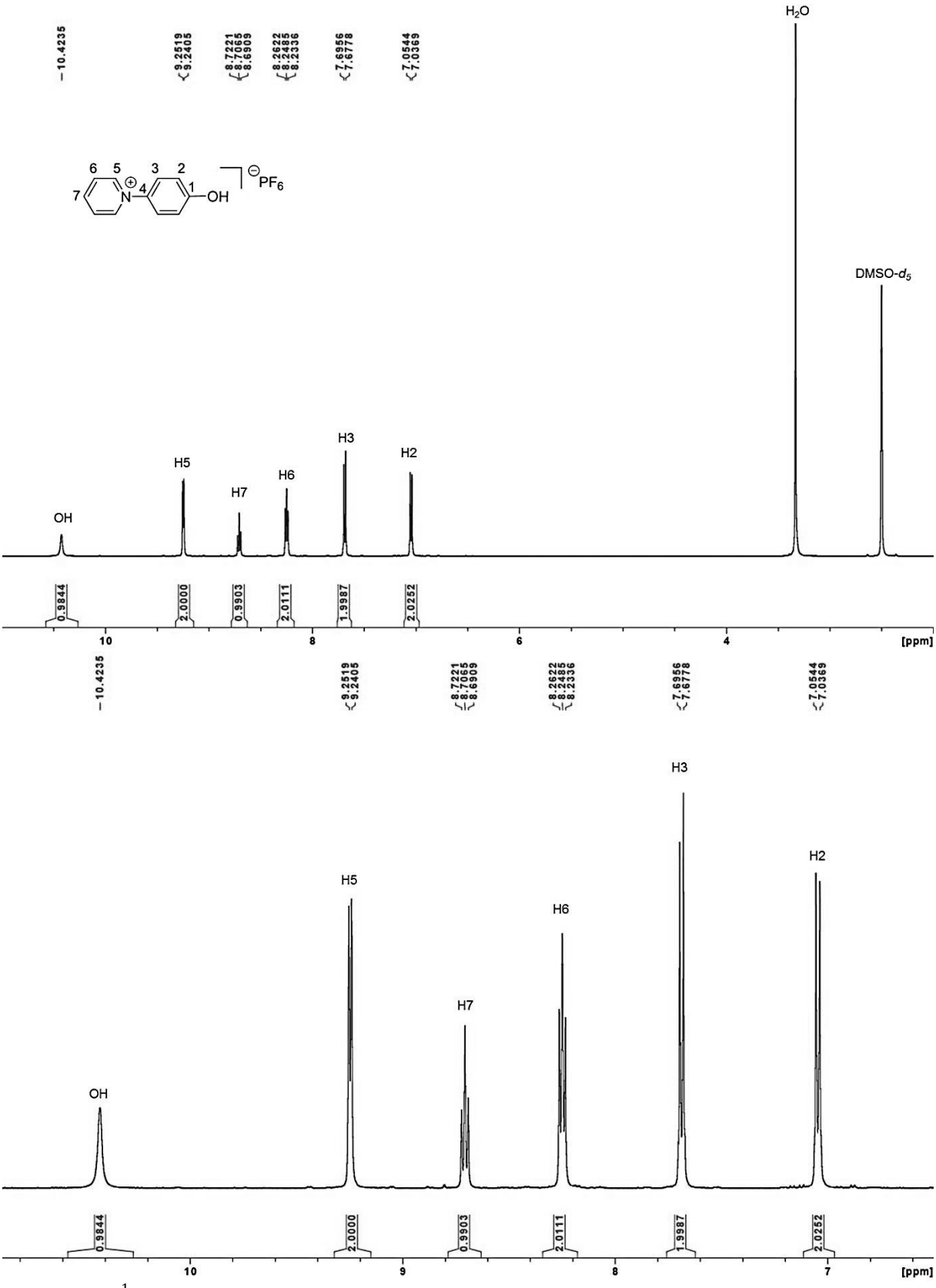

Figure 3.2. ^{1}H NMR spectrum of [pyC_6H_4OH][PF_6] in DMSO-d_6.

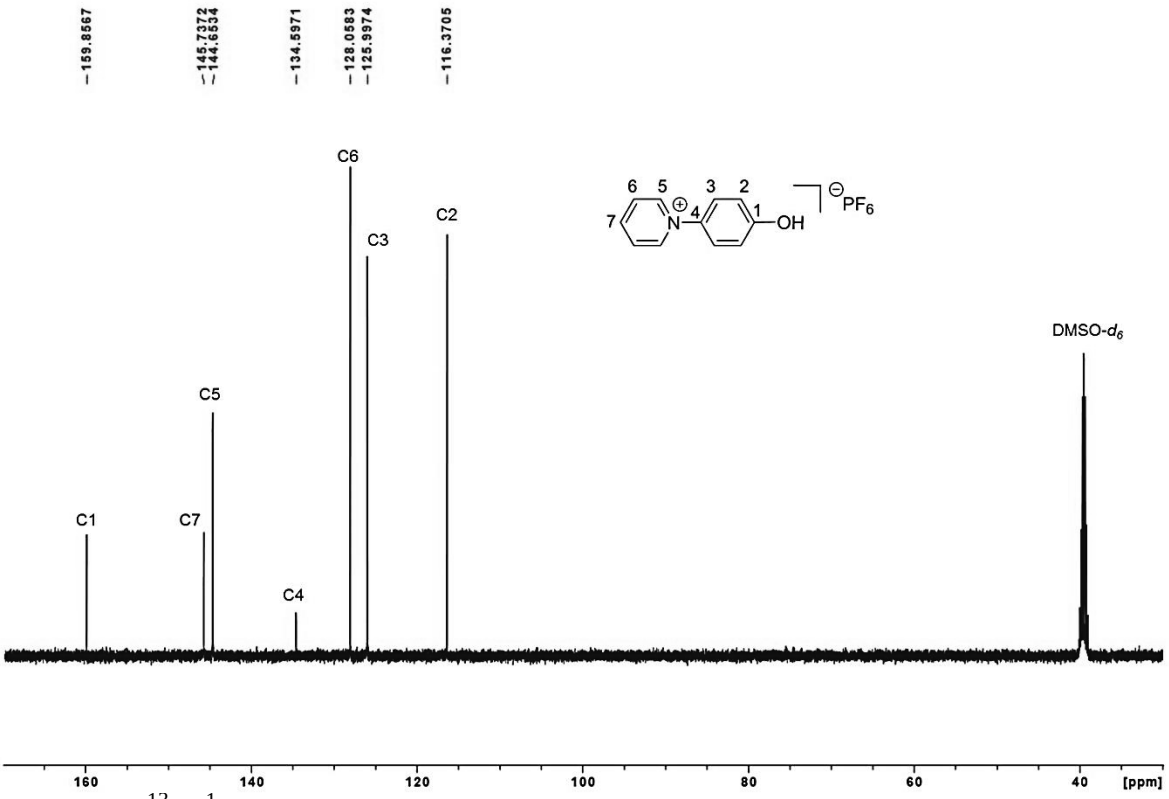

Figure 3.3. $^{13}C\{^{1}H\}$ NMR spectrum of $[pyC_6H_4OH][PF_6]$ in DMSO-d_6.

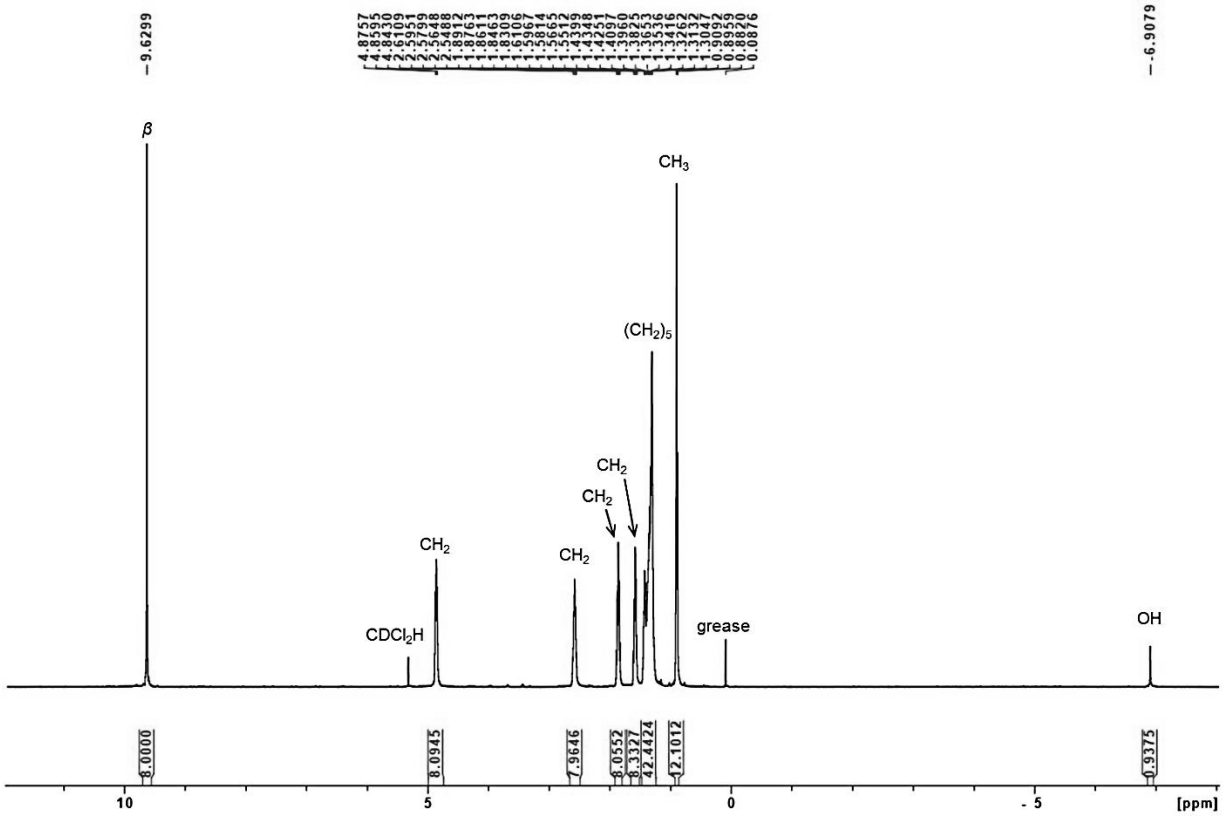

Figure 3.4. ^{1}H NMR spectrum of $Ga(TC_{10}P)(OH)$ in CD_2Cl_2.

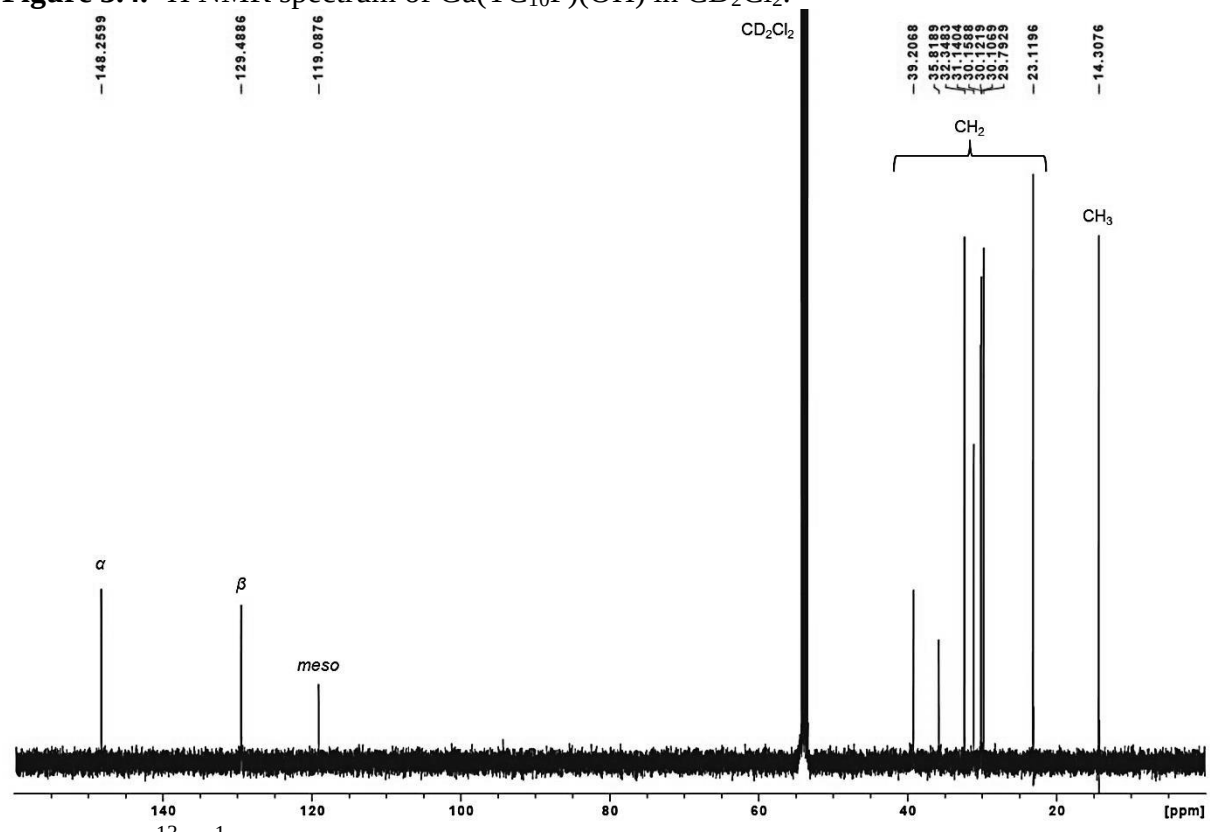

Figure 3.5. $^{13}C\{^{1}H\}$ NMR spectrum of $Ga(TC_{10}P)(OH)$ in CD_2Cl_2.

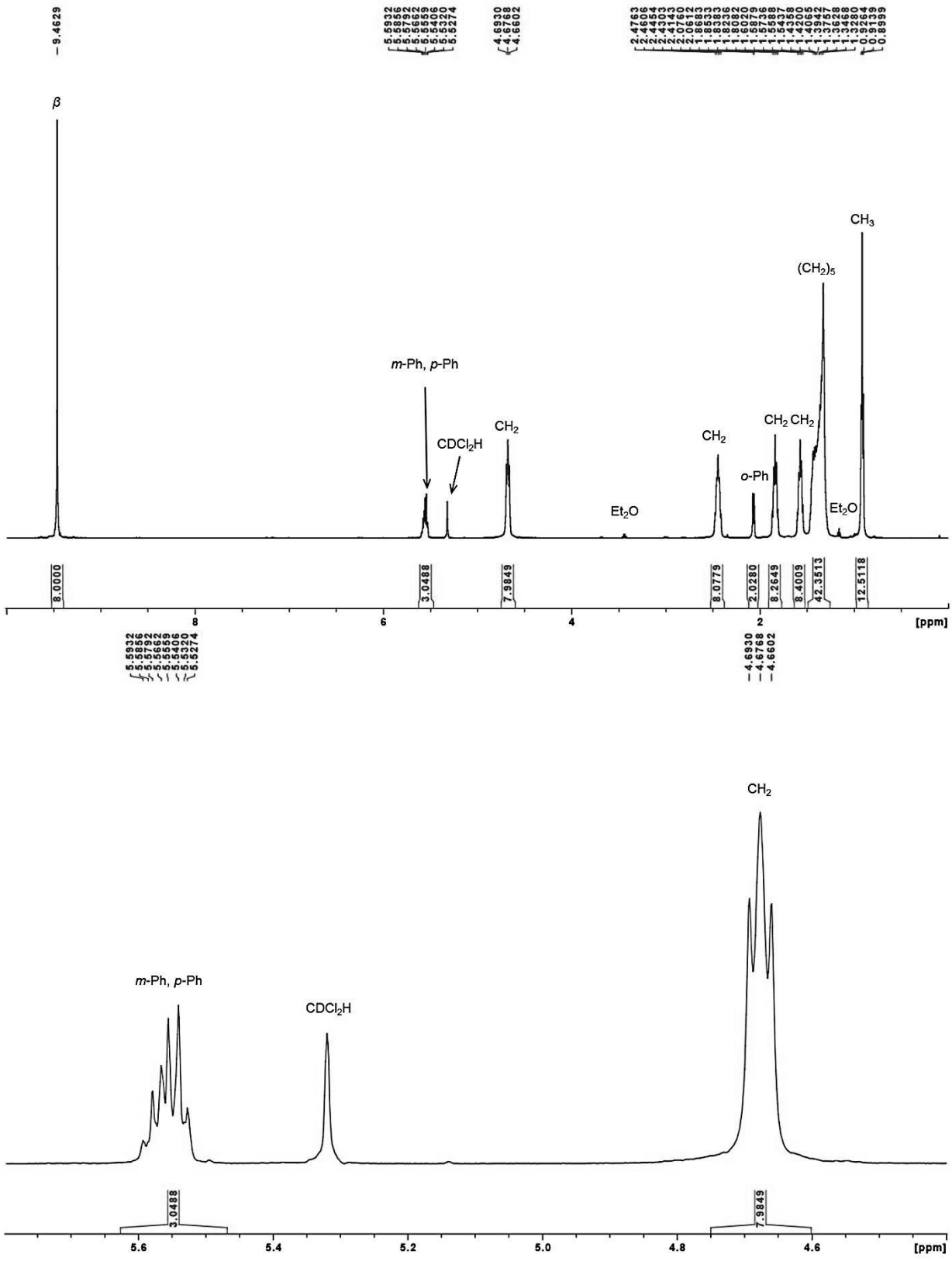

Figure 3.6a,b. ^{1}H NMR spectrum of $Ga(TC_{10}P)(OPh)$ in CD_2Cl_2. The bottom spectrum is an expansion of the top spectrum.

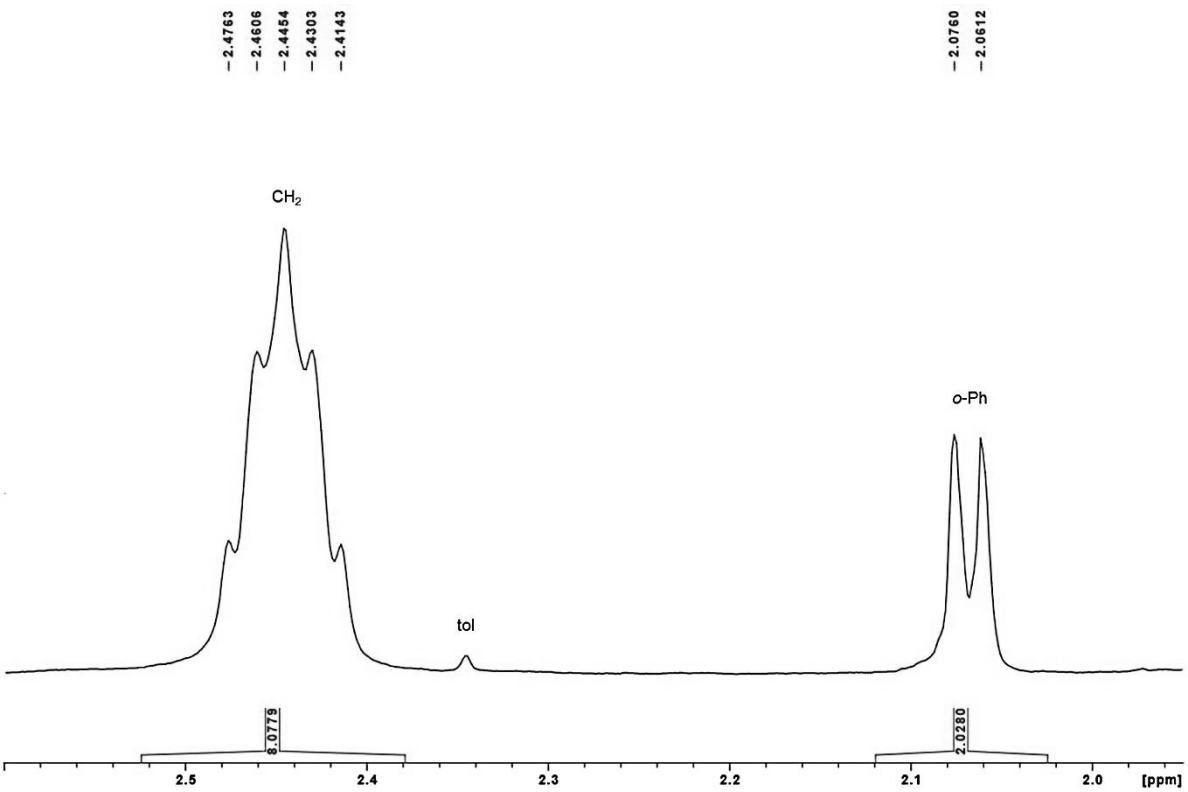

Figure 3.6c. Expansion of the ^{1}H NMR spectrum of $Ga(TC_{10}P)(OPh)$ in CD_2Cl_2 showing the upfield shifted aryl resonance.

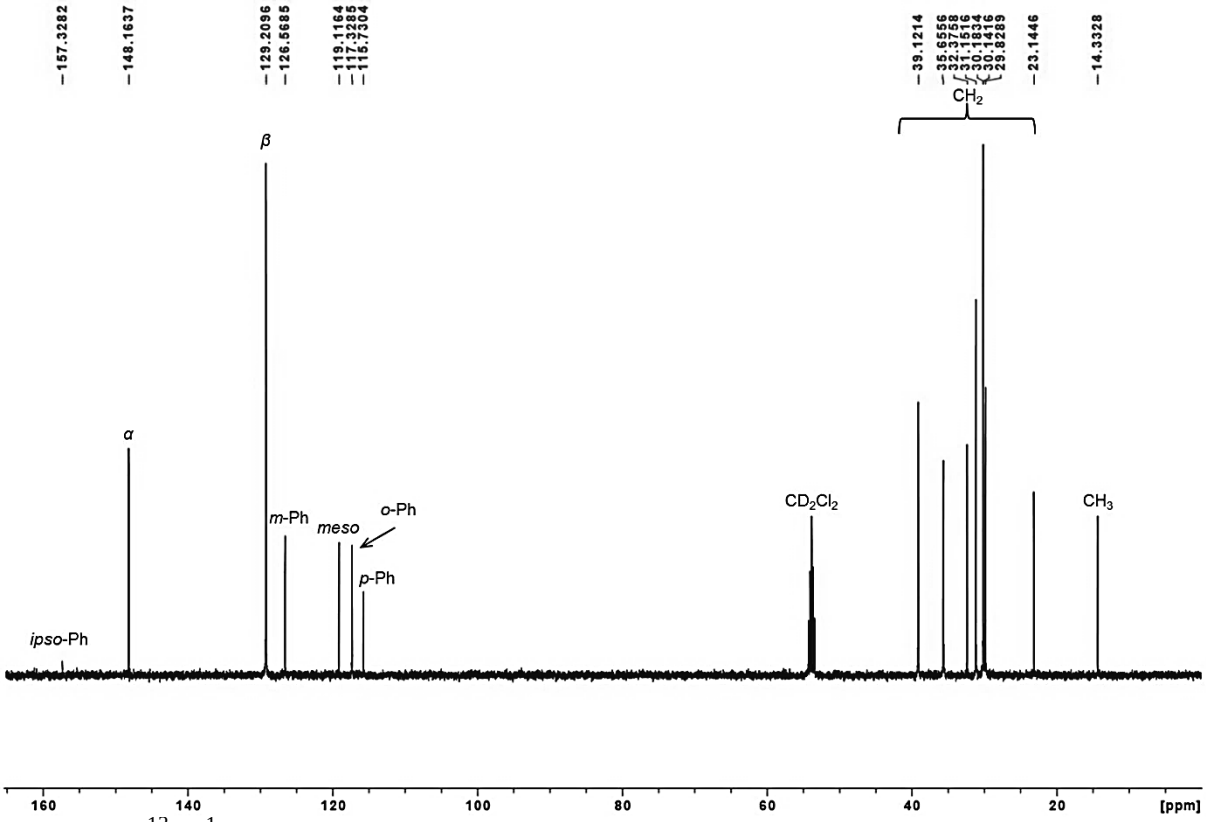

Figure 3.7. $^{13}C\{^{1}H\}$ NMR spectrum of $Ga(TC_{10}P)(OPh)$ in CD_2Cl_2.

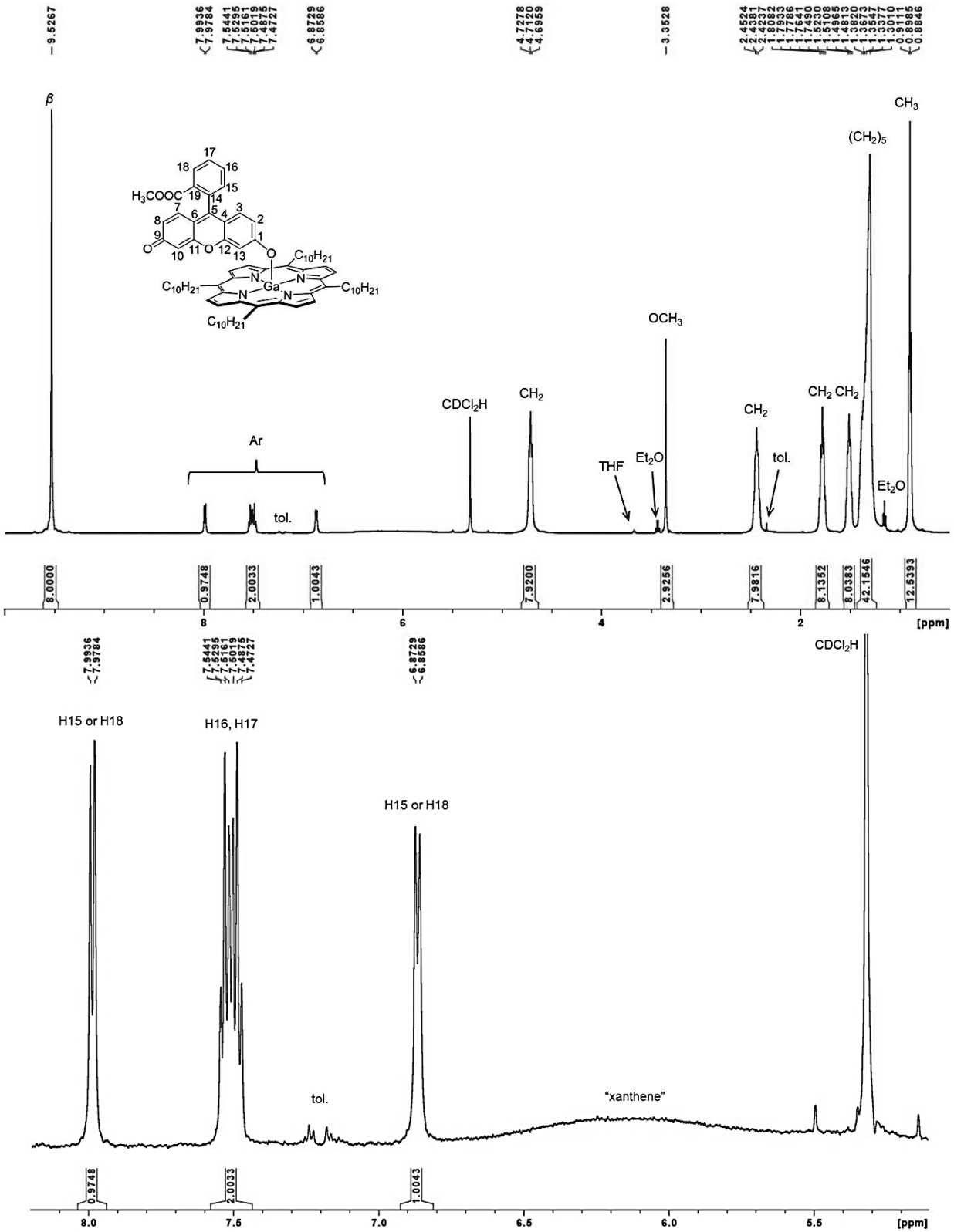

Figure 3.8. ^{1}H NMR spectrum of Ga(TC$_{10}$P)(FME) in CD_2Cl_2. The bottom spectrum is an expansion of the top spectrum. The broad feature (5.60–6.60 ppm) is tentatively attributed to xanthene resonances.

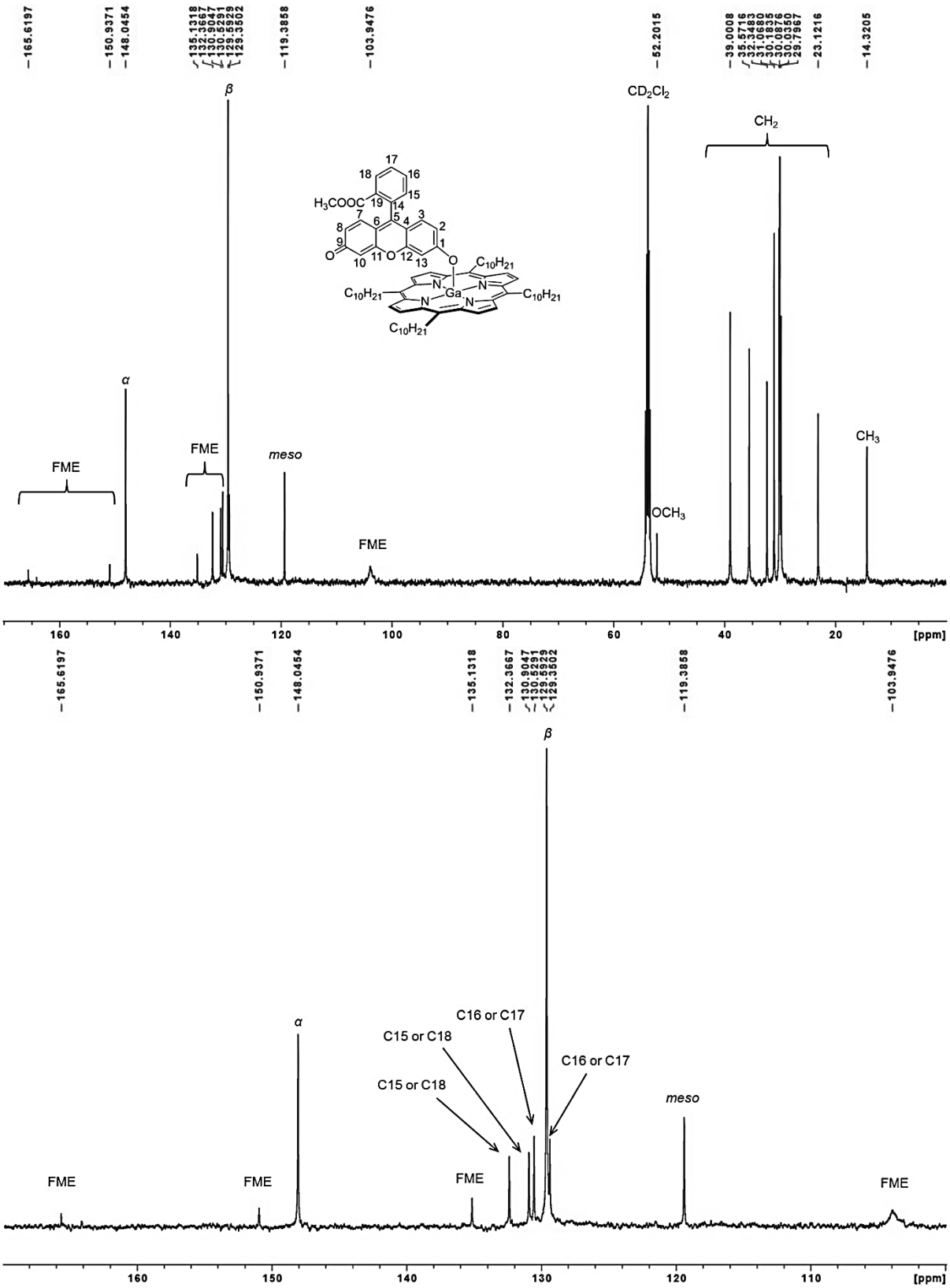

Figure 3.9. $^{13}C\{^{1}H\}$ NMR spectrum of Ga($TC_{10}P$)(FME) in CD_2Cl_2. The bottom spectrum is an expansion of the top spectrum.

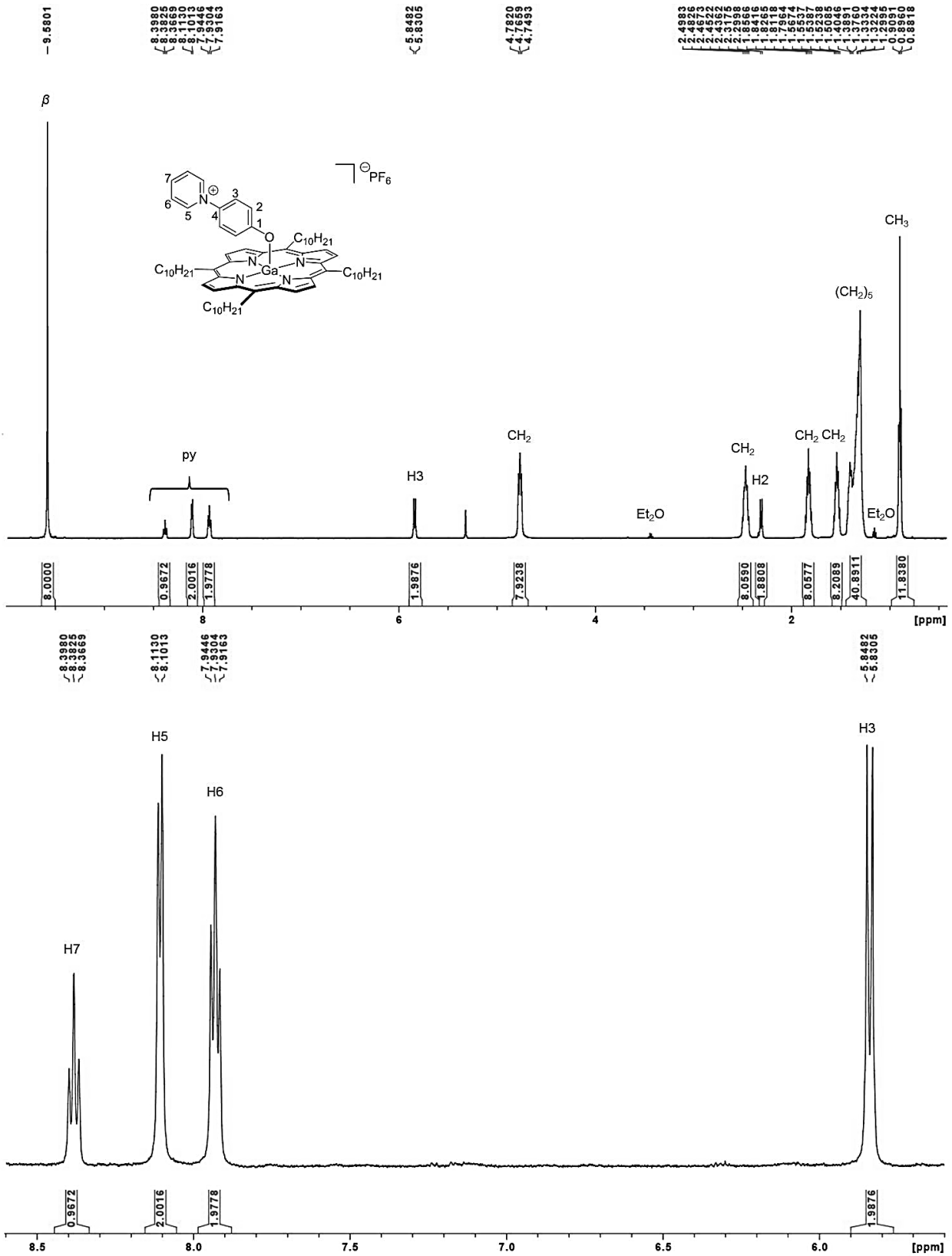

Figure 3.10a,b. ^{1}H NMR spectrum of $[Ga(TC_{10}P)(OC_6H_4py)][PF_6]$ in CD_2Cl_2. The bottom spectrum is an expansion of the top spectrum.

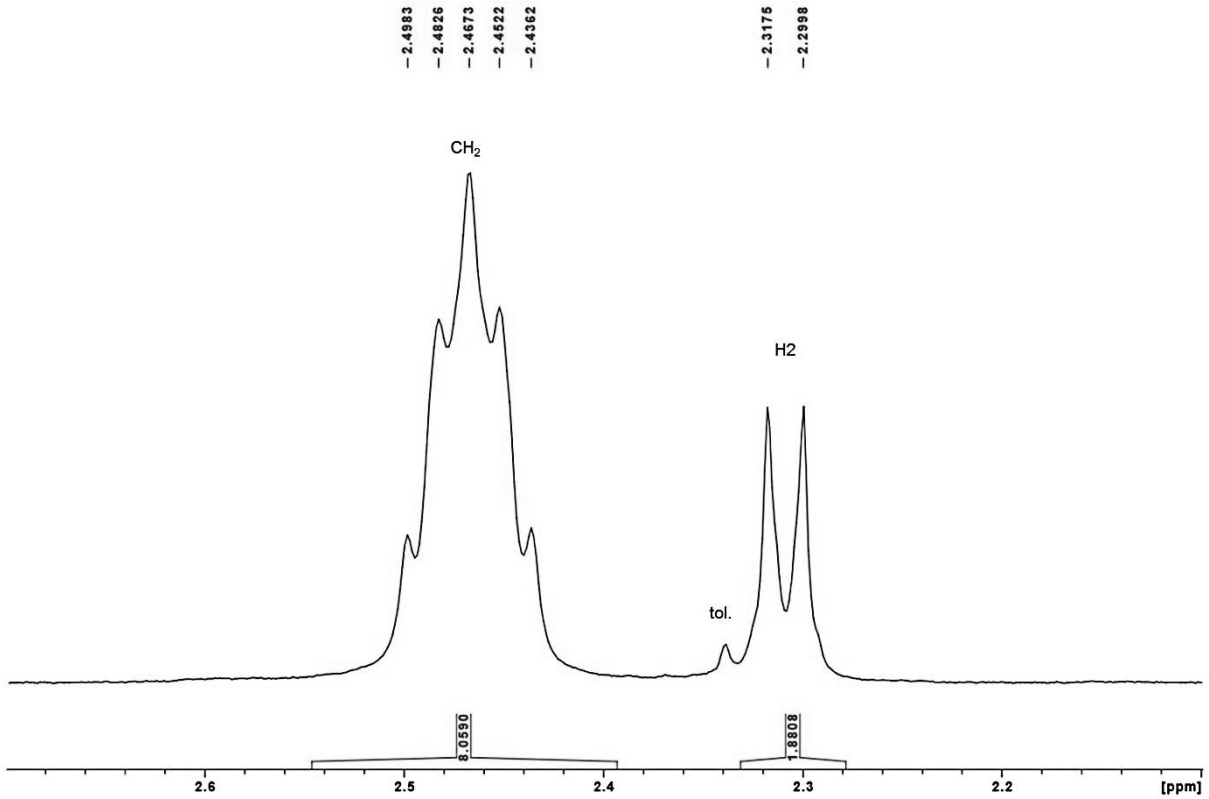

Figure 3.10c. Expansion of the ^{1}H NMR spectrum of $[Ga(TC_{10}P)(OC_6H_4py)][PF_6]$ in CD_2Cl_2 showing the upfield shifted aryl proton resonance.

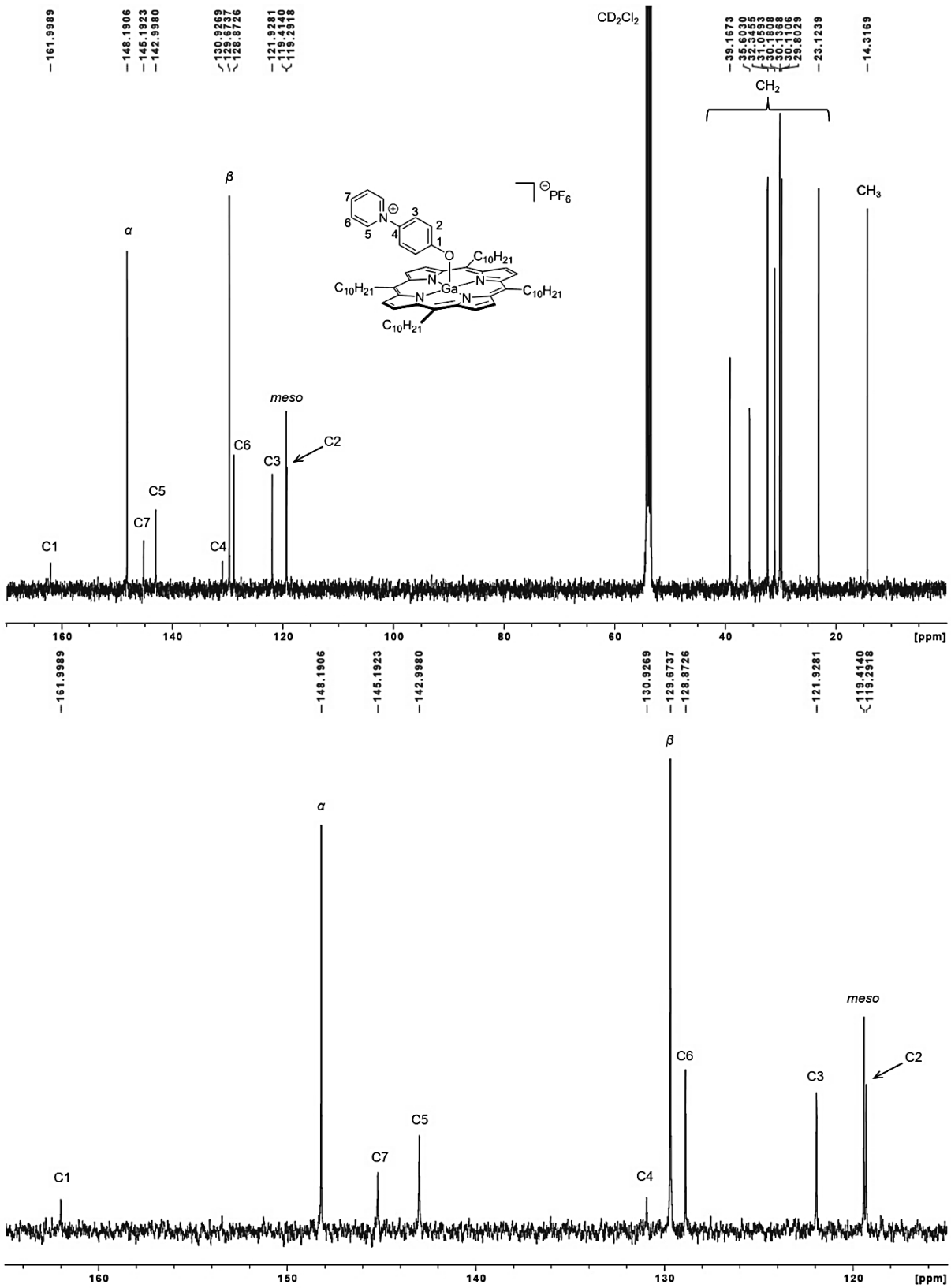

Figure 3.11. $^{13}C\{^{1}H\}$ NMR spectrum of $[Ga(TC_{10}P)(OC_6H_4py)][PF_6]$ in CD_2Cl_2. The bottom spectrum is an expansion of the top spectrum.

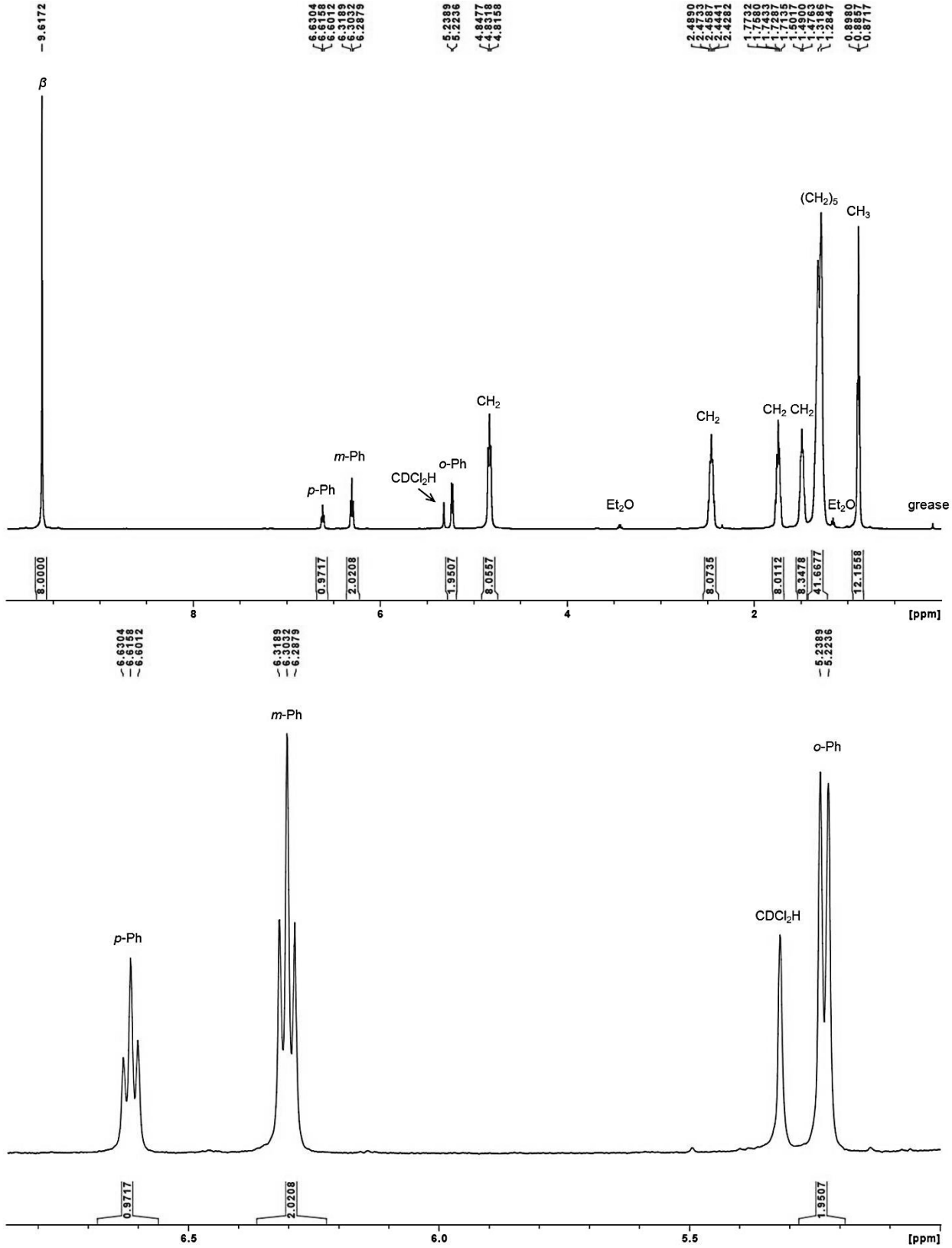

Figure 3.12. ^{1}H NMR spectrum of Ga($TC_{10}P$)(O_2CPh) in CD_2Cl_2. The bottom spectrum is an expansion of the top spectrum.

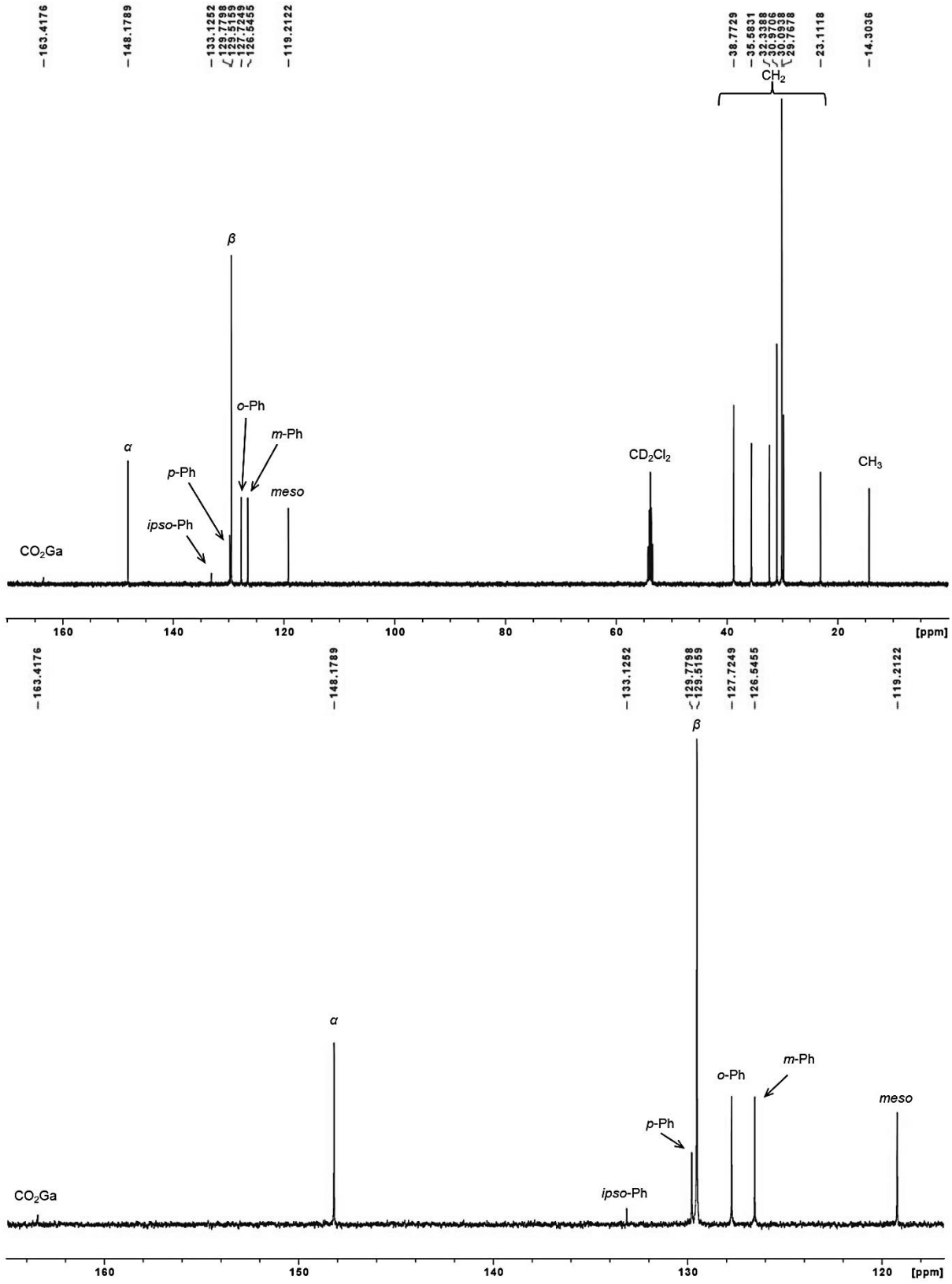

Figure 3.13. $^{13}C\{^{1}H\}$ NMR spectrum of $Ga(TC_{10}P)(O_2CPh)$ in CD_2Cl_2. The bottom spectrum is an expansion of the top spectrum.

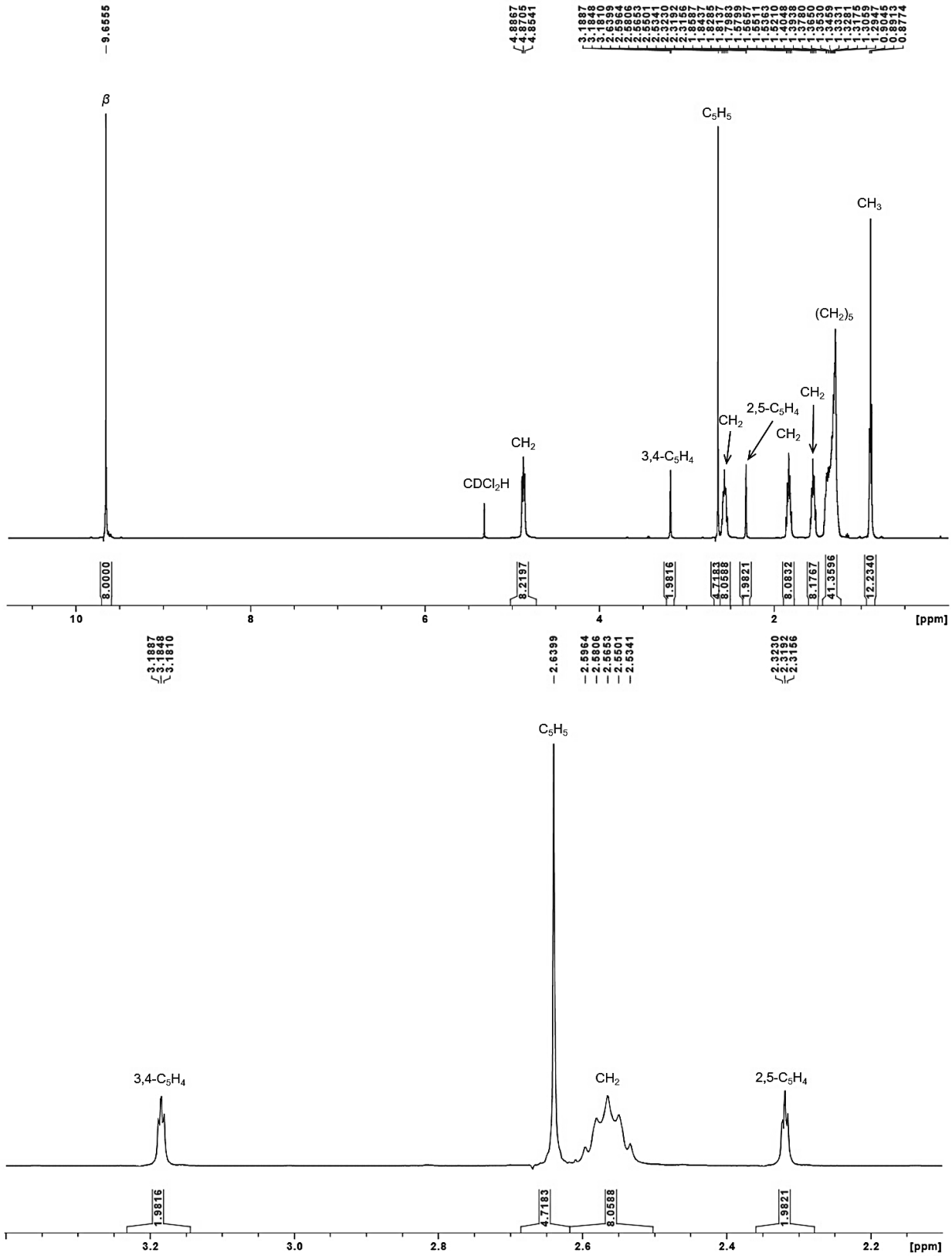

Figure 3.14. ^{1}H NMR spectrum of Ga(TC$_{10}$P)(O$_2$CFc) in CD_2Cl_2. The bottom spectrum is an expansion of the top spectrum.

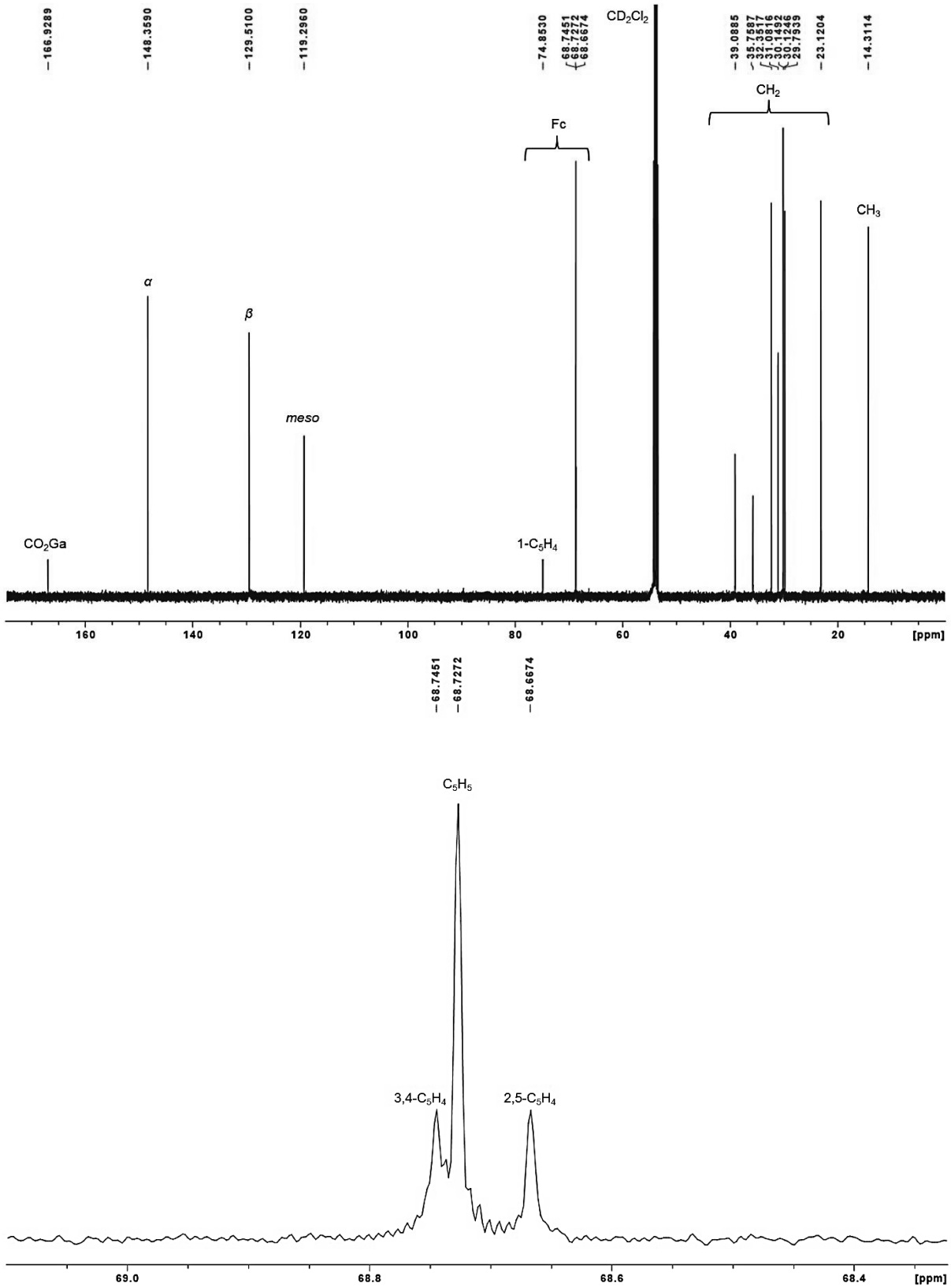

Figure 3.15. $^{13}C\{^{1}H\}$ NMR spectrum of $Ga(TC_{10}P)(O_2CFc)$ in CD_2Cl_2. The bottom spectrum is an expansion of the top spectrum.

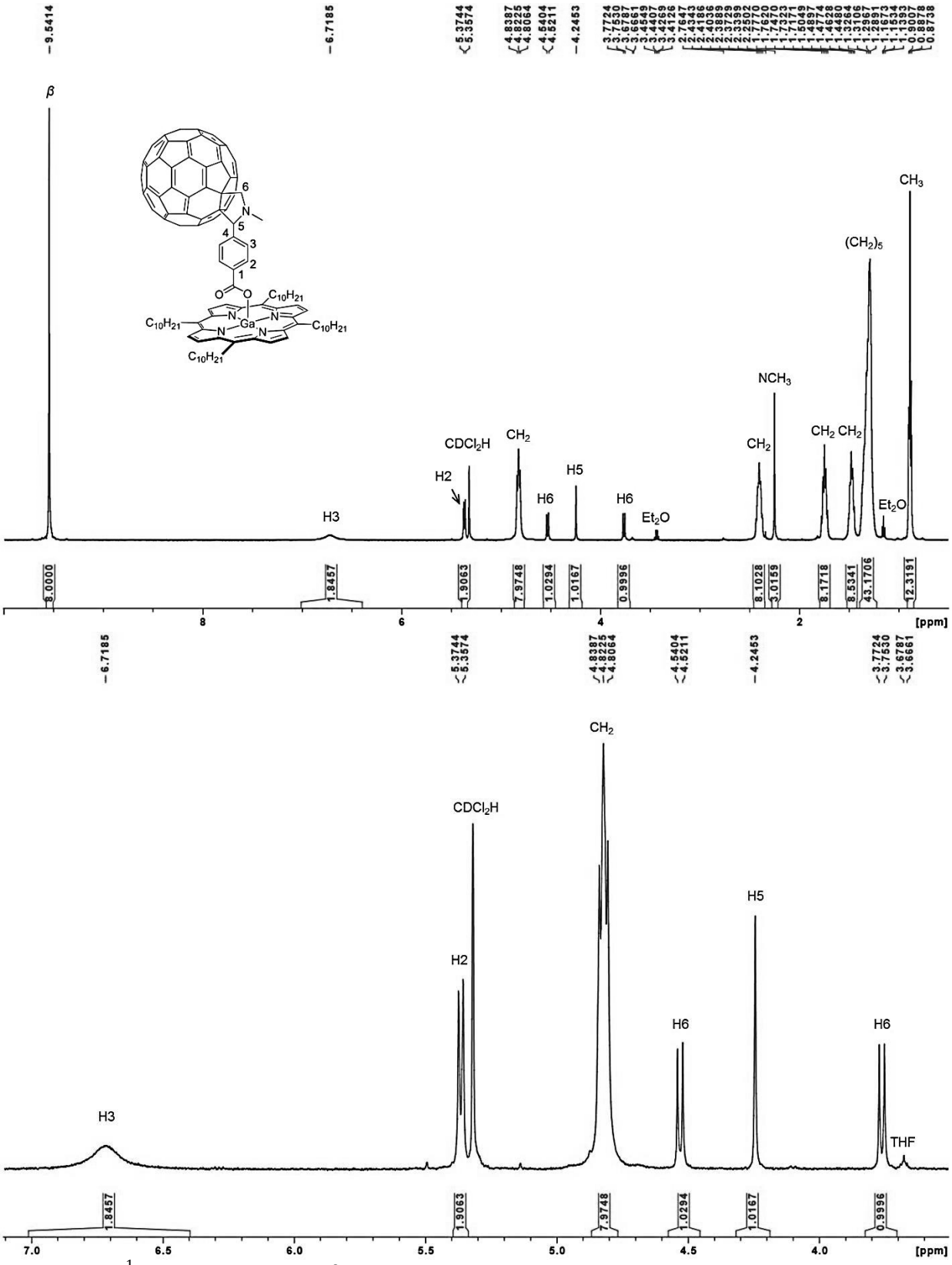

Figure 3.16. ^{1}H NMR spectrum of Ga(TC$_{10}$P)(O$_2$CC$_6$H$_4$pyrC$_{60}$) in CD_2Cl_2. The bottom spectrum is an expansion of the top spectrum.

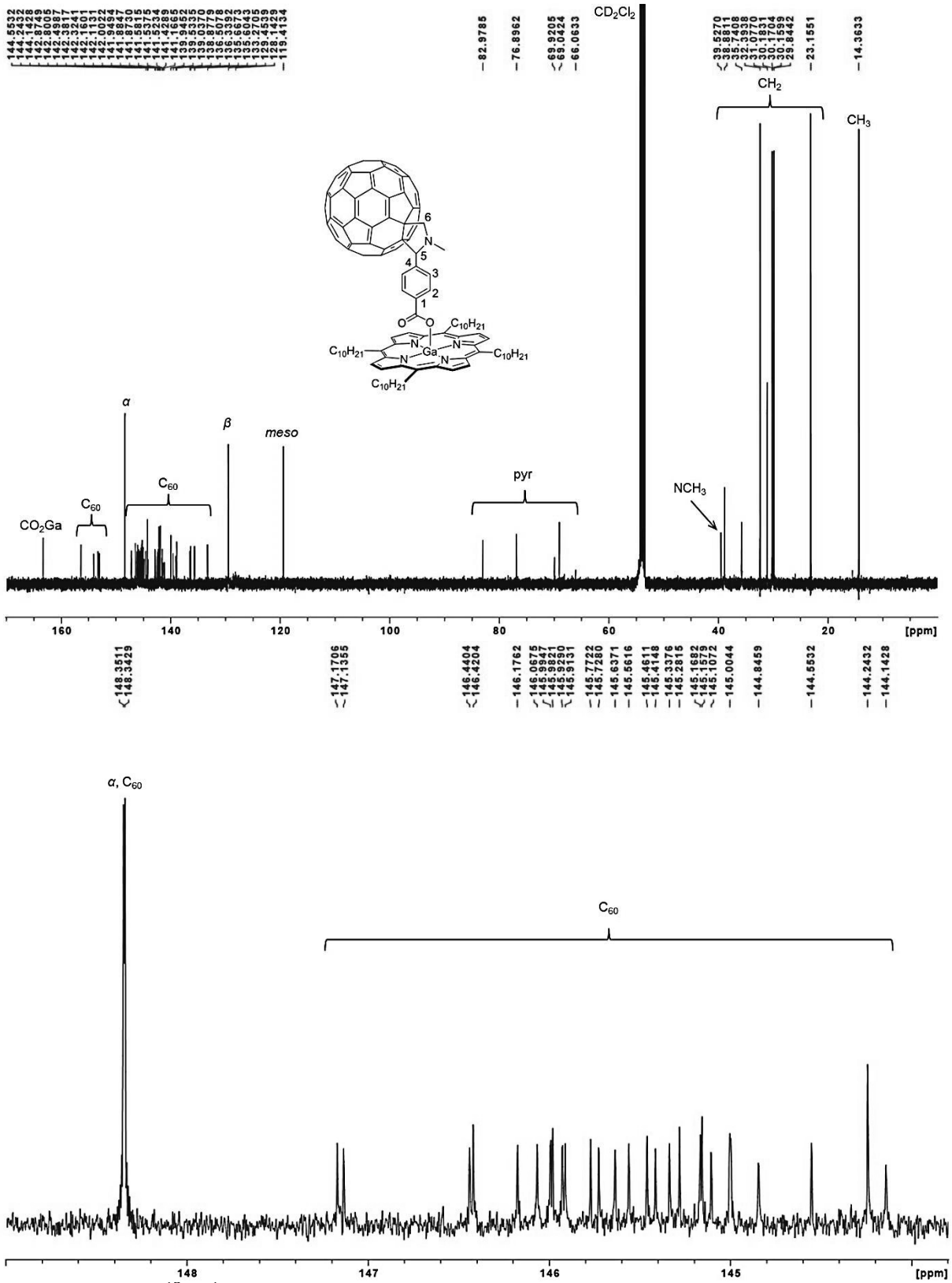

Figure 3.17a,b. $^{13}C\{^{1}H\}$ NMR spectrum of $Ga(TC_{10}P)(O_2CC_6H_4pyrC_{60})$ in CD_2Cl_2. The bottom spectrum is an expansion of the top spectrum.

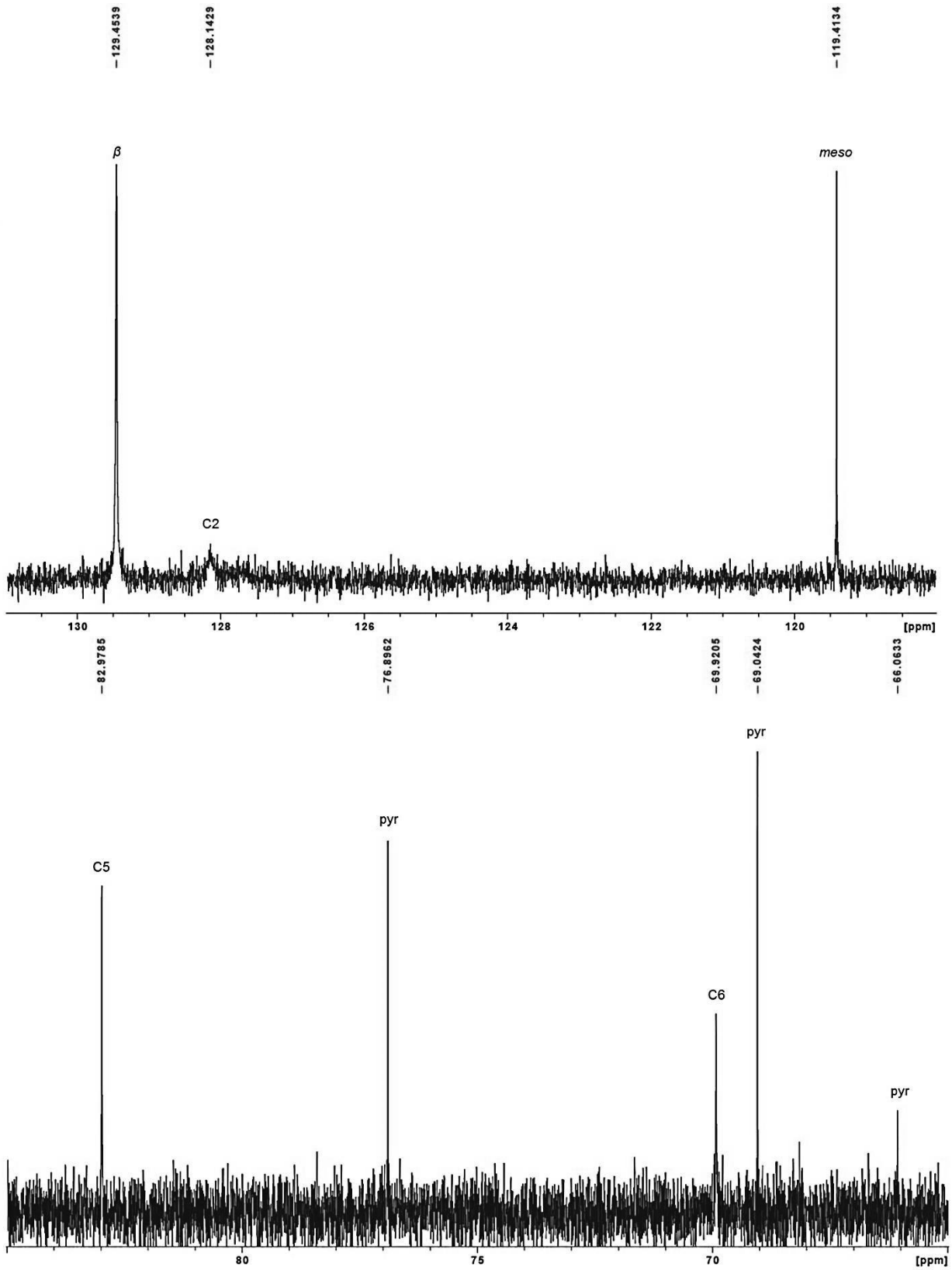

Figure 3.17c,d. Expansions of the $^{13}C\{^{1}H\}$ NMR spectrum of $Ga(TC_{10}P)(O_2CC_6H_4pyrC_{60})$ in CD_2Cl_2.

3.3. Results and Discussion

3.3.1. Synthesis and Characterization of the Functional Ligand $C_{60}pyrC_6H_4CO_2H$.

The synthesis of $Ga(TC_{10}P)(O_2CC_6H_4pyrC_{60})$ required preparation of the precursor carboxylic acid $C_{60}pyrC_6H_4CO_2H$. Although two synthetic procedures for this compound have been previously reported, it was found that a modified procedure provided material better suited to our purposes. The two reported procedures both involve reaction between C_{60}, 4-carboxybenzaldehyde, and sarcosine but use different reaction conditions and starting-material ratios. Hau et al. reported that a mixture of C_{60}, 4-carboxybenzaldehyde, and sarcosine at a 1:5:5 ratio, refluxed in chlorobenzene under argon overnight, provided the product in 95% yield after purification of the crude product via silica gel. The second synthetic procedure was reported by Poddutoori et al.,[17] where the ratio of C_{60}, 4-carboxybenzaldehyde, and sarcosine was reported to be 1:2:5, and the reaction mixture was refluxed in toluene for 2 h under nitrogen with a reported yield of 48% after purification via silica gel chromatography.

Due to the higher reported yield, the preparation of $C_{60}pyrC_6H_4CO_2H$ was first attempted using the Hau procedure, with the only deviation in conditions being that the reaction mixture was refluxed under nitrogen instead of argon. While the reaction mixture did change color from purple to brown as reported, subsequent purification via silica gel chromatography using the reported solvent mixture provided no product. A second attempt using the Poddutoori procedure also provided no product, although unreacted C_{60} was recovered. A third attempt that combined aspects of the two procedures (the ratio of C_{60}, 4-carboxybenzaldehyde, and sarcosine was 1:5:5, per Hau, and the reaction was run overnight in toluene, per Poddutoori) resulted in no product, and no unreacted C_{60} was isolated from the reaction mixture.

An investigation into Prato reaction conditions for other C_{60} derivatives revealed that the use of excess aldehyde can result in the formation of polyadducts,[48-51] and that this may have been occurring in our attempts to repeat the Hau and Poddutoori procedures, which call for the use of excess aldehyde. For example, preparations of $C_{60}pyrC_6H_4CCSi(CH_3)_3$ note specifically that stoichiometric[52] or substoichiometric[53] amounts of the 4-(2-trimethylsilylethynyl)benzaldehyde are used in its preparation, rather than the excess quantities referred to above. Similarly, a recent paper by Erten-Ela et al.[54] reported the preparation of a benzoic acid fullerene bisadduct from C_{60} and 4-carboxybenzaldehyde in a 1:2 ratio. Based on these observations, the procedure reported by Hau was modified by reducing the C_{60}:4-carboxybenzaldehyde ratio to 1:1. The change in the reactant ratio resulted in the successful preparation of $C_{60}pyrC_6H_4CO_2H$ with a 23% yield. The identity and purity of the product were confirmed by LDI-TOF-MS and ^{1}H NMR spectroscopy, with the latter providing chemical shifts identical to those reported by Poddutoori et al.

3.3.2. Synthesis and Characterization of Ga($TC_{10}P$)(O_2CR) Complexes. The reactions between Ga($TC_{10}P$)(OH) and carboxylic acids were initially investigated by NMR-scale test reactions, in which the carboxylic acids (benzoic acid, $FcCO_2H$, and $C_{60}pyrC_6H_4CO_2H$) were added to a Ga($TC_{10}P$)(OH) solution in C_6D_6 and allowed to react at room temperature in air. The formation of the corresponding Ga($TC_{10}P$)(O_2CR) complexes was complete within ~5 minutes, as shown in the first ^{1}H NMR spectra recorded after the initial addition of the free ligands. The products were identified by the appearance of $O_2C\underline{R}$ ligand resonances with characteristic upfield shifts due to porphyrin ring-current effects[55] (Table 3.3), and the completion of the reactions was indicated by the presence of a single set of porphyrinic *β*-H and meso α-CH_2 resonances that are easily distinguishable from those of Ga($TC_{10}P$)(OH). The preparation of the Ga($TC_{10}P$)(O_2CR)

complexes in minutes at room temperature is in contrast to the reported procedures for the preparation of the analogous Al(Por)(O_2CR) complexes Al(TPP)(O_2CPh) and Al(TPP)($O_2CC_6H_4pyrC_{60}$), both of which are reported to require reflux conditions for extended reaction times under inert conditions.[17]

Table 3.3. Selected ^{1}H NMR Chemical Shifts of Ga($TC_{10}P$)(OH) and Ga($TC_{10}P$)(O_2CR) Complexes in C_6D_6.

	β	α-CH_2	($\underline{R}CO_2$)Ga($TC_{10}P$)[a]	$\underline{R}CO_2H$[b]
Ga($TC_{10}P$)(OH)	9.55	4.81	-	-
Ga($TC_{10}P$)(O_2CPh)	9.59	4.81	6.28 (t, 1H, *p*-Ph)	8.10 (d, 2H, *o*-Ph)
			6.05 (m, 2H, *m*-Ph)	7.07 (t, 1H, *p*-Ph)
			5.87 (d, 2H, *o*-Ph)	6.98 (m, 2H, *m*-Ph)
Ga($TC_{10}P$)(O_2CFc)	9.63	4.87	3.02 (m, 2H, 3,4-C_5H_4)	4.86 (m, 2H, C_5H_4)
			2.81 (s, 5H, C_5H_5)	4.01 (m, 2H, C_5H_4)
			2.79 (m, 2H, 2,5-C_5H_4)	3.97 (s, 5H, C_5H_5)
Ga($TC_{10}P$)($O_2CC_6H_4pyrC_{60}$)	9.47	4.79	6.63 (br s, 2H, H3)	8.03 (d, 2H, H2)
			6.05 (d, 2H, H2)	7.94 (br s, 2H, H3)
			4.05 (d, 1H, H6)	5.22 (s, 1H, H5)
			3.93 (s, 1H, H5)	5.10 (d, 1H, H6)
			3.32 (d, 1H, H6)	4.34 (d, 1H, H6)
			1.87 (s, 3H, NCH_3)	2.75 (s, 3H, NCH_3)

[a] Assigned based on spectra recorded in CD_2Cl_2. [b] $C_{60}pyrC_6H_4CO_2H$ resonances not observed in C_6D_6 due to low solubility; values reported for spectrum recorded in DMSO-d_6.

The facile synthesis of the Ga($TC_{10}P$)(O_2CR) complexes observed at the NMR scale was also found in preparatory scale reactions. The syntheses of Ga($TC_{10}P$)(O_2CPh) and

Ga($TC_{10}P$)(O_2CFc) were achieved by reacting Ga($TC_{10}P$)(OH) with slight excesses of the corresponding carboxylic acids (1.3 equiv. of benzoic acid, 1.1 equiv. of $FcCO_2H$) in toluene. Since the effect of reactant concentration on reaction rate was not determined in the NMR-scale reactions, the preparatory-scale reactions were allowed to run for 15 min to ensure completion; this was evidenced by the absence of resonances due to Ga($TC_{10}P$)(OH) starting material in the ^{1}H NMR spectrum of the crude product. Purification of the dyads was achieved by taking advantage of the disparity between the solubility of the dyad molecules and the unreacted carboxylic acids in acetonitrile. The yields of these products were reasonable (Ga($TC_{10}P$)(O_2CPh): 75%; Ga($TC_{10}P$)(O_2CFc): 65%). Their composition and purity were established by ^{1}H NMR, $^{13}C\{^1H\}$ NMR, LDI-MS and CHN elemental analysis.

Ga($TC_{10}P$)($O_2CC_6H_4pyrC_{60}$) was prepared using the same general procedure, but due to the small quantity of free ligand available an excess could not be used. In practice, at this small scale, inaccuracies in weighing the reagents resulted in Ga($TC_{10}P$)(OH) being present in a slight excess. The removal of unreacted Ga($TC_{10}P$)(OH) required an alternative purification procedure, because precipitation of the product from THF/acetonitrile or diethyl ether/acetonitrile also induced the precipitation of unreacted Ga($TC_{10}P$)(OH). Instead, the compound was purified by taking advantage of the fact that the solubility of Ga($TC_{10}P$)($O_2CC_6H_4pyrC_{60}$) in hexanes is lower than that of Ga($TC_{10}P$)(OH); this allowed isolation of Ga($TC_{10}P$)(OH) from the product from layered toluene:hexanes (1:6 by volume) at –20 ^{0}C. The product was obtained in 77% yield, which was reduced from a crude yield of 95%. The composition of the compound was established by ^{1}H NMR, $^{13}C\{^1H\}$ NMR, and CHN elemental analysis. One complication in analyzing Ga($TC_{10}P$)($O_2CC_6H_4pyrC_{60}$) was that the mass spectrum did not exhibit the molecular ion peak. Furthermore, the mass spectrum obtained for this complex was obscured by the

fragmentation pattern attributed to the free fullerene. The possibility that free C_{60} is present as an appreciable impurity is excluded by the fact that the elemental analysis in good agreement with expected values. It seems likely that the observed C_{60} LDI-MS peak is a product of the ionization process; indeed, MALDI experiments carried out with monofunctionalized fullerene derivatives revealed the formation of bisadducts, which were hypothesized to be result of a retro-cycloaddition process that also resulted in the simultaneous formation of unsubstituted C_{60}.[56]

3.3.3. Synthesis and Characterization of Ga(TC_{10}P)(OPh), Ga(TC_{10}P)(FME), and [Ga(TC_{10}P)(OC_6H_4py)][PF_6]. The reactivity of Ga(TC_{10}P)(OH) with phenol was investigated on the NMR scale in C_6D_6. The reaction was found to be much slower than those between Ga(TC_{10}P)(OH) and carboxylic acids. The NMR spectra of the reaction between Ga(TC_{10}P)(OH) and phenol (~7 equiv.) recorded at 5, 30, and 60 minutes from the start of the reaction are presented in Figure 3.18. Several resonances were diagnostic for monitoring the reaction (Table 3.4): the β resonances of Ga(TC_{10}P)(OPh) (9.53 ppm) and Ga(TC_{10}P)(OH) (shifted from 9.55 ppm to 9.53 ppm after the addition of phenol), the upfield-shifted aryl resonances of the bound ligand (2.86 ppm, 5.89–5.97 ppm), and the OH resonance of Ga(TC_{10}P)(OH) at –6.41 ppm.

Within 5 min of the addition of phenol, the β resonance of Ga(TC_{10}P)(OH) is observed to be weak relative to that of Ga(TC_{10})(OPh), whose presence was further confirmed by the appearance of upfield shifted aryl proton resonances. At 30 min, the β resonance of Ga(TC_{10}P)(OH) had weakened further in intensity relative to the product, and at 60 min it was absent. Interestingly, the OH resonance of Ga(TC_{10}P)(OH) at –6.41 ppm was not observed after the addition of phenol, even though Ga(TC_{10}P)(OH) is still present. This is possibly due to hydrogen bonding between Ga-OH moiety and phenol, the OH resonance of which was also broad at 5 min but gradual sharpened as the reaction progressed.

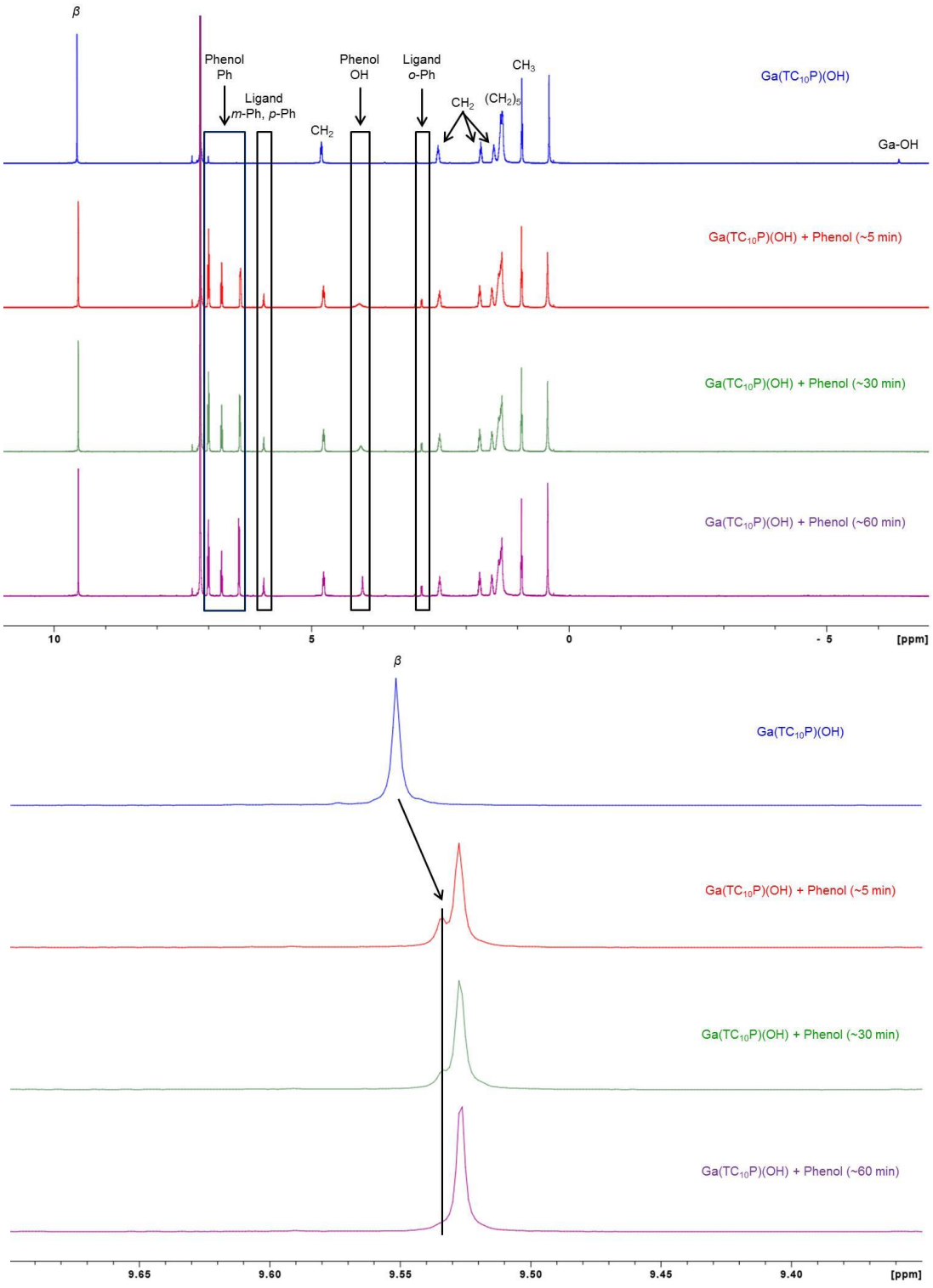

Figure 3.18. ^{1}H NMR spectra of the NMR-scale reaction between Ga($TC_{10}P$)(OH) and phenol in C_6D_6. The top spectrum shows the rapid appearance of shifted aryl proton resonances of the bound ligand. The bottom panel shows the disappearance of Ga($TC_{10}P$)(OH) β proton resonance over time.

In addition to changes in resonances corresponding to the porphyrin core and the ligand over the course of the reaction, the integration of the H_2O resonance is also expected to increase because H_2O is a byproduct of the reaction. When comparing the integration of the H_2O resonance relative to the total integration of β proton resonances (8), its integration was observed to increase from 13.18 before the addition of phenol (arising from adventitious water in the NMR solvent) to 15.53 in the spectrum recorded 60 min after the addition of phenol. Since the total amount of porphyrin in solution was constant, an increase of the integration by ~2 corresponds to the generation of 1 equivalent of H_2O for the formation of each equivalent of Ga(TC_{10}P)(OPh). These observations indicate that the reaction between Ga(TC_{10}P)(OH) and phenol could readily occur in air at room temperature.

The reactivity between Ga(TC_{10}P)(OH) and FME-H to form Ga(TC_{10}P)(FME) was also studied on the NMR scale. Several resonances were diagnostic for monitoring the reaction (Table 3.4): the β proton resonances of both Ga(TC_{10})(FME) (9.49 ppm) and Ga(TC_{10}P)(OH) (shifted from 9.55 ppm to 9.53 ppm after the addition of FME-H), the α-CH_2 resonances of both complexes (Ga(TC_{10}P)(OH): 4.81 ppm; Ga(TC_{10}P)(FME): 4.70 ppm), the FME ligand proton resonances (2.01, 2.96, 5.32, 6.20, 6.37, 6.53, 6.53, 6.65, 6.74–6.86, 7.80 ppm), and the OH resonance of Ga(TC_{10}P)(OH) at –6.41 ppm (not observed after the addition of FME-H).

Although FME-H is not soluble in C_6D_6, proton resonances attributable to a bound FME ligand were observed within 5 min after the addition of FME-H to a Ga(TC_{10}P)(OH) solution in C_6D_6. As shown by ^{1}H NMR spectra recorded at 5 min, 30 min, and 75 min after the addition of FME-H to the NMR sample (Figure 3.19), the reaction between Ga(TC_{10}P)(OH) and FME also proceeded within a similar time scale in C_6D_6 when compared to the formation of Ga(TC_{10}P)(OPh) (complete in ~75 minutes). The integration of the H_2O resonance was observed

to increase from 4.08 before the addition of FME to 6.30 in the spectrum recorded 75 min after the addition of FME, which corresponds to the generation of 1 equivalent of H_2O per 1 equivalent of Ga($TC_{10}P$)(FME) formed.

Table 3.4. Selected ^{1}H NMR Chemical Shifts of Ga($TC_{10}P$)(OH) and Ga($TC_{10}P$)(OR) Complexes in C_6D_6.

	β	α-CH_2	(R<u>O</u>)Ga($TC_{10}P$)[a]	R<u>O</u>H[b]
Ga($TC_{10}P$)(OH)	9.55	4.81	-	-
Ga($TC_{10}P$)(OPh)	9.53	4.76	5.89–5.97 (m, 3H, *m*-Ph and *p*-Ph)	7.00 (m, 2H, *m*-Ph)
			2.86 (d, 2H, *o*-Ph)	6.74 (t, 1H, *p*-Ph)
				6.41 (d, 2H, *o*-Ph)
Ga($TC_{10}P$)(FME)[c]	9.49	4.70	7.80 (d, 1H, H15 or H18)	8.20 (d, 1H)
			6.74–6.86 (m, 2H, H16 and H17)	7.86 (m, 1H)
			6.65 (br s, 1H)	7.77 (m, 1H)
			6.53 (br s, 1H)	7.49 (d, 1H)
			6.37 (br s, 1H)	6.05–7.01 (m, 6H)
			6.20 (d, 1H, H15 or H18)	3.58 (s, 3H)
			5.32 (br s, 1H)	
			2.96 (s, 3H, OCH_3)	
			2.01 (br s, 1H)	

[a] Assigned based on spectra obtained in CD_2Cl_2. [b] FME-H values obtained from a spectrum recorded in DMSO-d_6 due to insolubility in C_6D_6. [c] Broad peaks only observed during reaction; see Figure 3.21.

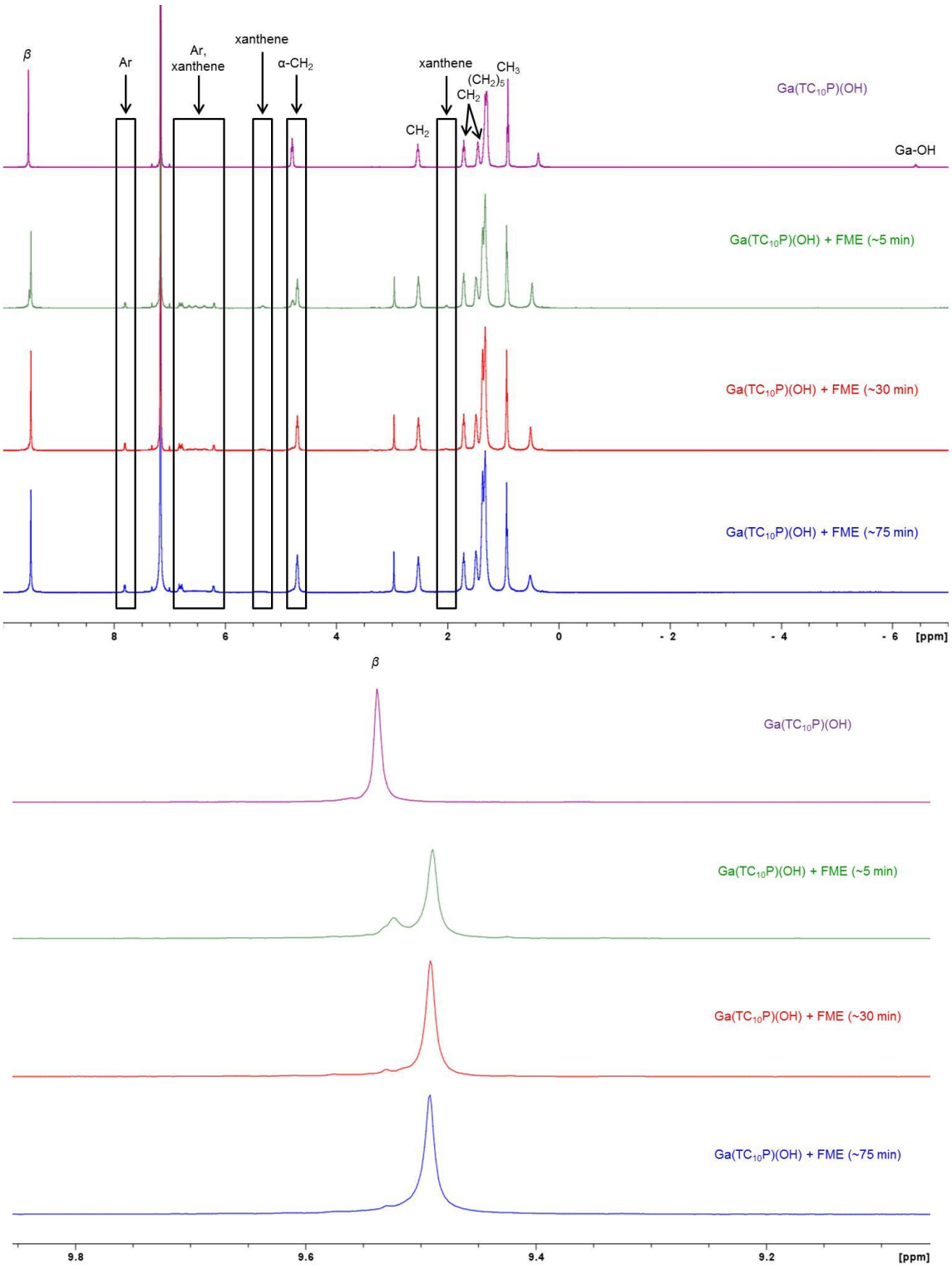

Figure 3.19a,b. ^{1}H NMR spectra of the NMR-scale reaction between Ga($TC_{10}P$)(OH) and FME-H in C_6D_6. The top spectrum shows the rapid appearance of shifted aryl proton resonances of the bound FME ligand. The bottom panel shows the disappearance of Ga($TC_{10}P$)(OH) β proton resonance over time.

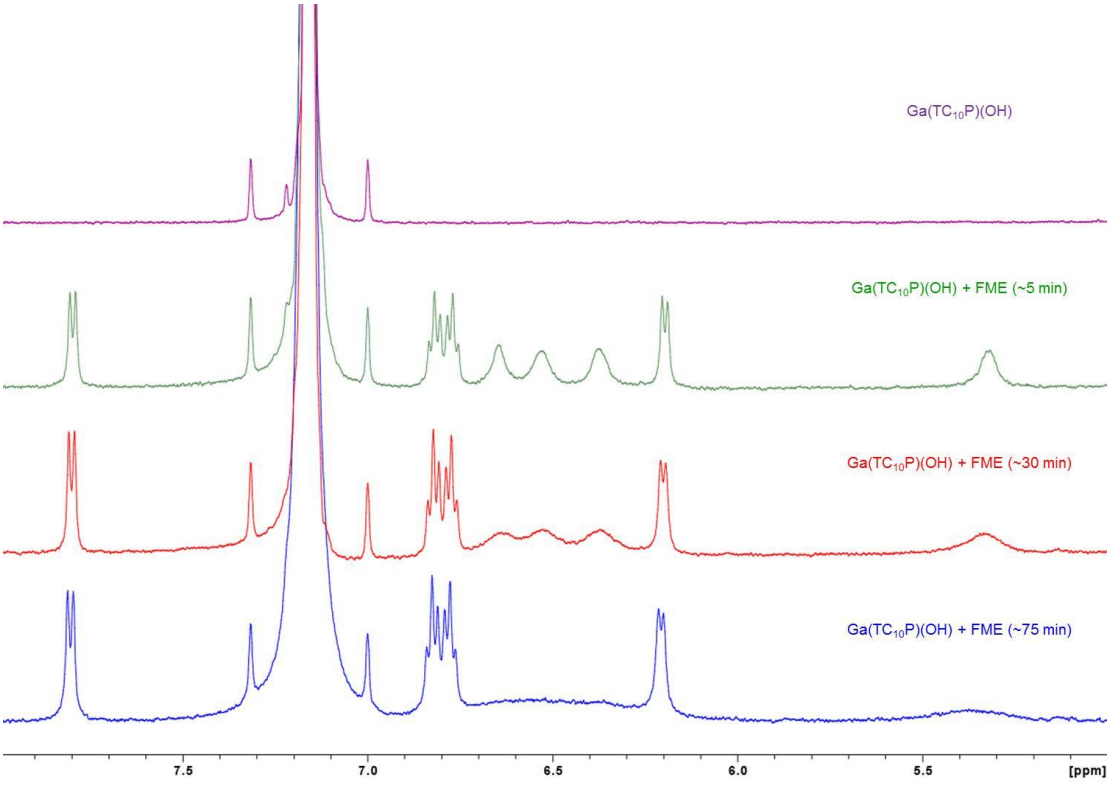

Figure 3.19c. An expansion of the aryl region of the ^{1}H NMR spectra of the NMR-scale reaction between Ga($TC_{10}P$)(OH) and FME-H in C_6D_6. The gradual broadening of the xanthene proton resonances of Ga($TC_{10}P$)(FME) over the course of the reaction is observed; see discussion in Section 3.3.4.

From the results of the NMR-scale reactions between Ga($TC_{10}P$)(OH) and aryl alcohols, it was determined that the reactions rates are slower than those of reactions between Ga($TC_{10}P$)(OH) and carboxylic acids. The difference in reactivity between carboxylic acids and aryl alcohols with M(porphyrin)(OH) derivatives has been noted by Lazarides et al. in their report on the synthesis of Sn(porphyrin)X_2 complexes, where reactions between Sn(TPP)$(OH)_2$ and aryl alcohols required higher reaction temperatures (~60 °C for aryl alcohols; room temperature for carboxylic acids) and longer reaction times (5–12 h for aryl alcohols; 30 min to 2 h for carboxylic acids) than reactions with carboxylic acids.[31]

Based on the results of the test reactions, Ga($TC_{10}P$)(OPh) was synthesized on a preparative scale in air at room temperature in toluene. Only a small excess of the alcohol forms

of the ligands were used for the reactions, although the reaction times were increased to 1.5 h to ensure complete formation of the products, which was confirmed by ^{1}H NMR spectra of the crude products. Due to the high solubility of phenol in acetonitrile the purification of Ga(TC$_{10}$P)(OPh) was achieved by dissolving the crude product in a mixture of THF and acetonitrile and reducing the solvent volume *in vacuo* to induce precipitation of pure compound. On the other hand, the purification of Ga(TC$_{10}$P)(FME) was easily achieved by filtering the reaction mixture to remove the unreacted FME-H since it is insoluble in toluene. Both complexes were prepared in high yield (Ga(TC$_{10}$P)(OPh): 95%; Ga(TC$_{10}$P)(FME): 91%), and their compositions were established by ^{1}H NMR and ^{13}C{^{1}H} NMR. Ga(TC$_{10}$P)(OPh) was further characterized by CHN elemental analysis.

The synthesis of [Ga(TC$_{10}$P)(OC$_6$H$_4$py)][PF$_6$] required reaction conditions different from those of the other aryloxide complexes. Attempts to prepare the complex using the procedure for Ga(TC$_{10}$P)(OPh) and Ga(TC$_{10}$P)(FME) resulted in the reaction of approximately 20% of the starting Ga(TC$_{10}$P)(OH), as shown by ^{1}H NMR spectra of the reaction mixtures, and neither increasing the reaction time from 1.5 h to 3 h nor heating the reaction mixture to reflux increased the yield. The reaction solvent was subsequently changed from toluene to a mixture of toluene and acetonitrile (1:1 by volume) in order to increase the solubility of [HOC$_6$H$_4$py][PF$_6$], which resulted in final reaction mixture with a 95:5 ratio of product to unreacted Ga(TC$_{10}$P)(OH) after 2 h at room temperature. While the unreacted Ga(TC$_{10}$P)(OH) could be partially removed by washing the crude product with hexanes, purification of [Ga(TC$_{10}$P)(OC$_6$H$_4$py)][PF$_6$] was only successfully obtained by layering a toluene solution of the crude product with hexamethyldisiloxane. This resulted in a reduction of yield of the product to 25% due to its unusual solubility in the nonpolar solvent mixture; reports of hexafluorophosphate organic salts

soluble in hydrocarbon solvents have largely been limited to ionic liquids.[57] The composition was established by ^{1}H NMR, ^{13}C{^{1}H} NMR, ^{31}P{^{1}H} NMR, and LDI-MS. While the preparation and purification procedure of [Ga($TC_{10}P$)(OC_6H_4py)][PF_6] have yet to be optimized, the successful preparation of this complex demonstrates the feasibility of preparing ionic Ga-porphyrin complexes.

3.3.4. Unusual NMR-Spectroscopic Features of Ga($TC_{10}P$)(OR) and Ga($TC_{10}P$)(O_2CR) Compounds. For all Ga($TC_{10}P$)(OR) and Ga($TC_{10}P$)(O_2CR) complexes, a characteristic feature of the ^{1}H NMR spectra is that the OR and O_2CR resonances are shifted upfield relative to those of the acid forms of the free ligands. This is a consequence of their close proximity to the porphyrin ring and its associated ring current;[55] more pronounced upfield shifts are observed for protons that are closer to the porphyrin core, as has been observed for other axially substituted porphyrin compounds.[23, 31] For example, the phenyl proton resonances of Ga($TC_{10}P$)(O_2CPh) are found at 5.87 ppm (*o*-Ph), 6.05 ppm (*m*-Ph), and 6.28 (*p*-Ph) in C_6D_6 (Table 3.3), whereas the corresponding resonances of benzoic acid are found at 8.10 ppm, 6.98 ppm, and 7.07 ppm; the magnitudes of the upfield shifting of resonances (Δδ: *o*-Ph: 2.33 ppm; *m*-Ph: 0.93 ppm; *p*-Ph: 0.79 ppm) clearly shows that the protons that are closer to the porphyrin core experience greater shielding. For Ga($TC_{10}P$)(OPh), the upfield shifts of ligand resonances (Δδ: *o*-Ph: 3.55 ppm; *m*-Ph: ~1.07 ppm; *p*-Ph: ~0.81 ppm; the latter two values are measured with respect to the center of the *m*-Ph and *p*-Ph multiplet at 5.89–5.97 ppm) are greater compared to Ga($TC_{10}P$)(O_2CPh) due to the reduced distance between the ligand and the porphyrin core.

All ^{1}H-NMR resonances of the axial ligands are observed for all complexes except Ga($TC_{10}P$)(FME). In the NMR-scale reaction (Figure 3.21), five of the six xanthene resonances of the FME ligand could be observed ~5 min after the addition of FME-H to a Ga($TC_{10}P$)(OH)

solution in C_6D_6 as broad singlets (6.65, 6.53, 6.37, 5.32, and 2.01 ppm; the sixth resonance likely overlaps with the C_6D_6 solvent resonance). These resonances broadened over the course of the reaction, and could not be resolved upon reaction completion. In contrast, the resonances of the methyl benzoate moiety at 7.80 ppm, 6.74–6.86 ppm, 6.20 ppm, and 2.96 ppm, which were used to confirm the attachment of FME, remained sharp and well-resolved. The line broadening of xanthene core resonances was also observed in the ^{1}H NMR spectrum of the purified compound recorded in CD_2Cl_2, which suggested that this observation was not solvent dependent or due to the presence of suspended solid (FME-H) in solution. Similarly, only 9 of the 21 chemical shifts expected for the FME ligand in the $^{13}C\{^{1}H\}$ NMR spectrum could be observed; 5 of 9 were assigned to carbons of the aryl ester moiety on the basis of the HMQC spectrum. Due to the observation that the xanthene proton resonances were better resolved at the onset of the NMR-scale reaction, where the solvent temperature was elevated due to the exothermic nature of the reaction, the broadening of xanthene resonances is tentatively attributed to structural anisotropy and slow rotation of the FME ligand.[58]

For $Ga(TC_{10}P)(O_2CC_6H_4pyrC_{60})$, ligand attachment was confirmed by the appearance of the resonances pertaining to the aryl and pyrrolidinyl moieties in the ^{1}H NMR spectrum but the $^{13}C\{^{1}H\}$ NMR spectrum could not be fully assigned due to the large number of inequivalent fullerene resonances that resulted from the attachment of the Prato adduct. However, pertinent features of $Ga(TC_{10}P)(O_2CC_6H_4pyrC_{60})$, such as the aryl and pyrrolidinyl resonances, could be identified on the basis of the HMQC spectrum.

3.3.5. Physical Characterization of $Ga(TC_{10}P)(OR)$ and $Ga(TC_{10}P)(O_2CR)$ Complexes. UV-vis absorption spectra of $Ga(TC_{10}P)(OH)$, $Ga(TC_{10}P)(OR)$, and $Ga(TC_{10}P)(O_2CR)$ complexes are shown in Figures 3.20 and 3.21, and are summarized in Table

3.5. The spectra of $Ga(TC_{10}P)(OH)$, $Ga(TC_{10}P)(OPh)$, $Ga(TC_{10}P)(O_2CPh)$, and $Ga(TC_{10}P)(O_2CFc)$ exhibit typical metalloporphyrin absorption bands, with a strong Soret band at ~420 nm, and two Q-bands at ~560 nm and ~600 nm. While ferrocene also exhibits absorption bands in the visible wavelength region, the extinction coefficient of the stronges absorption band at 440 nm is 91 $M^{-1}cm^{-1}$ in toluene,[59] which is negligible when compared to the extinction coefficients of the porphyrin absorption bands (Soret: ~10^5 $M^{-1}cm^{-1}$; Q: ~10^4 $M^{-1}cm^{-1}$). As a result, the band maxima and relative intensities of $Ga(TC_{10}P)(O_2CFc)$ and $Ga(TC_{10}P)(O_2CPh)$ are essentially identical (Table 3.5).

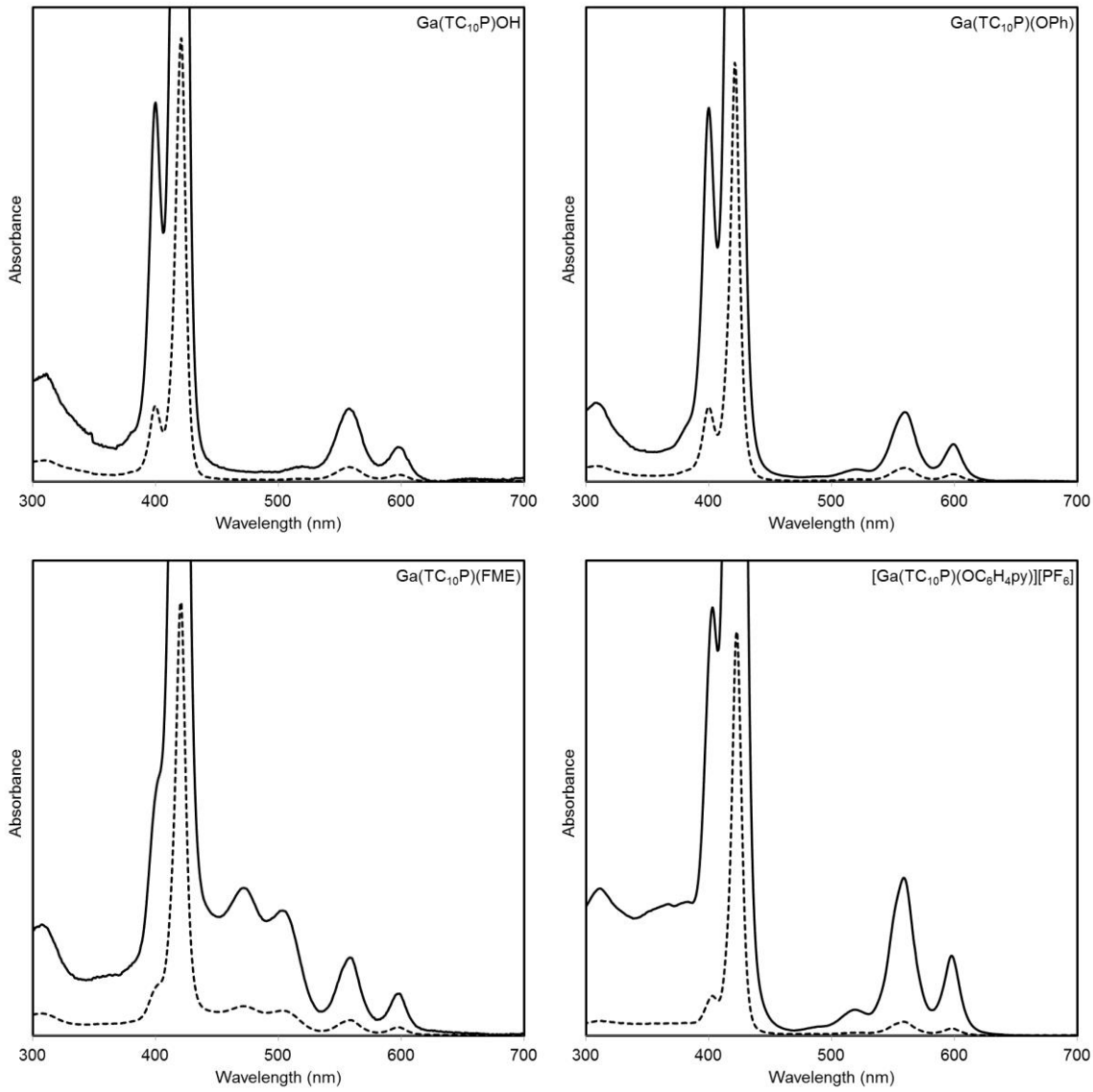

Figure 3.20. Electronic-absorption spectra of $Ga(TC_{10}P)(OH)$ and $Ga(TC_{10}P)(OR)$ compounds. The spectra for $[Ga(TC_{10}P)(OC_6H_4py)][PF_6]$ was recorded in toluene; all other spectra were recorded CH_2Cl_2. The solid black lines represent magnified versions of spectra represented by the dashed lines.

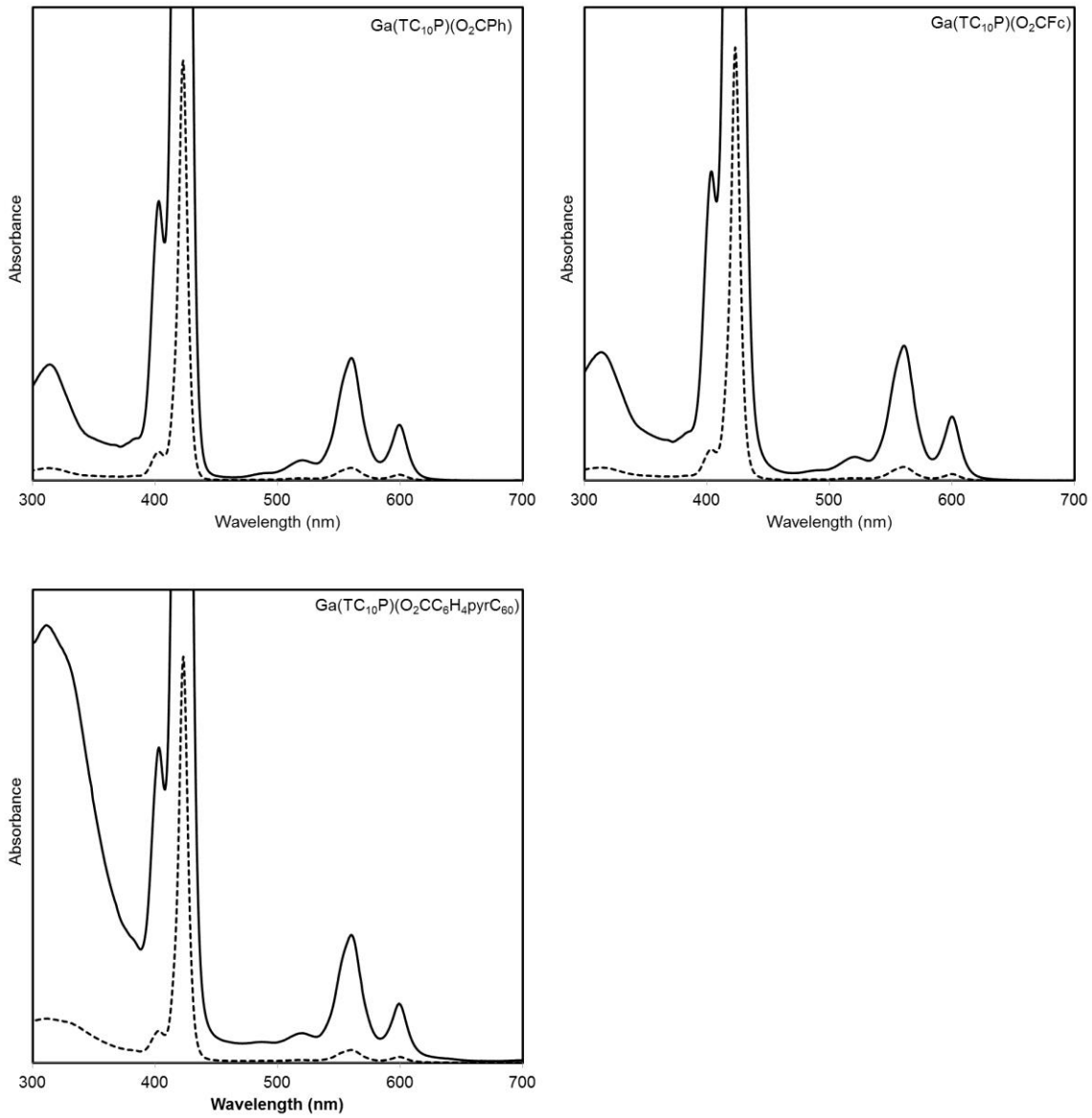

Figure 3.21. Electronic-absorption spectra of $Ga(TC_{10}P)(O_2CR)$ compounds in toluene. The spectra represented by the solid lines and dashed lines were obtained using 1 cm and 1 mm cuvettes.

Table 3.5. Electronic-Absorption Band Maxima (nm) and Relative Intensities of Ga($TC_{10}P$)(OH), Ga($TC_{10}P$)(OR), and Ga($TC_{10}P$)(O_2CR) Compounds.[a]

Compound	Solvent	λ, nm (rel. int.)
Ga($TC_{10}P$)(OH)	CH_2Cl_2	311 (4.9), 400 (17.1), 421 (100), 520 (0.7), 558 (3.3), 597 (1.6)
Ga($TC_{10}P$)(OPh)	CH_2Cl_2	307 (3.8), 400 (17.9), 421 (100), 519 (0.6), 559 (3.3), 599 (1.8)
Ga($TC_{10}P$)(FME)	CH_2Cl_2	307 (5.1), 402 (11.8), 420 (100), 472 (6.8), 504 (5.8), 558 (3.6), 597 (1.9)
FME-H	CH_2Cl_2	308 (35.0), 353 (33.1), 404 (49.7), 435 (87.2), 455 (100), 486 (63.2)
[Ga($TC_{10}P$)(OC_6H_4py)][PF_6]	toluene	312 (3.5), 367 (3.1), 383 (3.1), 403 (9.8), 423 (100), 485 (0.3), 519 (0.7), 559 (3.5), 598 (1.8)
Ga($TC_{10}P$)(O_2CPh)	toluene	314 (2.9), 385 (1.1), 403 (6.9), 423 (100), 485 (0.2), 520 (0.5), 560 (3.0), 599 (1.4)
Ga($TC_{10}P$)(O_2CFc)	toluene	314 (3.0), 385 (1.1), 404 (7.2), 423 (100), 487 (0.2), 520 (0.5), 561 (3.1), 600 (1.5)
Ga($TC_{10}P$)($O_2CC_6H_4pyrC_{60}$)	toluene	311 (10.9), 329 (10.0), 380 (3.2), 403 (7.9), 423 (100), 486 (0.5), 520 (0.7), 560 (3.2), 599 (1.5)
		λ, nm (log ε)
Al(TPP)($O_2CC_6H_4pyrC_{60}$)[b]	CH_2Cl_2	256 (5.06), 310 (4.68), 416 (5.72), 547 (4.33), 585 (3.52)
$C_{60}pyrC_6H_4CO_2CH_3$[b]	CH_2Cl_2	256 (5.06), 309 (4.55)

[a] Spectra recorded between 300 and 700 nm. [b] Reference 17.

The electronic absorption spectrum of Ga($TC_{10}P$)(FME) is different from the complexes mentioned above due to the presence of the chromophore FME, which contributes absorption bands that are clearly distinguishable from the typical porphyrin bands. In comparing the absorption spectra of Ga($TC_{10}P$)(FME) and Ga($TC_{10}P$)(OPh) (Figure 3.23), it is apparent that the porphyrinic absorption bands are not perturbed by the introduction of the FME ligand as shown

by the minimal deviations of their absorption maxima and relative intensities from those of Ga(TC_{10}P)(OPh) (Table 3.5). The absorption maxima attributed to the FME ligand, on the other hand, are red shifted relative to those of FME-H and exhibit different band shapes. In particular, the vibronic bands observed for FME-H at 455 and 486 nm are shifted to 472 and 504 nm, with the longer-wavelength band being more sharply resolved in Ga(TC_{10}P)(FME) than in FME-H (Figure 3.22 and Table 3.5). Although the effects on the absorption bands of FME when ligated have not been reported, its bands are known to undergo changes as a function of molecular charge, which was demonstrated by absorption spectra reported at various pH in aqueous media;[60] the change in the FME absorption features upon ligation is consistent with the transition of the FME-H from a neutral species to a monovalent anion, and therefore is not attributed to the electronic perturbation by the porphyrin. Metalloporphyrin-based multichromophoric complexes with axially ligated fluorescent dyes such as In(TPP)(O-BDP)[23] and Sn(TPP)(O-BDP)$_2$[31] (HO-BDP = *N*,*N*′-5-(*p*-hydroxyphenyl)dipyrrin), have been shown to exhibit negligible shifts in absorption peaks when compared to their free components, which suggested weak electronic coupling between the constituent chromophores in the ground state.

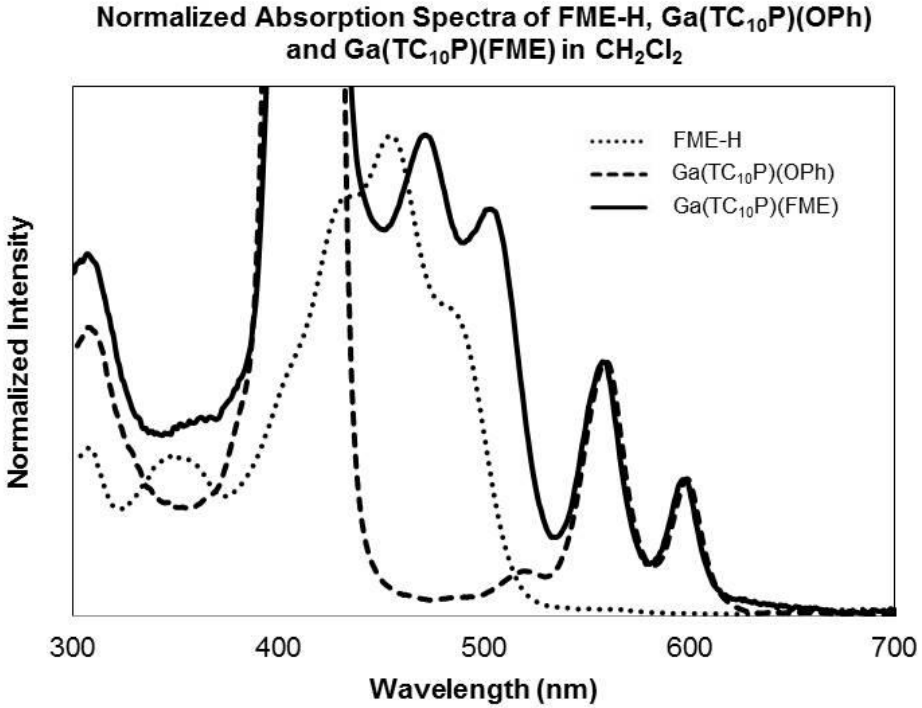

Figure 3.22. Overlaid absorption spectra of FME-H, Ga(TC_{10}P)(OPh), Ga(TC_{10}P)(FME) and FME-H in CH_2Cl_2. The intensities were normalized with respect to the Q bands.

In the electronic absorption spectrum of Ga(TC_{10}P)($O_2CC_6H_4pyrC_{60}$), the porphyrinic absorption bands are not perturbed by the introduction of the axial ligand, which is evidenced by the minimal deviations of their absorption wavelengths and relative intensities compared to the Ga(TC_{10}P)(O_2CPh) model complex. The large increase in the absorption band at 311 nm can be attributed to the modified fullerene ligand; the methyl ester derivative of $C_{60}pyrC_6H_4CO_2H$, $C_{60}pyrC_6H_4CO_2CH_3$, which was previously prepared by Poddutoori et al. as a reference compound for Al(TPP)($O_2CC_6H_4pyrC_{60}$), was found to have an absorption band at 309 nm in CH_2Cl_2 (Table 3.5).[17] The electronic absorption spectrum of Ga(TC_{10}P)($O_2CC_6H_4pyrC_{60}$) can therefore be described as the superposition of the absorption spectra of the individual components of the dyad, which is consistent with the findings of Poddutoori et al. with Al(TPP)($O_2CC_6H_4pyrC_{60}$).

3.4. Conclusion

Through NMR-scale test reactions, it has been shown that five-coordinate Ga($TC_{10}P$)(O_2CR) and Ga($TC_{10}P$)(OR) complexes can be easily prepared via the reaction between Ga($TC_{10}P$)(OH) and the corresponding carboxylic acid or aryl alcohol. We took advantage of this reactivity to prepare novel Ga(III) porphyrin dyads containing axially ligated functional moieties. In contrast to the synthetic procedures used for other five- and six-coordinate metalloporphyrins with the same axial ligand binding motifs, which reported the use of elevated temperatures and a requirement for the reactions to be performed under an inert atmosphere, the preparations of Ga($TC_{10}P$)(OR) and Ga($TC_{10}P$)(O_2CR) complexes have been shown to readily occur at room temperature in air. Through the use of these binding motifs, a variety of functional moieties have been successfully incorporated as axial ligands of five-coordinate Ga(III) porphyrin complexes, showing the versatility of this synthetic approach to prepare novel molecular dyads.

3.5. References

1. Coenen, M. J. J.; Cremers, M.; den Boer, D.; van den Bruele, F. J.; Khoury, T.; Sintic, M.; Crossley, M. J.; van Enckevort, W. J. P.; Hendriksen, B. L. M.; Elemans, J. A. A. W.; Speller, S. Little Exchange at the Liquid/Solid Interface: Defect-Mediated Equilibration of Physisorbed Porphyrin Monolayers. *Chem. Commun.* **2011**, *47*, 9666-9668.

2. Coenen, M. J. J.; den Boer, D.; van den Bruele, F. J.; Habets, T.; Timmers, K. A. A. M.; van der Maas, M.; Khoury, T.; Panduwinata, D.; Crossley, M. J.; Reimers, J. R.; van Enckevort, W. J. P.; Hendriksen, B. L. M.; Elemans, J. A. A. W.; Speller, S. Polymorphism in Porphyrin Monolayers: the Relation Between Adsorption Configuration and Molecular Conformation. *Phys. Chem. Chem. Phys.* **2013**, *15*, 12451-12458.

3. Reimers, J. R.; Panduwinata, D.; Visser, J.; Chin, Y.; Tang, C. G.; Goerigk, L.; Ford, M. J.; Baker, M.; Sum, T. J.; Coenen, M. J. J.; Hendriksen, B. L. M.; Elemans, J. A. A. W.; Hush, N. S.; Crossley, M. J. From Chaos to Order: Chain-Length Dependence of the Free Energy of Formation of Meso-tetraalkylporphyrin Self-Assembled Monolayer Polymorphs. *J. Phys. Chem. C* **2016**, *120*, 1739-1748.

4. Plamont, R.; Kikkawa, Y.; Takahashi, M.; Kanesato, M.; Giorgi, M.; Shun, A. C. K.; Roussel, C.; Balaban, T. S. Nanoscopic Imaging of *meso*-Tetraalkylporphyrins Prepared in High Yields Enabled by Montmorrilonite K10 and 3Å angstrom Molecular Sieves. *Chem. - Eur. J.* **2013**, *19*, 11293-11300.

5. Coutsolelos, A.; Guilard, R.; Bayeul, D.; Lecomte, C. Gallium(Iii) Porphyrins - Synthesis and Physicochemical Characteristics of Halogeno Gallium(Iii) Porphyrins X-Ray Crystal-Structure of Chloro-(5,10,15,20-Tetraphenylporphyrinato) Gallium(Iii). *Polyhedron* **1986**, *5*, 1157-1164.

6. Kamm, J. M.; Iverson, C. P.; Lau, W.-Y.; Hopkins, M. D. Axial Ligand Effects on the Structures of Self-Assembled Gallium-Porphyrin Monolayers on Highly Oriented Pyrolytic Graphite. *Langmuir* **2016**, *32*, 487-495.

7. Coutsolelos, A.; Guilard, R.; Boukhris, A.; Lecomte, C. Synthesis and Characterization of Azido-Gallium(III) and Thiocyanato-Gallium(III) Porphyrins - Crystal-Structure of Azido(2,3,7,8,12,13,17,18-Octaethyl-Porphyrinato)Gallium(III). *J. Chem. Soc., Dalton Trans.* **1986**, 1779-1783.

8. Boukhris, A.; Lecomte, C.; Coutsolelos, A.; Guilard, R. Alkylsulfonato(Porphyrinato)Gallium(III): Crystal-Structure Determination of Methylsulfonato(Octaethyl-2,3,7,8,12,13,17,18-Porphyrinato)-Gallium(III). *J. Organomet. Chem.* **1986**, *303*, 151-165.

9. Balch, A. L.; Hart, R. L.; Parkin, S. Axial Alkyl Ligand Reactivity in 5-Coordinate Gallium(III) Porphyrin Complexes. *Inorg. Chim. Acta* **1993**, *205*, 137-143.

10. Okamura, T.; Nishikawa, N.; Ueyama, N.; Nakamura, A. Synthesis and Structures of (Porphinato)(thiolato)gallium(III) Complexes. *Chem. Lett.* **1998**, 199-200.

11. Kadish, K. M.; Boisselier-Cocolios, B.; Coutsolelos, A.; Mitaine, P.; Guilard, R. Electrochemistry and Spectroelectrochemistry of Gallium(III) Porphyrins. Redox Properties of Five-Coordinate Ionic and σ-Bonded Complexes. *Inorg. Chem.* **1985**, *24*, 4521-4528.

12. Kadish, K. M.; Maiya, G. B.; Xu, Q. Y. Photoreactivity of σ-Bonded Metalloporphyrins.I. Formation of Zwitterionic Indium and Gallium Porphyrin Complexes in Tetrahydrofuran. *Inorg. Chem.* **1989**, *28*, 2518-2523.

13. Coutsolelos, A.; Guilard, R. Synthesis and Physicochemical Characteristics of Porphyrins Containing a Metal-Carbon σ-Bond. *J. Organomet. Chem.* **1983**, *253*, 273-282.

14. Kadish, K. M.; Cornillon, J. L.; Coutsolelos, A.; Guilard, R. Synthesis, Electrochemistry, and Ligand-Addition Reactions of Gallium(III) Porphyrins. *Inorg. Chem.* **1987**, *26*, 4167-4173.

15. Buchler, J. W.; Puppe, L.; Rohbock, K.; Schneehage, H. H. Metal-Complexes of Tetrapyrrole Ligands, VIII. Methoxo-Metal and Phenoxo-Metal Complexes of Octaethylporphin Containing

Central Ions of Type M^{3+}, M^{4+}, and $MO3^{+}$: New Tungsten and Rhenium Porphins. *Chem. Ber.* **1973**, *106*, 2710-2732.

16. Poddutoori, P. K.; Lim, G. N.; Sandanayaka, A. S. D.; Karr, P. A.; Ito, O.; D'Souza, F.; Pilkington, M.; van der Est, A. Axially Assembled Photosynthetic Reaction Center Mimics Composed of Tetrathiafulvalene, Aluminum(III) Porphyrin and Fullerene Entities. *Nanoscale* **2015**, *7*, 12151-12165.

17. Poddutoori, P. K.; Sandanayaka, A. S. D.; Hasobe, T.; Ito, O.; van der Est, A. Photoinduced Charge Separation in a Ferrocene-Aluminum(III) Porphyrin-Fullerene Supramolecular Triad. *J. Phys. Chem. B* **2010**, *114*, 14348-14357.

18. Kumar, P. P.; Maiya, B. G. Aluminium(III) Porphyrin Based Dimers and Trimers: Synthesis, Spectroscopy and Photochemistry. *New J. Chem.* **2003**, *27*, 619-625.

19. Davidson, G. J. E.; Tong, L. H.; Raithby, P. R.; Sanders, J. K. M. Aluminium(III) Porphyrins as Supramolecular Building Blocks. *Chem. Commun.* **2006**, 3087-3089.

20. Ghosh, A.; Maity, D. K.; Ravikanth, M. Aluminium(III) Porphyrin Based Axial-Bonding Type Dyads Containing Thiaporphyrins and Expanded Thiaporphyrins as Axial Ligands. *New J. Chem.* **2012**, *36*, 2630-2641.

21. Iengo, E.; Pantos, G. D.; Sanders, J. K. M.; Orlandi, M.; Chiorboli, C.; Fracasso, S.; Scandola, F. A Fully Self-Assembled Non-Symmetric Triad for Photoinduced Charge Separation. *Chem. Sci.* **2011**, *2*, 676-685.

22. Metselaar, G. A.; Sanders, J. K. M.; de Mendoza, J. A Self-Assembled Aluminium(III) Porphyrin Cyclic Trimer. *Dalton Trans.* **2008**, 588-590.

23. Panda, M. K.; Lazarides, T.; Charalambidis, G.; Nikolaou, V.; Coutsolelos, A. G. Five-Coordinate Indium(III) Porphyrins with Hydroxy and Carboxy BODIPY as Axial Ligands: Synthesis, Characterization and Photophysical Studies. *Eur. J. Inorg. Chem.* **2015**, 468-477.

24. Liu, J.; Yang, X. C.; Sun, L. C. Axial Anchoring Designed Silicon-Porphyrin Sensitizers for Efficient Dye-Sensitized Solar Cells. *Chem. Commun.* **2013**, *49*, 11785-11787.

25. Hartmann, M.; Meyer, G.; Wohrle, D. Polykondensationsreaktionen mit Germaniumkomplexen des Phthalocyanins und *meso*-TetraphenylporphinsPolykondensationsreaktionen mit Germaniumkomplexen des Phthalocyanins und *meso*-Tetraphenylporphins. *Makromol. Chem.* **1975**, *176*, 831-847.

26. Giribabu, L.; Rao, T. A.; Maiya, B. G. "Axial-Bonding"-Type Hybrid Porphyrin Arrays: Synthesis, Spectroscopy, Electrochemistry, and Singlet State Properties. *Inorg. Chem.* **1999**, *38*, 4971-4980.

27. Patra, R.; Titi, H. M.; Goldberg, I. Crystal Engineering of Molecular Networks: Tailoring Hydrogen-Bonding Self-Assembly of Tin-Tetrapyridylporphyrins with Multidentate Carboxylic Acids As Axial Ligands. *Cryst. Gowth Des.* **2013**, *13*, 1342-1349.

28. Smith, G.; Arnold, D. P.; Kennard, C. H. L.; Mak, T. C. W. Tin(IV) Porphyrin Complexes - IV. Crystal-Structures of *meso*-Tetraphenylporphyrinatotin(IV) Complexes with Hydroxide, Water, Benzoate, Salicylate and Acetylsalicylate as Axial Ligands. *Polyhedron* **1991**, *10*, 509-516.

29. Arnold, D. P.; Blok, J. The Coordination Chemistry of Tin Porphyrin Complexes. *Coord. Chem. Rev.* **2004**, *248*, 299-319.

30. Shetti, V. S.; Pareek, Y.; Ravikanth, M. Sn(IV) Porphyrin Scaffold for Multiporphyrin Arrays. *Coord. Chem. Rev.* **2012**, *256*, 2816-2842.

31. Lazarides, T.; Kuhri, S.; Charalambidis, G.; Panda, M. K.; Guldi, D. M.; Coutsolelos, A. G. Electron vs Energy Transfer in Arrays Featuring Two Bodipy Chromophores Axially Bound to a Sn(IV) Porphyrin via a Phenolate or Benzoate Bridge. *Inorg. Chem.* **2012**, *51*, 4193-4204.

32. Waggoner, A. Fluorescent Labels for Proteomics and Genomics. *Curr. Opin. Chem. Biol.* **2006**, *10*, 62-66.

33. Imahori, H. Porphyrin-Fullerene Linked Systems as Artificial Photosynthetic Mimics. *Org. Biomol. Chem.* **2004**, *2*, 1425-1433.

34. Bucher, C.; Devillers, C. H.; Moutet, J. C.; Royal, G.; Saint-Aman, E. Ferrocene-Appended Porphyrins: Syntheses and Properties. *Coord. Chem. Rev.* **2009**, *253*, 21-36.

35. Sánchez-Díaz, A.; Burtone, L.; Riede, M.; Palomares, E. Measurements of Efficiency Losses in Blend and Bilayer-Type Zinc Phthalocyanine/C_{60} High-Vacuum-Processed Organic Solar Cells. *J. Phys. Chem. C* **2012**, *116*, 16384-16390.

36. Credgington, D.; Liu, S.-W.; Nelson, J.; Durrant, J. R. In Situ Measurement of Energy Level Shifts and Recombination Rates in Subphthalocyanine/C_{60} Bilayer Solar Cells. *J. Phys. Chem. C* **2014**, *118*, 22858-22864.

37. Saha, S.; Stoddart, J. F. Photo-Driven Molecular Devices. *Chem. Soc. Rev.* **2007**, *36*, 77-92.

38. Pathem, B. K.; Claridge, S. A.; Zheng, Y. B.; Weiss, P. S. Molecular Switches and Motors on Surfaces. *Annu. Rev. of Phys. Chem.* **2013**, *64*, 605-630.

39. Yang, Y. W.; Sun, Y. L.; Song, N. Switchable Host-Guest Systems on Surfaces. *Acc. Chem. Res.* **2014**, *47*, 1950-1960.

40. Pangborn, A. B.; Giardello, M. A.; Grubbs, R. H.; Rosen, R. K.; Timmers, F. J. Safe and Convenient Procedure for Solvent Purification. *Organometallics* **1996**, *15*, 1518-1520.

41. Zhao, S. H.; Xu, X. M.; Zheng, L.; Liu, H. An Efficient Ultrasonic-Assisted Synthesis of Imidazolium and Pyridinium Salts Based on the Zincke Reaction. *Ultrason. Sonochem.* **2010**, *17*, 685-689.

42. Fulmer, G. R.; Miller, A. J. M.; Sherden, N. H.; Gottlieb, H. E.; Nudelman, A.; Stoltz, B. M.; Bercaw, J. E.; Goldberg, K. I. NMR Chemical Shifts of Trace Impurities: Common Laboratory Solvents, Organics, and Gases in Deuterated Solvents Relevant to the Organometallic Chemist. *Organometallics* **2010**, *29*, 2176-2179.

43. González, D.; Neilands, O.; Rezende, M. C. The Solvatochromic Behaviour of 2- and 4-Pyridiniophenoxides. *J. Chem. Soc., Perkin Trans. 2* **1999**, 713-717.

44. Adamczyk, M.; Grote, J.; Moore, J. A. Chemoenzymatic Synthesis of 3 '-O-(Carboxyalkyl)fluorescein Labels. *Bioconjugate Chem.* **1999**, *10*, 544-547.

45. Kazarian, A. A.; Smith, J. A.; Hilder, E. F.; Breadmore, M. C.; Quirino, J. P.; Suttil, J. Development of a novel fluorescent tag O-2-[aminoethyl]fluorescein for the electrophoretic separation of oligosaccharides. *Anal. Chim. Acta* **2010**, *662*, 206-213.

46. Compound prepared by Hannah Friedman (Friedman, H., Chemistry Honors Thesis, The University of Chicago, 2016), under the direction of the author.

47. Hau, S. K.; Cheng, Y. J.; Yip, H. L.; Zhang, Y.; Ma, H.; Jen, A. K. Y. Effect of Chemical Modification of Fullerene-Based Self-Assembled Monolayers on the Performance of Inverted Polymer Solar Cells. *ACS Appl. Mater. Interfaces* **2010**, *2*, 1892-1902.

48. Lu, Q.; Schuster, D. I.; Wilson, S. R. Preparation and Characterization of Six Bis(*N*-methylpyrrolidine)-C_{60} Isomers: Magnetic Deshielding in Isomeric Bisadducts of C_{60}. *J. Org. Chem.* **1996**, *61*, 4764-4768.

49. Kordatos, K.; Bosi, S.; Da Ros, T.; Zambon, A.; Lucchini, V.; Prato, M. Isolation and Characterization of All Eight Bisadducts of Fulleropyrrolidine Derivatives. *J. Org. Chem.* **2001**, *66*, 2802-2808.

50. Campidelli, S.; Vázquez, E.; Milic, D.; Lenoble, J.; Castellanos, C. A.; Sarova, G.; Guldi, D. M.; Deschenaux, R.; Prato, M. Liquid-Crystalline Bisadducts of [60]Fullerene. *J. Org. Chem.* **2006**, *71*, 7603-7610.

51. Kop, T.; Bjelaković, M.; Đorđević, J.; Žekić, A.; Milić, D. Fulleropyrrolidines Derived from Dioxa- and Trioxaalkyl-Tethered Diglycines. *RSC Adv.* **2015**, *5*, 94599-94606.

52. Ho, K. H. L.; Campidelli, S. Synthesis and Self-Assembly Properties of Fulleropyrrolidine Prepared by Prato Reaction. *Adv. Nat. Sci.: Nanosci. Nanotechnol.* **2014**, *5*, 025008.

53. Mahmud, I. M.; Zhou, N. Z.; Wang, L.; Zhao, Y. M. Triazole-Linked Dendro[60]Fullerenes: Modular Synthesis via a 'Click' Reaction and Acidity-Dependent Self-Assembly on the Surface. *Tetrahedron* **2008**, *64*, 11420-11432.

54. Erten-Ela, S.; Chen, H. W.; Kratzer, A.; Hirsch, A.; Brabec, C. J. Perovskite Solar Cells Fabricated Using Dicarboxylic Fullerene Derivatives. *New J. Chem.* **2016**, *40*, 2829-2834.

55. Buchler, J. W., Synthesis and Properties of Metalloporphyrins. In *The Porphyrins V1: Structure and Synthesis, Part 1*, Dolphin, D., Ed. Academic Press, Inc.: New York, 1978; Vol. I, pp 390-474.

56. Bottari, G.; Dammann, C.; Torres, T.; Drewello, T. Laser-Induced Azomethine Ylide Formation and Its Covalent Entrapment by Fulleropyrrolidine Derivatives During MALDI Analysis. *J. Am. Soc. Mass Spectrom.* **2013**, *24*, 1413-1419.

57. Ferreira, A. R.; Freire, M. G.; Ribeiro, J. C.; Lopes, F. M.; Crespo, J. G.; Coutinho, J. A. P. An Overview of the Liquid-Liquid Equilibria of (Ionic Liquid plus Hydrocarbon) Binary Systems and Their Modeling by the Conductor-like Screening Model for Real Solvents. *Ind. Eng. Chem. Res.* **2011**, *50*, 5279-5294.

58. Kessler, H. Detection of Hindered Rotation and Inversion by NMR Spectroscopy. *Angew. Chem., Int. Ed.* **1970**, *9*, 219-235.

59. Vorotyntsev, M. A.; Zinovyeva, V. A.; Konev, D. V.; Picquet, M.; Gaillon, L.; Rizzi, C. Electrochemical and Spectral Properties of Ferrocene (Fc) in Ionic Liquid: 1-Butyl-3-methylimidazolium Triflimide, [BMIM][NTf_2]. Concentration Effects. *J. Phys. Chem. B* **2009**, *113*, 1085-1099.

60. Chen, S. C.; Nakamura, H.; Tamura, Z. Supplemental Studies on Relationship Between Structure and Spectrum of Fluorescein. *Chem. Pharm. Bull.* **1979**, *27*, 475-479.

CHAPTER 4

Monolayers on HOPG of Five-Coordinate Gallium-Porphyrin Carboxylate and Aryloxide Complexes Containing Functional Axial Subunits

4.1. Introduction

The controlled patterning of functional molecules on surfaces is of great interest due to its importance in the development of nanoscale functional systems.[1, 2] This has led to extensive research in the synthesis of surface-confined supramolecular structures using planar organic and organometallic molecules as structural building blocks, where the molecular planes orient parallel to the substrate. A variety of structural motifs based on supramolecular and covalent designs have been developed, which demonstrated varying degrees of success in organizing nanoscale structures in a predictable fashion.[3, 4] In recent years, there have been efforts to extend the use of these two-dimensional supramolecular structures to develop three-dimensional systems by incorporating functional molecules into the molecular frameworks. This "platform approach" has been demonstrated by self-assembled monolayers of molecular building blocks such as triazatriangulenium derivatives[5-10] and Janus tectons[11-13] (see Chapter 1) that were shown to support functional molecules such as porphyrins, ferrocene, and fullerene above the self-assembled monolayers in well-ordered arrays. However, the variation in 2D packing arrangements exhibited by monolayers of these two classes of molecules is currently limited. Due to the known synthetic modularity of metalloporphyrins, which allows for the incorporation of structure-directing peripheral substituents, our group has investigated the hypothesis this class of compounds can be used as molecular building blocks to achieve greater 2D proximity control in 3D structures.[14]

In Chapter 2, the organization of oligo-phenylene-ethynylene (OPE) molecular wires perpendicular to a HOPG surface using gallium(III) 5,10,15,20-tetra(*n*-$C_{10}H_{21}$)porphyrins (Ga($TC_{10}P$)(OPE)) as molecular platforms was reported. Scanning tunneling microscopy (STM) studies revealed that the introduction of tall axial pillars did not interrupt the formation of self-assembled monolayers with the porphyrin molecular platforms oriented parallel to the surface, and that this class of molecules consistently form large molecular assemblies with long-range order. The Ga($TC_{10}P$)(OPE) derivatives formed the same lamellar packing geometry despite observations of structural polymorphism (depending on the length of the axial ligand) upon initial formation of self-assembled structures, a phenomenon that was allowed by the conformational flexibility of peripheral alkyl chains.[15-18]

Although these results suggested that Ga($TC_{10}P$)X compounds with axial ligands supported through the Ga-acetylide linkage represent suitable molecular building blocks for patterning functional molecules on atomically flat substrates, additional ligand-attachment chemistry was explored in order to expand the scope of functional molecules that could be incorporated as axial subunits. Inspired by literature reports of metalloporphyrins with axial aryloxide [M(Por)$(OR)_n$] and carboxylate [M(Por)$(O_2CR)_n$] ligands (n = 1: Al,[19-26] In;[27] n = 2: Ge,[28, 29] Sn[29-34]), a series of novel Ga-porphyrin complexes with axial ligands bound through Ga-carboxylate and Ga-aryloxide subunits was prepared (Scheme 4.2), as described in Chapter 3 The selection of axial ligands was motivated by the desire to controllably pattern functional molecules which have been commonly used as components of photonic devices,[35-37] molecular switches,[38, 39] light-harvesting systems,[40] and molecular electronic devices.[41]

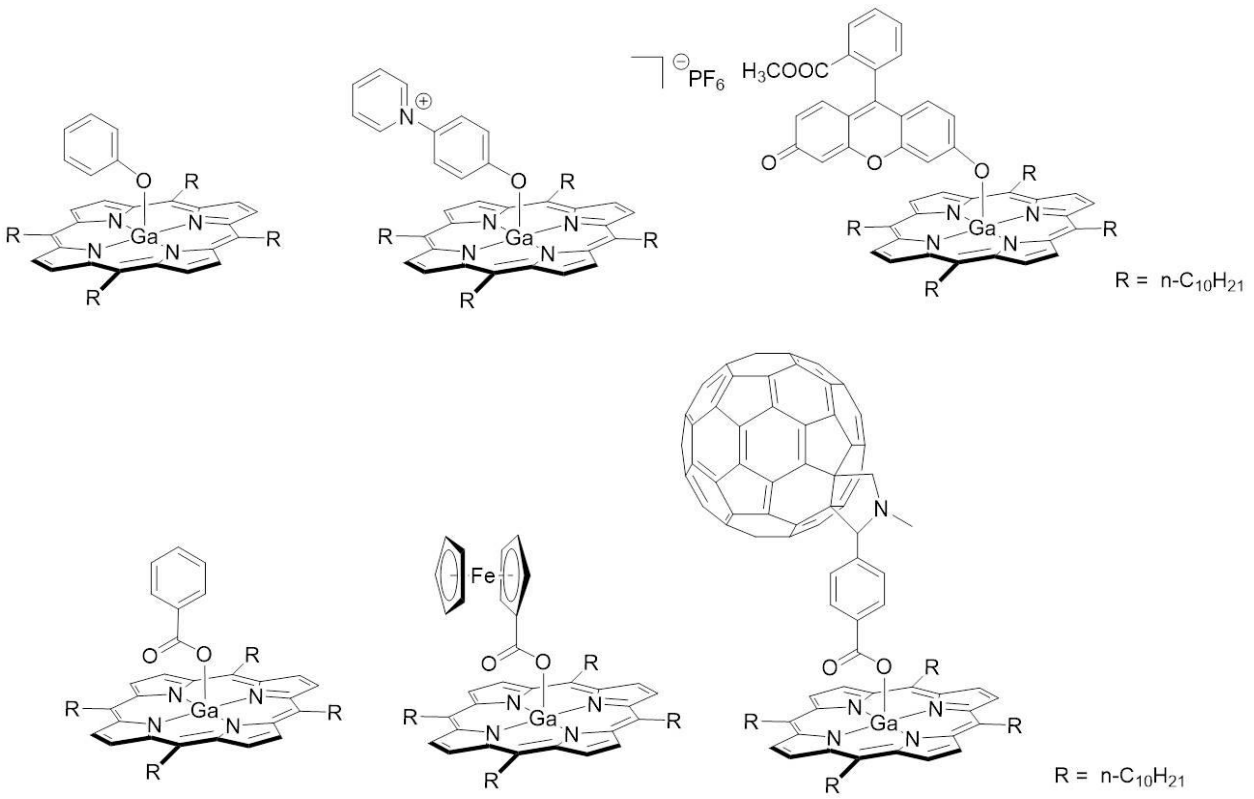

Scheme 4.1. Molecular structures (left to right, top to bottom) of Ga($TC_{10}P$)(OPh), [Ga($TC_{10}P$)(OC_6H_4py)][PF_6], Ga($TC_{10}P$)(FME), Ga($TC_{10}P$)(O_2CPh), Ga($TC_{10}P$)(O_2CFc), and Ga($TC_{10}P$)($O_2CC_6H_4pyrC_{60}$).

In this chapter, the self-assembly of Ga($TC_{10}P$)(OR) and Ga($TC_{10}P$)(O_2CR) complexes at the 1-phenyloctane/HOPG is reported. STM investigations revealed that while the two classes of compounds could form self-assembled structures on HOPG, their self-assembling behaviors were drastically affected by the axial ligands. It was found that only Ga($TC_{10}P$)(OPh) and [Ga($TC_{10}P$)(OC_6H_4py)][PF_6] formed monolayers with structures similar to those of the Ga($TC_{10}P$)Cl and Ga($TC_{10}P$)(OPE) monolayers described in Chapter 2; all other complexes form monolayers that exhibited structural arrangements that were previously uncharacterized for $TC_{10}P$-based complexes, showing the range of 2D structural variations that can be achieved using the $TC_{10}P$ molecular platform.

4.2. Experimental Section

4.2.1. Materials and General Methods. All synthetic procedures were carried in air at room temperature unless noted otherwise. Toluene was purified by passing it under nitrogen pressure through an anaerobic, stainless-steel system consisting of one column of activated A2 alumina and one column of activated BASF R3-11 catalyst.[42] Heptadecanal was prepared by the oxidation of 1-heptadecanol (Fisher, 97%) using pyridinium chlorochromate as the oxidant following standard procedures.[43] The preparation and characterization of Ga($TC_{10}P$)(OH), Ga($TC_{10}P$)(OPh), Ga($TC_{10}P$)(FME), [Ga($TC_{10}P$)(OC_6H_4py)][PF_6], Ga($TC_{10}P$)(O_2CPh), Ga($TC_{10}P$)(O_2CFc), and Ga($TC_{10}P$)($O_2CC_6H_4pyrC_{60}$) were reported in Chapter 3. All other solvents, compounds, and reagents were obtained from commercial sources and used as received.

4.2.2. Characterization of Compounds. ^{1}H NMR spectra were recorded at room temperature using a Bruker DRX 400 MHz or Bruker Avance II$^+$ 500 MHz NMR spectrometer. Chemical shifts for all ^{1}H NMR spectra were measured relative to solvent residual resonances.[44]

4.2.3. Preparation of $H_2TC_{16}P$. The preparation of this compound was adapted from the reported procedure for the synthesis of 5,10,15,20-tetra(*n*-C_7H_{15})porphyrin.[45] In a round-bottom flask (1 L) fitted with a Dean-Stark trap and condenser, a solution of heptadecanal (4.40 g, 17.3 mmol), pyrrole (1.16 g pyrrole, 17.2 mmol), and $TsOH{\cdot}H_2O$ (0.060 g, 0.32 mmol) in toluene (500 mL) was stirred and heated at reflux in the dark for 2 h under nitrogen. The reaction was allowed to cool to room temperature and opened to air. 2,3,5,6-Tetrachloro-1,4-benzoquinone (2.04 g, 8.29 mmol) was added, and the reaction mixture was heated at reflux for 30 min. The reaction mixture was allowed to cool to room temperature, and the volatile components were removed *in vacuo*. The resulting residue was purified by column chromatography over silica (hexanes/CH_2Cl_2, 2:1). The purple band was collected, and the volatile components were

removed *in vacuo*. The resulting brown solid was dissolved in CH_2Cl_2 (5 mL), and the product was precipitated as a brown solid by layering the CH_2Cl_2 solution with methanol (40 mL) overnight, collected via filtration and dried under vacuum (0.105 g, 0.087 mmol, 2% yield). The ^{1}H NMR spectrum of the product indicated the presence of a porphyrinic impurity (~7%), which was identified by chemical shifts at 9.33 ppm (s) and –2.64 ppm (s), the latter of which corresponded to a porphyrin NH resonance. The material was used for the preparation of Ga($TC_{16}P$)(OH) without further purification. The chemical shifts in the ^{1}H NMR spectrum obtained in $CDCl_3$ did not agree with literature values and are listed below.[18] ^{1}H NMR ($CDCl_3$, 500.13 MHz): δ 9.38 (s, 8H, *β*), 4.85 (t, 8H, $CH_2CH_2C\underline{H}_2$Por), 2.43 (m, 8H, $CH_2C\underline{H}_2CH_2$Por), 1.72 (m, 8H, $C\underline{H}_2CH_2CH_2$Por), 1.35–1.50 (m, 8H, $CH_3(CH_2)_{11}C\underline{H}_2$), 1.00–1.35 (m, 88H, $CH_3(C\underline{H}_2)_{11}CH_2$), 0.79 (t, 12H, CH_3), –2.72 (NH). Literature values for ^{1}H NMR ($CDCl_3$, 300 MHz):[18] δ 9.46 (s, 8H, *β*), 4.92 (t, 8H, $CH_2CH_2C\underline{H}_2$Por), 2.52 (m, 8H, $CH_2C\underline{H}_2CH_2$Por), 1.81 (m, 8H, $C\underline{H}_2CH_2CH_2$Por), 1.20–1.43 (m, 80H, $CH_3(C\underline{H}_2)_{11}CH_2$), 0.87 (t, 12H, CH_3), –2.65 (NH).

4.2.4. Preparation of Ga($TC_{16}P$)(OH). This procedure was adapted from that reported for the preparation of Ga(OEP)Cl[46] and Ga($TC_{10}P$)(OH). A solution of $H_2TC_{16}P$ (0.105 g, 0.087 mmol), $GaCl_3$ (0.023 g, 0.131 mmol), and NaOAc (0.200 g, 2.44 mmol) in glacial acetic acid (20 mL) was refluxed overnight under nitrogen, during which the color of the reaction mixture turned from dark green to dark purple. The reaction mixture was opened to air and cooled to room temperature, which resulted in the precipitation of the crude product as a purple solid. The precipitate was collected via filtration, washed with cold glacial acetic acid (5 mL) and water (10 mL), extracted into toluene, and filtered. The volatile components were removed *in vacuo*, and the resulting purple solid was dissolved in CH_2Cl_2 (20 mL). A 2N NaOH solution (20 mL) was added, and the resulting solvent layers were stirred vigorously to form an emulsion for 1 h. The

organic layer was isolated, washed with water, and dried with $NaSO_4$. The product was isolated as a purple solid upon removal of volatile components *in vacuo* (0.087 g, 0.067 mmol, 77% yield). The ^{1}H NMR spectrum of the product showed the presence of a porphyrinic impurity (~7%), which was identified by chemical shifts at 9.51 ppm (s) and –6.38 ppm (s); the chemical shift at –6.38 ppm indicated that the porphyrinic impurity contained an axial OH ligand and was expected to be reactive towards FME-H. The material was used for the preparation of Ga($TC_{16}P$)(FME) without further purification. ^{1}H NMR (C_6D_6, 500.13 MHz): δ 9.54 (s, 8H, *β*), 4.79 (t, 8H, $CH_2CH_2C\underline{H}_2Por$), 2.54 (m, 8H, $CH_2C\underline{H}_2CH_2Por$), 1.72 (m, 8H, $C\underline{H}_2CH_2CH_2Por$), 1.41–1.52 (m, 8H, $CH_3(CH_2)_{11}C\underline{H}_2$), 1.19–1.41 (m, 88H, $CH_3(C\underline{H}_2)_{11}CH_2$), 0.92 (t, 12H, CH_3), –6.44 (OH).

4.2.5. Preparation of Ga($TC_{16}P$)(FME). To a solution of Ga($TC_{16}P$)(OH) (0.087 g, 0.067 mmol) in toluene (15 mL), FME-H (0.030 g, 0.086 mmol) was added to form a suspension. The reaction mixture was stirred for 1.5 h, during which the solution color changed from purple to red. The solvent was then filtered to remove the unreacted FME-H. The product was isolated as a red-purple solid after the removal of volatile components *in vacuo* (0.097 g, 0.060 mmol, 90% yield). ^{1}H NMR (C_6D_6, 400.13 MHz): δ 9.51 (s, 8H, *β*), 7.99 (d, 1H, *J* = 7.2 Hz, H15 or H18), 6.75–6.90 (m, 2H, H16, H17), 6.65 (br s, 1H), 6.55 (br s, 1H), 6.40 (br s, 1H), 6.22 (d, 1H, J = 8.4 Hz, H15 or H18), 5.33 (br s, 1H), 4.73 (t, 8H, $CH_2CH_2C\underline{H}_2Por$), 2.98 (s, 3H, OCH_3), 2.54 (m, 8H, $CH_2C\underline{H}_2CH_2Por$), 2.08 (br s, 1H), 1.71 (m, 8H, $C\underline{H}_2CH_2CH_2Por$), 1.52 (m, 8H, $CH_3(CH_2)_{11}C\underline{H}_2$), 1.15–1.47 (m, 88H, $CH_3(C\underline{H}_2)_{11}CH_2$), 0.92 (t, 12H, CH_3); one of the six xanthene proton resonances was not observed. The disappearance of the OH resonance of the porphyrinic impurity observed at –6.38 ppm in the Ga($TC_{16}P$)(OH) ^{1}H NMR spectrum indicated

its reaction with FME-H to form a dyad, although chemical shifts attributed to the impurity could not be observed, most likely due to spectral overlap with the Ga($TC_{16}P$)(FME) resonances.

4.2.6. Sample Preparation for STM Experiments. Highly oriented pyrolytic graphite (HOPG) wafers (SPI-2 grade, SPI Supplies) measuring 7 mm × 7 mm × 1 mm were mounted to 12 mm diameter metal specimen discs with colloidal silver paste (PELCO, Ted Pella, Inc.). The surface of the HOPG substrate was cleaved with adhesive tape immediately prior to dosing. For STM experiments, one drop of a solution of the porphyrin compound in 1-phenyloctane was deposited HOPG with syringe equipped with a 25-guage needle (Ga($TC_{10}P$)(OPh): 2.0×10^{-4} M, 5.0×10^{-4} M; [Ga($TC_{10}P$)(OC_6H_4py)][PF_6]: 5.0×10^{-4} M; Ga($TC_{10}P$)(FME): 2.5×10^{-5} M, 7.5×10^{-4} M, 1.5×10^{-3} M, 5.0×10^{-3} M; Ga($TC_{16}P$)(FME): 2.0×10^{-4} M, 5.0×10^{-4} M, 7.5×10^{-4} M; Ga($TC_{10}P$)(O_2CPh): 1.0×10^{-4} M; Ga($TC_{10}P$)(O_2CFc), 5.0×10^{-5} M, 1.0×10^{-4} M; Ga($TC_{10}P$)($O_2CC_6H_4pyrC_{60}$), 5.0×10^{-5} M, 1.0×10^{-4} M, 2.0×10^{-4} M). The STM tip was then engaged through the drop and the sample was imaged.

4.2.7. STM Measurements and Data Analysis. STM images were acquired at room temperature using a Digital Instruments Nanoscope IIIa standalone STM. The $Pt_{0.8}Ir_{0.2}$ tips were mechanically cut from a Pt/Ir (80/20) wire (Goodfellow). All measurements were performed in constant current mode. The data were corrected for drift post-acquisition in the SPIP software package[47] using the underlying graphite lattice parameters ($a = b = 0.246$ nm, $\Gamma = 60°$) as a reference.[48] Data analysis was performed using WSxM 5.0 software.[49] All of the images presented were flattened, low-pass filtered, and sharpened by adjusting the contrast. Reported lattice parameters are averages of those determined from consecutive up-scan and down-scan images. For samples that were characterized by a single unit cell, the unit-cell distances were determined from spacings within 100 sets of five consecutive porphyrin molecules, and the unit-

cell angles were determined from the average of 40 measurements. For samples that exhibited the alternating unit cell arrangement [Ga($TC_{10}P$)(O_2CPh), Ga($TC_{10}P$)(O_2CFc)], the unit-cell-distances were the averages of 100 measurements of the porphyrin center-to-center distances, and the unit-cell angles were the average of 40 measurements.

4.2.8. Density Functional Theory (DFT) Calculations. Calculations were performed using Gaussian09.[50] Calculations employed the B3P86 functional,[51, 52] which was determined by a previous density functional benchmarking study to provide the best agreement between the calculated and experimentally determined molecular structures of Ga(octaethylporphyrin)Cl.[53] The calculations were performed for the 5,10,15,20-tetramethylporphyrin derivatives of the Ga($TC_{10}P$)(O_2CR) complexes. The LANL2DZ effective core potential basis set was used for Ga[54] and Fe[55] while the 6-31G* basis set[56, 57] was used for all other atoms. Geometries were optimized without symmetry constraints. No imaginary frequencies were obtained in subsequent vibrational calculations, confirming that the optimized structures reside at potential-surface minima.

4.3. Results and Discussion

4.3.1. STM Imaging of Ga($TC_{10}P$)(OPh) at the 1-Phenyloctane/HOPG Interface. The self-assembly of Ga($TC_{10}P$)(OPh) monolayers at the 1-phenyloctane/HOPG interface was studied in order to provide a reference point for [Ga($TC_{10}P$)(OC_6H_4py)][PF_6] and Ga($TC_{10}P$)(FME), whose axial ligands are attached through phenoxide-like linkages. Deposition of a 1-phenyloctane solution of Ga($TC_{10}P$)(OPh) onto HOPG results in formation of self-assembled monolayers that span hundreds of nanometers in width, as exemplified by 100 nm × 100 nm STM images (Figure 4.1, 5.0×10^{-4} M; Figure 4.2, 2.0×10^{-4} M). Small-scale images of the self-assembled monolayers show that the absorbed molecules are arranged in a highly

ordered lattice. The adsorbed molecules appear as bright but diffuse features that are separated by dark regions, which are attributed to areas occupied by decyl chains at the porphyrin periphery. The Ga(TC_{10}P)(OPh) monolayers adopt the β packing structure at both concentrations, with statistically indistinguishable lattice parameters (5.0×10^{-4} M: a = 1.64 ± 0.05 nm, b = 2.14 ± 0.04 nm, Γ = 69 ± 3°; 2.0×10^{-4} M: a = 1.64 ± 0.04 nm, b = 2.17 ± 0.03 nm, Γ = 70 ± 2°; Table 4.1), and there is no noticeable difference in surface coverage by the monolayers at the two concentrations. This is the same structure found for Ga(TC_{10}P)Cl, but different from that for Ga(TC_{10}P)(OPE) (α lattice). Samples prepared at both concentrations are monitored for 2 h for possible phase transitions and structural polymorphism; neither is observed.

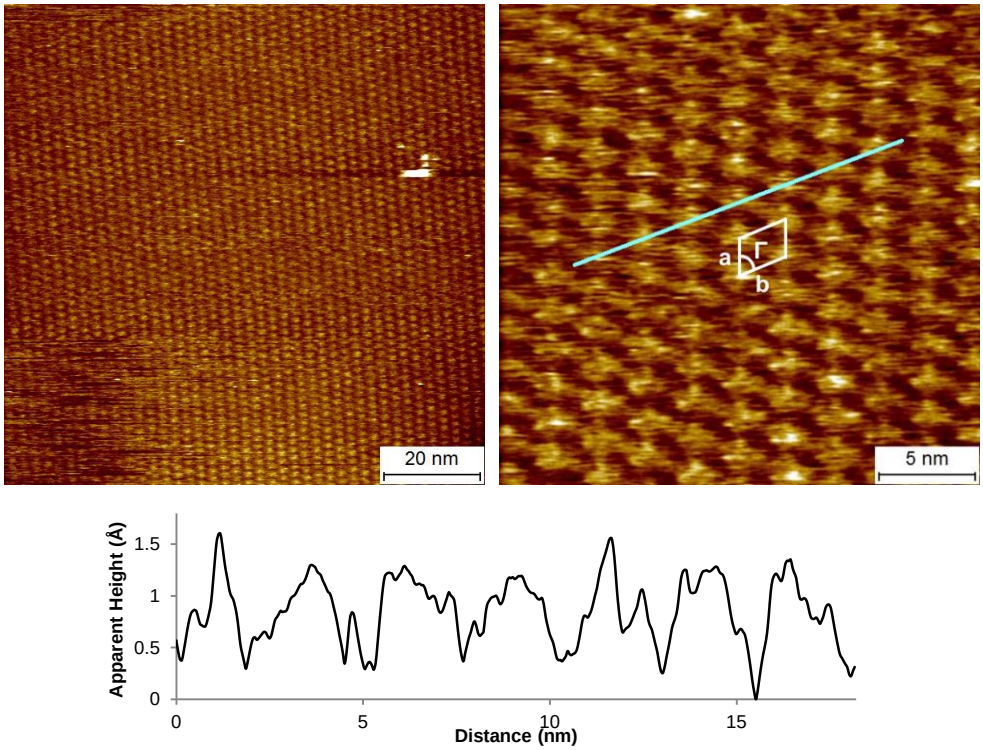

Figure 4.1. STM images and cross-sectional profile of a monolayer of Ga(TC_{10}P)(OPh) on HOPG at the solid–liquid interface (1-phenyloctane, 5.0×10^{-4} M; I = 7 pA, V = –1000 mV). The cross-sectional profile corresponds to the teal line in the image, drawn along the b lattice vector.

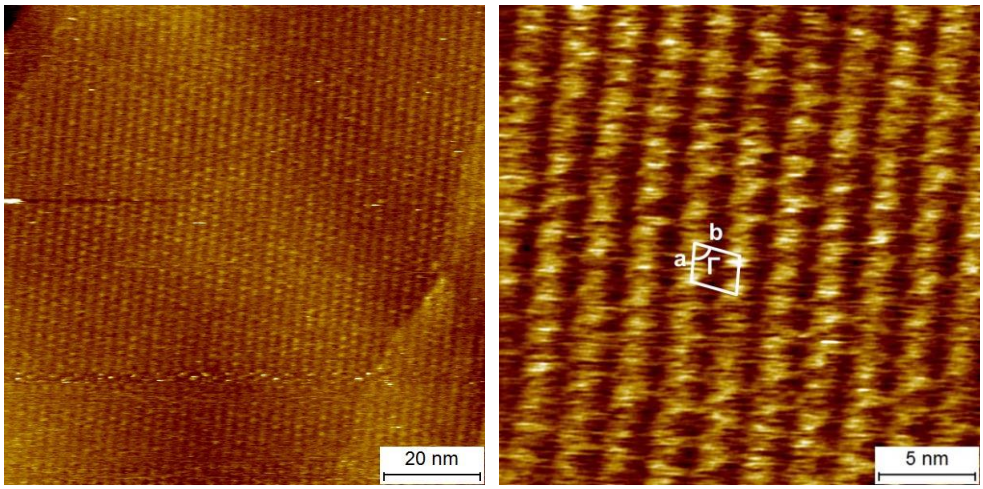

Figure 4.2. STM images of a monolayer of Ga(TC_{10}P)(OPh) on HOPG at the solid–liquid interface (1-phenyloctane, 2.0×10^{-4} M; I = 6 pA, V = –950 mV).

Table 4.1. Lattice Parameters of Monolayers of Ga(TC_{10}P)(OR) Complexes at the 1-Phenyloctane/HOPG Interface.[a]

Compound (lattice)	Conc. (10^{-4} M)	a (nm)	b (nm)	Γ (°)	A (nm^2)	density (molecules/nm^2)
$H_2TC_{10}P$ (α)[b]	7.5	1.37(4)	1.75(5)	86(2)	2.39(14)	0.42
Ga(TC_{10}P)Cl (β)[b]	7.5	1.71(3)	2.09(4)	70(2)	3.36(17)	0.30
Ga(TC_{10}P)(OPh) (β)	2.0	1.64(5)	2.14(4)	69(3)	3.28(23)	0.31
	5.0	1.64(4)	2.17(3)	70(2)	3.34(17)	0.30
[Ga(TC_{10}P)(OC_6H_4py)][PF_6] (α)	5.0	1.36(6)	1.75(3)	85(2)	2.37(15)	0.42

[a] Values in parentheses are standard deviations of the last digit(s). [b] Representative examples of observed packing structures; see Chapter 2 for the definition of the α and β lattices.

As shown by the cross-sectional profile in Figure 4.1, the apparent height of Ga(TC_{10}P)(OPh) monolayers ranges from ~1 Å to 1.5 Å, which is shorter than the calculated height of ~8.7 Å. The discrepancy between apparent and physical heights has been observed for metalloporphyrin complexes with multi-atom axial ligands,[53, 58, 59] and is attributed to the poor electronic coupling between the ligand and the porphyrin macrocycle since the apparent height is directly correlated to the local tunneling probability.[60, 61] The observation of the molecules as diffuse features is expected since the STM imaging process (on the order of seconds) is orders of

magnitude slower than typical molecular rotations at room temperature (on the order of picoseconds),[62] hence a molecule that freely rotates can only be imaged as the time average of the various rotation configurations.[63]

4.3.2. STM Imaging of [Ga(TC$_{10}$P)(OC$_6$H$_4$py)][PF$_6$] at the 1-Phenyloctane/HOPG Interface. Due to the unusual solubility of the salt [Ga(TC$_{10}$P)(OC$_6$H$_4$py)][PF$_6$] in hydrocarbon solvents such as benzene and toluene (see Chapter 3), 1-phenyloctane was successfully used to prepare STM solutions of this complex. Addition of a drop of 5.0×10^{-4} M solution results in self-assembled monolayers that cover areas of hundreds of nanometers in width, as shown by STM imaging (Figure 4.3). The monolayers are persistent, with no observable disruptions in the structure or structural transformations during the scanning process. The structure is characterized by alternating rows of bright features that are separated by dark rows, which is indicative of a lamellar structure (see Chapter 1). Analysis of the lattice shows that the packing geometry conforms to the α structure with lattice parameters a = 1.36 ± 0.06 nm, b = 1.75 ± 0.03 nm, Γ = 85 ± 2° (Table 4.1), which is in contrast to the β lattice exhibited by Ga(TC$_{10}$P)(OPh). The difference in packing arrangement is likely due to a difference between molecule-solvent interactions. Tahara et al. has previously investigated the self-assembly of dehydrobenzo[12]annulene derivatives containing long-alkyl-chain substituents on HOPG at the solid–liquid interface, where self-assembled monolayers formed from solutions prepared in "poor solvents," in which the molecules had lower solubility, resulted in structures with higher packing densities.[64] Since [Ga(TC$_{10}$P)(OC$_6$H$_4$py)][PF$_6$] contains a charged axial ligand, the higher packing density of [Ga(TC$_{10}$P)(OC$_6$H$_4$py)][PF$_6$] monolayers can potentially be a result of increased solvophobic effects, which favors the formation of denser molecular assemblies.

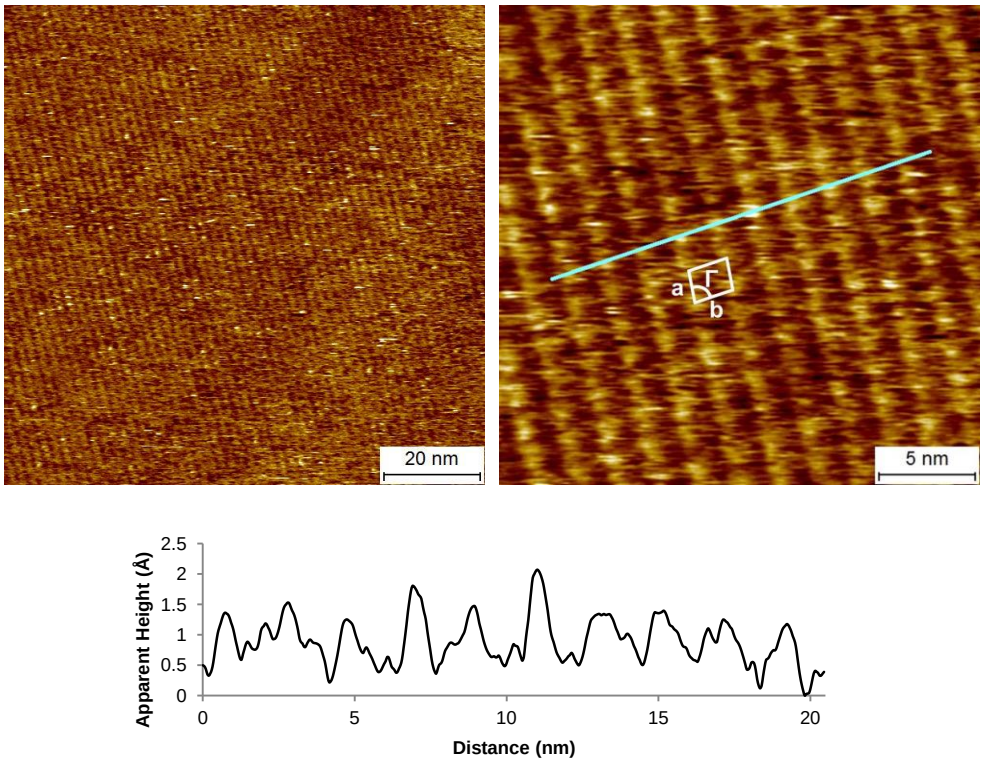

Figure 4.3. STM images and cross-sectional profile of a $[Ga(TC_{10}P)(OC_6H_4py)][PF_6]$ monolayer on HOPG at the solid–liquid interface (1-phenyloctane, 5.0×10^{-4} M; left: I = 7 pA, V = –500 mV; right: I = 7 pA, V = –700 mV). The cross-sectional profile corresponds to the teal line in the image, drawn along the b lattice vector.

Similar to $Ga(TC_{10}P)(OPh)$, adsorbed molecules of $[Ga(TC_{10}P)(OC_6H_4py)][PF_6]$ appear as bright but diffuse spots that exhibit an apparent height range of 1.5–2 Å. While the dyad contains the electroactive pyridinium moiety on the axial ligand, the conductance of electroactive molecules adsorbed on atomically flat surfaces has been shown to be highly dependent on bias voltage. Tao et al. has previously studied self-assembled monolayers of Fe-protoporphyrin IX (FePP) and free-base protoporphyrin IX (PP) on HOPG using electrochemical STM, where the monolayers were imaged at a fixed tip-substrate potential while the substrate potential was varied.[65] In mixed monolayers of FePP and PP, the two components were structurally identical when the substrate was held far from the electron transfer reaction potential of FePP, but the apparent heights of FePP molecules showed an increase of up to ~2.2 Å when the substrate

potential was adjusted to a value close to the reduction potential of FePP; the increase in apparent height corresponded to a ten-fold increase in tunneling current. The PP molecules, which had molecular orbitals with energy levels far from the substrate and tip Fermi levels and also lacked the Fe(III) metal centers that provided unoccupied orbitals in the HOMO-LUMO gap, did not respond to the change in substrate potential and hence remained as low contrast features in STM images. These observations revealed that STM could be used to distinguish molecules based on different redox properties, and also that the size of the tunneling current through electroactive molecules was bias-dependent. The small apparent heights observed for [Ga(TC_{10}P)(OC_6H_4py)][PF_6] can therefore be attributed to a mismatch between the STM tip potential and the redox-potential of the dyad molecules on the surface.

4.3.3. STM Imaging of Ga(TC_{10}P)(FME) at the 1-Phenyloctane/HOPG Interface. Monolayers of Ga(TC_{10}P)(FME) on HOPG differ significantly from those of other Ga(TC_{10}P)(OR) complexes, both in terms of the concentration at which they are observed and the homogeneity and lattice parameters of its structure. A 7.5×10^{-4} M Ga(TC_{10}P)(FME) solution in 1-phenyloctane was initially used to prepare STM samples on HOPG because the higher solution concentration was expected to facilitate the formation of self-assembled monolayers on the surface, as shown by the consistent formation of Ga(TC_{10}P)(OPE) monolayers with long-range order at the same solution concentration (see Chapter 2). STM scanning of the samples, however, does not reveal the formation of ordered porphyrin monolayers but instead provides images that are difficult to interpret; the quality of the images do not allow for the clear distinction between bare graphite and multilayered, amorphous films. Subsequent attempts to prepare porphyrin monolayers using solutions of increasing dyad concentration (1.5×10^{-3} M, 5.0×10^{-3} M) resulted in the same observations.

Reducing the concentration of the Ga($TC_{10}P$)(FME) solution to 2.5×10^{-5} M results in the formation of ordered monolayers spanning tens of nanometers in width. Multiple domains and structural polymorphism are observed; Figure 4.4 shows a region in which seven separate islands (highlighted by white borders), represented by three types of packing structures (labeled as I, II, III in Figure 4.4), can be identified. While each domain is periodic, by eye, the adsorption configurations (e.g., the orientation of the porphyrin core with respect to the substrate) that resulted in these packing arrangements are indeterminate due to the repeating units exhibiting shapes and substructures that are uncharacteristic of porphyrin molecules adsorbed with the heterocyclic cores parallel to the substrate. Specifically, in the type I lattice, the "boomerang-shaped" repeating units can be subdivided into four parallel stripes; the type II lattice appears to be a close packed arrangement of alternating bright and dark dots which are separated by a distance of ~1 nm; and the type III lattice appears to either consist of columns of bright discs separated by a distance of ~1 nm, commonly attributed to porphyrins adsorbed in the "edge-on" configuration (shown in red),[66, 67] or an array of molecules imaged as pairs of bright lobes (shown in green). Since the monolayers are gradually disrupted by STM imaging within minutes, further attempts to elucidate the nature of the observed features or to reproduce the results with samples prepared under the same experimental conditions are unsuccessful.

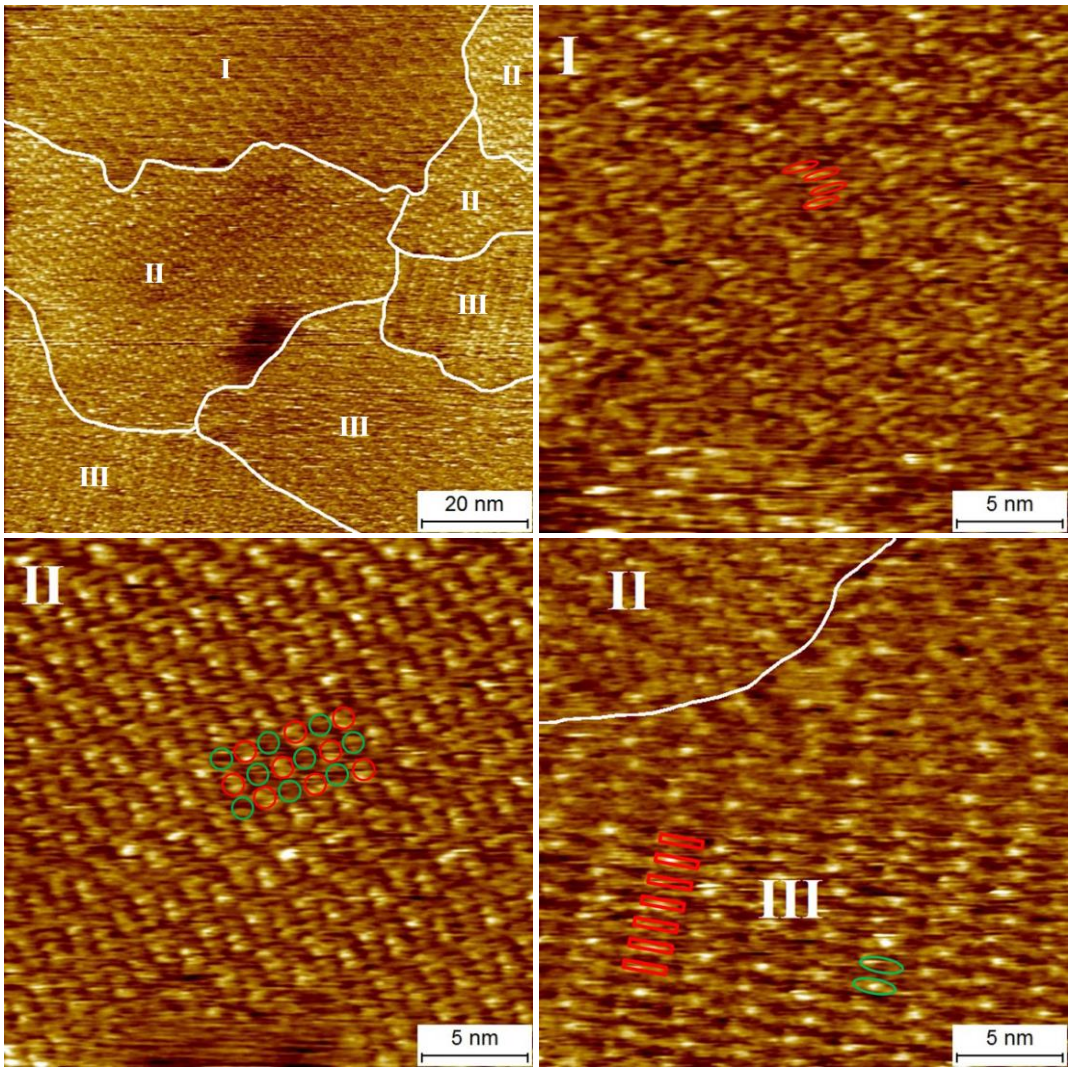

Figure 4.4. STM images of Ga($TC_{10}P$)(FME) monolayers on HOPG at the solid–liquid interface (1-phenyloctane, 2.5×10^{-5} M; I = 6 pA, V = –300 mV). Possible substructures of the repeating units in each lattice are highlighted in the STM images.

Since the use of higher solution concentrations has been shown to result in the formation of $CuTC_{11}P$ monolayers with higher packing densities,[15] the observation of ordered Ga($TC_{10}P$)(FME) domains at 2.5×10^{-5} M but not at 7.5×10^{-4} M, 1.5×10^{-3} M, nor 5.0×10^{-3} M is unexpected. However, the absence of ordered domains in samples prepared at higher concentrations can potentially be a result of the formation of multilayered, amorphous structures on HOPG due to the rapid deposition of molecules from solution, which can be a kinetically

favorable phenomenon caused by low solubility.[68] To probe this possibility, and to address the problem that stable structures of Ga($TC_{10}P$)(FME) could not be prepared, $TC_{16}P$ was investigated as an alternate platform. In a recent computational study by Reimers et al., where the chain-length dependence of TC_mP molecules was investigated, the authors found that an increase in chain length should increase the free energy of self-assembled monolayer formation, as well as reduce the number of energetically similar polymorphs; the adsorption of multiple energetically similar polymorphs was noted to hinder the formation of stable monolayers with long-range order.[17] Based on this report, we hypothesized that an increase in alkyl chain length of the porphyrin platform should facilitate the self-assembly of the Ga-porphyrin-FME dyad by reducing the number of energetically similar polymorphs and increasing the free energy of self-assembled monolayer formation.

The compound Ga($TC_{16}P$)(FME) was prepared using similar methods to those for Ga($TC_{10}P$)(FME). Unfortunately, the compound could not be prepared in pure form (due to an impurity in the $H_2TC_{16}P$ starting material); thus, the STM results and conclusions drawn must be considered tentative, and the experiments would need to be repeated in future with pure material to verify them. Solutions of Ga($TC_{16}P$)(FME) with concentrations of 5.0×10^{-4} M and 7.5×10^{-4} M in 1-phenyloctane yield no self-assembled monolayers on HOPG, which is consistent with the experimental results for Ga($TC_{10}P$)(FME) at the same concentrations. Reduction of the solution concentration to 2.0×10^{-4} M results in the formation of self-assembled monolayers with small domain sizes (~30–80 nm in width), which are characterized by bright, diffuse features separated by darker regions, as shown in Figure 4.5. The appearance of the adsorbed molecules, as well as the short apparent heights (as shown in the cross-sectional profile), are characteristic of monolayers formed by metalloporphyrins with multi-atom axial ligands.[53, 58, 59] While the

presence of multiple domains is apparent, they exhibit the same packing structure defined by the lattice parameters a = 2.01 ± 0.05 nm, b = 2.33 ± 0.06 nm, Γ = 81 ± 2°; these are statistically indistinguishable from the lattice parameters of $H_2TC_{16}P$ monolayers at the 1-phenyloctane/HOPG interface.[18] Compared to Ga($TC_{10}P$)(FME), Ga($TC_{16}P$)(FME) is able to form monolayers with ordered, stable structures with a single packing geometry at a higher concentration, which shows that the axial-ligand-induced effects in self-assembling behavior can indeed be mitigated by changes in the peripheral substituents of the porphyrin core.

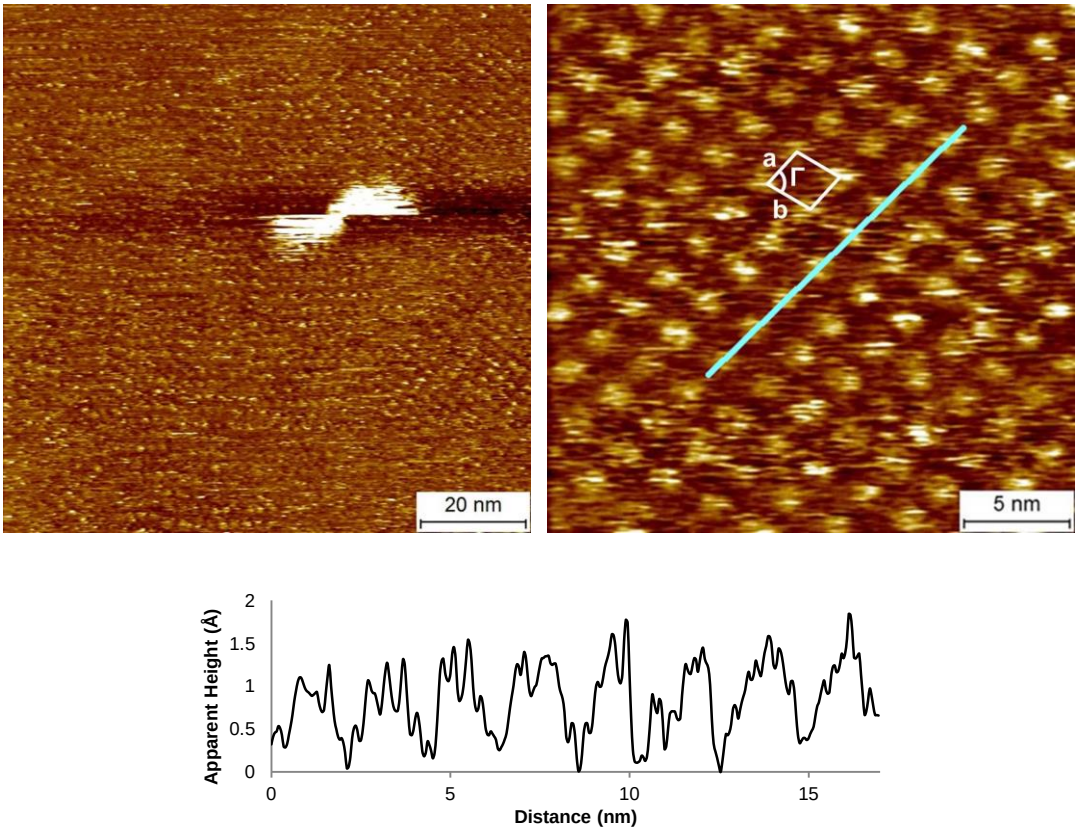

Figure 4.5. STM images and cross-sectional profile of Ga($TC_{16}P$)(FME) monolayers on HOPG at the solid–liquid interface (1-phenyloctane, 2.0 × 10^{-4} M; left: I = 8 pA, V = –700 mV; right: I = 10 pA, V = –600 mV). The cross-sectional profile corresponds to the teal line in the image, drawn along the a lattice vector.

4.3.4. STM Imaging of Ga($TC_{10}P$)(O_2CPh) and Ga($TC_{10}P$)(O_2CFc) at the 1-Phenyloctane/HOPG Interface. Similar to Ga($TC_{10}P$)(OPh), Ga($TC_{10}P$)(O_2CPh) served as the model compound for Ga-porphyrin complexes with axial carboxylate ligands. Samples were prepared by depositing a drop of a 1.0×10^{-4} M solution of these complexes in 1-phenyloctane onto HOPG. A representative large-scale image of Ga($TC_{10}P$)(O_2CPh) is shown in Figure 4.6, where an ordered monolayer spanning widths of ~80 nm is observed. In contrast to Ga($TC_{10}P$)(OPh), which only forms monolayers with the β structure, Ga($TC_{10}P$)(O_2CPh) consistently self-assembled into structures that are formed by alternating rows of two different unit cells. The smaller of the two unit cells (denoted as γ) is defined by lattice parameters a = 1.32 ± 0.08 nm, b = 1.69 ± 0.04 nm, Γ = 64 ± 3°, and the larger unit cell (denoted as δ) is defined by lattice parameters a = 1.69 ± 0.04 nm, b = 1.89 ± 0.10 nm, Γ = 73 ± 4° (Table 4.2). This 1:1 alternating arrangement, highlighted in the small scale image in Figure 4.6, persists without disruption throughout entire domains, and does not change during observations made over a 2 h period. These observations contrast with those for the self-assembled monolayers of Ga($TC_{10}P$)(*p*-CCC_6H_4CCCPh) and Ga($TC_{10}P$)(4,4′-$CCC_6H_4CCC_6H_4CCPh$) described in Chapter 2. Shortly following deposition, monolayers of the Ga($TC_{10}P$)(OPE) derivatives showed domains containing alternating structures consisted of α and β unit cells, but after 2 h only α domains were observed. This suggests that the alternating cell arrangement is a kinetic structure for the Ga($TC_{10}P$)(OPE) compounds, and that the α structure is the thermodynamically stable form. For Ga($TC_{10}P$)(O_2CPh), in contrast, the alternating structure appears to be stable.

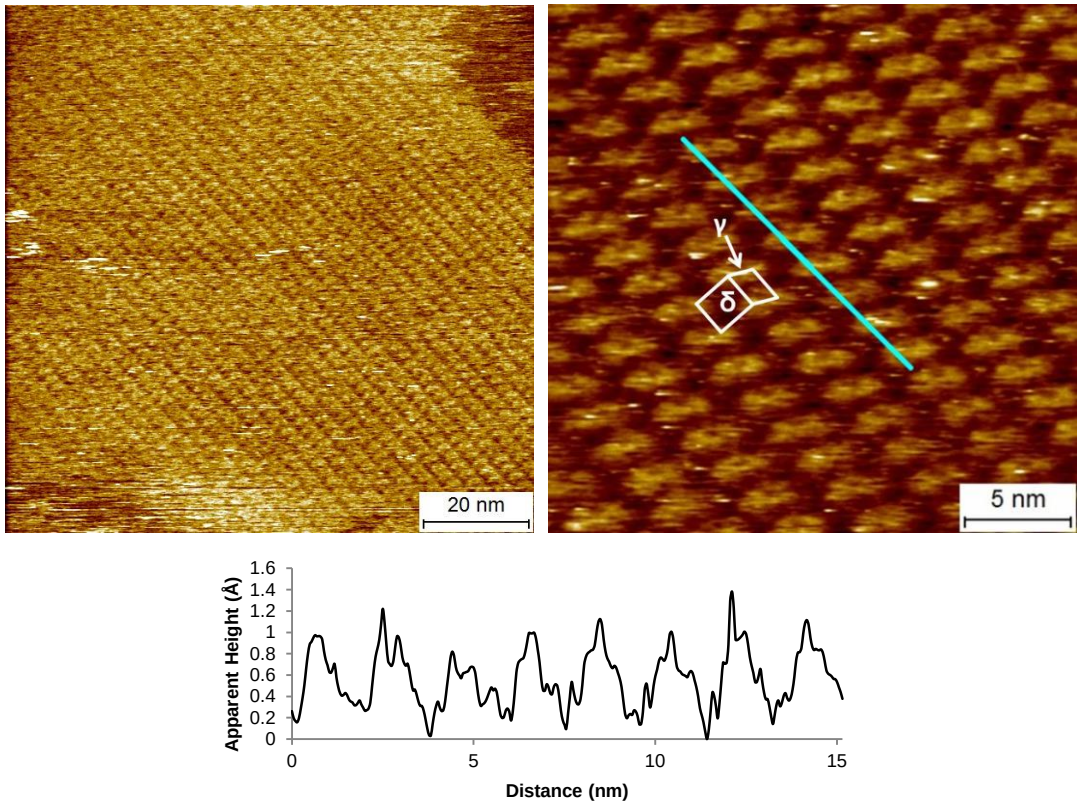

Figure 4.6. STM images and cross-sectional profile of a Ga($TC_{10}P$)(O_2CPh) monolayer on HOPG at the solid–liquid interface (1-phenyloctane, 1.0×10^{-4} M; left: I = 8 pA, V = –1050 mV; right: I = 10 pA, V = –1200 mV). Exposed graphite is seen in the upper right and bottom left corners of the left-hand image. The cross-sectional profile corresponds to the teal line in the image, drawn along the *b* lattice vector of the γ unit cell (the *a* lattice vector of the δ unit cell).

Table 4.2. Lattice Parameters of Monolayers of Ga($TC_{10}P$)(O_2CR) at the 1-Phenyloctane/HOPG Interface. [a]

Compound (lattice)	Conc. (10^{-4} M)	*a* (nm)	*b* (nm)	*Γ* (°)	*A* (nm^2)	density (molecules/nm^2)
$H_2TC_{10}P$ (α)	7.5	1.37(4)	1.75(5)	86(2)	2.39(14)	0.42
Ga($TC_{10}P$)Cl (β)	7.5	1.71(3)	2.09(4)	70(2)	3.36(17)	0.30
Ga($TC_{10}P$)(O_2CPh) (γ)	1.0	1.32(8)	1.69(4)	64(3)	2.01(22)	0.50
(δ)		1.69(4)	1.89(10)	73(4)	3.05(30)	0.33
Ga($TC_{10}P$)(O_2CFc) (γ)	0.5	1.33(7)	1.78(5)	63(3)	2.11(23)	0.47
(δ)		1.78(5)	1.96(10)	71(3)	3.30(32)	0.30
Ga($TC_{10}P$)(O_2CFc) (γ)	1.0	1.34(8)	1.72(3)	63(3)	2.05(21)	0.49
(δ)		1.72(3)	1.89(10)	72(4)	3.09(29)	0.32
Ga($TC_{10}P$)($O_2CC_6H_4pyrC_{60}$) (δ)	1.0	1.75(3)	1.88(4)	68(2)	3.05(16)	0.33
	2.0	1.74(3)	1.88(2)	68(2)	3.03(13)	0.33

[a] Values in parentheses are standard deviations of the last digit(s).

Based on the approximation of the surface contact area of a $TC_{10}P$-containing complex, discussed in Chapter 2, it was determined that the maximum contact areas for $TC_{10}P$ complexes with two and all four decyl side chains fully extended and lying flat on the surface are ~2.2 nm^2 and ~3.4 nm^2, respectively, hence the α (unit cell area = ~2.4 nm^2) and β (unit cell area = ~3.4 nm^2) unit cells were expected to accommodate the adsorption of two and four fully extended decyl chains. The areas occupied by the γ (~2.0 nm^2) and δ (3.0 nm^2) unit cells, however, are smaller than the maximum contact areas approximated for $TC_{10}P$-containing complexes and thus are not expected to allow for the adsorption of two and four fully extended decyl chains. This indicates that in addition to the solvation of alkyl side chains, the molecular configurations of adsorbed Ga($TC_{10}P$)(O_2CPh) and Ga($TC_{10}P$)(O_2CFc) likely involve the folding and overlaying of alkyl chains on top of interdigitated alkyl chains that are adsorbed on the substrate. These phenomena have been suggested by Coenen, et al. in their investigations on $CuTC_{11}P$ monolayers at the 1-octanoic acid/HOPG interface, where STM imaging revealed contrast

variations between regions where alkyl chains were expected to overlap and regions occupied only by alkyl chains directly adsorbed on HOPG.[16]

The formation of $CuT_{11}P$ monolayers characterized by an alternating packing structure is also a known phenomenon.[15, 16] $CuTC_{11}P$ has been reported to form self-assembled structures at the 1-octanoic acid/HOPG interface that exhibited four distinguishable unit cells ("large" (L): l_1 = 1.74 ± 0.08 nm, l_2 = 2.16 ± 0.09 nm, Γ = 76 ± 5°, A = 3.65 ± 0.30 nm^2; "border" (B): b_1 = 1.92 ± 0.09 nm, b_2 = 2.05 ± 0.05 nm, Γ = 71 ± 4°, A = 3.72 ± 0.30 nm^2; "medium" (M): m_1 = 1.26 ± 0.05 nm, m_2 = 1.92 ± 0.09 nm, Γ = 79 ± 4°, A = 2.54 ± 0.12 nm^2; "small" (S): s_1 = 1.26 ± 0.05 nm, s_2 = 1.70 ± 0.15 nm, Γ = 68 ± 4°, A = 2.07 ± 0.16 nm^2), where the L, M, and S polymorphs are favored at concentrations 10^{-7} M , 10^{-4} M , and $>10^{-3}$ M; the alternating row arrangement, formed by a near 1:1 mixture of M and B cells, was favored at a solution concentration of 10^{-6} M. Therefore, the packing structure of $Ga(TC_{10}P)(O_2CPh)$ monolayers can potentially vary as a function of concentration, where an increase in concentration can result in the formation of polymorphs with higher packing densities. Further STM experiments will be required to test this hypothesis.

Self-assembled monolayers of $Ga(TC_{10}P)(O_2CFc)$ are also characterized by an alternating unit cell arrangement when deposited on HOPG from solutions (1.0×10^{-4} M, 5.0×10^{-4} M; the latter concentration is relevant for the post-deposition modification studies discussed in Chapter 5) in 1-phenyloctane. At both concentrations, the monolayers span hundreds of nanometers in width, as shown by a representative images of $Ga(TC_{10}P)(O_2CFc)$ monolayers in Figure 4.7 (1.0×10^{-4} M) and Figure 4.8 (5.0×10^{-4} M), where complete surface coverage can be observed within 100 nm × 100 nm regions of the samples. Despite the similar surface coverage at the onset of STM imaging, monolayers prepared from 5.0×10^{-4} M solutions are not persistent; this is

shown by a comparison between images of the same scan region recorded 15 minutes apart, where the reduction in domain size can be observed (Figure 4.9). Structural analysis (Table 4.2) reveals that the monolayers consist of alternating γ (1.0×10^{-4} M: a = 1.34 ± 0.08 nm, b = 1.72 ± 0.03 nm, Γ = 63 ± 3°; 5.0×10^{-5} M: a = 1.72 ± 0.03 nm, b = 1.89 ± 0.10 nm, Γ = 72 ± 4°) and δ (1.0×10^{-4} M: a = 1.72 ± 0.03 nm, b = 1.89 ± 0.10 nm, Γ = 72 ± 4°; 5.0×10^{-5} M: a = 1.78 ± 0.05 nm, b = 1.96 ± 0.10 nm, Γ = 71 ± 3°) unit cells, which is identical to the packing geometry of Ga($TC_{10}P$)(O_2CPh) monolayers.

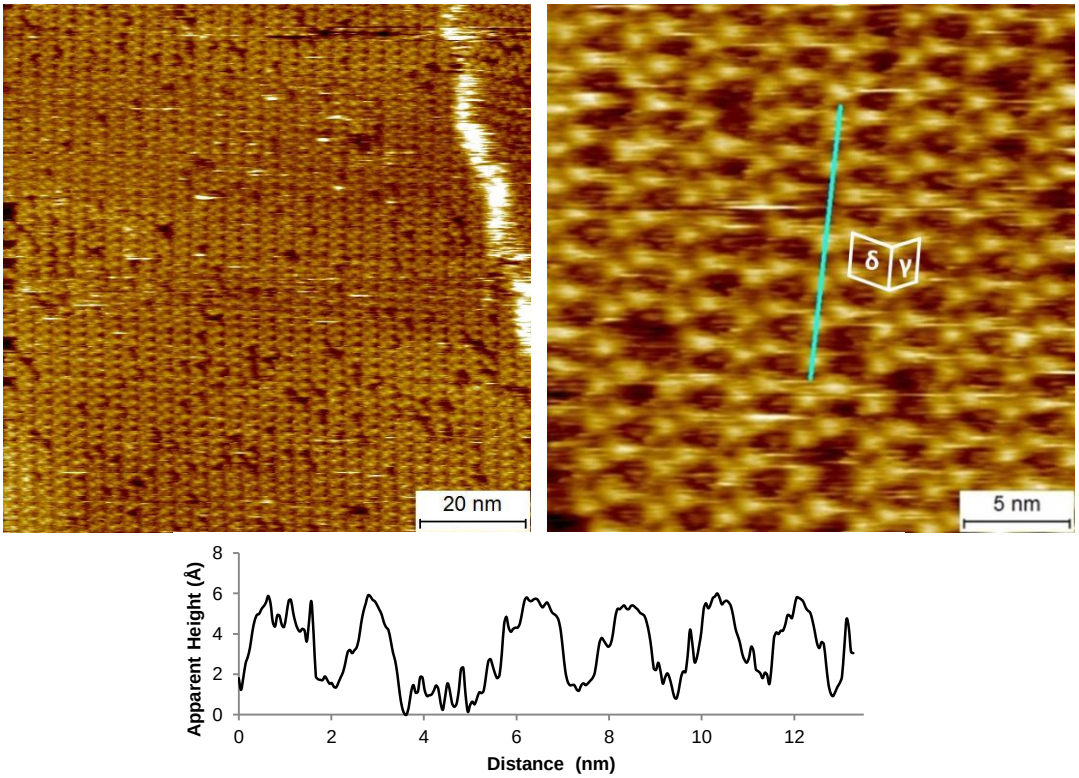

Figure 4.7. STM images and cross-sectional profile of Ga($TC_{10}P$)(O_2CFc) monolayers on HOPG at the solid–liquid interface (1-phenyloctane, 1.0×10^{-4} M; I = 7 pA, V = –950 mV). The cross-sectional profile corresponds to the teal line in the image, drawn along the b lattice vector of the γ unit cell (the a lattice vector of the δ unit cell).

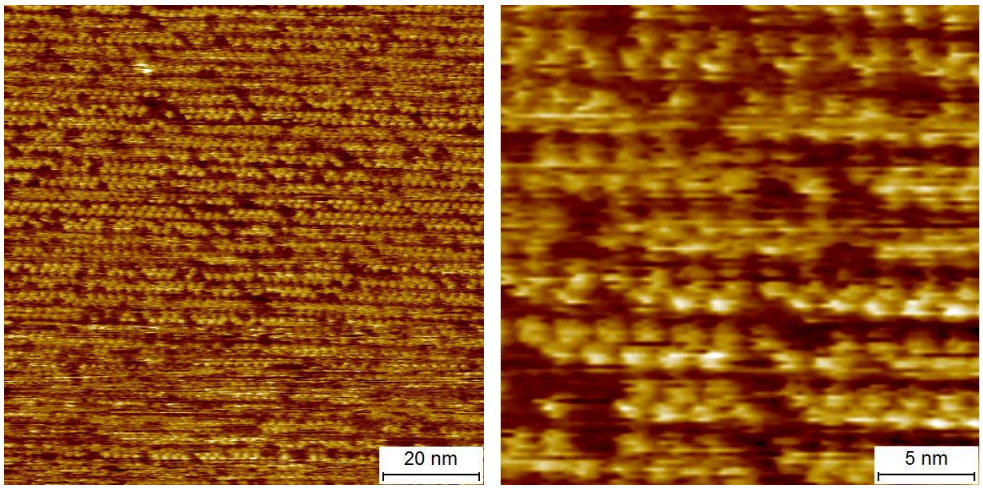

Figure 4.8. STM images of a Ga($TC_{10}P$)(O_2CFc) monolayer on HOPG at the solid–liquid interface (1-phenyloctane, 5.0×10^{-5} M; I = 6 pA, V = –1200 mV).

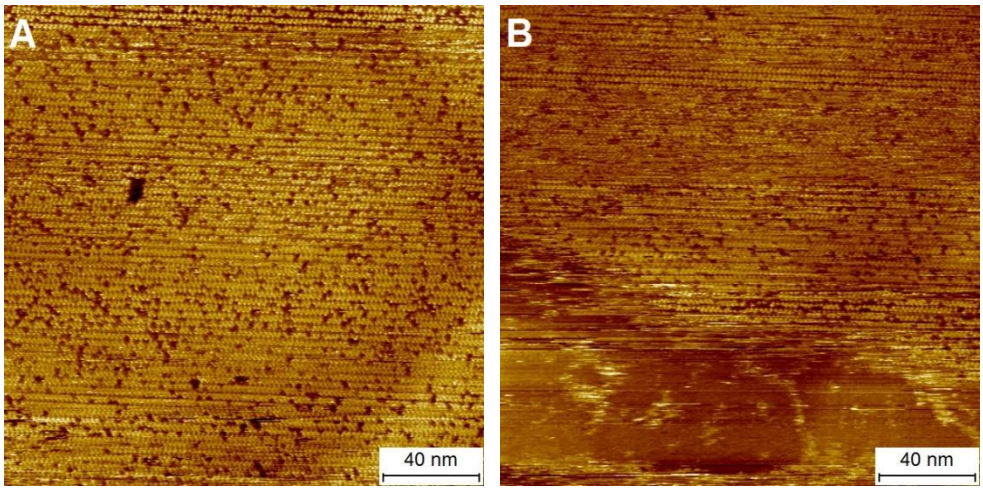

Figure 4.9. STM images of the same scan area of a Ga($TC_{10}P$)(O_2CFc) monolayer on HOPG at the solid–liquid interface (1-phenyloctane, 5.0×10^{-5} M; I = 8 pA, V = –950 mV). (A) was obtained immediately after sample deposition; (B) was recorded 15 minutes later. Note the disruption of the porphyrin monolayer as a result of the scanning process, as evidenced by the bare graphite across the bottom of (B).

Monolayers formed by Ga($TC_{10}P$)(O_2CPh) and Ga($TC_{10}P$)(O_2CFc) can be easily distinguished by their apparent heights. In the cross-sectional profile of a Ga($TC_{10}P$)(O_2CPh) monolayer, the apparent height of the bright spots are ~1 Å, whereas the apparent height of Ga($TC_{10}P$)(O_2CFc) is typically ~5–7 Å, which is consistently observed within the bias voltage range (–800 mV to –1200 mV) used to image monolayers of this complex. The greater apparent

height of Ga($TC_{10}P$)(O_2CFc) is attributed to the molecular orbitals of the electroactive ferrocene moiety being energetically accessible under our STM imaging conditions.[65, 69] In addition to the discrepancy in apparent heights, defects (~5% of the lattice) are consistently observed in Ga($TC_{10}P$)(O_2CFc) monolayers, unlike Ga($TC_{10}P$)(O_2CPh) monolayers which are observed to be defect-free despite the lower surface coverage. The presence of defects appears to have no effect on the packing structure, as evidenced by the lack of structural disorder in the vicinity of the defect sites. The defect sites exhibit apparent heights of ~1.5–2.0 Å, which suggests that they are not vacant; instead, these sites can potentially be filled by Ga($TC_{10}P$)(OH), which may be present as a trace impurity, or fully extended alkyl chains that would otherwise be solvated[70, 71] or overlapped with other adsorbed alkyl chains if the sites were filled by Ga($TC_{10}P$)(O_2CFc).[16]

In order to probe for possible generation of defects during the STM imaging process, consecutive images of the same scan area are analyzed. Figure 4.10a-d shows four consecutive images (Figures 4.10a,c: up scan; Figures 4.10b,d: down scan) that are recorded within a span of ~2 min, and the defect sites are marked with red squares. Aside from the fuzzy features seen in the upper right corners of Figures 4.10b-d attributed to mobile molecules along the lattice edge, and two defect sites which are observed to move out of the scan area due to sample drift, it is apparent that there is no variation in the positions and numbers of defects across all four images, indicating that they are not generated by the imaging process.

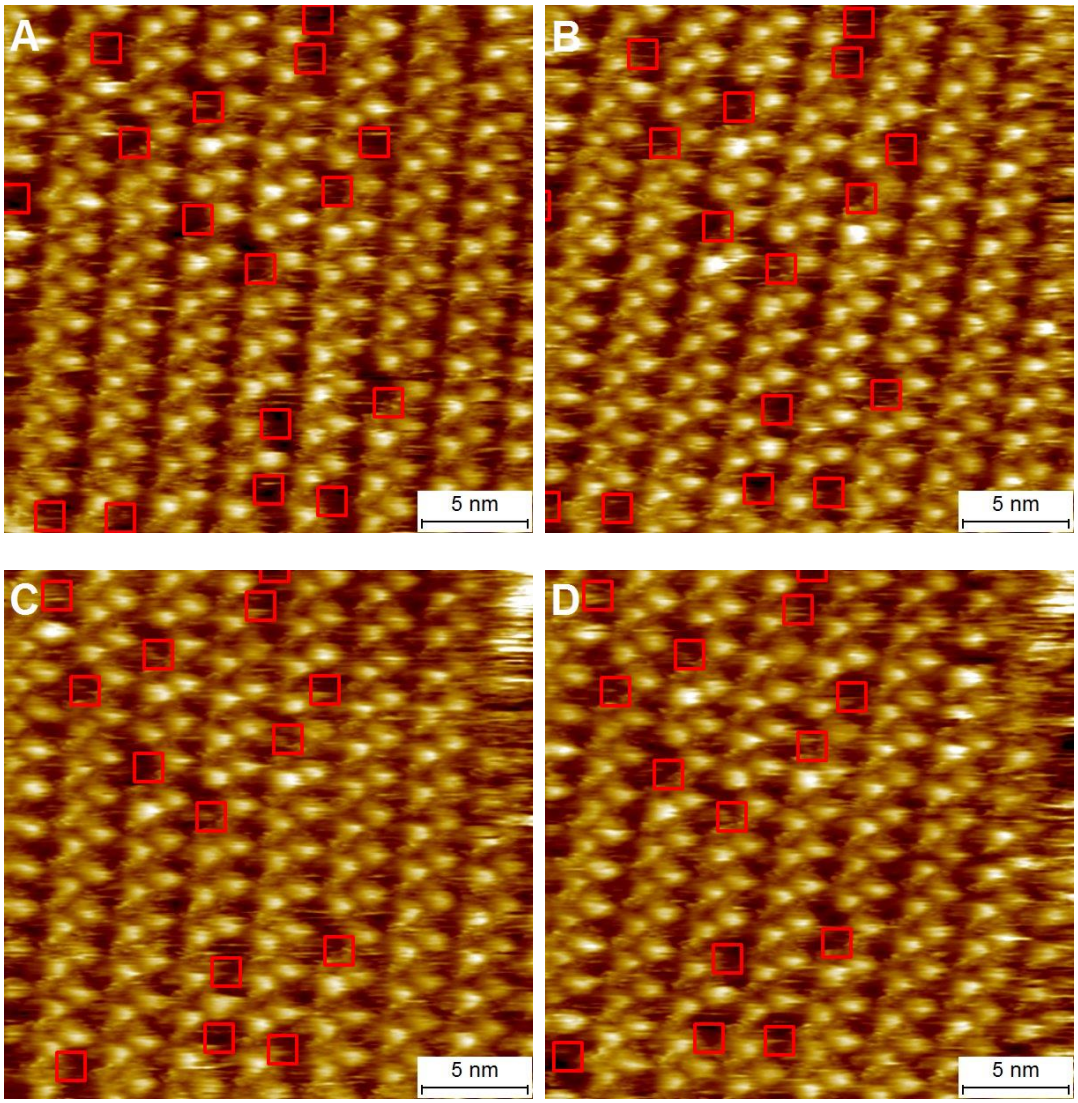

Figure 4.10a-d. Consecutive STM images of a Ga($TC_{10}P$)(O_2CFc) monolayer on HOPG at the solid–liquid interface (1-phenyloctane, 1.0×10^{-4} M; I = 7 pA, V = –950 mV). The defect sites are indicated by red squares. The edge of the lattice can be observed in the upper right corners of B–D.

Further analysis is performed to identify possible causes for the difference between the packing arrangements of the two Ga($TC_{10}P$)(O_2CR) complexes and those of Ga($TC_{10}P$)X compounds that exhibit the α and β structures. First, molecular models of both Ga($TC_{10}P$)(O_2CPh) and Ga($TC_{10}P$)(O_2CFc) arrays are constructed to elucidate the distances between the axial ligands when confined to the observed structural arrangements (Figure 4.11).

This was achieved by positioning the optimized structures of TMeP derivatives of the molecules (see Appendix B) using the unit cell parameters obtained the from STM images; the alkyl chains are omitted since their orientations are not determined from experimental observations.

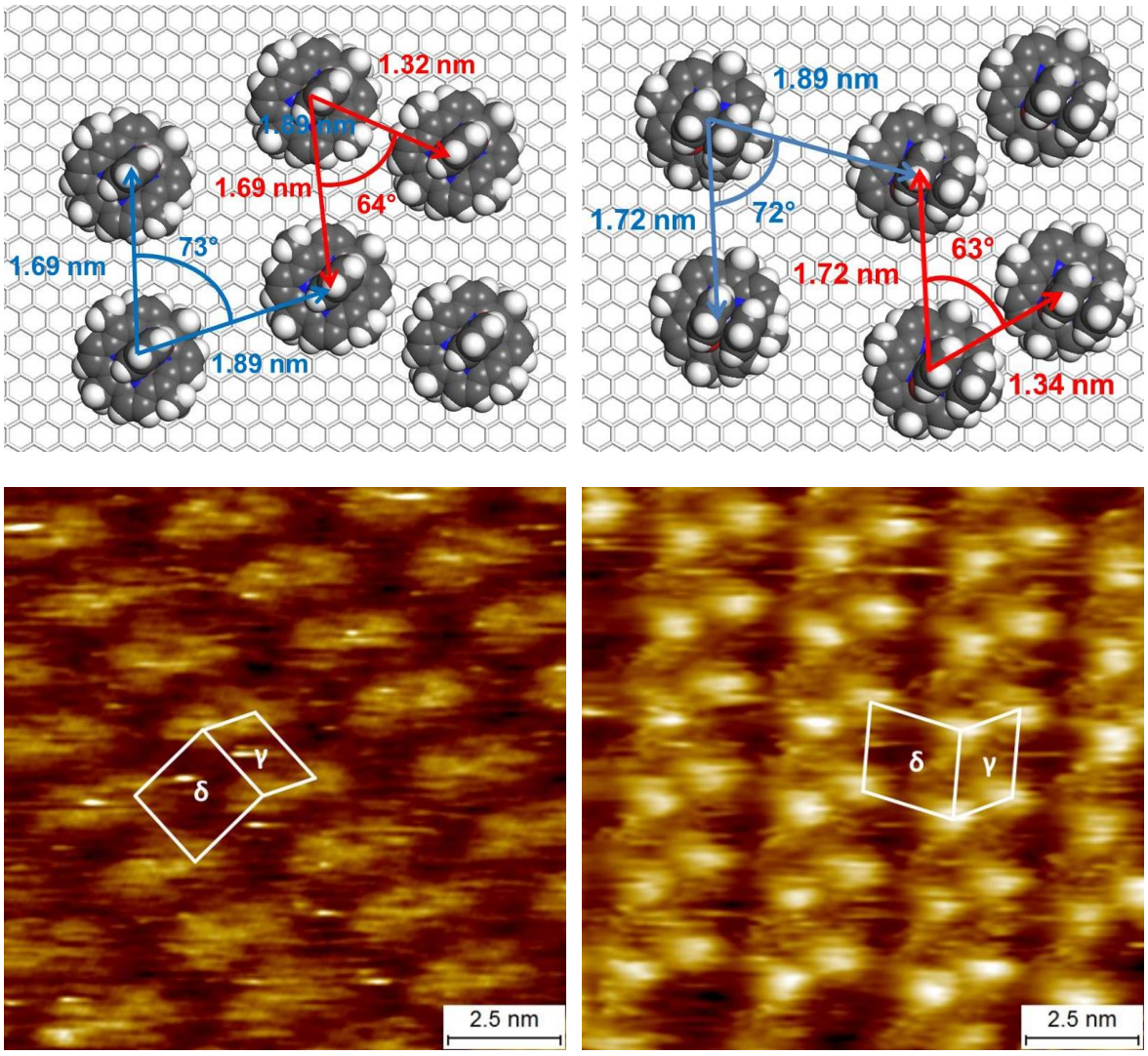

Figure 4.11. Molecular models representing proposed structures of Ga($TC_{10}P$)(O_2CPh) (top left) and Ga($TC_{10}P$)(O_2CFc) (top right) monolayers based on the observed unit cell parameters. The alkyl chains are omitted since their orientations are not observed; the rotational orientation of the porphyrin relative to the lattice vectors is not known. The corresponding STM images, expanded from the 25 nm × 25 nm STM images in Figures 4.6 and 4.7, are shown below the structural models.

After positioning the dyads, the centroid-to-centroid distances between axial ligands are measured along the *a* lattice vector of the γ unit cell — the shortest observed porphyrin-to-

porphyrin distance in the alternating structure — in order to probe for possible inter-ligand π–π stacking or C–H···π interactions. For Ga($TC_{10}P$)(O_2CPh), orienting the axial benzoate groups in the T-shaped configuration (Figure 4.12a) and in the face-to-face configuration (Figure 4.12b) provides centroid-to-centroid distances of ~12.4 Å and ~13.0 Å, respectively. For Ga($TC_{10}P$)(O_2CFc), when the ferrocene ligands are in the face-to-face orientation (Figure 4.12c), the centroid-to-centroid distance between the unsubstituted Cp rings is ~7.5 Å. Since these values are all greater than the length-scale required for π–π stacking (3.54 Å) and C–H···π interactions (4.96 Å), we conclude that the alternating lattice structure is not induced by these particular intermolecular interactions between axial ligands.[72] Given that the steric and electronic characteristics of the Fc and Ph R groups are quite different, it seems more likely that the common structure is a consequence of the carboxylate OCO unit. One speculative possibility, which would require further theoretical and experimental work to probe, is that the arrangement is in some way related to the C=O dipole.

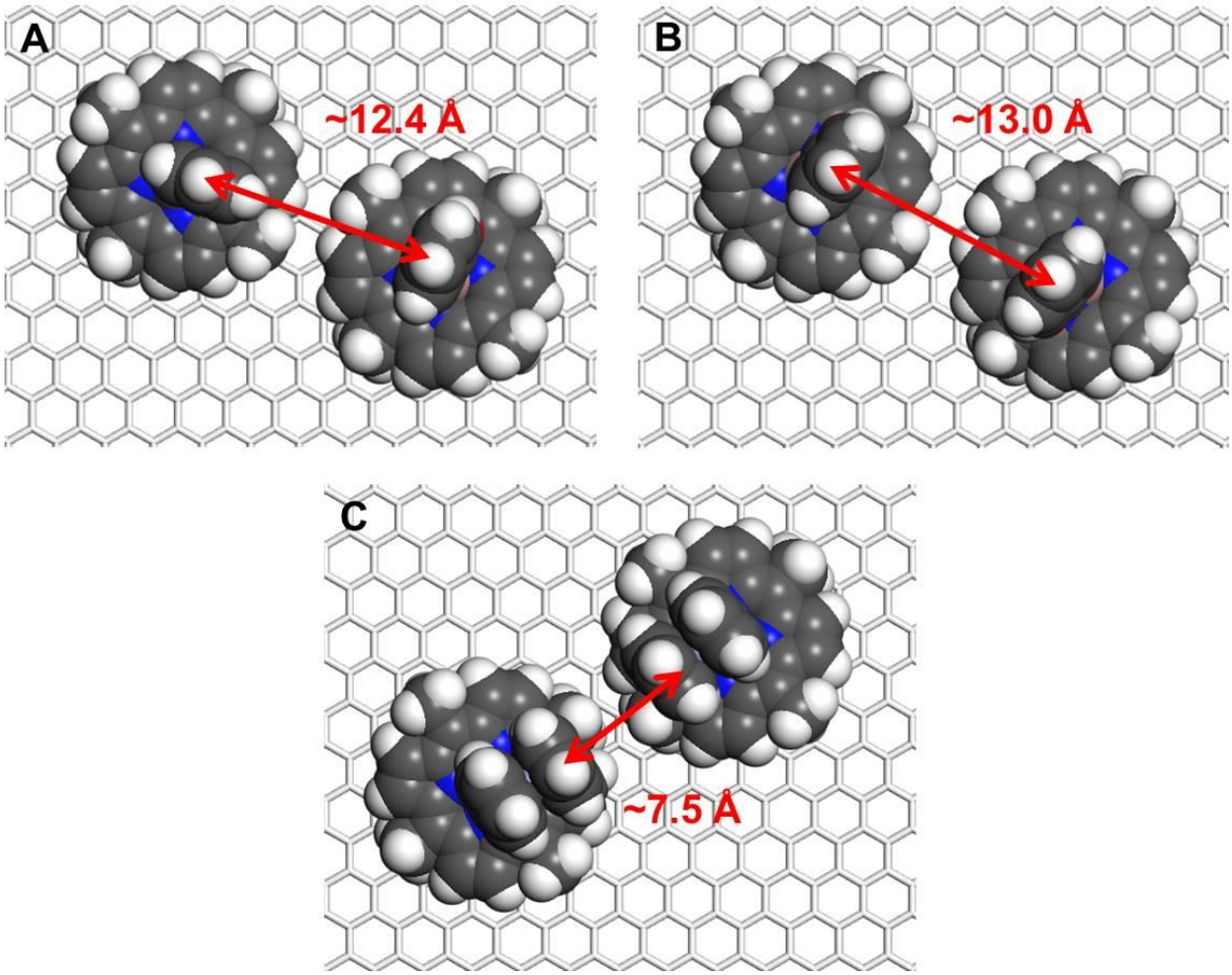

Figure 4.12. Molecular models showing various axial ligand orientations: (A) Ga(TMeP)(O_2CPh) molecules with the axial ligands oriented in the T-shaped configuration; (B) Ga(TMeP)(O_2CPh) molecules with the axial ligands oriented in the face-to-face configuration; (C) Ga(TMeP)(O_2CFc) molecules with the axial ligands oriented in the face-to-face configuration. The molecules are placed along the *a* lattice vector of the γ unit cell. The values represent centroid-to-centroid distances between the phenyl groups of Ga(TMeP)(O_2CPh), and the centroid-to-centroid distance between the Cp groups of Ga(TMeP)(O_2CFc).

4.3.5. STM Imaging of $Ga(TC_{10}P)(O_2CC_6H_4pyrC_{60})$ at the 1-Phenyloctane/HOPG Interface.

Deposition of one drop of a 1.0×10^{-4} M solution $Ga(TC_{10}P)(O_2CC_6H_4pyrC_{60})$ in 1-phenyloctane on HOPG results in the formation of well-ordered self-assembled monolayers spanning tens of nanometers in width (Figure 4.13). Although exposed graphite and defects within the lattices are observed, the $Ga(TC_{10}P)(O_2CC_6H_4pyrC_{60})$ monolayers are stable towards STM imaging, with no noticeable removal of adsorbed molecules after over 50 scans of the same region. Instead of the alternating unit cell structure formed by the previously discussed $Ga(TC_{10}P)(O_2CR)$ compounds, $Ga(TC_{10}P)(O_2CC_6H_4pyrC_{60})$ reproducibly forms self-assembled monolayers with a pseudohexagonal arrangement. Structural analysis provides the lattice parameters a = 1.75 ± 0.03 nm, b = 1.88 ± 0.04 nm, Γ = 68 ± 2° (Table 4.2). This packing arrangement is denoted as the δ structure, since the lattice parameters are within experimental error of the parameters for the δ substructure observed as part of the alternating γ/δ lattice. The periodicity of the monolayer shown in Figure 4.13 is evident in the small-scale image and in the cross-sectional profile, where the adsorbed molecules appeared as bright spherical structures exhibiting apparent heights of ~3–4 Å; both the appearance of apparent height exhibited by $Ga(TC_{10}P)(O_2CC_6H_4pyrC_{60})$ are largely independent of the bias voltage range (−600 mV to −1300 mV) used to image the monolayers. A molecular model of the proposed structural arrangement is shown in Figure 4.14.

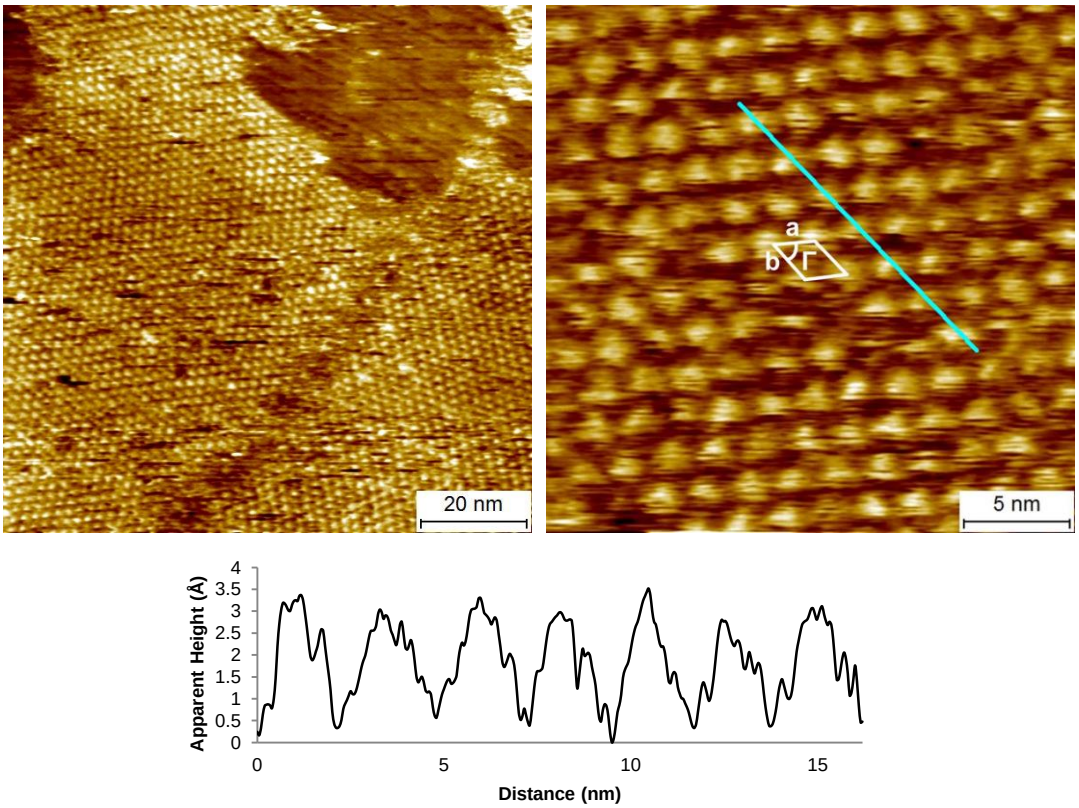

Figure 4.13. STM images and cross-sectional profile of a monolayer of Ga($TC_{10}P$)($O_2CC_6H_4pyrC_{60}$) on HOPG at the solid–liquid interface (1-phenyloctane, 1.0×10^{-4} M; I = 6 pA, V = –900 mV). The cross-sectional profile corresponds to the teal line in the image, drawn along the *b* lattice vector.

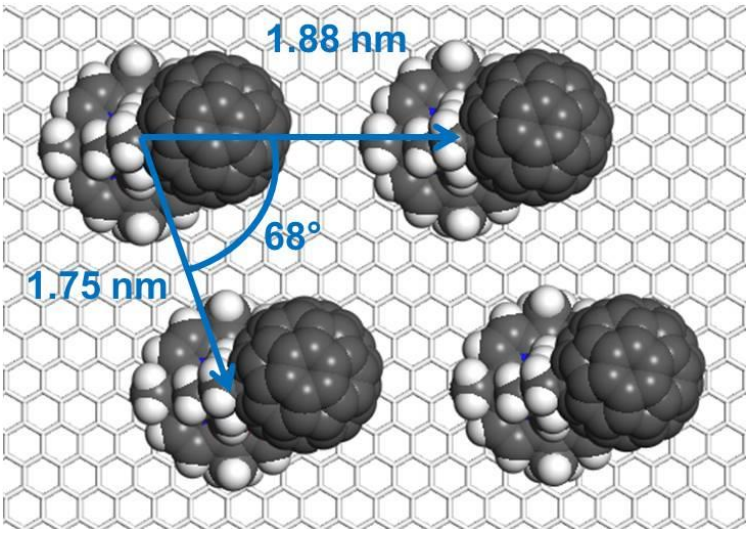

Figure 4.14. Molecular model of a Ga($TC_{10}P$)($O_2CC_6H_4pyrC_{60}$) monolayer constructed using the unit cell parameters obtained from the STM images. The alkyl chains are omitted since their orientations are not observed; the rotational orientation of the porphyrin relative to the lattice vectors is not known.

The self-assembly of $Ga(TC_{10}P)(O_2C_6H_4pyrC_{60})$ is also investigated at solution concentrations of 5.0×10^{-5} M and 2.0×10^{-4} M to probe for possible concentration effects on the packing geometry. While $Ga(TC_{10}P)(O_2C_6H_4pyrC_{60})$ monolayers do not form at 5.0×10^{-5} M, samples prepared 2.0×10^{-4} M solutions contain monolayers that exhibit the δ structure observed above for 1.0×10^{-4} M samples, with lattice parameters $a = 1.74 \pm 0.03$ nm, $b = 1.88 \pm 0.02$ nm, $\Gamma = 68 \pm 2°$ (Figure 4.15). The only notable difference observed for samples prepared with 2.0×10^{-4} M solutions is that the surface coverage is consistently greater, with monolayers spanning widths of hundreds of nanometers.

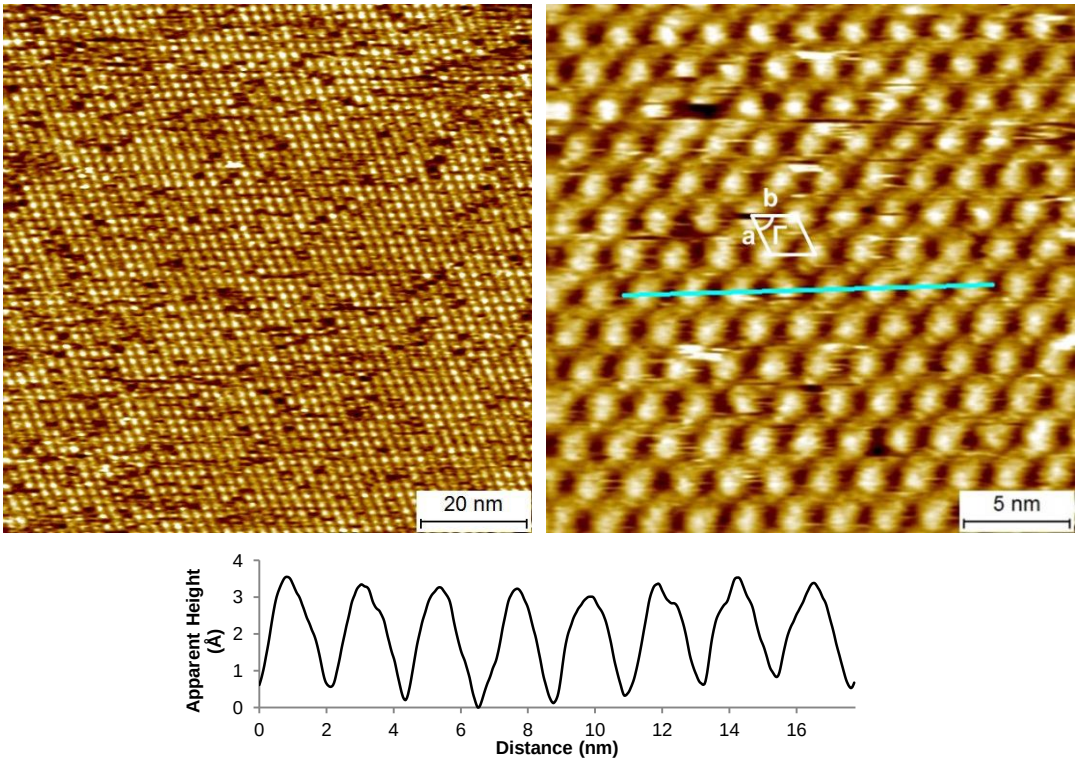

Figure 4.15. STM images and cross-sectional profile of a monolayer of $Ga(TC_{10}P)(O_2CC_6H_4pyrC_{60})$ on HOPG at the solid–liquid interface (1-phenyloctane, 2.0×10^{-4} M; $I = 8$ pA, $V = -1300$ mV). The cross-sectional profile corresponds to the teal line in the image, drawn along the *b* lattice vector.

The similarity between the packing structure of $Ga(TC_{10}P)(O_2CC_6H_4pyrC_{60})$ monolayer and the δ substructure of the alternating unit cell lattice exhibited by $Ga(TC_{10}P)(O_2CPh)$ and

$Ga(TC_{10}P)(O_2CFc)$ monolayers is likely not coincidental. In the aforementioned study on the formation of $CuTC_{11}P$ at the 1-octanoic acid/HOPG interface, Coenen et al. observed monolayers that consisted of mixtures of the M, B, and S polymorphs, which were seamlessly connected due to the sharing of unit cell vectors between the M and B polymorphs, as well as the M and S polymorphs ($b_1 = m_2 = 1.92 \pm 0.09$ nm; $m_1 = s_1 = 1.26 \pm 0.05$ nm).[16] The sharing of unit cell vectors was suggested to be correlated to the conformations of alkyl substituents. For instance, a molecule positioned at the border of an M domain and an S domain would have two alky chains in the $m_1 = s_1$ configuration, one alkyl chain in the m_2 configuration, and one alkyl chain in the s_2 configuration; the latter two alkyl chains would be oriented towards the M domain and the S domain, respectively, which enabled the structural transition between the two domains.

Based on this example, we attribute the similarities between the δ substructure of the alternating arrangement and the packing geometry of the $Ga(TC_{10}P)(O_2CC_6H_4pyrC_{60})$ monolayers to the sharing of alkyl chain conformations. A model depicting the proposed relationship between the alternating γ and δ arrangement and the δ packing structure is shown in Figure 4.16. In this model, each square represents a dyad molecule, and each triangle represents an alkyl chain which extends into the unit cell, where the different colors correspond to unique alkyl chain orientations.

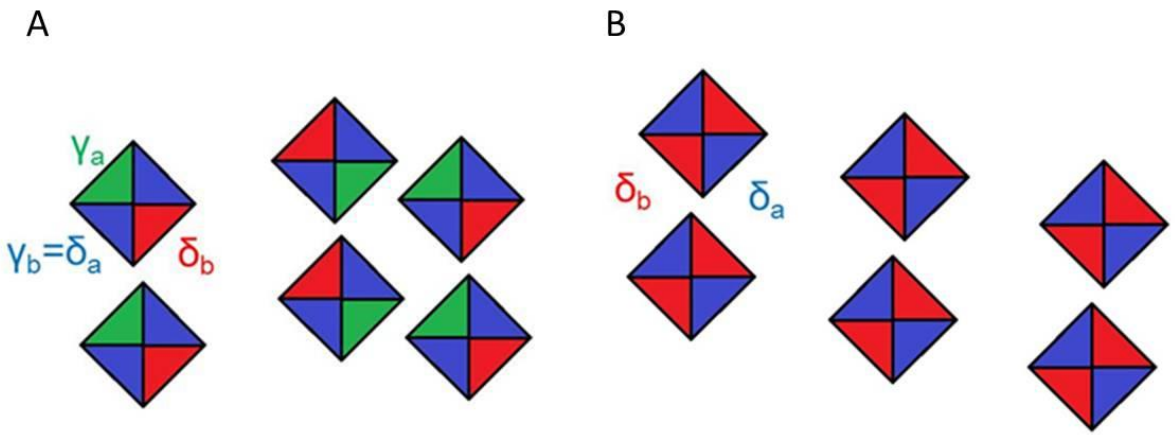

Figure 4.16. Proposed model for the relationship between the (A) alternating γ and δ structure and the (B) packing structure exhibited by Ga($TC_{10}P$)($O_2CC_6H_4pyrC_{60}$) monolayers, denoted as δ. Each colored triangle corresponds to a unique alkyl chain conformation. This model is adapted from Ref. 16.

In Ga($TC_{10}P$)(O_2CPh) and Ga($TC_{10}P$)(O_2CFc) monolayers, the *b* lattice vector of the γ cell and the *a* vector of the δ cell are equivalent, and should therefore correspond to the same alkyl chain conformation (denoted as γ_b/δ_a, shown in blue in Figure 4.16). The *a* lattice vector of the γ cell and the *b* lattice vector of the δ cell, in contrast, are unique to each substructure and represent two additional alkyl chain conformation (denoted as γ_a and δ_b; shown in green and red in Figure 4.14) that are found only in the respective unit cells. The molecular configuration of Ga($TC_{10}P$)(O_2CPh) and Ga($TC_{10}P$)(O_2CFc) within the alternating lattice can therefore be described as having two alkyl chains in the $\gamma_b = \delta_a$ configuration, one alkyl chain in the δ_b configuration, and one alkyl chain in the γ_a configuration (Figure 4.16a). Since the unit cell of Ga($TC_{10}P$)($O_2CC_6H_4pyrC_{60}$) monolayers have the same lattice parameters as the δ substructure in the alternating arrangement but is not connected to γ domains, only one of the alkyl chains of a Ga($TC_{10}P$)($O_2CC_6H_4pyrC_{60}$) molecule should have a different conformation from those of Ga($TC_{10}P$)(O_2CPh) or Ga($TC_{10}P$)(O_2CFc) in the alternating arrangement since; the adsorption

configuration of Ga($TC_{10}P$)($O_2CC_6H_4pyrC_{60}$) should therefore consist of two alkyl chains in the δ_a configuration, and two in the δ_b configuration (Figure 4.14b).

Unlike the previously described Ga($TC_{10}P$)(O_2CR) derivatives, the axial ligand of Ga($TC_{10}P$)($O_2CC_6H_4pyrC_{60}$) extends beyond the porphyrin plane as shown by its space-filling model of the gas-phase optimized structure (Figure 4.17; see Appendix B). The approximate distance from the center of the porphyrin to the outer edge of the molecule (as measured from the plane that bisects the porphyrin core and also contains the benzoic acid moiety, represented by the black lines in Figure 4.17), is approximated to be 1.07 nm. Although this value is smaller than the unit cell vectors of the γ cell, the space between porphyrin molecules above the surface can potentially be occupied by solvated alkyl chains, hence the steric bulk of the ligand can possibly disrupt the formation of the alternating structure.

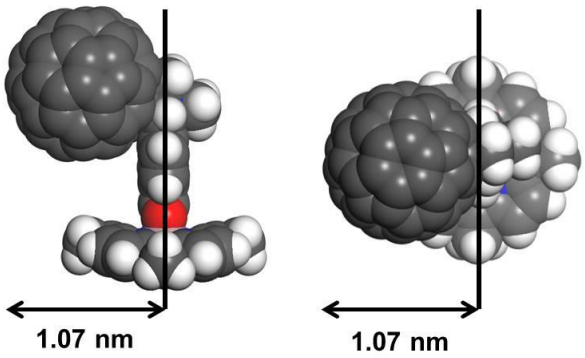

Figure 4.17. Space-filling model of the gas-phase optimized structure of Ga(TMeP)($O_2CC_6H_4pyrC_{60}$).

4.4. Conclusion

The self-assembly of monolayers of gallium-porphyrin carboxylate and aryloxide complexes containing functional axial ligands has been demonstrated at the 1-phenyloctane/HOPG interface. The monolayer structures of Ga($TC_{10}P$)(OR) and Ga($TC_{10}P$)(O_2Ph) complexes were shown to be affected by the axial ligands, which was

exemplified by the observation of four distinctive unit cells; while Ga(TC_{10}P)(OPh) and [Ga(TC_{10}P)(OC_6H_4py)][PF_6] monolayers exhibited the β and α packing structures that were observed in previously investigated TC_{10}P-based systems, two newly observed unit cells, γ and δ, were found in self-assembled monolayers of Ga(TC_{10}P)(O_2CR) complexes. Ga(TC_{10}P)(O_2CPh) and Ga(TC_{10}P)(O_2CFc) monolayers consistently exhibited a packing structure that was characterized by a 1:1 alternating arrangement of γ and δ unit cells, while Ga(TC_{10}P)($O_2CC_6H_4$pyrC_{60}) consistently formed monolayers exclusively in the δ arrangement; the two packing structures were hypothesized to be related by the alkyl chain conformations of the adsorbed Ga(TC_{10}P)(O_2CR) molecules due to the sharing of unit cell vectors. The axial ligand influence on influence on self-assembled monolayer formation was further exemplified by Ga(TC_{10}P)(FME) which, in contrast to other Ga(TC_{10}P)X complexes investigated in this work, appeared to only form ordered monolayers under reduced solution concentrations. The observed monolayers exhibited structural polymorphism and were unstable, although such qualities could be counteracted by the use of the TC_{16}P porphyrin, which forms more stable monolayers. Despite the apparent variations in self-assembling behavior, the high periodicity and reproducibility of the observed monolayers formed by gallium-porphyrin carboxylate and aryloxide complexes suggest that these two classes of compounds are promising as molecular platforms for organizing functional molecules on surfaces, where the 2D packing arrangement can be altered by changing the linker between the Ga-porphyrin and the functional axial subunit.

4.5. References

1. Lehn, J. M. Toward Complex Matter: Supramolecular Chemistry and Self-Organization. *PNAS* **2002**, *99*, 4763-4768.

2. Whitesides, G. M.; Boncheva, M. Beyond Molecules: Self-Assembly of Mesoscopic and Macroscopic Components. *PNAS* **2002**, *99*, 4769-4774.

3. Barth, J. V. Molecular Architectonic on Metal Surfaces. *Annu. Rev. Phys. Chem.* **2007**, *58*, 375-407.

4. Ciesielski, A.; Palma, C. A.; Bonini, M.; Samorì, P. Towards Supramolecular Engineering of Functional Nanomaterials: Pre-Programming Multi-Component 2D Self-Assembly at Solid-Liquid Interfaces. *Adv. Mater.* **2010**, *22*, 3506-3520.

5. Baisch, B.; Raffa, D.; Jung, U.; Magnussen, O. M.; Nicolas, C.; Lacour, J.; Kubitschke, J.; Herges, R. Mounting Freestanding Molecular Functions onto Surfaces: The Platform Approach. *J. Am. Chem. Soc.* **2009**, *131*, 442-443.

6. Kuhn, S.; Baisch, B.; Jung, U.; Johannsen, T.; Kubitschke, J.; Herges, R.; Magnussen, O. Self-Assembly of Triazatriangulenium-Based Functional Adlayers on Au(111) Surfaces. *Phys. Chem. Chem. Phys.* **2010**, *12*, 4481-4487.

7. Jung, U.; Kuhn, S.; Cornelissen, U.; Tuczek, F.; Strunskus, T.; Zaporojtchenko, V.; Kubitschke, J.; Herges, R.; Magnussen, O. Azobenzene-Containing Triazatriangulenium Adlayers on Au(111): Structural and Spectroscopic Characterization. *Langmuir* **2011**, *27*, 5899-5908.

8. Otte, F. L.; Lemke, S.; Schütt, C.; Krekiehn, N. R.; Jung, U.; Magnussen, O. M.; Herges, R. Ordered Monolayers of Free-Standing Porphyrins on Gold. *J. Am. Chem. Soc.* **2014**, *136*, 11248-11251.

9. Lemke, S.; Chang, C.-H.; Jung, U.; Magnussen, O. M. Reversible Potential-Induced Switching of Alkyl Chain Aggregation in Octyl-Triazatriangulenium Adlayers on Au(111). *Langmuir* **2015**, *31*, 3115-3124.

10. Lemke, S.; Ulrich, S.; Claußen, F.; Bloedorn, A.; Jung, U.; Herges, R.; Magnussen, O. M. Triazatriangulenium Adlayers on Au(111): Superstructure as a Function of Alkyl Side Chain Length. *Surf. Sci.* **2015**, *632*, 71-76.

11. Bleger, D.; Mathevet, F.; Kreher, D.; Attias, A. J.; Bocheux, A.; Latil, S.; Douillard, L.; Fiorini-Debuisschert, C.; Charra, F. Janus-Like 3D Tectons: Self-Assembled 2D Arrays of Functional Units at a Defined Distance from the Substrate. *Angew. Chem., Int. Ed.* **2011**, *50*, 6562-6566.

12. Du, P.; Bléger, D.; Charra, F.; Bouchiat, V.; Kreher, D.; Mathevet, F.; Attias, A. J. A Versatile Strategy Towards Non-Covalent Functionalization of Graphene by Surface-Confined Supramolecular Self-Assembly of Janus Tectons. *Beilstein J. Nanotechnol.* **2015**, *6*, 632-639.

13. Du, P.; Kreher, D.; Mathevet, F.; Maldivi, P.; Charra, F.; Attias, A. J. Surface-Confined Supramolecular Self-Assembly of Molecular Nanocranes for Chemically Lifting and Positioning C_{60} above a Conducting Substrate. *ChemPhysChem* **2015**, *16*, 3774-3778.

14. Otsuki, J. STM Studies on Porphyrins. *Coord. Chem. Rev.* **2010**, *254*, 2311-2341.

15. Coenen, M. J. J.; Cremers, M.; den Boer, D.; van den Bruele, F. J.; Khoury, T.; Sintic, M.; Crossley, M. J.; van Enckevort, W. J. P.; Hendriksen, B. L. M.; Elemans, J. A. A. W.; Speller, S. Little Exchange at the Liquid/Solid Interface: Defect-Mediated Equilibration of Physisorbed Porphyrin Monolayers. *Chem. Commun.* **2011**, *47*, 9666-9668.

16. Coenen, M. J. J.; den Boer, D.; van den Bruele, F. J.; Habets, T.; Timmers, K. A. A. M.; van der Maas, M.; Khoury, T.; Panduwinata, D.; Crossley, M. J.; Reimers, J. R.; van Enckevort, W. J. P.; Hendriksen, B. L. M.; Elemans, J. A. A. W.; Speller, S. Polymorphism in Porphyrin Monolayers: the Relation Between Adsorption Configuration and Molecular Conformation. *Phys. Chem. Chem. Phys.* **2013**, *15*, 12451-12458.

17. Reimers, J. R.; Panduwinata, D.; Visser, J.; Chin, Y.; Tang, C. G.; Goerigk, L.; Ford, M. J.; Baker, M.; Sum, T. J.; Coenen, M. J. J.; Hendriksen, B. L. M.; Elemans, J. A. A. W.; Hush, N. S.; Crossley, M. J. From Chaos to Order: Chain-Length Dependence of the Free Energy of Formation of Meso-tetraalkylporphyrin Self-Assembled Monolayer Polymorphs. *J. Phys. Chem. C* **2016**, *120*, 1739-1748.

18. Plamont, R.; Kikkawa, Y.; Takahashi, M.; Kanesato, M.; Giorgi, M.; Shun, A. C. K.; Roussel, C.; Balaban, T. S. Nanoscopic Imaging of *meso*-Tetraalkylporphyrins Prepared in High Yields Enabled by Montmorrilonite K10 and 3Å angstrom Molecular Sieves. *Chem. - Eur. J.* **2013**, *19*, 11293-11300.

19. Poddutoori, P. K.; Bregles, L. P.; Lim, G. N.; Boland, P.; Kerr, R. G.; D'Souza, F. Modulation of Energy Transfer into Sequential Electron Transfer upon Axial Coordination of Tetrathiafulvalene in an Aluminum(III) Porphyrin-Free-Base Porphyrin Dyad. *Inorg. Chem.* **2015**, *54*, 8482-8494.

20. Poddutoori, P. K.; Lim, G. N.; Sandanayaka, A. S. D.; Karr, P. A.; Ito, O.; D'Souza, F.; Pilkington, M.; van der Est, A. Axially Assembled Photosynthetic Reaction Center Mimics Composed of Tetrathiafulvalene, Aluminum(III) Porphyrin and Fullerene Entities. *Nanoscale* **2015**, *7*, 12151-12165.

21. Poddutoori, P. K.; Lim, G. N.; Vassiliev, S.; D'Souza, F. Ultrafast Charge Separation and Charge Stabilization in Axially Linked Tetrathiafulvalene-Aluminum(III) Porphyrin-Gold(III) Porphyrin Reaction Center Mimics. *Phys. Chem. Chem. Phys.* **2015**, *17*, 26346-26358.

22. Poddutoori, P. K.; Sandanayaka, A. S. D.; Hasobe, T.; Ito, O.; van der Est, A. Photoinduced Charge Separation in a Ferrocene-Aluminum(III) Porphyrin-Fullerene Supramolecular Triad. *J. Phys. Chem. B* **2010**, *114*, 14348-14357.

23. Davidson, G. J. E.; Tong, L. H.; Raithby, P. R.; Sanders, J. K. M. Aluminium(III) Porphyrins as Supramolecular Building Blocks. *Chem. Commun.* **2006**, 3087-3089.

24. Ghosh, A.; Maity, D. K.; Ravikanth, M. Aluminium(III) Porphyrin Based Axial-Bonding Type Dyads Containing Thiaporphyrins and Expanded Thiaporphyrins as Axial Ligands. *New J. Chem.* **2012**, *36*, 2630-2641.

25. Iengo, E.; Pantos, G. D.; Sanders, J. K. M.; Orlandi, M.; Chiorboli, C.; Fracasso, S.; Scandola, F. A Fully Self-Assembled Non-Symmetric Triad for Photoinduced Charge Separation. *Chem. Sci.* **2011**, *2*, 676-685.

26. Metselaar, G. A.; Sanders, J. K. M.; de Mendoza, J. A Self-Assembled Aluminium(III) Porphyrin Cyclic Trimer. *Dalton Trans.* **2008**, 588-590.

27. Panda, M. K.; Lazarides, T.; Charalambidis, G.; Nikolaou, V.; Coutsolelos, A. G. Five-Coordinate Indium(III) Porphyrins with Hydroxy and Carboxy BODIPY as Axial Ligands: Synthesis, Characterization and Photophysical Studies. *Eur. J. Inorg. Chem.* **2015**, 468-477.

28. Hartmann, M.; Meyer, G.; Wohrle, D. Polykondensationsreaktionen mit Germaniumkomplexen des Phthalocyanins und *meso*-TetraphenylporphinsPolykondensationsreaktionen mit Germaniumkomplexen des Phthalocyanins und *meso*-Tetraphenylporphins. *Makromol. Chem.* **1975**, *176*, 831-847.

29. Giribabu, L.; Rao, T. A.; Maiya, B. G. "Axial-Bonding"-Type Hybrid Porphyrin Arrays: Synthesis, Spectroscopy, Electrochemistry, and Singlet State Properties. *Inorg. Chem.* **1999**, *38*, 4971-4980.

30. Smith, G.; Arnold, D. P.; Kennard, C. H. L.; Mak, T. C. W. Tin(IV) Porphyrin Complexes - IV. Crystal-Structures of *meso*-Tetraphenylporphyrinatotin(IV) Complexes with Hydroxide, Water, Benzoate, Salicylate and Acetylsalicylate as Axial Ligands. *Polyhedron* **1991**, *10*, 509-516.

31. Lazarides, T.; Kuhri, S.; Charalambidis, G.; Panda, M. K.; Guldi, D. M.; Coutsolelos, A. G. Electron vs Energy Transfer in Arrays Featuring Two Bodipy Chromophores Axially Bound to a Sn(IV) Porphyrin via a Phenolate or Benzoate Bridge. *Inorg. Chem.* **2012**, *51*, 4193-4204.

32. Patra, R.; Titi, H. M.; Goldberg, I. Crystal Engineering of Molecular Networks: Tailoring Hydrogen-Bonding Self-Assembly of Tin-Tetrapyridylporphyrins with Multidentate Carboxylic Acids As Axial Ligands. *Cryst. Gowth Des.* **2013**, *13*, 1342-1349.

33. Arnold, D. P.; Blok, J. The Coordination Chemistry of Tin Porphyrin Complexes. *Coord. Chem. Rev.* **2004**, *248*, 299-319.

34. Shetti, V. S.; Pareek, Y.; Ravikanth, M. Sn(IV) Porphyrin Scaffold for Multiporphyrin Arrays. *Coord. Chem. Rev.* **2012**, *256*, 2816-2842.

35. Elemans, J. A. A. W.; Van Hameren, R.; Nolte, R. J. M.; Rowan, A. E. Molecular Materials by Self-Assembly of Porphyrins, Phthalocyanines, and Perylenes. *Adv. Mater.* **2006**, *18*, 1251-1266.

36. Jurow, M.; Schuckman, A. E.; Batteas, J. D.; Drain, C. M. Porphyrins as Molecular Electronic Components of Functional Devices. *Coord. Chem. Rev.* **2010**, *254*, 2297-2310.

37. Panda, M. K.; Ladomenou, K.; Coutsolelos, A. G. Porphyrins in Bio-Inspired Transformations: Light-Harvesting to Solar Cell. *Coord. Chem. Rev.* **2012**, *256*, 2601-2627.

38. Yang, Y. W.; Sun, Y. L.; Song, N. Switchable Host-Guest Systems on Surfaces. *Acc. Chem. Res.* **2014**, *47*, 1950-1960.

39. Pathem, B. K.; Claridge, S. A.; Zheng, Y. B.; Weiss, P. S. Molecular Switches and Motors on Surfaces. *Annu. Rev. of Phys. Chem.* **2013**, *64*, 605-630.

40. Imahori, H. Porphyrin-Fullerene Linked Systems as Artificial Photosynthetic Mimics. *Org. Biomol. Chem.* **2004**, *2*, 1425-1433.

41. Bucher, C.; Devillers, C. H.; Moutet, J. C.; Royal, G.; Saint-Aman, E. Ferrocene-Appended Porphyrins: Syntheses and Properties. *Coord. Chem. Rev.* **2009**, *253*, 21-36.

42. Pangborn, A. B.; Giardello, M. A.; Grubbs, R. H.; Rosen, R. K.; Timmers, F. J. Safe and Convenient Procedure for Solvent Purification. *Organometallics* **1996**, *15*, 1518-1520.

43. Khan, A. A.; Chee, S. H.; Stocker, B. L.; Timmer, M. S. M. The Synthesis of Long-Chain α-Alkyl-β-Hydroxy Esters Using Allylic Halides in a Frater-Seebach Alkylation. *Eur. J. Org. Chem.* **2012**, 995-1002.

44. Fulmer, G. R.; Miller, A. J. M.; Sherden, N. H.; Gottlieb, H. E.; Nudelman, A.; Stoltz, B. M.; Bercaw, J. E.; Goldberg, K. I. NMR Chemical Shifts of Trace Impurities: Common Laboratory Solvents, Organics, and Gases in Deuterated Solvents Relevant to the Organometallic Chemist. *Organometallics* **2010**, *29*, 2176-2179.

45. Crossley, M. J.; Thordarson, P.; Bannerman, J. P.; Maynard, P. J. A Convenient Procedure for Moderate-Scale Rothemund Synthesis of Lipophilic Porphyrins: An Alternative to the Adler-Longo and Lindsey Methodologies. *J. Porphyrins Phthalocyanines* **1998**, *2*, 511-516.

46. Coutsolelos, A.; Guilard, R.; Bayeul, D.; Lecomte, C. Gallium(III) Porphyrins - Synthesis and Physicochemical Characteristics of Halogeno Gallium(III) Porphyrins X-Ray Crystal-Structure of Chloro-(5,10,15,20-Tetraphenylporphyrinato) Gallium(III). *Polyhedron* **1986**, *5*, 1157-1164.

47. *SPIP Software*, version 6.0.9; Image Metrology A.S: Hørsholm, Denmark

48. Chung, D. D. L. Review Graphite. *J. Mater. Sci.* **2002**, *37*, 1475-1489.

49. Horcas, I.; Fernandez, R.; Gomez-Rodriguez, J. M.; Colchero, J.; Gomez-Herrero, J.; Baro, A. M. WSXM: A Software for Scanning Probe Microscopy and a Tool for Nanotechnology. *Rev. Sci. Instrum.* **2007**, *78*, 013705.

50. Frisch, M. J.; Trucks, G. W.; Schlegel, H. B.; Scuseria, G. E.; Robb, M. A.; Cheeseman, J. R.; Scalmani, G.; Barone, V.; Mennucci, B.; Petersson, G. A.; Nakatsuji, H.; Caricato, M.; Li, X.; Hratchian, H. P.; Izmaylov, A. F.; Bloino, J.; Zheng, G.; Sonnenberg, J. L.; Hada, M.; Ehara, M.; Toyota, K.; Fukuda, R.; Hasegawa, J.; Ishida, M.; Nakajima, T.; Honda, Y.; Kitao, O.; Nakai, H.; Vreven, T.; Montgomery, J., J. A. ; Peralta, J. E.; Ogliaro, F.; Bearpark, M.; Heyd, J. J.; Brothers, E.; Kudin, K. N.; Staroverov, V. N.; Kobayashi, R.; Normand, J.; Raghavachari, K.; Rendell, A.; Burant, J. C.; Iyengar, S. S.; Tomasi, J.; Cossi, M.; Rega, N.; Millam, J. M.; Klene, M.; Knox, J. E.; Cross, J. B.; Bakken, V.; Adamo, C.; Jaramillo, J.; Gomperts, R.; Stratmann, R. E.; Yazyev, O.; Austin, A. J.; Cammi, R.; Pomelli, C.; Ochterski, J. W.; Martin, R. L.; Morokuma, K.; Zakrzewski, V. G.; Voth, G. A.; Salvador, P.; Dannenberg, J. J.; Dapprich, S.; Daniels, A. D.; Farkas, Ö.; Foresman, J. B.; Ortiz, J. V.; Cioslowski, J.; Fox, D. J. *Gaussian 09*, Revision A.2; Gaussian, Inc.: Wallingford, CT, 2009.

51. Becke, A. D. Density-Functional Thermochemistry. III. The Role of Exact Exchange. *J. Chem. Phys.* **1993**, *98*, 5648-5652.

52. Perdew, J. P. Density-Functional Approximation for the Correlation-Energy of the Inhomogeneous Electron-Gas. *Phys. Rev. B* **1986**, *33*, 8822-8824.

53. Kamm, J. M.; Iverson, C. P.; Lau, W.-Y.; Hopkins, M. D. Axial Ligand Effects on the Structures of Self-Assembled Gallium-Porphyrin Monolayers on Highly Oriented Pyrolytic Graphite. *Langmuir* **2016**, *32*, 487-495.

54. Wadt, W. R.; Hay, P. J. *Ab Initio* Effective Core Potentials for Molecular Calculations - Potentials for Main Group Elements Na to Bi. *J. Chem. Phys.* **1985**, *82*, 284-298.

55. Hay, P. J.; Wadt, W. R. Abinitio Effective Core Potentials for Molecular Calculations - Potentials for the Transition-Metal Atoms Sc to Hg. *J. Chem. Phys.* **1985**, *82*, 270-283.

56. Francl, M. M.; Pietro, W. J.; Hehre, W. J.; Binkley, J. S.; Gordon, M. S.; Defrees, D. J.; Pople, J. A. Self-Consistent Molecular-Orbital Methods. XXIII. A Polarization-Type Basis Set for Second-Row Elements. *J. Chem. Phys.* **1982**, *77*, 3654-3665.

57. Hariharan, P. C.; Pople, J. A. Influence of Polarization Functions on Molecular-Orbital Hydrogenation Energies. *Theor. Chim. Acta* **1973**, *28*, 213-222.

58. Sakano, T.; Higashiguchi, K.; Matsuda, K. Comparison of Molecular Conductance Between Planar and Twisted 4-Phenylpyridines by Means of Two-Dimensional Phase Separation of Tetraphenylporphyrin Templates at a Liquid-HOPG Interface. *Chem. Commun.* **2011**, *47*, 8427-8429.

59. Ikeda, T.; Asakawa, M.; Goto, M.; Miyake, K.; Ishida, T.; Shimizu, T. STM Observation of Alkyl-Chain-Assisted Self-Assembled Monolayers of Pyridine-Coordinated Porphyrin Rhodium Chlorides. *Langmuir* **2004**, *20*, 5454-5459.

60. Scudiero, L.; Hipps, K. W. Controlled Manipulation of Self-Organized Ni(II)-Octaethylporphyrin Molecules Deposited from Solution on HOPG with a Scanning Tunneling Microscope. *J. Phys. Chem. C* **2007**, *111*, 17516-17520.

61. Lu, X.; Hipps, K. W.; Wang, X. D.; Mazur, U. Scanning Tunneling Microscopy of Metal Phthalocyanines: d^7 and d^9 Cases. *J. Am. Chem. Soc.* **1996**, *118*, 7197-7202.

62. Stöhr, M.; Wagner, T.; Gabriel, M.; Weyers, B.; Möller, R. Direct Observation of Hindered Eccentric Rotation of an Individual Molecule: Cu-phthalocyanine on C_{60}. *Phys. Rev. B* **2002**, *65*.

63. Gimzewski, J. K.; Joachim, C.; Schlittler, R. R.; Langlais, V.; Tang, H.; Johannsen, I. Rotation of a Single Molecule Within a Supramolecular Bearing. *Science* **1998**, *281*, 531-533.

64. Tahara, K.; Furukawa, S.; Uji-I, H.; Uchino, T.; Ichikawa, T.; Zhang, J.; Mamdouh, W.; Sonoda, M.; De Schryver, F. C.; De Feyter, S.; Tobe, Y. Two-Dimensional Porous Molecular Networks of Dehydrobenzo[12]annulene Derivatives via Alkyl Chain Interdigitation. *J. Am. Chem. Soc.* **2006**, *128*, 16613-16625.

65. Tao, N. J. Probing Potential-Tuned Resonant Tunneling Through Redox Molecules with Scanning Tunneling Microscopy. *Phys. Rev. Lett.* **1996**, *76*, 4066-4069.

66. Sakano, T.; Hasegawa, J.; Higashiguchi, K.; Matsuda, K. Chronological Change from Face-On to Edge-On Ordering of Zinc-Tetraphenylporphyrin at the Phenyloctane-Highly Oriented Pyrolytic Graphite Interface. *Chem. Asian J.* **2012**, *7*, 394-399.

67. Zhou, Y. S.; Wang, B.; Zhu, M. Z.; Hou, J. G. Observation of Co-existence of 'Face-On' and 'Edge-On' Stacking Styles in a Porphyrin Monolayer. *Chem. Phys. Lett.* **2005**, *403*, 140-145.

68. Uemura, S.; Tanoue, R.; Yilmaz, N.; Ohira, A.; Kunitake, M. Molecular Dynamics in Two-Dimensional Supramolecular Systems Observed by STM. *Materials* **2010**, *3*, 4252-4276.

69. Han, W. H.; Durantini, E. N.; Moore, T. A.; Moore, A. L.; Gust, D.; Rez, P.; Leatherman, G.; Seely, G. R.; Tao, N. J.; Lindsay, S. M. STM Contrast, Electron-Transfer Chemistry, and Conduction in Molecules. *J. Phys. Chem. B* **1997**, *101*, 10719-10725.

70. Katsonis, N.; Vicario, J.; Kudernac, T.; Visser, J.; Pollard, M. M.; Feringa, B. L. Self-Organized Monolayer of meso-Tetradodecylporphyrin Coordinated to Au(111). *J. Am. Chem. Soc.* **2006**, *128*, 15537-15541.

71. Visser, J.; Katsonis, N.; Vicario, J.; Feringa, B. L. Two-Dimensional Molecular Patterning by Surface-Enhanced Zn-Porphyrin Coordination. *Langmuir* **2009**, *25*, 5980-5985.

72. Lee, E. C.; Kim, D.; Jurečka, P.; Tarakeshwar, P.; Hobza, P.; Kim, K. S. Understanding of Assembly Phenomena by Aromatic-Aromatic Interactions: Benzene Dimer and the Substituted Systems. *J. Phys. Chem. A* **2007**, *111*, 3446-3457.

CHAPTER 5

Post-Deposition Modification of Gallium-Porphyrin Monolayers on HOPG

5.1. Introduction

Two dimensional assemblies of molecular building blocks such as triazatriangulenium derivatives,[1-6] Janus tectons,[7-9] and metalloporphyrins[10-14] on atomically flat substrates have been shown to serve as attachment points for molecules that extend from the surface. This "molecular platform approach" is a promising method of surface functionalization due to the ease of preparing molecular assemblies, as well as the predictability of the structural morphology of the molecular arrays. Metalloporphyrins are of particular interest due to their known synthetic modularity, which allows for a high degree of control in terms of their chemical properties and self-assembling behavior.[15, 16 17] The ability to exert precise control over the patterning of functional molecules, in turn, is of great importance to the development of functional nanoscale modules.[18-20]

Prior examples of Ga(TC_{10}P)X monolayers supporting functional axial groups were prepared by first synthesizing the molecular building blocks (Chapters 2 and 3), followed by the deposition of the dyads on highly ordered pyrolytic graphite (HOPG) (Chapters 2 and 4). Using this general method, self-assembled monolayers of Ga-porphyrin complexes bearing functional moieties such as oligo-phenylene-ethynylene (OPE) molecular wires, chromophores, and electroactive molecules have been prepared on HOPG at the solid–liquid interface. An alternative approach is to first prepare a self-assembled monolayer of a Ga(TC_{10}P)X precursor molecule, followed by the replacement of the leaving group with a functional ligand *in situ*. This method was previously not pursued in the earlier phase of this work due to the incompatibility of the Ga-acetylide ligand attachment chemistry, which requires the manipulation of precursors

under an inert atmosphere in polar solvents, with the scanning tunneling microscopy (STM) experiments, which are conducted in air at the solid–liquid interface with nonpolar solvents.

The study of the post-deposition modification of self-assembled porphyrin monolayers (Scheme 5.1) is made possible by the facile reactivity of Ga($TC_{10}P$)(OH) towards carboxylic acids. In Chapter 3, we showed that Ga-porphyrin-carboxylate complexes could be readily prepared in air at room temperature within ~5 min. Since the ligand attachment chemistry was performed in hydrocarbon solvents such as C_6D_6 and toluene, it is expected to be compatible with 1-phenyloctane, which is the solvent employed for our STM experiments.

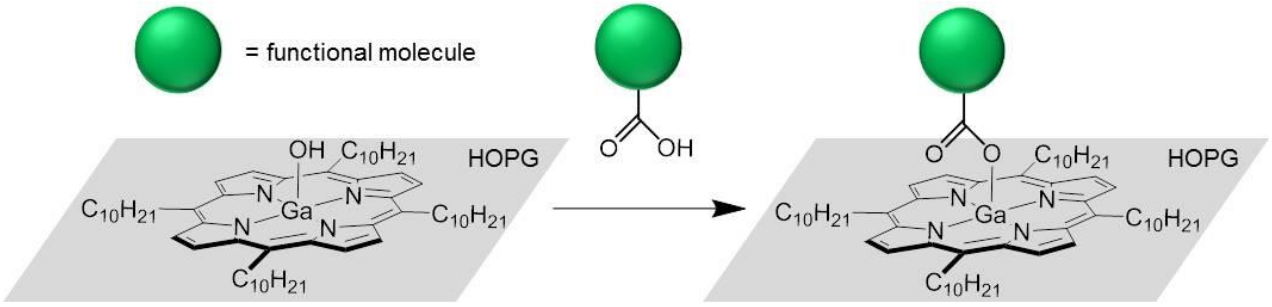

Scheme 5.1. In situ preparation of monolayers of Ga($TC_{10}P$)(O_2CR) bearing functional units via postdeposition modification of Ga($TC_{10}P$)(OH) monolayers with carboxylic acids.

There have been limited accounts of the post-deposition modification of porphyrin monolayers at the solid–liquid interface. Several reports have shown that zinc-porphyrins can bind nitrogenous bases after self-assembled monolayer formation. These occur via reversible dative metal–ligand interactions. Examples of this type include ZnOEP/4-4′-bipyridine coordination polymers supported by HOPG,[12, 13] Zn($TC_{12}P$) monolayers modified through the axial ligation of pyridine at the *n*-tetradecane/HOPG interface,[21] as well as Zn($C_{18}OPP$) ($C_{18}OPP$ = 5,10,15,20-tetra (4-octadecyloxyphenyl)porphyrin) monolayers appended with *cis*- and *trans*-4-(phenylazo)pyridine at the 1-phenylctane/HOPG interface.[22] The modification of Co octaethylporphyrin (Co(OEP)) monolayers on HOPG through the reversible binding of O_2 has

also been demonstrated at the 1-phenyloctane/HOPG interface under conditions of O_2 saturation.[23] Another example is represented by the modification of a Mn-porphyrin monolayer through axial-ligand-induced redox chemistry at the 1-octanoic acid/HOPG interface, although the various species generated *in situ* were transient.[24] In contrast to these previously reported systems, post-deposition modification of porphyrin monolayers using the Ga-carboxylate linkage can offer a way to synthesize persistent surface structures based on kinetically inert covalent bonds.

In this chapter, the self-assembly of $Ga(TC_{10}P)(OH)$ at the 1-phenyloctane/HOPG interface and post-deposition modification of $Ga(TC_{10}P)(OH)$ monolayers with carboxylic acids are described. For post-deposition modification experiments, $FcCO_2H$ and $C_{60}pyrC_6H_4CO_2H$ were chosen because $Ga(TC_{10}P)(O_2CFc)$ and $Ga(TC_{10}P)(O_2CC_6H_4pyrC_{60})$ both form self-assembled structures with packing arrangements that are different from $Ga(TC_{10}P)(OH)$ monolayers (β; $Ga(TC_{10}P)(O_2CFc)$, γ/δ; $Ga(TC_{10}P)(O_2CC_6H_4pyrC_{60})$, δ). This is useful because the monolayers via post-deposition modification could possess a packing geometry distinguishable from those of monolayers formed from solutions of pre-assembled dyads. Additionally, since both dyads were found to exhibit great apparent heights ($Ga(TC_{10}P)(O_2CFc)$: ~5–7 Å; $Ga(TC_{10}P)(O_2CC_6H_4pyrC_{60})$: ~3–4 Å) than $Ga(TC_{10}P)(OH)$ (~1–1.5 Å), these ligands can potentially serve as "contrast agents" that allow for the differentiation between precursor and product porphyrins within a self-assembled monolayer. It is found that post-deposition modification of $Ga(TC_{10}P)(OH)$ monolayers can be achieved via the sequential deposition of $Ga(TC_{10}P)(OH)$ and $FcCO_2H$ solutions to form mixed $Ga(TC_{10}P)(O_2CFc)$/$Ga(TC_{10}P)(OH)$ monolayers that maintain the original structure.

5.2. Experimental Methods

5.2.1. Materials. The preparation and characterization of $C_{60}pyrC_6H_4CO_2H$, $Ga(TC_{10}P)(OH)$ and $Ga(TC_{10}P)(O_2CFc)$ are described in Chapter 3. 1-Phenyloctane and $FcCO_2H$ (Sigma-Aldrich) were used as received.

5.2.2. Sample Preparation for STM Experiments. Highly oriented pyrolytic graphite (HOPG) wafers (SPI-2 grade, SPI Supplies) measuring 7 mm × 7 mm × 1 mm were mounted to 12 mm diameter metal specimen discs with colloidal silver paste (PELCO, Ted Pella, Inc.). The surface of the HOPG substrate was cleaved with adhesive tape immediately prior to dosing. All solutions were deposited with syringes equipped with 25-gauge needles. For STM experiments on $Ga(TC_{10}P)(OH)$ and $Ga(TC_{10}P)(O_2CFc)$ self-assembled monolayers, one drop of a freshly prepared porphyrin solution in 1-phenyloctane [$Ga(TC_{10}P)(OH)$: 5.0×10^{-5} M , 1.0×10^{-4} M, 2.0×10^{-4} M; $Ga(TC_{10}P)(O_2CFc)$: 1.0×10^{-4} M] was deposited on HOPG. The STM tip was then engaged through the drop and the sample was imaged. For post-deposition modification experiments, one drop of $Ga(TC_{10}P)(OH)$ solution in 1-phenyloctane (1.0×10^{-4} M, 2.0×10^{-4} M) was deposited on HOPG surface via syringe, and the resulting sample was imaged. After confirming the presence of porphyrin monolayers on the surface, the STM tip was disengaged, and one drop of a 1-phenyloctane solution of $FcCO_2H$ (1.3×10^{-5} M, 1.0×10^{-4} M) or $C_{60}pyrC_6H_4CO_2H$ (5.0×10^{-5} M, 1.0×10^{-4} M, 2.0×10^{-4} M) was applied to the porphyrin solution on HOPG along the exposed portion of the STM tip. The STM tip was reengaged and the sample was imaged. For the supernatant dilution control experiment, one drop of 1-phenyloctane was added to the porphyrin solution after the formation of $Ga(TC_{10}P)(O_2CFc)$ monolayers was confirmed by STM.

5.2.3. STM Measurements and Data Analysis. STM images were acquired at room temperature using a Digital Instruments Nanoscope IIIa standalone STM. The $Pt_{0.8}Ir_{0.2}$ tips were mechanically cut from a Pt/Ir (80/20) wire (Goodfellow). All measurements were performed in constant current mode. For each sample, an image of the underlying graphite surface was acquired. The data were corrected for drift post-acquisition in the SPIP software package[25] using the underlying graphite lattice parameters (a = b = 0.246 nm, Γ = 60°) as a reference.[26] Data analysis was performed using WSxM 5.0 software.[27] All of the images presented were flattened, low-pass filtered, and sharpened by adjusting the contrast. Reported lattice parameters are averages of those determined from consecutive up-scan and down-scan images. The unit-cell distances were determined from spacings within 100 sets of five consecutive porphyrin molecules, and the unit-cell angles were determined from the average of 40 measurements. For samples that exhibited the alternating unit cell structure, the unit-cell-distances were the averages of 100 measurements of the porphyrin center-to-center distances, and the unit-cell angles were the average of 40 measurements.

5.3. Results and Discussion

5.3.1. STM Imaging of Ga($TC_{10}P$)(OH) at the 1-Phenyloctane/HOPG Interface. In order to provide a structural reference point for post-deposition modification experiments, the self-assembly and structure of monolayers of Ga($TC_{10}P$)(OH) at the 1-phenyloctane/HOPG interface were investigated. The structures of Ga($TC_{10}P$)(OH) self-assembled monolayers were studied at three different concentrations (2.0×10^{-4} M, 1.0×10^{-4} M, 5.0×10^{-5} M) to probe for differences that might result when the Ga($TC_{10}P$)(OH) supernatant is diluted upon subsequent deposition of a carboxylic acid solution.

Deposition on HOPG of one drop of a Ga($TC_{10}P$)(OH) solution in 1-phenyloctane resulted in the formation of monolayers spanning widths of hundreds of nanometers. There is not an apparent difference in surface coverage at the various concentrations (Figure 5.1a, 2.0×10^{-4} M; Figure 5.1b, 1.0×10^{-4} M; Figure 5.1c, 5.0×10^{-5} M). Although regions of exposed graphite are occasionally observed, the monolayers persist for hours without noticeable changes in surface coverage during the scanning process, which indicates that the monolayers are stable towards STM imaging. A representative 25 nm × 25 nm image of Ga($TC_{10}P$)(OH) (Figure 5.1d) shows that the adsorbed molecules appear as bright, ring-like features that are arranged in a periodic pattern. At all concentrations, Ga($TC_{10}P$)(OH) exclusively forms monolayers with the β structure with statistically indistinguishable lattice parameters (Table 5.1); these values are in good agreement with the lattice parameters of Ga($TC_{10}P$)Cl monolayers, which have only been observed to form monolayers with the β packing structure (Chapter 2).

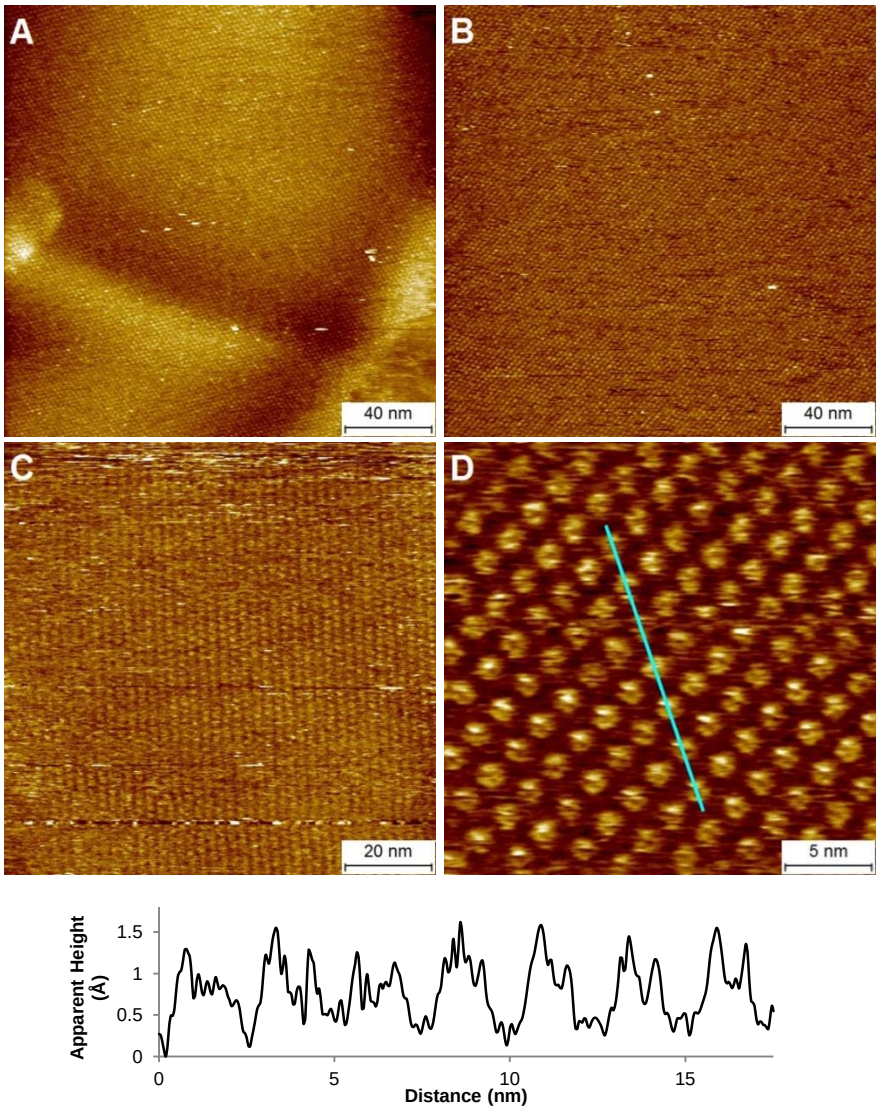

Figure 5.1. STM images and cross-sectional profile of Ga($TC_{10}P$)(OH) monolayers on HOPG at the solid–liquid interface (1-phenyloctane): (A) 2.0×10^{-4} M, I = 9 pA, V = –950 mV; (B) 1.0×10^{-4} M, I = 8 pA, V = –1000 mV; (C) 5.0×10^{-5} M; I = 8 pA, V = –950 mV; (D) 1.0×10^{-4} M, I = 8 pA, V = –950 mV. The cross-sectional profile corresponds to the teal line in (D), drawn along the *b* lattice vector.

Table 5.1. Lattice Parameters of Packing Structures Exhibited by Ga($TC_{10}P$)(OH) and Selected Ga($TC_{10}P$)X Complexes at the 1-Phenyloctane/HOPG Interface.[a]

Compound (lattice)	Conc. (10^{-4} M)	*a* (nm)	*b* (nm)	*Γ* (°)	*A* (nm^2)	density (molecules/nm^2)
Ga($TC_{10}P$)(OH) (β)	0.5	1.66(5)	2.15(4)	67(2)	3.29(21)	0.30
	1.0	1.66(3)	2.14(5)	71(2)	3.36(18)	0.30
	2.0	1.69(3)	2.19(3)	69(2)	3.46(15)	0.29
Ga($TC_{10}P$)Cl (β)[b]	7.5	1.71(3)	2.09(4)	70(2)	3.36(17)	0.30
Ga($TC_{10}P$)(O_2CFc) (γ)[c]	1.0	1.34(8)	1.72(3)	63(3)	2.05(21)	0.49
(δ)[c]		1.72(3)	1.89(10)	72(4)	3.09(29)	0.32
Ga($TC_{10}P$)($O_2CC_6H_4pyrC_{60}$) (δ)[c]	1.0	1.75(3)	1.88(4)	68(2)	3.05(16)	0.33
	2.0	1.74(3)	1.88(2)	68(2)	3.03(13)	0.33

[a] Values in parentheses are standard deviations of the last digit(s). [b] See Chapter 2. [c] See Chapter 4.

The bias-voltage dependence of the monolayer feature shapes and apparent heights exhibited by Ga($TC_{10}P$)(OH) were investigated to determine whether this information could be used to distinguish unreacted surface-bound Ga($TC_{10}P$)(OH) from Ga($TC_{10}P$)(O_2CR) dyad molecules. Depending on the bias voltage, Ga($TC_{10}P$)(OH) monolayers appeared as arrays of lobes (–400 mV to –800 mV; Figure 5.2a–e), rings (–950 mV; Figure 5.2f), or circular features (–1100 mV to –1400 mV; Figure 5.2g–i). These features are attributed to tunneling through the porphyrin macrocycle rather than through the axial ligand, since the measured widths of the features (~1 nm) are comparable to approximate diameter of a porphyrin ring.[28] This is in contrast to Ga($TC_{10}P$)Cl and Ga(OEP)X (X = Cl, Br, I),[14] which can appear as ring-shaped features or bright dots depending on the bias voltage. The former appearance was attributed to tunneling through the porphyrin periphery, and the latter was attributed to axial halide ligands extended above the surface. In addition to the previously reported Ga-porphyrin complexes, the four-coordinate NiOEP has also been imaged with either a bright protrusion or a cavity in the center depending on the bias voltage.[29] The bias-dependent appearance of the Ga($TC_{10}P$)(OH)

monolayer features also contrasts with the observations for Ga($TC_{10}P$)(O_2CFc) and Ga($TC_{10}P$)($O_2CC_6H_4pyrC_{60}$), the shapes of which are largely independent of the bias voltage (Chapter 4).

The apparent height ranges also varied across bias voltages (Table 5.2), but are, on average, consistently shorter than the observed apparent height of Ga($TC_{10}P$)(O_2CFc) and Ga($TC_{10}P$)($O_2CC_6H_4pyrC_{60}$) monolayers (Chapter 4), suggesting that the hydroxide and these carboxylato compounds would be distinguishable by height if they were both present in a mixed monolayer. In STM images obtained at –1100 mV, –1300 mV, and –1400 mV, sporadic bright features with higher contrast (–1100 mV: ~1.6 Å; –1300 mV: ~2.5 Å; –1400 mV: ~5.0 Å) than the background are sometimes observed (identified with red circles in Figures 5.4g–i). Although the reason for the appearance of features with higher contrast within the lattice was unclear, the presence of a different molecular species[30] is unlikely since consecutive images show that the high contrast features are not recurrent.

Table 5.2. Apparent Height Ranges Exhibited by Ga($TC_{10}P$)(OH) Monolayers at Various Bias Voltages.

Bias Voltage (mV)	Figure	Shape	Apparent Height Range (Å)
–400	5.2a	Lobed	1.5 – 2.0
–500	5.2b	Lobed	1.5 – 2.0
–600	5.2c	Lobed	1.5 – 2.0
–700	5.2d	Lobed	1.5 – 2.0
–800	5.2e	Lobed	1.5 – 2.0
–950	5.2f	Ring	1.0 – 1.5
–1100	5.2g	Circular	0.8 – 1.2, 1.6[a]
–1300	5.2h	Circular	1.5 – 2.0, 2.5[a]
–1400	5.2i	Circular	2.5 – 3.0, 5.0[a]

[a] Apparent height exhibited by sporadic bright features.

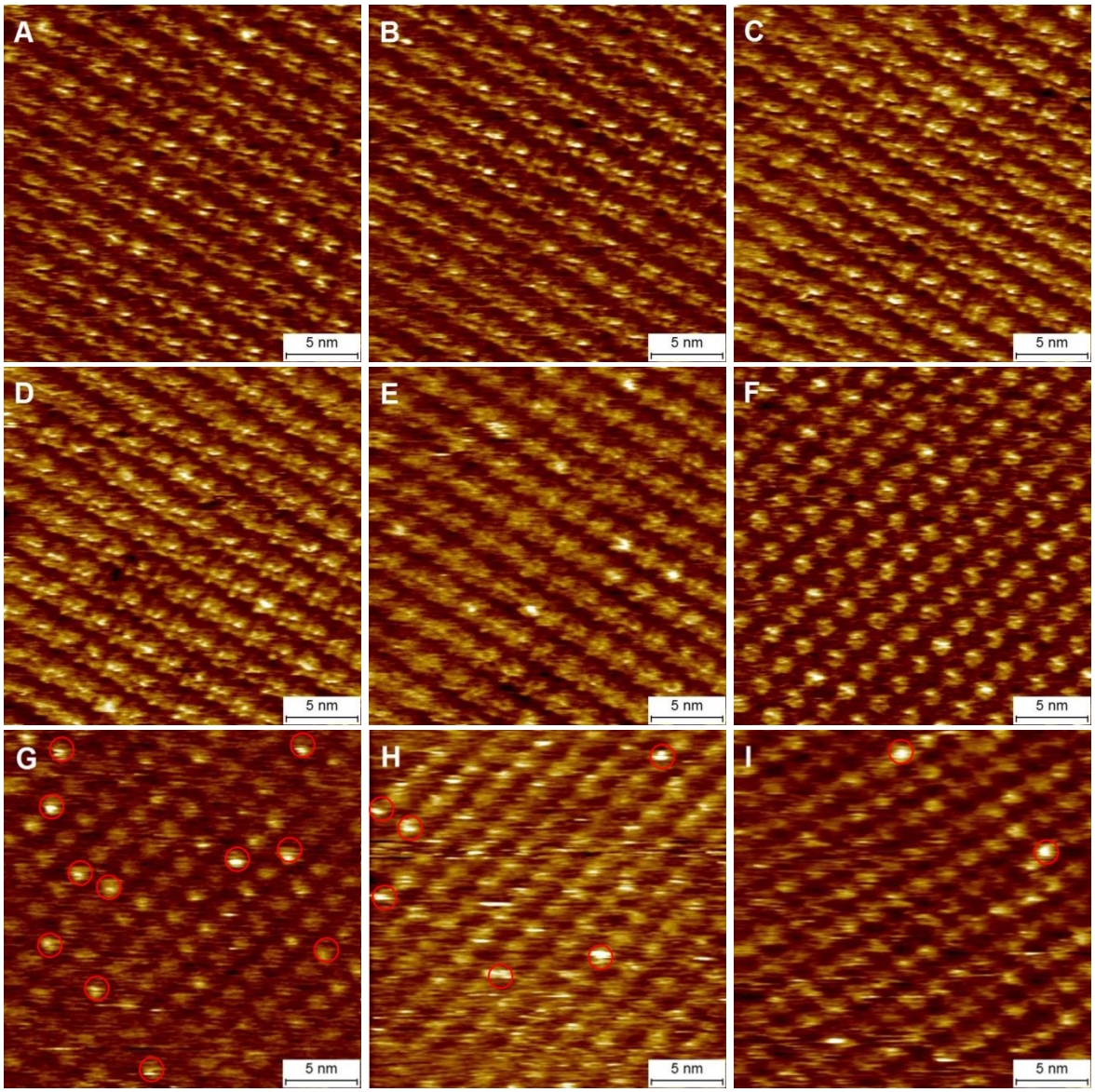

Figure 5.2. STM images of Ga($TC_{10}P$)(OH) monolayers on HOPG at the solid–liquid interface obtained at various bias voltages (1-phenyloctane): (A) 1.0×10^{-4} M, I = 9 pA, V = –400 mV; (B) 1.0×10^{-4} M, I = 9 pA, V = –500 mV; (C) 1.0×10^{-4} M, I = 9 pA, V = –600 mV; (D) 1.0×10^{-4} M, I = 9 pA, V = –700 mV; (E) 1.0×10^{-4} M, I = 9 pA, V = –800 mV; (F) 1.0×10^{-4} M, I = 8 pA, V = –950 mV; (G) 2.0×10^{-4} M, I = 7 pA, V = –1100 mV; (H) 1.0×10^{-4} M, I = 7 pA, V = –1300 mV; (I) 2.0×10^{-4} M, I = 8 pA, V = –1400 mV. Features are described in the text as lobed (A–E), ring-shaped (F), and circular (G–I). Sporadic bright features are marked with red circles in (G–I).

5.3.2. Sequential Deposition of Ga($TC_{10}P$)(OH) and $FcCO_2H$. The use of $FcCO_2H$ in post-deposition modification experiments was predicated not only on its reactivity towards Ga($TC_{10}P$)(OH) but also to the much larger apparent height of the ferrocene moiety compared to the hydroxide ligand in their Ga($TC_{10}P$)X complexes, which should allow the formation of

$Ga(TC_{10}P)(O_2CFc)$ within a $Ga(TC_{10}P)(OH)$ lattice to be clearly observed. To test this hypothesis, the first experiment involved treatment of a $Ga(TC_{10}P)(OH)$ monolayer with < 1 equivalent of $FcCO_2H$, so that conversion substitution of OH ligands in the monolayer by $FcCO_2$ ligands would be incomplete. STM samples were prepared by the sequential deposition of one drop each of a 1.0×10^{-4} M $Ga(TC_{10}P)(OH)$ solution and a 1.3×10^{-5} M $FcCO_2H$ solution, both in 1-phenyloctane, on HOPG. Prior to the addition of $FcCO_2H$, the STM samples were imaged; monolayers of $Ga(TC_{10}P)(OH)$ were observed with the structure and coverage noted in Section 5.3.1. The addition of one drop of $FcCO_2H$ solution to the $Ga(TC_{10}P)(OH)$ solution reduced the concentrations of both components to approximately one-half of the original values; as noted in Section 5.3.1, the structure and surface coverage of $Ga(TC_{10}P)(OH)$ monolayers are essentially identical at these two concentrations. Consistent with this, STM imaging ~5 min after the addition of $FcCO_2H$ (which is required for the STM tip to approach the surface) reveals self-assembled monolayers spanning of hundreds of nanometers in width (Figure 5.3). Bright features are observed to be randomly scattered within the monolayer; images obtained at smaller scan sizes reveal that the bright features with more well-defined shapes are largely aligned to the underlying lattice (Figure 5.3c). The lattice formed by the dim features exhibits the β packing geometry with lattice parameters a = 1.65 ± 0.04 nm, b = 2.05 ± 0.05 nm, Γ = 67 ± 3°; these are within experimental error of the parameters found for pristine $Ga(TC_{10}P)(OH)$ (Table 5.1). The cross-sectional profile shows a sharp contrast between the bright features, which have a height range of 6–7 Å, and the dimmer spots, which have a height range of 1–2 Å. Both sets of values correspond well to the expected height profiles of $Ga(TC_{10}P)(O_2CFc)$ and $Ga(TC_{10}P)(OH)$, respectively, indicating that the bright spots are the result of the incorporation of

$Ga(TC_{10}P)(O_2CFc)$ into the monolayer. Domains with the alternating unit cell structure found for $Ga(TC_{10}P)(O_2CFc)$ are not observed.

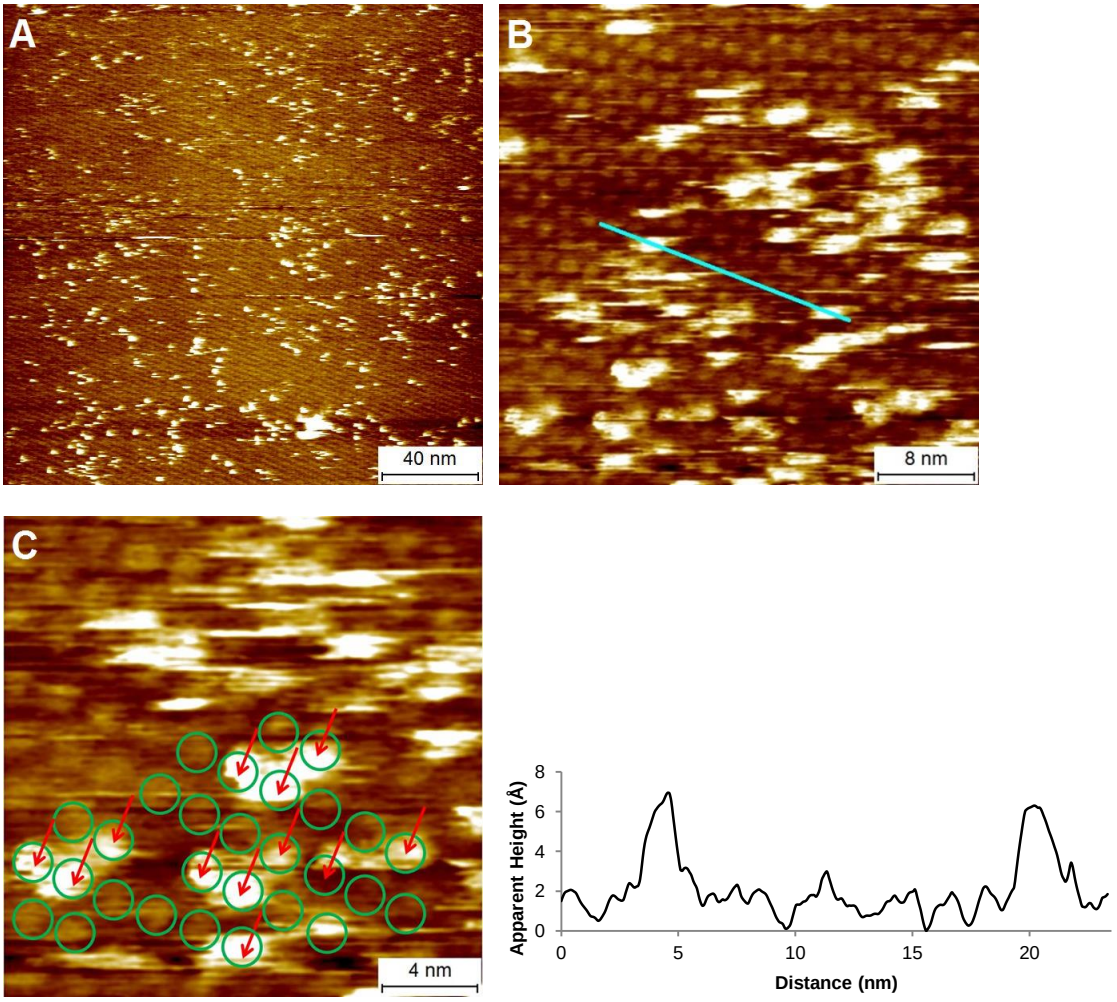

Figure 5.3. STM images and cross-sectional profile of a monolayer of $Ga(TC_{10}P)(OH)$ (1.0×10^{-4} M) on HOPG after the addition of a drop of $FcCO_2H$ solution (1.3×10^{-5} M) at the solid–liquid interface (1-phenyloctane; (A): I = 6 pA, V = -1000 mV; (B) and (C): I = 9 pA, V = –950 mV). The cross-sectional profile corresponds to the teal line in (B), drawn along the *a* lattice vector. (C) is cropped to the bottom left portion of (B); the lattice defined by the dim spots is highlighted with green circles, and the red arrows indicate locations where the bright features are clearly aligned to the lattice.

The sequential deposition experiments were repeated with solutions of $Ga(TC_{10}P)(OH)$ and $FcCO_2H$ of equal concentration (1.0×10^{-4} M), with the aim of increasing the extent of surface modification (ideally to full coverage). STM imaging ~5 min following addition of $FcCO_2H$ to the $Ga(TC_{10}P)(OH)$ monolayer (Figure 5.6) shows the presence of a highly ordered

monolayer that contained a mix of bright and dim spots, with the former predominating (~90%). Structural analysis reveals that both the bright and dim spots conform to the same lattice, with dimensions characteristic of the β structure (a = 1.71 ± 0.04 nm, b = 2.06 ± 0.05 nm, Γ = 71 ± 2°), suggesting that the original packing geometry of the Ga($TC_{10}P$)(OH) lattice was retained (Figure 5.4). The alternating unit cell arrangement found for monolayers prepared from pure Ga($TC_{10}P$)(O_2CFc) (Chapter 4) was not observed for any samples examined. The cross-sectional profile showed that the apparent height ranges of bright spots and the dim spots are 4.5–6 Å and 1.5–2.0 Å, respectively, which are consistent with the typical apparent height ranges exhibited by Ga($TC_{10}P$)(O_2CFc) and Ga($TC_{10}P$)(OH). Together, these observations indicate that the Ga($TC_{10}P$)(O_2CFc) molecules observed in the monolayer result from the on-surface reaction between Ga($TC_{10}P$)(OH) and $FcCO_2H$, rather than from the reaction between these compounds in solution and subsequent deposition on the surface. Although the positions of Ga($TC_{10}P$)(OH) molecules in the monolayer could not be tracked in consecutive images due to drift, we attribute the presence of Ga($TC_{10}P$)(OH) to incomplete reaction rather than the filling of defect sites because such defect site were not observed to be generated in Ga($TC_{10}P$)(O_2CFc) monolayers during STM scanning (see Chapter 4).

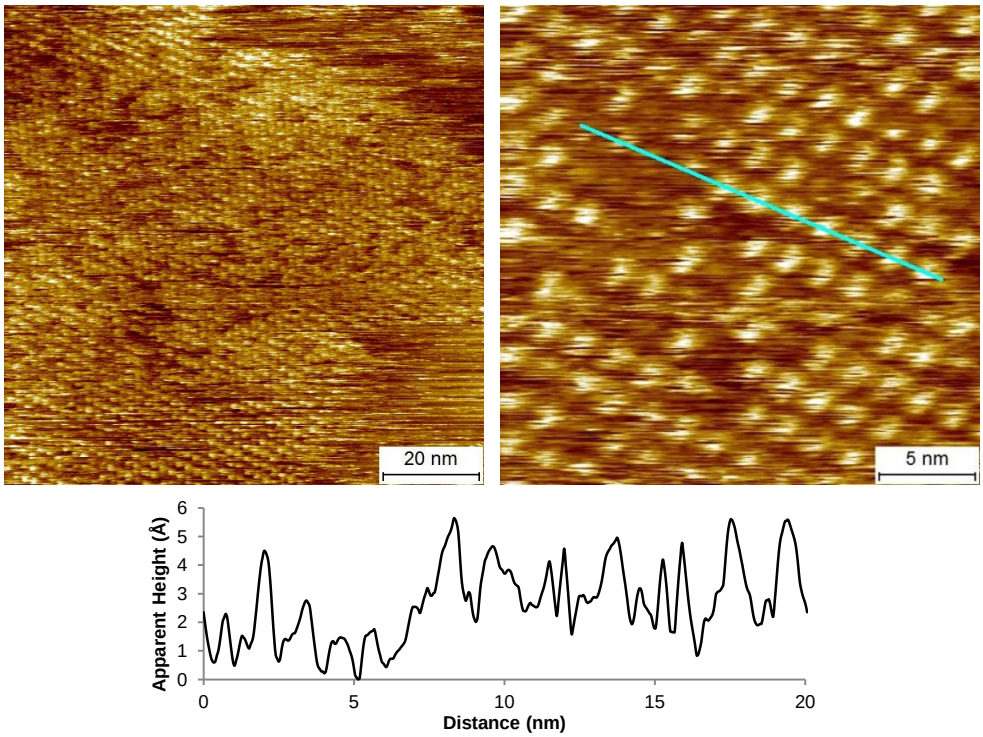

Figure 5.4. STM images and cross-sectional profile of a monolayer of Ga($TC_{10}P$)(OH) (1.0×10^{-4} M) on HOPG after the addition of one drop of $FcCO_2H$ solution (1.0×10^{-4} M) at the solid–liquid interface (1-phenyloctane; left: I = 7 pA, V = –1000 mV; right: I = 6 pA, V = –1100 mV). The cross-sectional profile corresponds to the teal line in the image, drawn along the *a* lattice vector.

Unlike the case where less than one equivalent of $FcCO_2H$ was added, the surface coverage of the monolayers resulting from the deposition of one equivalent of $FcCO_2H$ was less than that of the original Ga($TC_{10}P$)(OH) monolayer. Monolayers usually span ~80–100 nm in width, although monolayers with domains sizes of over 200 mm × 200 nm are occasionally observed (Figure 5.5). Figure 5.6 shows consecutive images of a Ga($TC_{10}P$)(O_2CFc) monolayer, which were recorded within ~7 min. Structural disorder ("fuzzy regions") can be observed along the left edge of the lattice as well as the bottom of the image, where the gradual expansion of a cavity within the monolayer is observed. This suggests that the mixed Ga($TC_{10}P$)(O_2CFc)/Ga($TC_{10}P$)(OH) monolayers are less stable in the β packing geometry than

either those of the pristine Ga($TC_{10}P$)(O_2CFc) alternating structure or the Ga($TC_{10}P$)(OH) monolayers.

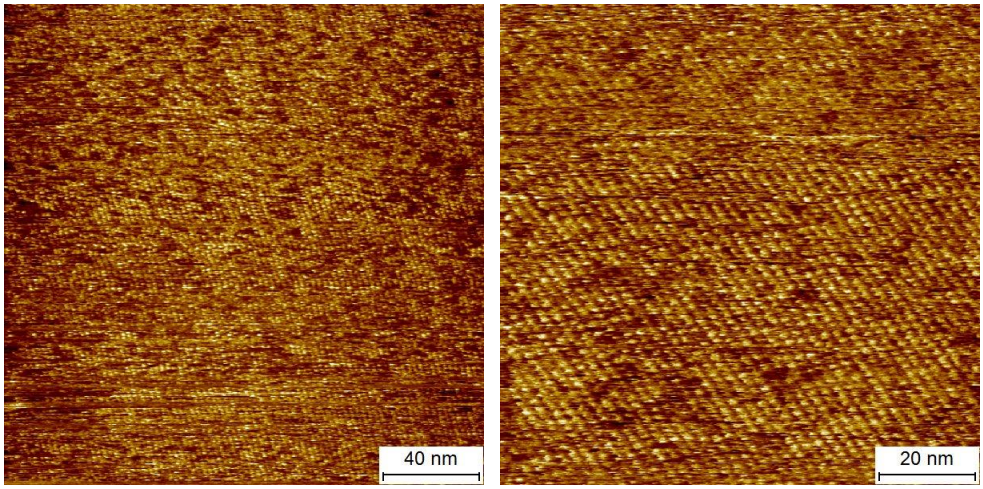

Figure 5.5. STM images of a monolayer of Ga($TC_{10}P$)(OH) (1.0×10^{-4} M) on HOPG after the addition of a drop of $FcCO_2H$ solution (1.0×10^{-4} M) at the solid–liquid interface with a greater domain size (1-phenyloctane; I = 8 pA, V = –950 mV; right: I = 6 pA, V = –1100 mV).

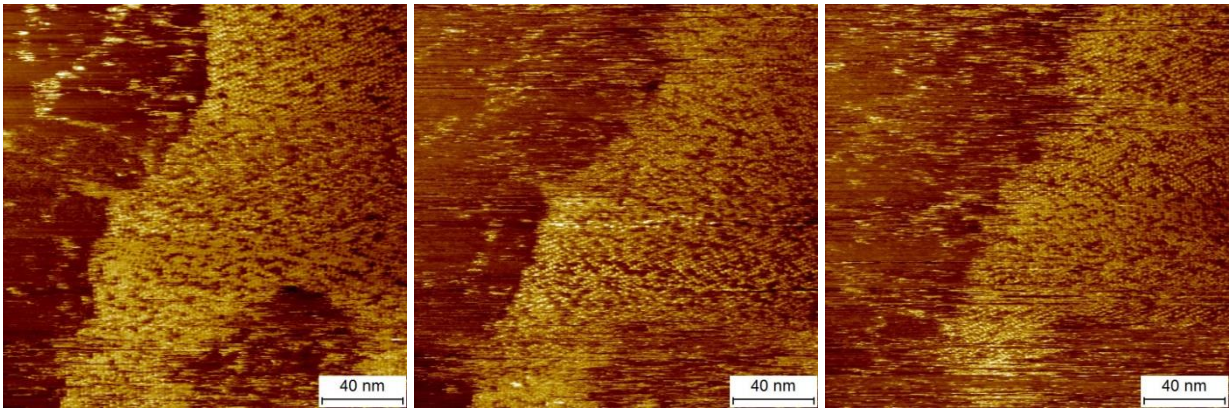

Figure 5.6. Sequential STM images (left to right) of a Ga($TC_{10}P$)(OH) (1.0×10^{-4} M) monolayer on HOPG after addition of one drop of $FcCO_2H$ solution (1.0×10^{-4} M) at the solid–liquid interface (1-phenyloctane; I = 8 pA, V = –950 mV). Removal of adsorbed molecules can be observed on the left edge of the lattice, as well as the cavity within the monolayer near the bottom of the images.

5.3.3. Sequential Deposition of Ga($TC_{10}P$)(OH) and 1-Phenyloctane. Post-deposition modification of Ga($TC_{10}P$)(OH) monolayers through addition of a $FcCO_2H$ solution dilutes the supernatant. It is known that the lattice parameters of Ga($TC_{10}P$)(O_2CFc) monolayers formed

from the presynthesized compound are independent of concentration, including that equivalent to the diluted supernatant (5.0×10^{-5} M, Chapter 4). However, the process of dilution during the postdeposition modification method could produce concentration gradients or other effects that might not be well modeled by the concentration dependence studies. To probe for possible structural changes in Ga($TC_{10}P$)(O_2CFc) monolayers induced by the sample preparation process, the sequential deposition of Ga($TC_{10}P$)(O_2CFc) and neat 1-phenyloctane was also investigated. Ga($TC_{10}P$)(O_2CFc) monolayers were first prepared by depositing a 1.0×10^{-4} M solution on HOPG and imaged to confirm they possessed the typical structure and lattice parameters (Figure 5.7a). The supernatant was then diluted by applying a drop of neat 1-phenyloctane, reducing the effective solution concentration to 5.0×10^{-5} M. For samples prepared in this manner, the alternating unit cell arrangement is retained after the addition of 1-phenyloctane, but a reduction in surface coverage is consistently observed at the onset of STM imaging (Figure 5.7b). In some trials, only small monolayer domains, measuring tens of nanometers on the sides, are observed, and are quickly removed during STM imaging, as shown by consecutive images recorded of the same domain (Figure 5.8). Despite the instability of these small domains, they are also clearly characterized by the alternating unit cell arrangement. The observation of reduced domain size in samples prepared via sequential deposition is in contrast to samples prepared from 5.0×10^{-5} M Ga($TC_{10}P$)(O_2CFc) solutions, where high surface coverage was consistently observed at the onset of STM imaging. Since the 1-phenyloctane droplet was added along the exposed portion of the STM tip, it could potentially cause inhomogeneity in concentration within the sample assuming that solution mixing was slow. The reduction in domain size may be the result of a reduced local concentration of Ga($TC_{10}P$)(O_2CFc) around the STM tip from the addition of 1-phenyloctane, which would favor the desorption of molecules from the substrate around the scan

area.[31, 32] Nonetheless, since the alternating unit cell arrangement is consistently observed regardless of domain size, this finding is consistent with the hypothesis that the β structure of the mixed Ga($TC_{10}P$)(O_2CFc)/Ga($TC_{10}P$)(OH) monolayers results from retention of the original Ga($TC_{10}P$)(OH) structure following reaction at the surface.

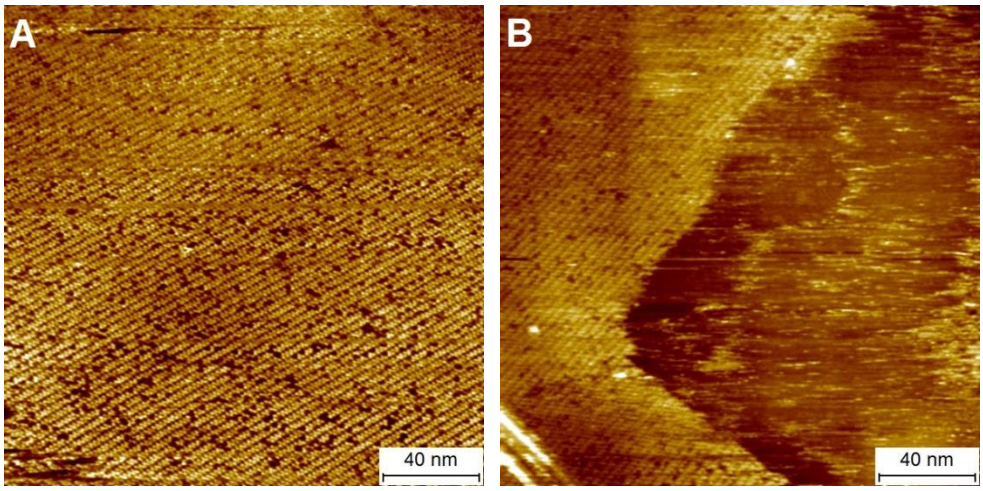

Figure 5.7. STM images of a Ga($TC_{10}P$)(O_2CFc) monolayer on HOPG before (A) and after (B) dilution of the 1.0 × 10^{-4} M supernatant (1-phenyloctane) with neat 1-phenyloctane (final concentration ~5.0 × 10^{-5} M); (A): I = 7 pA, –1000 mV; (B): I = 6 pA, –1000 mV.

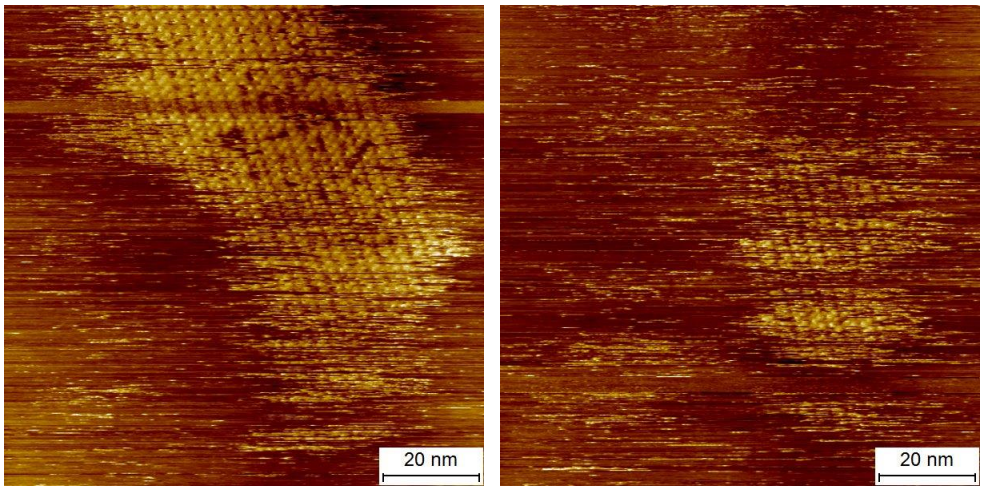

Figure 5.8. Consecutive STM images (recorded within ~3 min) of a Ga($TC_{10}P$)(O_2CFc) monolayer on after dilution of the 1.0 × 10^{-4} M supernatant (1-phenyloctane) with neat 1-phenyloctane (final concentration ~5.0 × 10^{-5} M; I = 7 pA, –1000 mV), showing the removal of adsorbed molecules during the imaging process.

5.3.4. Sequential Deposition of Ga($TC_{10}P$)(OH) and $C_{60}pyrC_6H_4CO_2H$. Post-deposition modification of Ga($TC_{10}P$)(OH) monolayers with $C_{60}pyrC_6H_4CO_2H$ was also

investigated to test for the generality of this surface functionalization method. $C_{60}pyrC_6H_4CO_2H$, like $FcCO_2H$, rapidly reacts with $Ga(TC_{10}P)(OH)$ in benzene and toluene to form $Ga(TC_{10}P)(O_2CC_6H_4pyrC_{60})$. Since $Ga(TC_{10}P)(O_2CC_6H_4pyrC_{60})$ exclusively forms self-assembled structures with a δ unit cell, which is distinguishable from the β structure exhibited by $Ga(TC_{10}P)(OH)$ monolayers, observation of $Ga(TC_{10}P)(O_2CC_6H_4pyrC_{60})$ monolayers with the β structure in post-deposition modification experiments would suggest that these complexes form via on-surface reactions.

Because $Ga(TC_{10}P)(O_2CC_6H_4pyrC_{60})$ does not form self-assembled monolayers on HOPG when deposited from a 5.0×10^{-5} M solution (Chapter 4), sequential deposition experiments were performed using 2.0×10^{-4} M solutions of $Ga(TC_{10}P)(OH)$ and $C_{60}pyrC_6H_4CO_2H$. After confirming the presence of $Ga(TC_{10}P)(OH)$ monolayers by STM imaging, one drop of $C_{60}pyrC_6H_4CO_2H$ solution was added to the $Ga(TC_{10}P)(OH)$ solution, which reduced the effective concentrations of both components to approximately 1.0×10^{-4} M. STM imaging of the sample reveals highly periodic structures spanning areas of up to 100 nm in width (Figure 5.9); this is much less than that of the original $Ga(TC_{10}P)(OH)$ monolayer, but is consistent with the surface coverage of pristine $Ga(TC_{10}P)(O_2CC_6H_4pyrC_{60})$ monolayers formed at a solution concentration of 1.0×10^{-4} M (Chapter 4). Regions of exposed graphite are also observed, but the disruption of monolayers does not result from repeated scanning, indicating that the porphyrin monolayers are persistent. The monolayers exhibit the δ structure, and the cross-sectional profile shows an apparent height range of ~2.5–3.5 Å, which is consistent with those observed for $Ga(TC_{10}P)(O_2CC_6H_4pyrC_{60})$ when imaged at the same bias voltage (Figure 5.10). Thus, the monolayer resulting from the sequential deposition of $Ga(TC_{10}P)(OH)$ and $C_{60}pyrC_6H_4CO_2H$ solutions is indistinguishable from monolayers prepared by depositing the pre-

formed dyad. Unlike the observations for Ga($TC_{10}P$)(O_2CFc) prepared by post-deposition modification, these monolayer do not show evidence for defects attributable to Ga($TC_{10}P$)(OH).

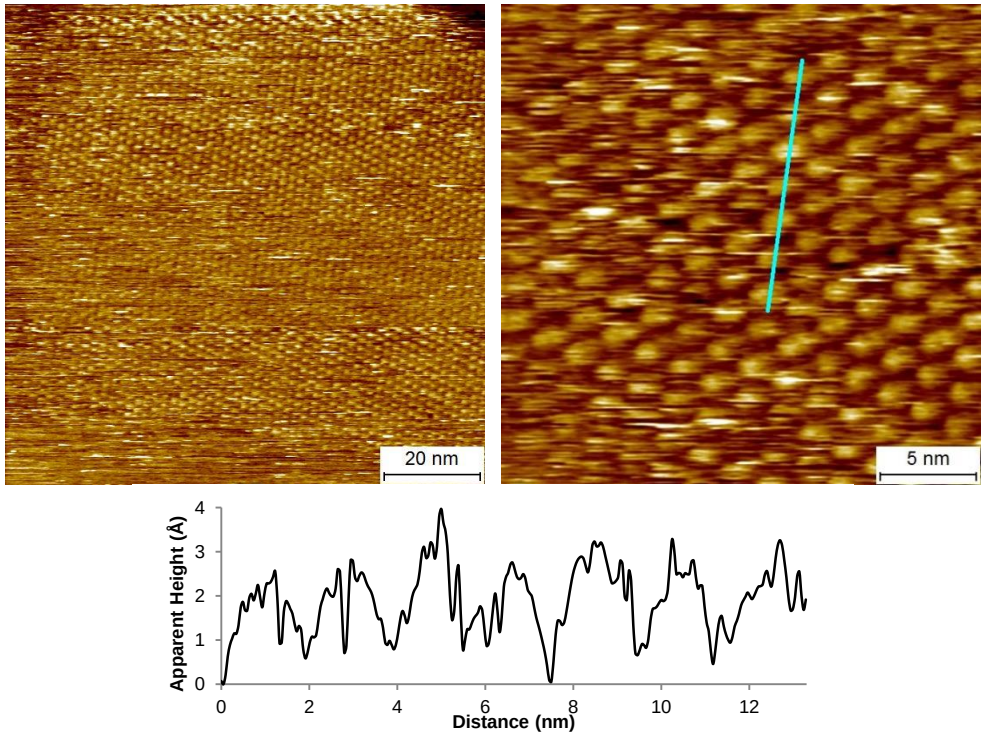

Figure 5.9. STM images and cross-sectional profile of a sample prepared by the sequential deposition of Ga($TC_{10}P$)(OH) and $C_{60}pyrC_6H_4CO_2H$ on HOPG ([Ga($TC_{10}P$)(OH)] = 2.0×10^{-4} M, [$C_{60}pyrC_6H_4CO_2H$] = 2.0×10^{-4} M) at the solid–liquid interface (1-phenyloctane; I = 6 pA, V = –1300 mV). The cross-sectional profile corresponds to the teal line in the image, drawn along the *b* lattice vector.

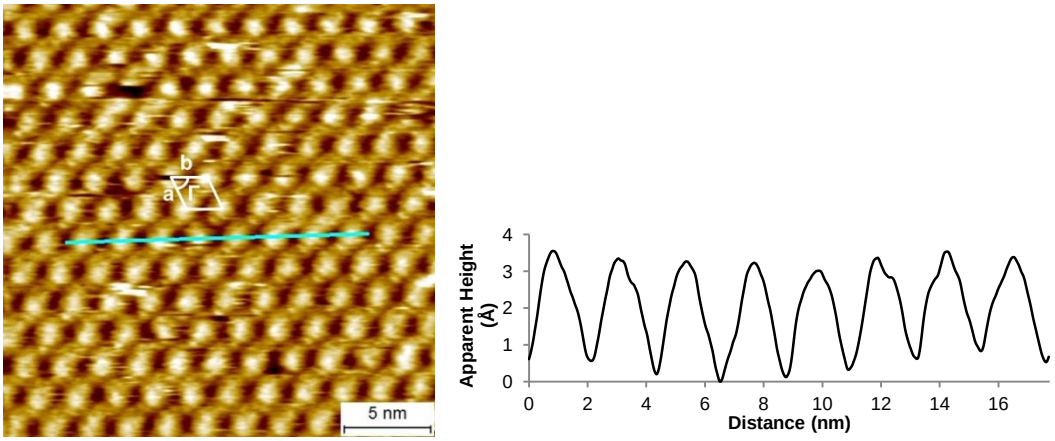

Figure 5.10. STM image and cross-sectional profile of a Ga($TC_{10}P$)($O_2CC_6H_4pyrC_{60}$) monolayer on HOPG at the solid–liquid interface (1-phenyloctane, 2.0×10^{-4} M; I = 8 pA, V = –1300 mV). The cross-sectional profile corresponds to the teal line in the image, drawn along the *a* lattice vector.

These observations are consistent with two possibilities. The first is that the observed monolayers result from deposition of $Ga(TC_{10}P)(O_2CC_6H_4pyrC_{60})$ molecules formed in solution onto bare HOPG formed as a result of dilution. The other possibility is that $Ga(TC_{10}P)(O_2CC_6H_4pyrC_{60})$ forms via reaction of surface-bound $Ga(TC_{10}P)(OH)$, but with the resulting monolayers undergoing structural rearrangement from the β to the δ structure in the ~5 min interval between the addition of the $C_{60}pyrC_6H_4CO_2H$ and STM tip engagement to the surface. In this second scenario, either the extent of reaction is much greater than for $Ga(TC_{10}P)(O_2CFc)$, or unreacted $Ga(TC_{10}P)(OH)$ molecules desorb during structural rearrangement of the $Ga(TC_{10}P)(O_2CC_6H_4pyrC_{60})$ monolayer.

5.3.5. Sequential Deposition of $Ga(TC_{10}P)(OH)$ and Substoichiometric $C_{60}pyrC_6H_4CO_2H$. In order to probe these possibilities further, the monolayers formed by reaction between a monolayer of $Ga(TC_{10}P)(OH)$ (2.0×10^{-4} M solution) with lower concentration solutions of $C_{60}pyrC_6H_4CO_2H$ (5.0×10^{-5} M and 1.0×10^{-4} M) on HOPG were investigated. In Section 5.3.1, it was shown that addition of 1.3×10^{-5} M $FcCO_2H$ to monolayers formed from a 2.0×10^{-4} M $Ga(TC_{10}P)(OH)$ solution resulted in the random incorporation of $Ga(TC_{10}P)(O_2CFc)$ into $Ga(TC_{10}P)(OH)$ lattice due to chemical modification of adsorbed molecules within the existing monolayers. If the reaction with substoichiometric $C_{60}pyrC_6H_4CO_2H$ proceeded similarly, newly formed $Ga(TC_{10}P)(O_2CC_6H_4pyrC_{60})$ molecules would be randomly scattered within a $Ga(TC_{10}P)(OH)$ lattice and would be distinguishable by comparing their molecular shapes and apparent heights to the unreacted molecules.

STM samples were prepared by depositing $Ga(TC_{10}P)(OH)$ from a 2.0×10^{-4} M solution, which resulted in the formation of self-assembled monolayers with the β structure. Addition of a drop of 5.0×10^{-5} M $C_{60}pyrC_6H_4CO_2H$ solution followed by STM imaging demonstrated the

presence of periodic monolayers spanning hundreds of nanometers in width (Figure 5.11). The monolayers retain the β packing geometry, with lattice parameters a = 1.63 ± 0.03 nm, b = 2.19 ± 0.06, Γ = 70 ± 2°; monolayers with the δ structure of Ga($TC_{10}P$)($O_2CC_6H_4pyrC_{60}$) were not observed across several samples. There is no evidence for incorporation of $C_{60}pyrC_6H_4CO_2H$ into the Ga($TC_{10}P$)(OH) monolayers, however; the adsorbed molecules uniformly appear as circular, ring-shaped features characteristic of Ga($TC_{10}P$)(OH) when imaged at this bias voltage (Figure 5.4f). In contrast, Ga($TC_{10}P$)($O_2CC_6H_4pyrC_{60}$) should appear as spherical features without a depression in the center, as indicated by images of a Ga($TC_{10}P$)($O_2CC_6H_4pyrC_{60}$) lattice recorded at –900 mV and –1000 mV (Figure 5.12). Based on these observations, it is concluded that the monolayers consist of unreacted Ga($TC_{10}P$)(OH) molecules.

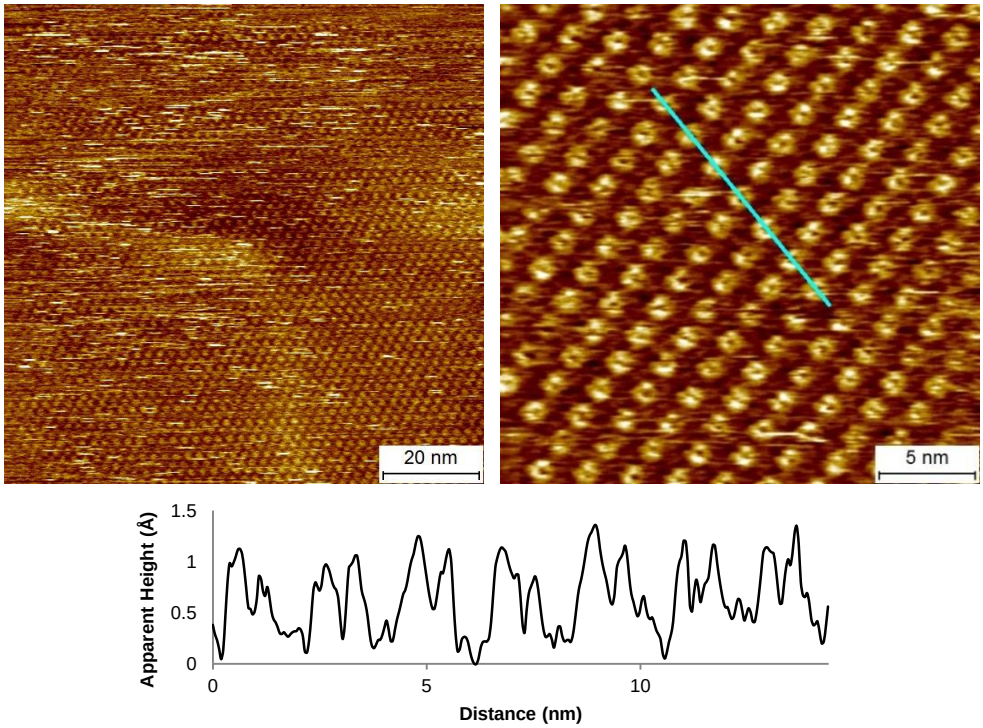

Figure 5.11. STM images of a Ga($TC_{10}P$)(OH) monolayer on HOPG at the solid–liquid interface after the addition of a drop of $C_{60}pyrC_6H_4CO_2H$ solution (1-phenyloctane, [Ga($TC_{10}P$)(OH)] = 2.0×10^{-4} M , [$C_{60}pyrC_6H_4CO_2H$] = 5.0×10^{-5} M; left: I = 8 pA, V = –950 mV; right: I = 7 pA, V = –950 mV). The cross-sectional profile corresponds to the teal line in the image, drawn along the *b* lattice vector.

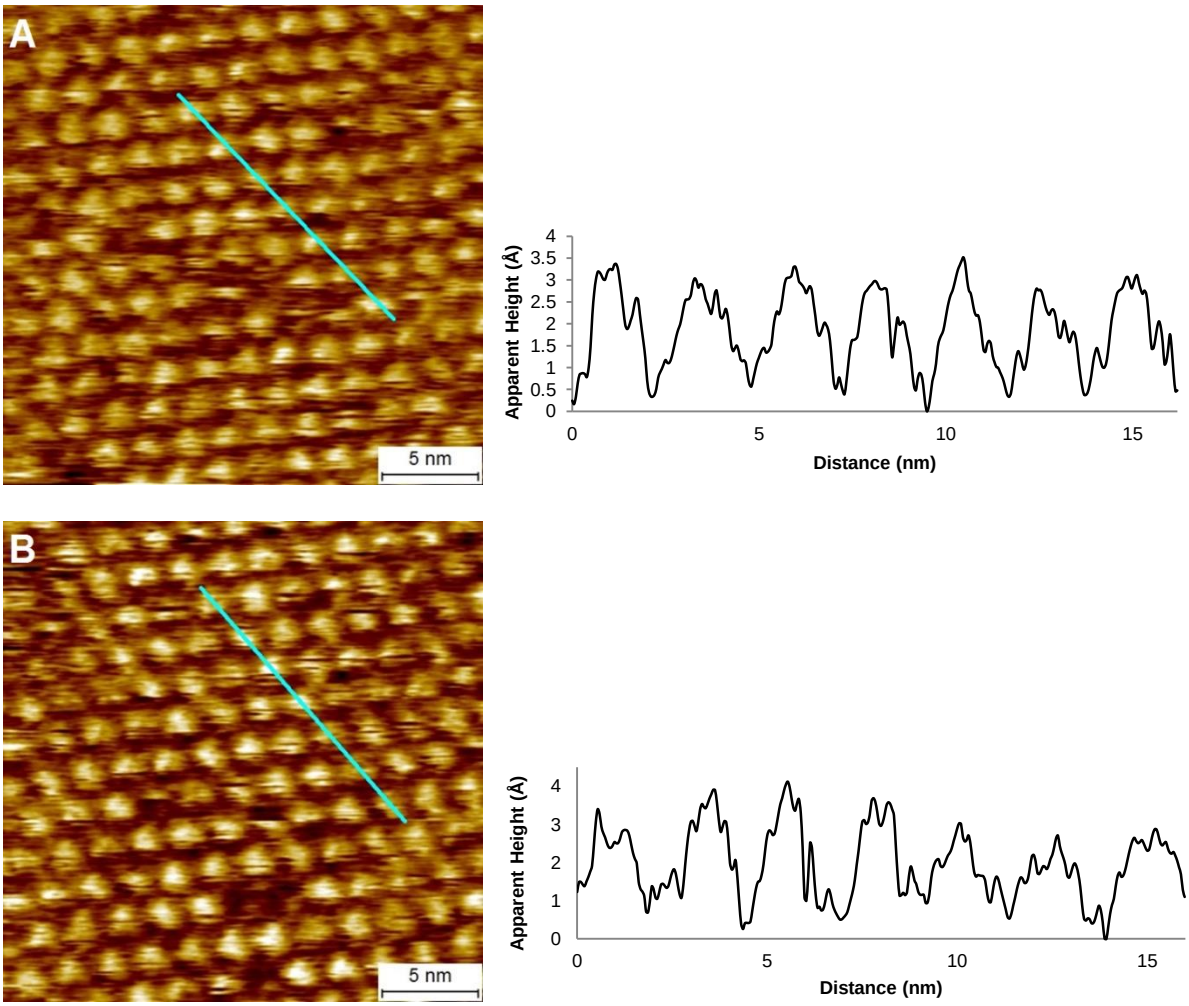

Figure 5.12. STM images and cross-sectional profile of a monolayer of Ga($TC_{10}P$)($O_2CC_6H_4pyrC_{60}$) (1.0×10^{-4} M, 1-phenyloctane; (A): I = 6 pA, V = –900 mV; (B): I = 6 pA, V = –1000 mV). The cross-sectional profiles correspond to the teal lines in the images, drawn along the *b* lattice vector.

The sequential deposition experiment was repeated using a solution of $C_{60}pyrC_6H_4CO_2H$ solution with a concentration of 1.0×10^{-4} M, which is double the concentration used in the preceding experiment but still one-half that of Ga($TC_{10}P$)(OH). When the samples were imaged after the addition of the $C_{60}pyrC_6H_4CO_2H$ solution to the pre-formed Ga($TC_{10}P$)(OH) monolayers, only small monolayers with widths of tens of nanometers were observed by STM (Figure 5.13). These structures exhibit the δ arrangement, with lattice parameters a = 1.73 ± 0.03 nm, b = 1.89 ± 0.08, Γ = 69 ± 2°. The adsorbates uniformly appeared as bright, spherical features

exhibiting apparent heights of ~3 Å; Ga($TC_{10}P$)(OH), when imaged at the same bias voltage (–1400 mV), shows less consistency in terms of feature shape and apparent heights (2.5–5 Å). These observations indicate that the monolayers resulting from the sequential deposition of 2.0×10^{-4} M Ga($TC_{10}P$)(OH) and 1.0×10^{-4} M $C_{60}pyrC_6H_4CO_2H$ solutions consist of Ga($TC_{10}P$)($O_2CC_6H_4pyrC_{60}$) molecules. Larger monolayer arrays, also with the δ structure, with widths spanning hundreds of nanometers were observed for the same samples when imaged 1 h after the initial addition of $C_{60}pyrC_6H_4CO_2H$ (Figure 5.14), suggesting the continuous deposition of molecules from solution.

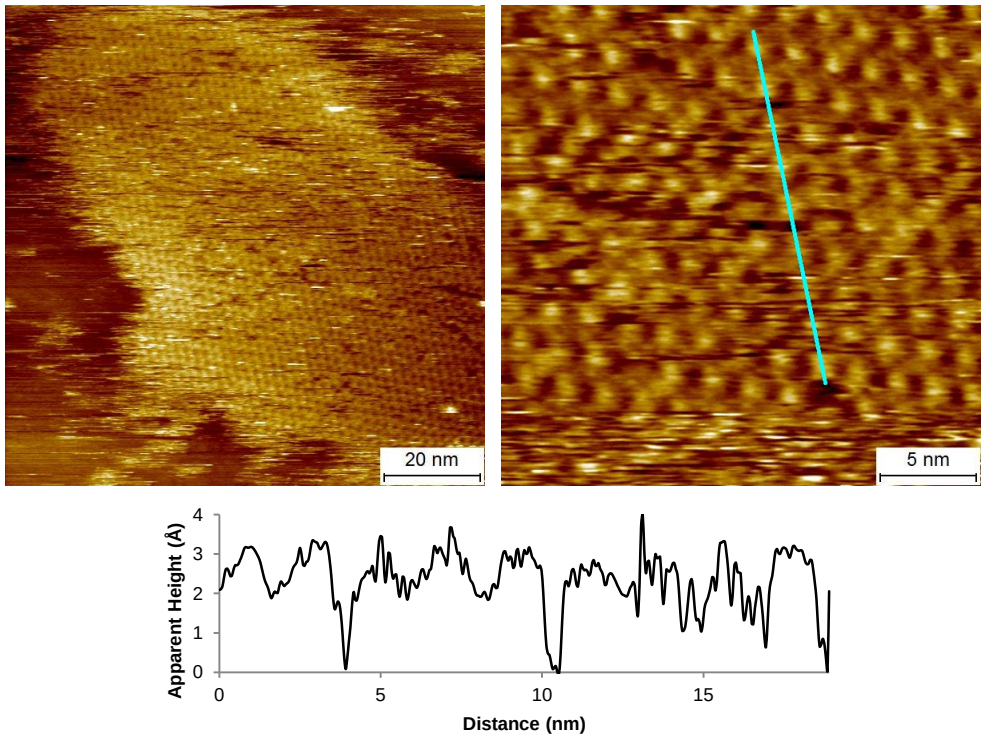

Figure 5.13. STM images and cross-sectional profile of a monolayer on HOPG prepared by the sequential deposition of Ga($TC_{10}P$)(OH) and $C_{60}pyrC_6H_4CO_2H$ ([Ga($TC_{10}P$)(OH)] = 2.0×10^{-4} M, [$C_{60}pyrC_6H_4CO_2H$] = 1.0×10^{-4} M) at the solid–liquid interface (1-phenyloctane; left: I = 6 pA, V = –1400 mV; right: I = 8 pA, V = –1400 mV). The cross-sectional profile corresponds to the teal line in the image, drawn along the *b* lattice vector.

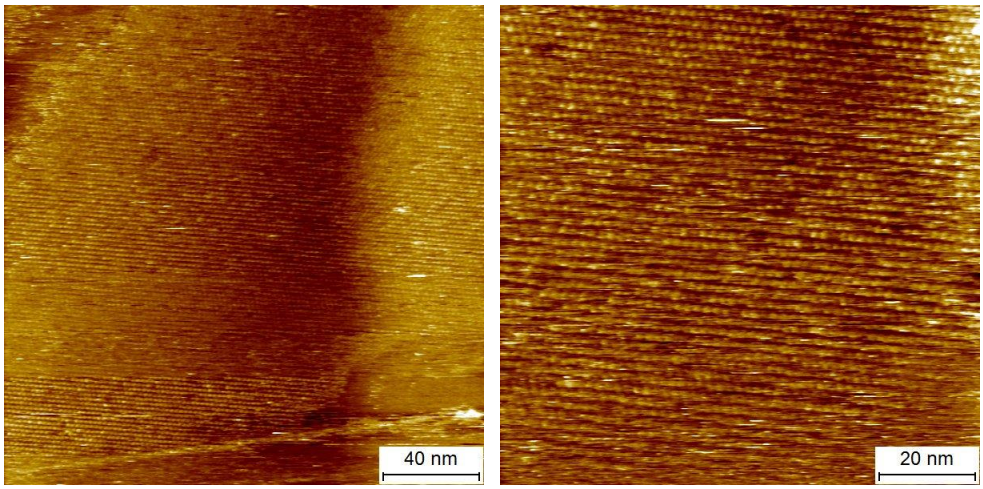

Figure 5.14. STM images of a sample prepared by the sequential deposition on HOPG of $Ga(TC_{10}P)OH$ and $C_{60}pyrC_6H_4CO_2H$ ($[Ga(TC_{10}P)(OH)] = 2.0 \times 10^{-4}$ M , $[C_{60}pyrC_6H_4CO_2H] = 1.0 \times 10^{-4}$ M) at the solid–liquid interface obtained 1 h after sample preparation (1-phenyloctane; $I = 8$ pA, $V = -1400$ mV).

The results from the STM studies of samples prepared via the sequential deposition of a 2.0×10^{-4} M $Ga(TC_{10}P)(OH)$ solution and substoichiometric $C_{60}pyrC_6H_4CO_2H$ are summarized as follows: 1) addition of a 5.0×10^{-5} M $C_{60}pyrC_6H_4CO_2H$ solution to $Ga(TC_{10}P)(OH)$ monolayers did not result in formation of adsorbed $Ga(TC_{10}P)(O_2CC_6H_4pyrC_{60})$ compounds within the existing porphyrin monolayer; 2) increasing the ligand concentration to 1.0×10^{-4} M resulted in replacement of $Ga(TC_{10}P)(OH)$ monolayers by small $Ga(TC_{10}P)(O_2CC_6H_4pyrC_{60})$ monolayers, which appeared to be larger when the samples were imaged again after 1 h. Based on these observations, it is concluded that the presence of $Ga(TC_{10}P)(O_2CC_6H_4pyrC_{60})$ monolayers with the δ structure after the sequential deposition of 2.0×10^{-4} M $Ga(TC_{10}P)(OH)$ and $C_{60}pyrC_6H_4CO_2H$ solutions is most likely the result of the deposition of $Ga(TC_{10}P)(O_2CC_6H_4pyrC_{60})$ molecules formed in solution. These observations may potentially be the result of a faster rate of reaction in the supernatant between $Ga(TC_{10}P)(OH)$ and $C_{60}pyrC_6H_4CO_2H$ compared to the reaction with $FcCO_2H$, which could prevent $C_{60}pyrC_6H_4CO_2H$ from reaching the $Ga(TC_{10}P)(OH)$ monolayers.

5.4. Conclusion

The post-deposition modification of $Ga(TC_{10}P)(OH)$ monolayers with $FcCO_2H$ to provide monolayers containing $Ga(TC_{10}P)(O_2CFc)$ has been successfully demonstrated by combining the propensity of $Ga(TC_{10}P)(OH)$ to form well-ordered structures and its reactivity towards $FcCO_2H$. Because the pre-assembled $Ga(TC_{10}P)(O_2CFc)$ dyad exclusively forms self-assembled monolayers with a structure that is distinct from that of $Ga(TC_{10}P)(OH)$ monolayers, observation of structural retention following the sequential deposition of $FcCO_2H$ and $Ga(TC_{10}P)(OH)$ indicated the successful incorporation of dyad molecules through the chemical modification of surface-bound $Ga(TC_{10}P)(OH)$. However, the generalizability of post-deposition modification as a sample preparation method has yet to be established because the sequential deposition of $Ga(TC_{10}P)(OH)$ and $C_{60}pyrC_6H_4CO_2H$ results in $Ga(TC_{10}P)(O_2CC_6H_4pyrC_{60})$ monolayers that appear to form from molecules made in solution; the chemical modification of the $Ga(TC_{10}P)(OH)$ monolayer cannot be conclusively established in this case. Since the formation of self-assembled monolayers is a complex process, further work will be required to understand the ways in which the incorporation of various axial ligands may affect the process, and to determine the requirements for the successful chemical modification of pre-assembled Ga-porphyrin monolayers.

5.5 References

1. Baisch, B.; Raffa, D.; Jung, U.; Magnussen, O. M.; Nicolas, C.; Lacour, J.; Kubitschke, J.; Herges, R. Mounting Freestanding Molecular Functions onto Surfaces: The Platform Approach. *J. Am. Chem. Soc.* **2009**, *131*, 442-443.

2. Kuhn, S.; Baisch, B.; Jung, U.; Johannsen, T.; Kubitschke, J.; Herges, R.; Magnussen, O. Self-Assembly of Triazatriangulenium-Based Functional Adlayers on Au(111) Surfaces. *Phys. Chem. Chem. Phys.* **2010**, *12*, 4481-4487.

3. Jung, U.; Kuhn, S.; Cornelissen, U.; Tuczek, F.; Strunskus, T.; Zaporojtchenko, V.; Kubitschke, J.; Herges, R.; Magnussen, O. Azobenzene-Containing Triazatriangulenium

Adlayers on Au(111): Structural and Spectroscopic Characterization. *Langmuir* **2011**, *27*, 5899-5908.

4. Otte, F. L.; Lemke, S.; Schütt, C.; Krekiehn, N. R.; Jung, U.; Magnussen, O. M.; Herges, R. Ordered Monolayers of Free-Standing Porphyrins on Gold. *J. Am. Chem. Soc.* **2014**, *136*, 11248-11251.

5. Lemke, S.; Chang, C.-H.; Jung, U.; Magnussen, O. M. Reversible Potential-Induced Switching of Alkyl Chain Aggregation in Octyl-Triazatriangulenium Adlayers on Au(111). *Langmuir* **2015**, *31*, 3115-3124.

6. Lemke, S.; Ulrich, S.; Claußen, F.; Bloedorn, A.; Jung, U.; Herges, R.; Magnussen, O. M. Triazatriangulenium Adlayers on Au(111): Superstructure as a Function of Alkyl Side Chain Length. *Surf. Sci.* **2015**, *632*, 71-76.

7. Bleger, D.; Mathevet, F.; Kreher, D.; Attias, A. J.; Bocheux, A.; Latil, S.; Douillard, L.; Fiorini-Debuisschert, C.; Charra, F. Janus-Like 3D Tectons: Self-Assembled 2D Arrays of Functional Units at a Defined Distance from the Substrate. *Angew. Chem., Int. Ed.* **2011**, *50*, 6562-6566.

8. Du, P.; Bléger, D.; Charra, F.; Bouchiat, V.; Kreher, D.; Mathevet, F.; Attias, A. J. A Versatile Strategy Towards Non-Covalent Functionalization of Graphene by Surface-Confined Supramolecular Self-Assembly of Janus Tectons. *Beilstein J. Nanotechnol.* **2015**, *6*, 632-639.

9. Du, P.; Kreher, D.; Mathevet, F.; Maldivi, P.; Charra, F.; Attias, A. J. Surface-Confined Supramolecular Self-Assembly of Molecular Nanocranes for Chemically Lifting and Positioning C_{60} above a Conducting Substrate. *ChemPhysChem* **2015**, *16*, 3774-3778.

10. Ikeda, T.; Asakawa, M.; Goto, M.; Miyake, K.; Ishida, T.; Shimizu, T. STM Observation of Alkyl-Chain-Assisted Self-Assembled Monolayers of Pyridine-Coordinated Porphyrin Rhodium Chlorides. *Langmuir* **2004**, *20*, 5454-5459.

11. Sakano, T.; Higashiguchi, K.; Matsuda, K. Comparison of Molecular Conductance Between Planar and Twisted 4-Phenylpyridines by Means of Two-Dimensional Phase Separation of Tetraphenylporphyrin Templates at a Liquid-HOPG Interface. *Chem. Commun.* **2011**, *47*, 8427-8429.

12. Ferreira, Q.; Alcácer, L.; Morgado, J. Stepwise Preparation and Characterization of Molecular Wires Made of Zinc Octaethylporphyrin Complexes Bridged by 4,4'-Bipyridine on HOPG. *Nanotechnology* **2011**, *22*, 435604.

13. Ferreira, Q.; Bragança, A. M.; Alcácer, L.; Morgado, J. Conductance of Well-Defined Porphyrin Self-Assembled Molecular Wires up to 14 nm in Length. *J. Phys. Chem. C* **2014**, *118*, 7229-7234.

14. Kamm, J. M.; Iverson, C. P.; Lau, W.-Y.; Hopkins, M. D. Axial Ligand Effects on the Structures of Self-Assembled Gallium-Porphyrin Monolayers on Highly Oriented Pyrolytic Graphite. *Langmuir* **2016**, *32*, 487-495.

15. Jurow, M.; Schuckman, A. E.; Batteas, J. D.; Drain, C. M. Porphyrins as Molecular Electronic Components of Functional Devices. *Coord. Chem. Rev.* **2010**, *254*, 2297-2310.

16. Otsuki, J. STM Studies on Porphyrins. *Coord. Chem. Rev.* **2010**, *254*, 2311-2341.

17. Yoshimoto, S.; Kobayashi, N. Supramolecular Nanostructures of Phthalocyanines and Porphyrins at Surfaces Based on the "Bottom-Up Assembly". *Struct. Bond* **2010**, *135*, 137-167.

18. Lehn, J. M. Toward Complex Matter: Supramolecular Chemistry and Self-Organization. *PNAS* **2002**, *99*, 4763-4768.

19. Whitesides, G. M.; Boncheva, M. Beyond Molecules: Self-Assembly of Mesoscopic and Macroscopic Components. *PNAS* **2002**, *99*, 4769-4774.

20. Barth, J. V. Molecular Architectonic on Metal Surfaces. *Annu. Rev. Phys. Chem.* **2007**, *58*, 375-407.

21. Visser, J.; Katsonis, N.; Vicario, J.; Feringa, B. L. Two-Dimensional Molecular Patterning by Surface-Enhanced Zn-Porphyrin Coordination. *Langmuir* **2009**, *25*, 5980-5985.

22. Otsuki, J.; Seki, E.; Taguchi, T.; Asakawa, M.; Miyake, K. STM Observation of Labile Axial Ligands to Zinc Porphyrin at Liquid/Solid Interface. *Chem. Lett.* **2007**, *36*, 740-741.

23. Friesen, B. A.; Bhattarai, A.; Mazur, U.; Hipps, K. W. Single Molecule Imaging of Oxygenation of Cobalt Octaethylporphyrin at the Solution/Solid Interface: Thermodynamics from Microscopy. *J. Am. Chem. Soc.* **2012**, *134*, 14897-14904.

24. den Boer, D.; Li, M.; Habets, T.; Iavicoli, P.; Rowan, A. E.; Nolte, R. J. M.; Speller, S.; Amabilino, D. B.; De Feyter, S.; Elemans, J. A. A. W. Detection of Different Oxidation States of Individual Manganese Porphyrins During Their Reaction with Oxygen at a Solid/Liquid interface. *Nat. Chem.* **2013**, *5*, 621-627.

25. *SPIP Software*, version 6.0.9; Image Metrology A.S: Hørsholm, Denmark

26. Chung, D. D. L. Review Graphite. *J. Mater. Sci.* **2002**, *37*, 1475-1489.

27. Horcas, I.; Fernandez, R.; Gomez-Rodriguez, J. M.; Colchero, J.; Gomez-Herrero, J.; Baro, A. M. WSXM: A Software for Scanning Probe Microscopy and a Tool for Nanotechnology. *Rev. Sci. Instrum.* **2007**, *78*, 013705.

28. Beggan, J. P.; Krasnikov, S. A.; Sergeeva, N. N.; Senge, M. O.; Cafolla, A. A. Self-Assembly of Ni(II) Porphine Molecules on the Ag/Si(111)-Ag/Si(111)-($\sqrt{3} \times \sqrt{3}$)R30° Surface Studied by STM/STS and LEED. *J. Phys.: Condens. Matter* **2008**, *20*, 015003.

29. Ogunrinde, A.; Hipps, K. W.; Scudiero, L. A Scanning Tunneling Microscopy Study of Self-Assembled Nickel(II) Octaethylporphyrin Deposited from Solutions on HOPG. *Langmuir* **2006**, *22*, 5697-5701.

30. Li, M.; den Boer, D.; Iavicoli, P.; Adisoejoso, J.; Uji-i, H.; Van der Auweraer, M.; Amabilino, D. B.; Elemans, J. A. A. W.; De Feyter, S. Tip-Induced Chemical Manipulation of Metal Porphyrins at a Liquid/Solid Interface. *J. Am. Chem. Soc.* **2014**, *136*, 17418-17421.

31. Baret, J. F. Kinetics of Adsorption from a Solution . Role of Diffusion and of the Adsorption-Desorption Antagonism. *J. Phys. Chem.* **1968**, *72*, 2755-2758.

32. Mikhailov, A.; Ertl, G. Pattern-Formation by Adsorbates with Attractive Lateral Interactions. *Chem. Phys. Lett.* **1995**, *238*, 104-109.

APPENDIX A

Synthesis and Characterization of Gallium-Porphyrin Double-Decker Complexes Bridged by Dicarboxylate Ligands

A.1. Experimental Section

A.1.1. Materials and General Methods. All synthetic and purification procedures were performed in air at room temperature. The synthesis of $Ga(TC_{10}P)(OH)$ is reported in Chapter 3. Pyrene-2,7-dicarboxylic acid was prepared from 2,7-dibromopyrene according to the literature procedure.[1] All other solvents, compounds and reagents were obtained from commercial sources and used as received.

A.1.2. Characterization of Compounds. ^{1}H NMR spectra were recorded at room temperature using a Bruker Avance II$^+$ 500 MHz NMR spectrometer. Chemical shifts for all ^{1}H NMR spectra are reported relative to $SiMe_4$ and were measured relative to solvent resonances.[2]

A.1.3. Preparation of $\{Ga(TC_{10}P)\}_2(\mu\text{-}O_2CC_6H_4CO_2)$ (DD1). To a solution of $Ga(TC_{10}P)(OH)$ (0.042 g, 0.044 mmol) in toluene (15 mL), terephthalic acid (0.004 g, 0.024 mmol) was added. The reaction mixture was stirred for 15 min, and the volatile components were removed *in vacuo*. The crude product was dissolved in diethyl ether (5 mL), after which acetonitrile (15 mL) was added. The solution was reduced in volume to ~15 mL under vacuum to induce precipitation of the product, which was isolated by filtration, washed with acetonitrile (5 mL), and dried under vacuum (0.038 g, 0.019 mmol, 85% yield). ^{1}H NMR (C_6D_6, 500.13 MHz): δ 9.38 (s, 16H, *β*), 4.70 (s. 4H, C_6H_4), 4.62 (t, 16H, $CH_2CH_2C\underline{H}_2Por$), 2.33 (m, 16H, $CH_2C\underline{H}_2CH_2Por$), 1.53 (m, 16H, $C\underline{H}_2CH_2CH_2Por$), 1.18–1.39 (m, 96H, $CH_3(C\underline{H}_2)_6CH_2$), 0.91 (t, 24H, CH_3). Chemical shifts at 9.58 ppm (s), and 9.54 ppm (s) indicated the presence of two

porphyrinic impurities (4% relative to the product), the latter of was attributed to $Ga(TC_{10}P)(OH)$; the former was tentatively attributed to $Ga(TC_{10}P)(O_2CC_6H_4CO_2H)$.

A.1.4. Preparation of $\{Ga(TC_{10}P)\}_2(\mu\text{-}O_2CC_{16}H_8CO_2)$ (DD2). To a solution of $Ga(TC_{10}P)(OH)$ (0.077 g, 0.081 mmol) in pyridine (15 mL), pyrene-2,7-dicarboxylic acid (0.011 g, 0.037 mmol) was added. The reaction mixture was refluxed for 1 h, and the volatile components were removed *in vacuo*. The crude product was dissolved in hot toluene (3 mL) and cooled at −20 °C overnight, which induced precipitation of the product as a dark purple solid. The product was collected via filtration, washed with toluene (3 × 5 mL) and hexanes (3 × 5 mL), then dried under vacuum (0.048 g, 0.020 mmol, 50% yield). ^{1}H NMR (C_6D_6, 500.13 MHz): δ 9.52 (s, 16H, *β*), 6.33 (s, 4H, Ar-$H_{4,5,9,10}$), 6.25 (s, 4H, Ar-$H_{1,3,6,8}$), 4.75 (t, 16H, $CH_2CH_2C\underline{H}_2$Por), 2.39 (m, 16H, $CH_2C\underline{H}_2CH_2$Por), 1.50 (m, 16H, $C\underline{H}_2CH_2CH_2$Por), 1.24 (m, 16H, $CH_3(CH_2)_5C\underline{H}_2$), 1.18–1.39 (m, 80H, $CH_3(C\underline{H}_2)_5CH_2$), 0.91 (t, 24H, CH_3). An unidentified impurity was observed at 1.37 ppm (m).

A.1.5. Sample Preparation for STM Experiments. Highly oriented pyrolytic graphite (HOPG) wafers (SPI-2 grade, SPI Supplies) measuring 7 mm × 7 mm × 1 mm were mounted to 12 mm diameter metal specimen discs with colloidal silver paste (PELCO, Ted Pella, Inc.). The surface of the HOPG substrate was cleaved with adhesive tape immediately prior to dosing. For STM experiments, one drop of a solution of the porphyrin compound in 1-phenyloctane was deposited onto the HOPG surface via syringe ($\{Ga(TC_{10}P)\}_2(\mu\text{-}O_2CC_6H_4CO_2)$, 2.5×10^{-4} M; $\{Ga(TC_{10}P)\}_2(\mu\text{-}O_2CC_{16}H_8CO_2)$, 1.0×10^{-4} M). The STM tip was then engaged through the drop and the sample was imaged.

A.2. Results and Discussion

A.2.1. Preparation and Characterization of Ga-Porphyrin Double Decker Complexes. The preparation of the two double-decker complexes, shown in Scheme A.1, was adapted from the synthesis of Ga-porphyrin-carboxylate compounds reported in Chapter 3. Ga($TC_{10}P$)(OH) was previously found to react with carboxylic acids in C_6D_6 to form Ga($TC_{10}P$)(O_2CR) complexes within ~5 min on the NMR scale in air at room temperature, even when the carboxylic acid (such as the C_{60}-modified benzoic acid, $C_{60}pyrC_6H_4CO_2H$) had low solubility. The facile synthesis of the Ga($TC_{10}P$)(O_2CR) complexes also applied to preparatory scale reactions performed in solvents such as toluene and diethyl ether.

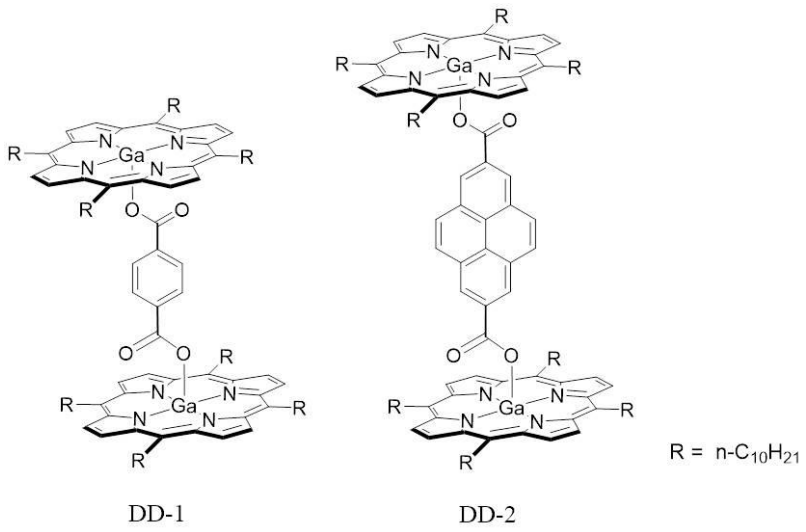

DD-1 DD-2

Scheme A.1. Molecular structures of DD-1 and DD-2.

The synthesis of DD-1 was achieved by reacting Ga($TC_{10}P$)(OH) with slightly more than 0.5 equivalents of terephthalic acid in toluene. Following the procedure used for the preparation of Ga($TC_{10}P$)(O_2CPh) and Ga($TC_{10}P$)(O_2CFc), the reaction mixture was allowed to stir for 15 min to ensure completion. Purification of the product also mimicked the procedure used for the aforementioned Ga($TC_{10}P$)(O_2CR) complexes due to the disparity in solubility of DD-1 and terephthalic acid in acetonitrile. The formation of DD-1 was established by ^{1}H NMR. A sharp

singlet at 4.70 ppm corresponded to the upfield shifted aryl proton resonance of the terephthalate bridging ligand. Compared to the ^{1}H NMR spectrum of Ga(TC$_{10}$P)(O$_2$CPh) recorded in the same solvent (C_6D_6), where the aryl proton resonances were found around 6 ppm, the upfield shifting of the aryl proton resonance of DD-1 is more pronounced, which was expected since the terephthalate ligand was subjected to ring current effects from two porphyrin subunits.[3] The ^{1}H NMR spectrum of DD-1, however, also revealed the presence of two porphyrinic impurities, as shown by the two sharp singlets observed at 9.54 ppm and 9.58 ppm; the former was attributed to Ga(TC$_{10}$P)(OH), and the latter was tentatively assigned as the monomeric Ga(TC$_{10}$P)(O$_2$CC$_6$H$_4$CO$_2$H) due its similarity to the β-H chemical shift of Ga(TC$_{10}$P)(O$_2$CPh) (9.59 ppm in C_6D_6). The two impurities (~4%) were persistently observed, and could not be removed or reduced in quantity through repeated precipitation from THF/acetonitrile.

DD-2 was initially prepared by the same procedure, and the unreacted pyrene-2,7-dicarboxylic acid was expected to be easily separable from the reaction mixture by filtration due to its insolubility in toluene. However, the crude samples of DD-2 were found to be only slightly soluble in toluene and required temperature of ~60 °C to dissolve (solutions with a concentration of 0.1 mM could be prepared), therefore modifications of the preparation method were required. In the modified procedure, pyridine was used as the solvent since both of the reactants were soluble, and a slight excess of Ga(TC$_{10}$P)(OH) was used to ensure complete consumption of pyrene-2,7-dicarboyxlic acid. The reaction mixture was heated at reflux for 1 h to ensure completion. After the volatile components were removed *in vacuo*, the crude reaction mixture was suspended in toluene and filtered to provide the product, which was washed with additional aliquots of toluene and hexanes to remove unreacted Ga(TC$_{10}$P)(OH) and possibly the monomeric Ga(TC$_{10}$P)(O$_2$CC$_{16}$H$_8$CO$_2$H). The formation of DD-2 was confirmed by ^{1}H NMR

characterization, where two sharp singlets at 6.33 ppm and 6.25 ppm, corresponding to the pyrenyl proton resonances, were observed. An impurity was consistently observed at 1.37 ppm, which was not removed by repeated washings with toluene and hexanes. However, since only one set of porphyrinic resonances was present, the impurity was thought to be unrelated to Ga($TC_{10}P$)(OH) and Ga($TC_{10}P$)($O_2CC_{16}H_8CO_2H$).

A.2.2. STM Imaging of the Double-Decker Complexes at the 1-Phenyloctane/HOPG Interface. The surface chemistry of the double-decker complexes was investigated at the 1-phenyloctane/HOPG interface. Deposition of a 2.5×10^{-4} M DD-1 solution in 1-phenyloctane on HOPG results in the formation of monolayers spanning tens of nanometers in width (Figure A.1). The adsorbed molecules appear as bright, disc-like features that exhibit apparent heights of ~1.5–2 Å, which is similar to the appearance of $H_2TC_{10}P$ molecules adsorbed on HOPG (see Chapter 2). The packing structure is described by the lattice parameters a = 1.68 ± 0.05 nm, b = 2.07 ± 0.03 nm, Γ = 76 ± 2°, which is similar to but distinct from the β structure exhibited by a number of Ga($TC_{10}P$)X complexes (X = Cl, OH, OPh; a = 1.7 nm, b = 2.1 nm, Γ = 70°) owing to the difference between their lattice angles. These observations are consistent with a structure in which one of the porphyrin cores of DD-1 is aligned parallel to the surface, with the second porphyrin forming part of a planar array placed above the surface by the terephthalate linker. Additional bias-dependence measurements are required to further elucidate their alignment. It is unlikely that these monolayers are associated with the trace impurities attributed to monomeric species (Ga($TC_{10}P$)(OH) and possibly Ga($TC_{10}P$)($O_2CC_6H_4CO_2H$)) because of the unique unit cell parameters.

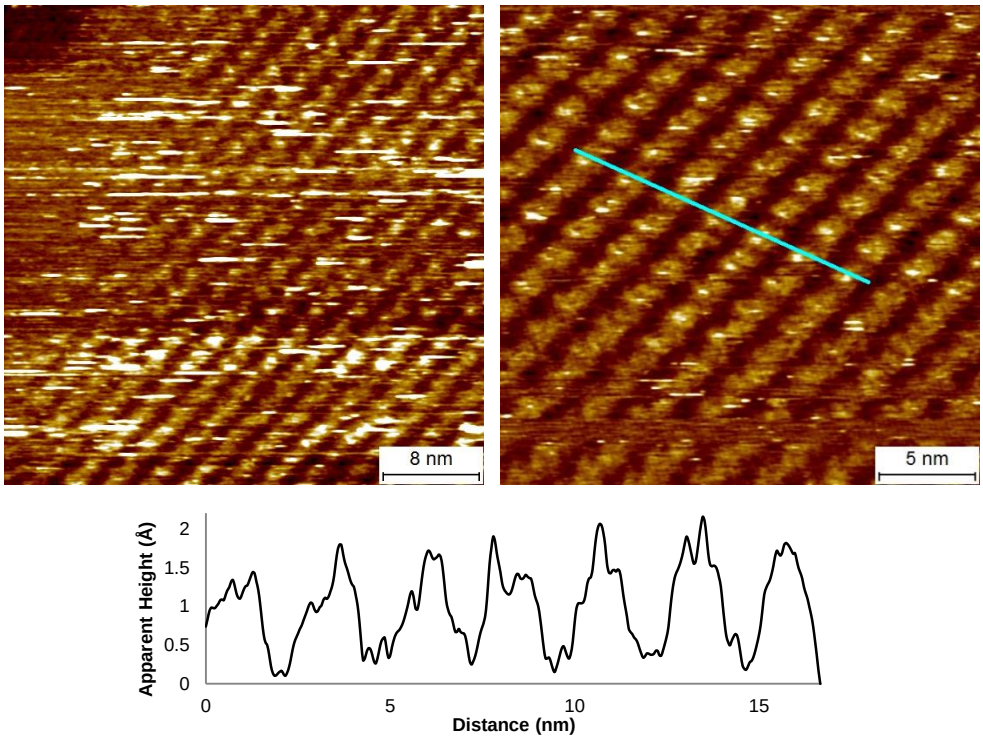

Figure A.1. STM images and cross-sectional profile of DD-1 monolayers on HOPG at the solid–liquid interface (1-phenyloctane, 2.5×10^{-4} M; left: I = 7 pA, V = −1050 mV; right: I = 10 pA, V = −975 mV). The cross-sectional profile corresponds to the teal line in the image, drawn along the *b* lattice vector.

Due to the lower solubility of DD-2 in 1-phenyloctane compared to DD-1, the STM solution was prepared at a concentration of 1.0×10^{-4} M. Deposition of the DD-2 solution on HOPG results in the formation of ordered monolayers, although a large number of small domains is observed as shown in the 100 nm × 100 nm STM image (Figure A.2). All of the observed domains exhibited a square lattice which had lattice vectors of ~1 nm, and a lattice angle of ~90°. The unit cell area is calculated to be ~1 nm^2, which is the same as the estimated surface-contact area of porphyrin ring.[4] If the monolayer consisted of DD-2 molecules, the unit cell area would require that none of the decyl chains be adsorbed; this is unlikely to result in a stable monolayer. While the observed structure does not resemble monolayers formed by $TC_{10}P$-based compounds, it is consistent with monolayers of pyrene-2,7-dicarboxylic acid studied formed at the solid-liquid interface.[1] In the reported system, which was prepared from a suspension of pyrene-2,7-

dicarboxylic acid in a mixture of heptanoic acid, 1,2,4-trichlorobenzene, and 1-undecanol in amounts equivalent to concentrations of approximately 10^{-4} M, monolayers exhibiting a square lattice were observed that were attributed to the hydrogen-bonding driven close-packing of pyrene-2,7-dicarboxylic acid molecules.

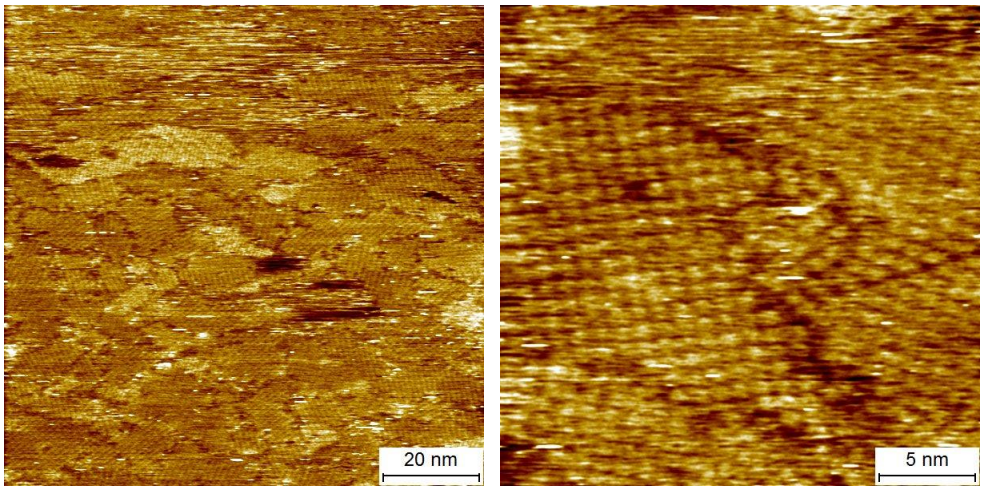

Figure A.2. STM images of an HOPG surface after the addition of a DD-2 solution obtained at the solid–liquid interface (1-phenyloctane, 2.5×10^{-4} M; $I = 8$ pA, $V = -800$ mV).

To account for the possibility that the observed structure is a result of the formation of self-assembled monolayer by a trace pyrene-2,7-dicarboxylic acid impurity in the DD-2 sample, the preparation of pyrene-2,7-dicarboxylic acid is attempted by adding a drop of 1-phenyloctane sonicated with pyrene-2,7-dicarboxylic acid on HOPG. STM imaging on multiple samples only shows bare HOPG, suggesting that pyrene-2,7-dicarboxylic acid monolayers cannot be prepared with 1-phenyloctane as the solvent. We do not yet understand why monolayers of pyrene-2,7-dicarboxylic acid are formed from DD-2 solutions when they cannot be prepared directly from the neat compound under comparable conditions.

A.3. References

1. Dang, H.; Maris, T.; Yi, J. H.; Rosei, F.; Nanci, A.; Wuest, J. D. Ensuring Homology Between 2D and 3D Molecular Crystals. *Langmuir* **2007**, *23*, 11980-11985.

2. Fulmer, G. R.; Miller, A. J. M.; Sherden, N. H.; Gottlieb, H. E.; Nudelman, A.; Stoltz, B. M.; Bercaw, J. E.; Goldberg, K. I. NMR Chemical Shifts of Trace Impurities: Common Laboratory Solvents, Organics, and Gases in Deuterated Solvents Relevant to the Organometallic Chemist. *Organometallics* **2010**, *29*, 2176-2179.

3. Buchler, J. W., Synthesis and Properties of Metalloporphyrins. In *The Porphyrins V1: Structure and Synthesis, Part 1*, Dolphin, D., Ed. Academic Press, Inc.: New York, 1978; Vol. I, pp 390-474.

4. Beggan, J. P.; Krasnikov, S. A.; Sergeeva, N. N.; Senge, M. O.; Cafolla, A. A. Self-Assembly of Ni(II) Porphine Molecules on the Ag/Si(111)-Ag/Si(111)-($\sqrt{3} \times \sqrt{3}$)R30° Surface Studied by STM/STS and LEED. *J. Phys.: Condens. Matter* **2008**, *20*, 015003.

APPENDIX B

Density Functional Theory Calculations of Gallium–Porphyrin Complexes

B.1. Experimental Section

B.1.1. Density Functional Theory (DFT) Calculations. Calculations were performed using Gaussian09.[1] Calculations employed the B3P86 functional,[2, 3] which was determined by a previous density functional benchmarking study to provide the best agreement between the calculated and experimentally determined molecular structures of Ga(octaethylporphyrin)Cl.[4] All calculations were performed on compounds in which the porphyrin 5,10,15,20-tetramethylporphyrin (TMeP) is used to model $TC_{10}P$. The LANL2DZ effective core potential basis set was used for Ga[5], Fe[6] and Ni,[6] while the 6-31G* basis set[7, 8] was used for all other atoms. No imaginary frequencies were obtained in subsequent vibrational calculations, confirming that the optimized structures reside at potential-surface minima.

B.2. Results and Discussion

B.2.1. DFT Calculations of Ga(TMeP)Cl and Ga(TMeP)(OPE) Complexes. The gas-phase molecular structures of the model complexes Ga(TMeP)Cl and Ga(TMeP)(OPE) (denoted **1′**, **2′**, **3′** see Chapter 2) were calculated using density functional theory in order to probe the influence of the axial ligand on the porphyrin core structure, with the aim of correlating any pronounced structural differences with the observed variations in adsorption behavior. The structure of 4-coordinate Ni(TMeP) was also calculated to provide a reference point for the structural effects of axial ligands. The calculated structures are shown in Figures B.1 (NiTMeP, Ga(TMeP)Cl) and Figure B.2 (Compounds **1′**–**3′**); selected bond distances and bond angles are presented in Table B.1.

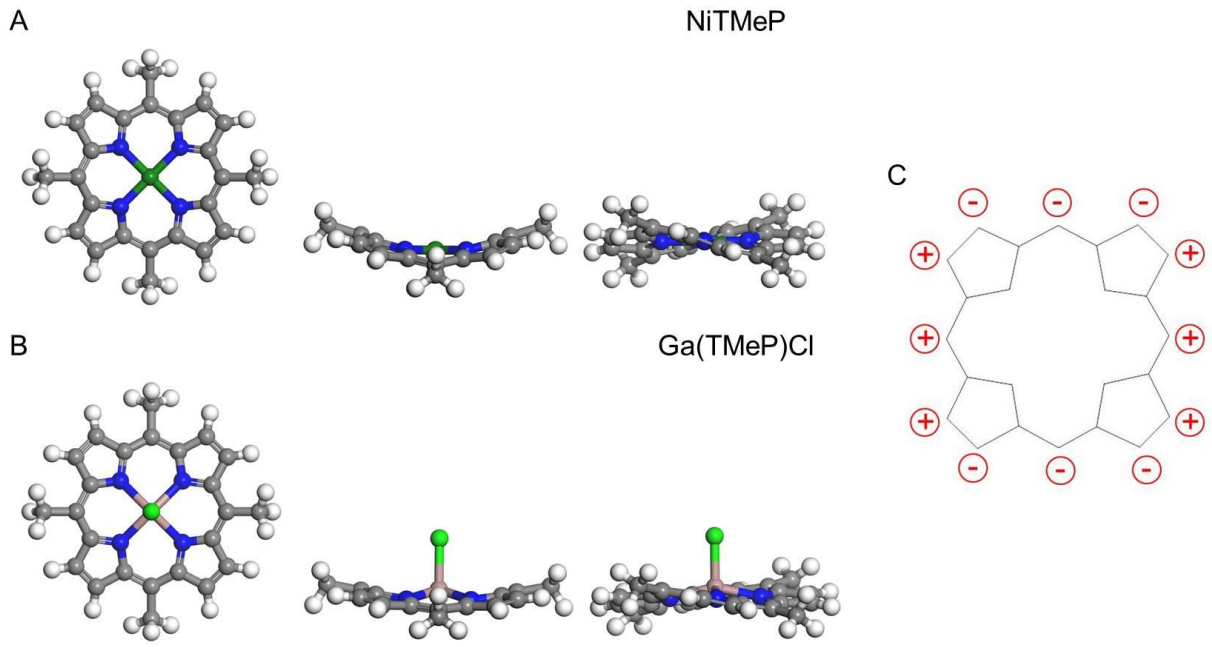

Figure B.1. Gas-phase DFT optimized structures of (A) NiTMeP and (B) Ga(TMeP)Cl. Atoms are color coded: Ga, pink; N, blue; C, black; O, red; H, white; Cl, light green; Ni, dark green. (C) Illustration of the *ruf* distortion.

Table B.1. Selected Bond Distances (Å) and Angles (°) for Ga(TMeP)Cl and Compounds **1′**–**3′** Complexes Calculated by Density Functional Theory.

		Compound			
Nuclei	NiTMeP	Ga(TMeP)Cl	**1′**	**2′**	**3′**
M–X	-	2.2360	1.9580	1.9612	1.9621
M–N(1)	1.921	2.040	2.058	2.057	2.057
M–N(2)	1.921	2.040	2.057	2.057	2.057
M–N(3)	1.921	2.040	2.059	2.056	2.056
M–N(4)	1.921	2.040	2.059	2.056	2.056
N(1)–M–X	-	102.9	104.5	104.2	104.2
N(2)–M–X	-	102.9	104.5	104.1	104.2
N(3)–M–X	-	102.9	104.4	104.4	104.3
N(4)–M–X	-	102.9	104.4	104.4	104.3
Ruffling Dihedral	38.1	23.4	23.5	23.6	23.7

Ga(TMeP)Cl is investigated to provide a reference point for the degree of core distortion that was inherent to *meso*-alkyl-substituted five-coordinate gallium complexes. As shown by its

optimized gas-phase structure in Figure B.1b, the porphyrin core of Ga(TMeP)Cl is distorted in the ruffled (*ruf*) conformation. The *ruf* deformation is characterized by the twisting of opposite pyrroles rings in opposite directions, which results in the distortion of the C_{20} plane with the *meso* carbons exhibiting the largest out-of-plane displacements; the N_4 plane, on the other hand, remains undistorted (Figure B.1c).[9] This mode of core distortion has been observed in crystal structures[10-13] and computational models[14] of 5,10,15,20-tetraalkylporphyrins with *meso*-substituents of various steric bulk. The magnitude of the ruffling deformation can be described by the *cis* C_α–N–N–C_α dihedral (ruffing dihedral) angle between opposite pyrrole rings, where a smaller angle represents distortion to a lesser degree.[15] The ruffling dihedral angle of Ga(TMeP)Cl is 26.2° (Table B.1), which is smaller than the ruffling dihedral angle calculated for NiTMeP (38.1°), showing that the incorporation of the GaCl subunit reduces the degree of core distortion. The four-fold symmetry of the inner core represented by the N_4 plane is preserved, as shown by the equivalence in the Ga–N bond lengths (2.040 Å) and the N–Ga–Cl bond angles (102.9°).

Previous work in our group has shown the introduction of CCPh as an axial ligand did not disrupt the approximate C_{4v} symmetry exhibited by other Ga(OEP)X (X = Cl, Br, I) complexes, but resulted in increased Ga–N bond lengths and N–Ga–X bond angles, accompanied by an increase in the degree of domed distortion.[4] A comparison between the calculated structures of compounds **1′**–**3′** to Ga(TMeP)Cl shows a similar increase in Ga–N bond lengths and N–Ga–X bond angles, signifying an increase in protrusion of the Ga atom from the N_4 plane. Although the introduction of the OPE ligands produces slight distortions from the local C_{4v} symmetry of the inner core (**1′**: ∠(N–Ga–C) = 104.4–104.5˚, *d*(Ga–N) = 2.057–2.059 Å; **2′**: ∠(N–Ga–C) = 104.1–104.4˚, *d*(Ga–N) = 2.056–2.057 Å; **3′**: ∠(N–Ga–C) = 104.2–104.3˚, *d*(Ga–

N) = 2.056–2.057 Å), unlike the symmetric core of Ga(TMeP)Cl, the magnitudes of the distortions are independent of OPE length. The local D_{2d} symmetry of the C_{20} core of all complexes largely ligand incorporation, as shown by the equivalence in all four *cis* C_{α}–N–N–C_{α} dihedral angles found in all complexes.

The degree of ruffling of compounds **1′**–**3′**, as measured by their ruffling dihedral angles (23.5–23.7°), are nearly identical to those of Ga(TMeP)Cl, suggesting that both the incorporation of CCR ligands and variation in OPE ligand length have little influence over the C_{20} plane distortion. Based on the comparisons between the calculated structures of Ga(TMeP)Cl and compounds **1′**–**3′**, it is unlikely that the observed differences in self-assembling behavior exhibited by Ga(TC_{10}P)Cl and the Ga(TC_{10}P)(OPE) complexes can be attributed to differences in porphyrin core distortions.

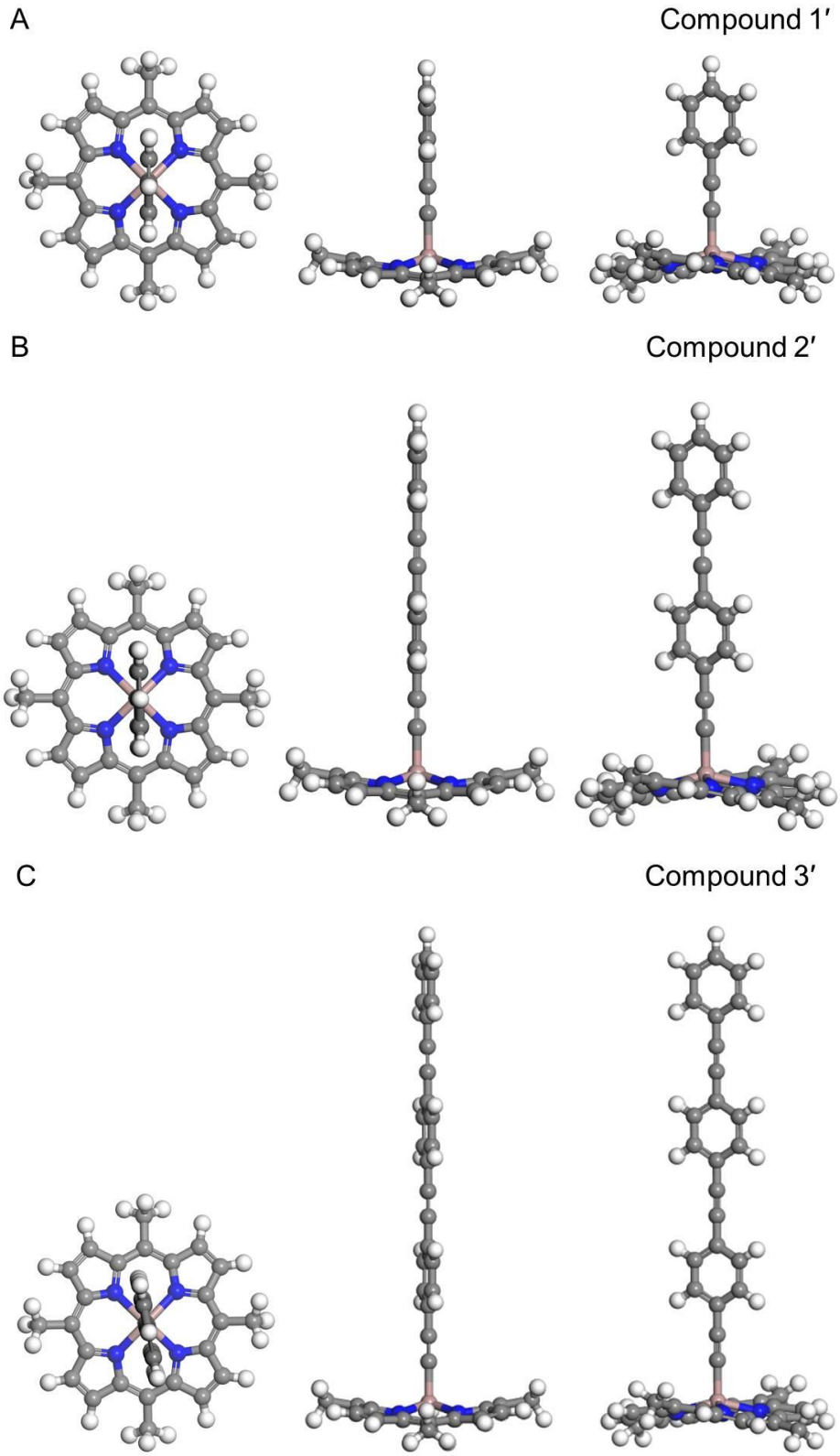

Figure B.2a–c. Gas-phase DFT optimized structures of compounds **1′**, **2′**, and **3′**. Atoms are color coded: Ga, pink; N, blue; C, black; O, red; H, white.

B.2.2. DFT Calculations on Ga(TMeP)(OR) and Ga(TMeP)(O_2CR) Complexes. The gas-phase molecular structures of Ga(TMeP)(OH), Ga(TMeP)(OR), and Ga(TCMeP)(O_2CR) model complexes were calculated using density functional theory in order to probe the influence of the axial ligand on the porphyrin core structure. The calculated structures are shown in Figures B.3; selected bond distances and bond angles are presented in Tables B.2 and B.3.

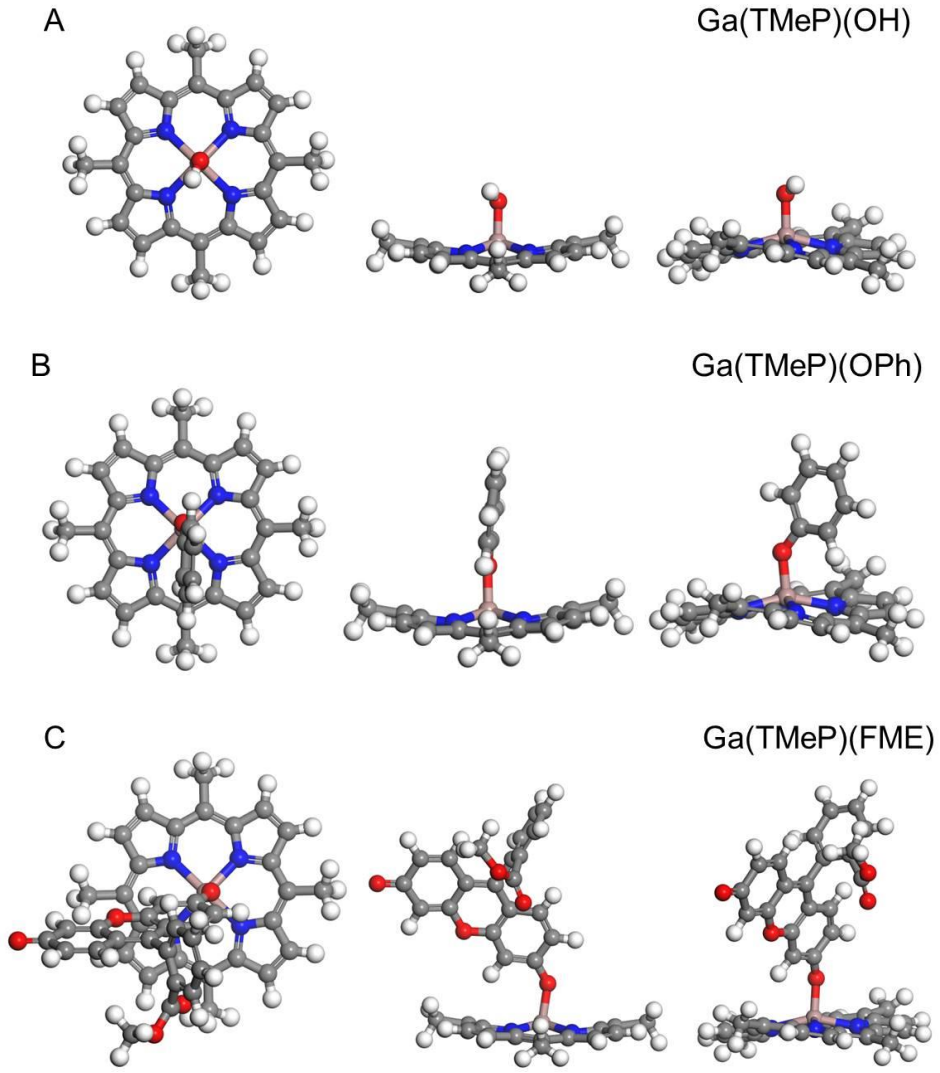

Figure B.3a–c. Gas-phase DFT optimized structures of (A) Ga(TMeP)(OH), (B) Ga(TMeP)(OPh), and (C) Ga(TMeP)(FME). Atoms are color coded: Ga, pink; N, blue; C, black; O, red; H, white.

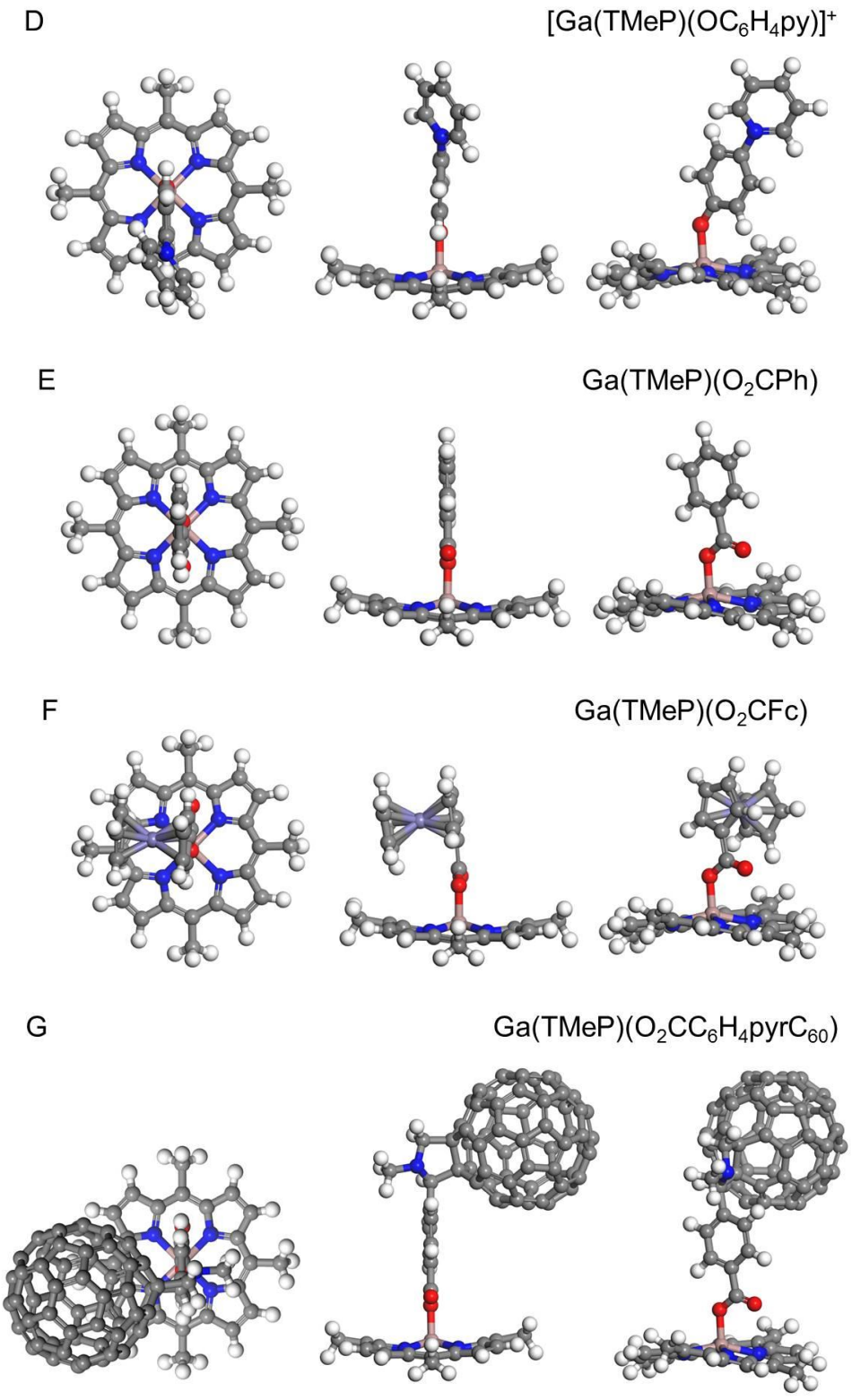

Figure 3.3d–g. Gas-phase DFT optimized structures of (D) $[Ga(TMeP)(OC_6H_4py)]^+$, (E) $Ga(TMeP)(O_2CPh)$, (F) $Ga(TMeP)(O_2CFc)$, and (G) $Ga(TMeP)(O_2CC_6H_4pyrC_{60})$. Atoms are color coded: Ga, pink; N, blue; C, black; O, red; H, white; Fe, purple.

Table B.2. Selected Bond Distances (Å) and Angles (°) for Ga(TMeP)(OR) Complexes Calculated by Density Functional Theory.

	Compound			
Nuclei	Ga(TMeP)(OH)	Ga(TMeP)(OPh)	[Ga(TMeP)(OC_6H_4py)]$^+$	Ga(TMeP)(FME)
Ga–O	1.7900	1.8190	1.8844	1.8465
Ga–N(1)	2.048	2.043	2.019	2.035
Ga–N(2)	2.066	2.045	2.028	2.039
Ga–N(3)	2.067	2.040	2.027	2.045
Ga–N(4)	2.060	2.043	2.018	2.044
Ga–N(avg)	2.060	2.043	2.023	2.041
N(1)–Ga–O	101.4	99.3	97.7	96.6
N(2)–Ga–O	106.9	107.6	104.2	107.5
N(3)–Ga–O	105.6	99.3	103.9	106.8
N(4)–Ga–O	104.6	107.0	97.7	98.0
N–Ga–O(avg)	104.6	103.3	100.9	102.2
Ga–O–R	114.0	135.7	137.1	137.5
C_α–N–N–C_α	21.7	26.1	23.7	18.4
	23.1	24.4	26.6	20.6
	22.1	24.7	24.0	20.5
	22.6	25.8	26.5	17.7
C_α–N–N–C_α (avg)	22.4	25.3	25.2	19.3

Table B.3. Selected Bond Distances (Å) and Angles (°) for Ga(TMeP)(O_2CR) Complexes Calculated by Density Functional Theory.

	Compound		
Nuclei	Ga(TMeP)(O_2CPh)	Ga(TMeP)(O_2CFc)	Ga(TMeP)($O_2CC_6H_4pyrC_{60}$)
Ga–O	1.8624	1.8582	1.8648
Ga–N(1)	2.049	2.033	2.047
Ga–N(2)	2.031	2.053	2.030
Ga–N(3)	2.031	2.034	2.031
Ga–N(4)	2.048	2.048	2.047
Ga–N(avg)	2.040	2.042	2.039
N(1)–Ga–O	98.5	107.2	98.6
N(2)–Ga–O	106.5	98.3	106.2
N(3)–Ga–O	106.4	105.9	106.2
N(4)–Ga–O	98.7	99.2	98.5
N–Ga–O(avg)	102.5	102.7	102.4
Ga–O–R	122.7	122.9	123.0
C_α–N–N–C_α	23.4	23.0	23.5
	21.4	20.6	21.3
	23.5	20.5	23.3
	21.3	22.9	21.4
C_α–N–N–C_α (avg)	22.4	21.8	22.4

The porphyrin cores of all complexes exhibit a ruffled structure, like those of Ga(TMeP)Cl and the Ga(TMeP)(OPE) complexes. Unlike the Ga(TMeP)(OPE) complexes, the axial ligands of Ga(TMeP)(OR) and Ga(TMeP)(O_2CR) complexes are axially unsymmetrical, which produce larger deviations in the N_4–Ga–R subunit; this is shown by the variations in Ga–N bond lengths, N–Ga–O bond angles, the ruffling dihedral angles (Table B.2, B.3). For the Ga(TMeP)(OR) complexes, the distortions in the N_4–Ga–O subunit mainly manifest in two sets of larger (e.g. Ga(TMeP)(OPh): ∠(Ga–O–R) = 107.0°, 107.6°) and smaller (e.g. Ga(TMeP)(OPh): ∠(Ga–O–R) = 99.3°, 99.3°) N–Ga–O bond angles, which is a result of the tilting of the Ga-aryloxide linkage towards the porphyrin plane (∠(Ga–O–R) = 135.7–137.5˚) as

well as the ligand orientations with respect to the N_4 plane. Similarly, the ruffling of the C_{20} cores of the Ga(TMeP)(OR) complexes are described by two sets of larger and smaller ruffling dihedral angles. However, the degree of ruffling varies between the three Ga(TMeP)(OR) complexes, with Ga(TMeP)(OPh) (average $\angle(C_\alpha\text{–N–N–}C_\alpha)$: 25.3°) and $[Ga(TMeP)(OC_6H_4py)]^+$ (average $\angle(C_\alpha\text{–N–N–}C_\alpha)$: 25.2°) exhibiting greater ruffling distortions compared to Ga(TMeP)Cl and the Ga(TMeP)(OPE) complexes, and Ga(TMeP)(FME) having a flatter C_{20} core (average $\angle(C_\alpha\text{–N–N–}C_\alpha)$: 19.3°). The structural characteristics of the axial ligand that determine the magnitude of deformation is unclear.

For the Ga(TMeP)(O_2CR) complexes, the axial asymmetry of the ligands also results in inequivalent Ga–N bond lengths, N–Ga–O bond angles, and ruffling dihedral angles, breaking the local C_{4v} symmetry of the N_4–Ga–O subunit and D_{2d} symmetry of the C_{20} core. All three structural parameters can be divided into two sets of larger and smaller values as a result of the alignment of the carboxylate subunit along the plane bisecting the two sets of Ga–N bonds. However, compared to the Ga(TMeP)(OR) complexes, the differences between the porphyrin structures of the three Ga(TMeP)(O_2CR) complexes are small, which can be attributed to the R group of the three complexes being oriented away from the porphyrin core by the carboxylic acid linker.

Although the observed differences in the surface chemistry of Ga(TC_{10}P)Cl and Ga(TC_{10}P)(OPE) complexes cannot be explained by the various porphyrin distortions, due to their subtle differences, the larger structural variations induced by the aryloxide and carboxylate ligands are larger and may influence the surface chemistry. Further theoretical and experimental work will be required to understand the relationship between molecular structure and self-assembling behavior.

B.3. References

1. Frisch, M. J.; Trucks, G. W.; Schlegel, H. B.; Scuseria, G. E.; Robb, M. A.; Cheeseman, J. R.; Scalmani, G.; Barone, V.; Mennucci, B.; Petersson, G. A.; Nakatsuji, H.; Caricato, M.; Li, X.; Hratchian, H. P.; Izmaylov, A. F.; Bloino, J.; Zheng, G.; Sonnenberg, J. L.; Hada, M.; Ehara, M.; Toyota, K.; Fukuda, R.; Hasegawa, J.; Ishida, M.; Nakajima, T.; Honda, Y.; Kitao, O.; Nakai, H.; Vreven, T.; Montgomery, J., J. A. ; Peralta, J. E.; Ogliaro, F.; Bearpark, M.; Heyd, J. J.; Brothers, E.; Kudin, K. N.; Staroverov, V. N.; Kobayashi, R.; Normand, J.; Raghavachari, K.; Rendell, A.; Burant, J. C.; Iyengar, S. S.; Tomasi, J.; Cossi, M.; Rega, N.; Millam, J. M.; Klene, M.; Knox, J. E.; Cross, J. B.; Bakken, V.; Adamo, C.; Jaramillo, J.; Gomperts, R.; Stratmann, R. E.; Yazyev, O.; Austin, A. J.; Cammi, R.; Pomelli, C.; Ochterski, J. W.; Martin, R. L.; Morokuma, K.; Zakrzewski, V. G.; Voth, G. A.; Salvador, P.; Dannenberg, J. J.; Dapprich, S.; Daniels, A. D.; Farkas, Ö.; Foresman, J. B.; Ortiz, J. V.; Cioslowski, J.; Fox, D. J. *Gaussian 09*, Revision A.2; Gaussian, Inc.: Wallingford, CT, 2009.

2. Becke, A. D. Density-Functional Thermochemistry. III. The Role of Exact Exchange. *J. Chem. Phys.* **1993**, *98*, 5648-5652.

3. Perdew, J. P. Density-Functional Approximation for the Correlation-Energy of the Inhomogeneous Electron-Gas. *Phys. Rev. B* **1986**, *33*, 8822-8824.

4. Kamm, J. M.; Iverson, C. P.; Lau, W.-Y.; Hopkins, M. D. Axial Ligand Effects on the Structures of Self-Assembled Gallium-Porphyrin Monolayers on Highly Oriented Pyrolytic Graphite. *Langmuir* **2016**, *32*, 487-495.

5. Wadt, W. R.; Hay, P. J. *Ab Initio* Effective Core Potentials for Molecular Calculations - Potentials for Main Group Elements Na to Bi. *J. Chem. Phys.* **1985**, *82*, 284-298.

6. Hay, P. J.; Wadt, W. R. Abinitio Effective Core Potentials for Molecular Calculations - Potentials for the Transition-Metal Atoms Sc to Hg. *J. Chem. Phys.* **1985**, *82*, 270-283.

7. Francl, M. M.; Pietro, W. J.; Hehre, W. J.; Binkley, J. S.; Gordon, M. S.; Defrees, D. J.; Pople, J. A. Self-Consistent Molecular-Orbital Methods. XXIII. A Polarization-Type Basis Set for Second-Row Elements. *J. Chem. Phys.* **1982**, *77*, 3654-3665.

8. Hariharan, P. C.; Pople, J. A. Influence of Polarization Functions on Molecular-Orbital Hydrogenation Energies. *Theor. Chim. Acta* **1973**, *28*, 213-222.

9. Senge, M. O. Exercises in Molecular Gymnastics - Bending, Stretching and Twisting Porphyrins. *Chem. Commun.* **2006**, 243-256.

10. Ema, T.; Senge, M. O.; Nelson, N. Y.; Ogoshi, H.; Smith, K. M. 5,10,15,20-Tetra-Tert-Butylporphyrin and Its Remarkable Reactivity in the 5- and 15-Positions. *Angew. Chem., Int. Ed. Engl.* **1994**, *33*, 1879-1881.

11. Runge, S.; Senge, M. O.; Ruhlandt-Senge, K. 5,10,15,20-Tetrakis(diphenylmethyl)porphyrin - A Nonplanar Porphyrin with Intermediate Degree of Ruffling. *Z. Naturforsch.* **1999**, *54*, 662-666.

12. Senge, M. O.; Bischoff, I.; Nelson, N. Y.; Smith, K. M. Synthesis, Reactivity and Structural Chemistry of 5,10,15,20-Tetraalkylporphyrins. *J. Porphyrins and Phthalocyanines* **1999**, *3*, 99-116.

13. Senge, M. O.; Ema, T.; Smith, K. M. Crystal-Structure of a Remarkably Ruffled Nonplanar Porphyrin (Pyridine)[5,10,15,20-Tetra(Tert-Butyl)Porphyrinato]Zinc(II). *J. Chem. Soc., Chem. Commun.* **1995**, 733-734.

14. Jentzen, W.; Simpson, M. C.; Hobbs, J. D.; Song, X.; Ema, T.; Nelson, N. Y.; Medforth, C. J.; Smith, K. M.; Veyrat, M.; Mazzanti, M.; Ramasseul, R.; Marchon, J. C.; Takeuchi, T.; Goddard, W. A.; Shelnutt, J. A. Ruffling in a Series of Nickel(II) meso-Tetrasubstituted Porphyrins as a Model for the Conserved Ruffling of the Heme of Cytochromes *c*. *J. Am. Chem. Soc.* **1995**, *117*, 11085-11097.

15. Cullen, D. L.; Desai, L. V.; Shelnutt, J. A.; Zimmer, M. Conformational Analysis of the Nonplanar Deformations of Cobalt Porphyrin Complexes in the Cambridge Structural Database. *Struct. Chem.* **2001**, *12*, 127-136.